The University Of Sheffield.

Fatigue Performance of Ti-6Al-4V Drilled Plates

Ioannis Violatos

The University of Sheffield

Department of Materials Science and Engineering

A thesis submitted in partial fulfilment of the requirements for the degree

of

Doctor of Philosophy

March 2017

This page has been intentionally left blank

Abstract

Ti-6Al-4V drilled plates were subjected to cyclic loading tests in a previous study, which investigated the machining-induced effects on fatigue [1]. The majority of the specimens failed between low to moderate number of cycles, close to the surface of the hole, around the half thickness plane, with no clear crack initiation point. Differences in the performance of the plates were associated to the initiation of cracks from subsurface microstructure defects. However, a clear explanation of the mode of failure and the mechanisms behind it were not established due to the scattering of the fatigue data and the need for a more detailed examination of deformed microstructures and elastoplastic strain fields. This postulated the main research objective for the current study. A selected number of specimens after the fatigue tests were re-examined to identify the critical defects. The preliminary analysis included surface roughness, micro-hardness, LOM, and SEM of the machining-affected layer. Then, advanced characterization techniques, namely EBSD and FIB, were transformed into semi and fully quantitative methods to identify plastic strain gradients and residual stress profiles within the material. Despite the different drilling conditions, the specimens had similar roughness values. However, the plastic deformation and residual stress profiles within the material were directly related to each other and to the drilling conditions. All specimens displayed strain localization within smaller alpha grains of the sheared underlying microstructure, while tensile twins and slip bands were visible below the heavily deformed and strain hardened zone. Tensile, surface or near-surface stresses were measured for all drilling conditions at different locations around the hole. The results indicated that specimens with lower levels of deformation had superior fatigue performance. Since all specimens had identical defects, though to a different depth, it was deemed necessary to examine the fractured surface of the specimens. A closer inspection of the machined surfaces at the locations of the crack initiation revealed that chip fragments, embedded on the surface of the hole, were the critical defect dominating the fatigue life. Surface smearing and intense drilling marks were generating non-critical cracks. Chip cracking, voids within the chip, surface damage and cavities from the embedment of the chip, and shielding of surface twins by the chip were observed in the specimens. An exact description of the failure mechanism(s) was not possible because all of them appeared to be crack nucleation sites. The current study was concluded at this point providing the groundwork and the tools for future work.

Acknowledgements

I would like to thank everyone who has helped me become a better professional, researcher and person. It was a big journey and starting a long time ago, but I do not regret taking it. This journey started from the Department of Environmental Engineering at the Technical University of Crete, continued to the Department of Civil Engineering at the University of Surrey and to the Department of Civil Engineering at the University of Sheffield and concluded at the Department of Materials Science & Engineering at the University of Sheffield. I am very grateful for what they have done for me.

There are certain people who played an important role during this research project, my supervisors, Dr. Meurig Thomas, Dr. James Castle and Prof. Bradley Wynne. They provided all the necessary means to carry out my research and they challenged me to achieve even greater heights. I feel indebted to a number of fellow researchers and technicians for assisting with experimental work: Dr. Le Ma, Dr. Peng Zeng, Dr. Cheryl Shaw and Dr. Peter Korgul from the Sorby Center for Electron Microscopy for their valuable technical support. I should not fail to acknowledge the Advanced Forming Research Center and the Cullum Center for Fusion Energy for providing access to their equipment.

The Department of Materials Science and Engineering has been a wonderful place, full of great people that I am really missing it now that I have moved away. Some people made the everyday routine a bit more interesting and I would like to wish the best to Mark Todd, Mat Hand, and James Pollard. Special thanks to the Advanced Metallic Systems Centre for Doctoral Training for providing the opportunity and the skills to undertake this project and Dr. Claire Hincliffe who did an excellent job coordinating this programme.

I'd like to recognise the financial support of the Engineering and Physical Sciences Research Council and BOEING for providing the funding which made all of this possible. I'd also like to express my gratitude towards the United Kingdom for providing me the opportunity to study in one of the best educational and research institutes and build the foundation for a successful career.

However, I would never have achieved anything without the continuous support from my family. My parents Artemis and Andreas, my two sisters Anastasia and Sapfo, and my grandmother Sapfo have been a big influence in my life, a source of inspiration and drive, and my constant in this world. This thesis is dedicated to all of you.

Contents

List of Tables

List of Figures - Thesis

List of Figures - Appendix

Nomenclature

General	
bcc	body centered cubic (crystal structure)
CP-Ti	Commercial pure Titanium (alpha Titanium alloy with specific oxygen content)
DIC	Digital image correlation
FE	Finite element
hcp	hexagonal closed packed (crystal structure)
IST	Intermediate strain and twinnig zone
LS	Low strain zone
Ti	Titanium
Ti-6Al-4V	Titanium alloy
PE	Plastic strain
RS	Residual stresses
SPD	Severe plastic deformation zone
α	alpha phase, hexagonal close packed crystal structure of Titanium
β	beta phase, body centered cubic crystal structure of Titanium
Bragg's equation	
n	Integer
λ	Wavelength of the incident electrons
d	Spacing of diffracting planes
θ	Angle of the incident electrons
Characterization Techniques	
AMIS	Average intragrain misorientation
BC	Band contrast (EBSP image quality factor)
BS	Band slope (EBSP image quality factor)
BSE	Backscatter electrons
CD	Crystal deformation
EBSD	Electron Backscattered Diffraction
EBSP	Electron Backscattered Pattern
FEG	Field emission gun
GAM	Grain average misorientation
GND	Geometric necessary dislocations
GOS	Grain orientation spread
IMD	Integrated angular misorientation density
KAM	Kernel average misorientation
MAD	Mean Angular Deviation (Goodness of fit between simulated and detected EBSPs)
LGB	low-angle grain boundaries
LOM	Light Optical Microscopy
MGM	Mean grain misorientation
ND	Normal direction
RD	Rolling direction
SEM	Scanning Electron Microscopy
SSD	Statistically stored dislocations
TD	Transverse direction
wMGM	weighted mean grain misorientation
Orientation relationships	
G	Rotation matrix of sample axes to crystal axes
Oc	Symmetry operators for crystals

rm	rotation axis vector
φ_1	Euler angle-first rotation by Bunge convection
Φ	Euler angle-second rotation by Bunge convection
φ_2	Euler angle-third rotation by Bunge convection
Δgd	Disorientation
θm	Misorientation angle

Residual stress measurement

RS	Residual stresses
ESPI	Electronic Speckle Particle Interferometry
FIB	Focused ion beam (FEG/SEM microscope)
PT	Platinum
XRD	X-ray diffraction
YSZ	Yttrium stabilize Zirconia

Surface Topography

CTF	Fourier fitting after Cylindrical & Tilt corrections on surface topography
F	Fourier fitting on surface topography
VSI	Vertical Scanning Interferometry
Ra	Average roughness (μm)
Rp	Max Peak Height (μm)
Rq	Root Mean Square Roughness (μm)
Rv	Max Valley Depth (μm)
Rt	Maximum Height (μm)
Sa	Average Roughness (μm)
Sku	Kurtosis (μm)
Sp	Max Peak Height (μm)
Sq	Root Mean Square Roughness (μm)
Ssk	Skewness (μm)
Sv	Max Valley Depth (μm)
Sz	Ten Point Height (μm)

Chapter 1. Introduction

1.1 Preface

Titanium alloys have become an attractive option for the aerospace industry. Due to their mechanical properties and good strength to weight ratio, they have replaced more traditional materials. The percentage of titanium in modern aircraft is rising, driven by the increasing demands for weight reduction and safety improvements. As the production route of titanium alloys is optimized and new alloys are developed, titanium will become an, even more, cost effective solution and access other industries [2].

Machining operations are one of the last manufacturing processes for most components. Advancements in the field of cutting tools and equipment have been dramatic over the past decades, in response to the introduction of new and difficult to machine materials, the requirement for very tight tolerances and the design of parts with complex geometry or very detailed features [3]. In contrast, surface integrity of final components has not received the same attention. Furthermore, the links of surface integrity to the in-service performance are not well established or investigated. This is particularly true for titanium and its alloys.

The research project was initiated by the need to drill holes in Ti-6Al-4V plates at higher speeds, under controlled and repeatable conditions in an automated machine, which would result in an acceptable fatigue performance. Different cutting conditions and strategies were examined in the parent study [1] and ranked according to their fatigue life. Fatigue tests were carried out in strip coupons with seven holes to obtain more information in partially cracked or uncracked holes. There was a significant variation of the fatigue lives, even between specimens with the same drilling conditions, attributed to the microstructure aspects of surface integrity. Surface roughness was moderate and equivalent for all specimens. However, it was not possible to examine other aspects of surface integrity, particularly deformed microstructures, strain hardening, residual stresses and plastic strain gradients/concentrations. Thus, it was not possible to identify the critical defect and the dominant failure mechanism.

This thesis contains the continuation study, carried out based on the findings and recommendations for future work of the parent study. As part of the current research project, it was required to fully characterize the surface integrity and correlate it to the drilling conditions and the fatigue lives of the specimens. The main hypothesis was that the failure of the plates had its origins in the crack nucleation and initiation within the deformed microstructure, in line with the literature review and the parent study. The

features which could have nucleated the crack were assumed to be machining-induced crystal defects, like twins and slip bands, or strain localization and distorted grain/phase boundaries. Strain hardening and residual stresses should also affect the short and long crack propagation path and/or rates, hence the fatigue life of the specimens. If all the machining-induced effects were characterized, it should be possible to explain variations in the fatigue lives of the drilled plates.

There was a clear aim to develop tools, capable of quantifying elastoplastic micro-strains, with excellent spatial resolution, to obtain location specific information. Plastic strain mapping has been carried out in the past with a variety of techniques [4] [5], but mainly area-average, macro-methods are available for elastic strains, often limited in flat specimens [6]. The transformation of advanced characterization techniques based on Electron Back Scatter Diffraction (EBSD) and Focused Ion Beam (FIB) milling/imaging provided the required level of detail. Both methods were developed and validated on peened CP-Ti [7]. The specimens investigated by EBSD and FIB were un-cracked parts of the drilled plate strips after the fatigue tests.

Surface roughness was equivalent for all conditions, but LOM and SEM images indicated that the depth of the deformed layer was different for each machining condition. However, all specimens displayed shearing of the microstructure, sites of strain localization, distortion of alpha and beta grains, twins, slip bands and variations in the thickness of the deformed layer, along and across the hole. A severe plastic deformation (SPD) zone existed close to the edge of the hole, followed by an intermediate strain zone where twinning occurs (IST). No beta phase depletion or alpha case formation were observed near the machined edge. There were evidence of strain hardening within the distorted microstructure and significant variations thereafter. The preliminary analysis served as a reference for the detailed characterization of the machined specimens with EBSD.

EBSD revealed the depth of the plastic deformation, low strain regions, strain localization, the limits of each zone, slip band formation and tensile twins within the deformed material. There was a variation of the profiles around the hole due to the highly textured material. More aggressive drilling conditions were associated with higher levels of plastic strains, deeper strain profiles and had reduced fatigue life. The links between the depth of deformed layer, machining conditions, and fatigue performance were confirmed, but it was understood that all specimens had identical microstructural defects. Thus, it was unlikely that the critical defect had its origins in the deformed microstructure. Further characterization work was rendered redundant with regard to the main research

objective. Instead, the direction of the project was shifted towards another parameter of surface integrity, the residual stresses.

FIB micro-machining provided residual stress measurements in the microscale. It was found that residual stresses generally followed the plastic strain profile, i.e. deeper plastic strain profiles resulted in deeper residual stresses profiles with the peak of the stresses close to the limit of the plastic deformation zone, at the end of the twinning zone. Tensile peaks were also detected close to the hole in both low and highly deformed specimens. The tensile peaks were part of a continuous profile, located in the severe plastic deformation zone, close to the edge of the hole(s), which would then dissipate and transition to prolonged compressive stresses. Peak compressive stresses were approximately half the yield stress of the material and occurred below the twinning regions. Similarly, to plastic strains, more aggressive drilling conditions were associated with higher levels of residual stresses, deeper profiles and had reduced fatigue life. Due to the nature of the deformation processes, it was possible to associate the measured profiles with plastic strain gradients and microstructure features. However, there was considerable variation of the residual stresses, even for the same process conditions, attributed to the chip formation process and the underlying microstructure.

The microstructural defects between the specimens were identical and only the location was varying, though to higher depth for more deformed material. At the same time, all specimens exhibited tensile peaks close to the edge as part of the prolonged compressive stress field. Furthermore, it was not possible to identify a critical defect or pre-cracking in the specimens under investigation. That led to the re-examination of the fracture surfaces of the specimens to obtain the exact crack initiation point, in an attempt to correlate it with a specific defect.

A total of thirty-two (32) specimens were examined in a Scanning Electron Microscope (SEM). This study verified the parent study where it was reported the absence of a clear crack initiation point [1]. Some fracture lines would originate exactly from the drilled surface, while others sub-surface, making a relatively wide crack initiation area. The vast majority of the specimens with low fatigue lives failed close to the machined surface, due to the presence of chip fragments embedded on the surface (pick-up sites). Further examination of the critical defects identified voids within the chip, cracking of the chip, damage and cavitation on the surface of the hole, and twins at the edge of the hole, shielded by the chip. The short crack path was perpendicular to the severely deformed sub-region immediately below the surface and then inter-granular along the deformed

microstructure. A qualitative analysis of the machined surfaces and the crack propagation path(s) along them verified the proposed failure mechanism and eliminated any ambiguities. Non-critical cracks were nucleated in intense drilling marks and smeared sites on the machined surface.

The main research hypothesis, that the dominant failure mechanism was based on microstructure defects, proved to be completely amiss. Surface defects, namely chip embedment on the machined surface, were the dominant defects, responsible for the crack nucleation and initiation sites on the machined surface. Subsequently, variations in the fatigue lives were proposed to be a combination of the location of the surface defect, the level of interactions between defect and matrix, the size of the defect and sub-surface elastoplastic strain fields.

This work had significant contributions towards the mapping of elastoplastic micro-strains in engineering materials and provided a definitive fatigue failure mechanism in a specific category of machined parts. However, more than anything else, it exposed the limitations in understanding surface integrity and its links to fatigue performance.

1.2 Thesis outline

Chapter 1 is the introductory chapter of the thesis. It establishes the drive behind the current project and the main research objective, i.e. the investigation of the early failures in drilled Ti-6Al-4V plates during cyclic loading. The secondary objectives were to develop a suitable framework of analysis for the surface integrity of machined specimens and the tools for elastoplastic strain mapping in the microscale. As proposed by the parent study, the main hypothesis was that the failure mechanism had its origins to the crack initiation in the deformed microstructure.

Chapter 2 contains an extended literature review with reference to the specific Titanium alloy(s) under investigation. This section covers the drilling process, the basic metallurgy of Titanium alloys, and the surface integrity and fatigue performance of machined components. Since the design of experiments was part of the parent study [1], the literature review is mainly focused towards the mechanisms of fatigue failure rather than the drilling or fatigue conditions. Monocrystalline and polycrystalline Titanium alloys provided baseline failure mechanisms, in absence of other defects. Then surface and sub-surface defects were examined from fatigue studies on peened and machined material.

Chapter 3 describes the tools and results from the preliminary analysis of the drilled plates. Elements of the parent study were displayed in this section for completeness of the analysis. Then, the specimens were re-examined to acquire detailed information

regarding the surface roughness of the holes, the deformed microstructures, and potential strain hardening. Results were compared against fatigue lives.

Chapter 4 investigates the deformed microstructures with advanced characterization techniques based on EBSD. Particular emphasis was given to the mapping of plastic strains with semi-quantitative tools and the identification of microstructural defects, like twins, slip bands, and strain localization. There was also an attempt to calculate elastic strains with DIC on the detected EBSPs, but the application of this technique was not successful and failed to yield meaningful results.

Chapter 5 describes the FIB micromachining, stress relaxation technique, which was employed for the measurement of localized residual stresses. The technique was verified on peened CP-Ti and then it was applied successfully on the drilled Ti-6Al-4V plates. Residual stress profiles were compared against plastic strain and microstructure features.

Chapter 6 provides a detailed examination of the fracture surfaces, crack initiation sites and crack propagation paths. It contains all the evidence of the critical surface defect, pickup sites, which were responsible for the early failures of the drilled plates and the variation of the fatigue lives. A preliminary qualitative analysis of the defects provided potential failure mechanisms.

Chapter 7 is the final chapter of this thesis. It summarizes the findings and draws the final conclusions regarding the fatigue performance of the drilled plates. The thesis concludes with an outline of the recommended future work, necessary to investigate the failure mechanism in more detail and potentially utilize the tools for elastoplastic strain mapping in other fields.

Chapter 2. Literature Review

Titanium and titanium alloys have an excellent combination of characteristic, mechanical, thermal and chemical properties, which make them particularly attractive to the aerospace industry. The high strength to density ratio, the good fatigue performance and the low to medium temperature creep resistance, allow for applications ranging from structural parts of the fuselage to critical components in the jet engines of the aircraft. [8] [9] [10]

The bulk microstructure and mechanical properties of materials are tailored to the specific application by a series of manufacturing processes. The last step in the production line is the machining to final dimensions and the cutting of special features or details, including a number of holes, *Figure 2-1*. However, the surface integrity and properties of the machined components are compromised by surface and subsurface defects. A clear understanding of the machining-induced effects and their links to the fatigue performance of the materials requires the investigation of the key deformation characteristics of the cutting processes with respect to the metallurgy of the materials.

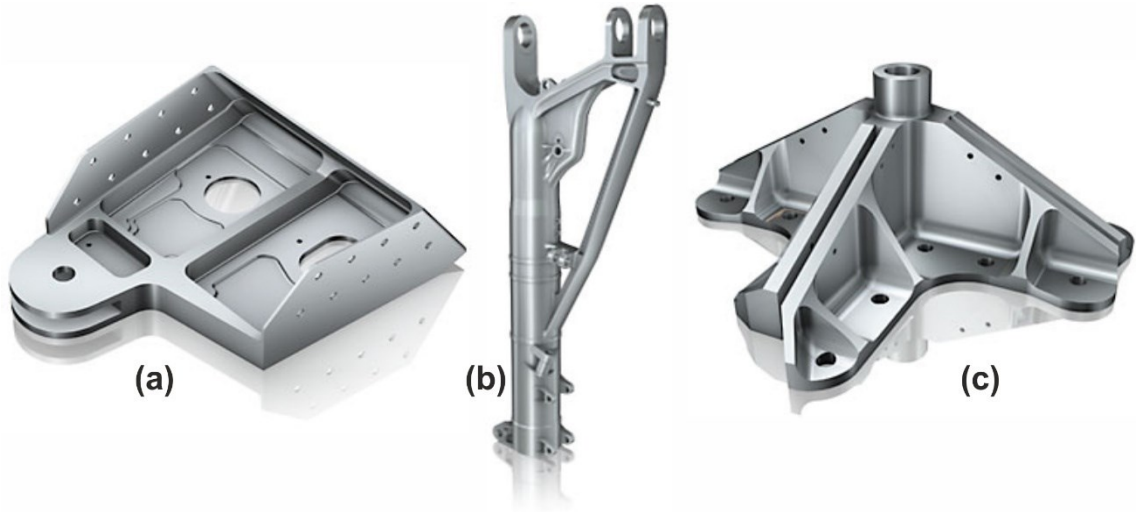

Figure 2-1 Titanium parts in modern aircraft[1]. a) Pylon bracket of wings; b) Main fitting of landing gear; c) Thrust fitting

2.1 Metallurgical aspects of Titanium alloys

The main production route of Titanium (Ti) is through the Kroll process [11] [9], where TiO_2 is chlorinated to $TiCl_4$, purified by distillation and reduced to Ti sponge by Magnesium (Mg). A notable alternative is through the FFC Cambridge process [12], an electrochemical, direct reduction of TiO_2 to pure titanium with the ionization and dissolution of oxygen in molten salt.

[1] http://www.sandvik.coromant.com/en-gb/industrysolutions/aerospace/titanium/pages/default.aspx

Titanium has a hexagonal close-packed crystal structure (*hcp* – alpha phase) up to 882 ºC and a body-centered cubic one (*bcc* – beta phase) above that temperature, with a melting point at 1670 ºC. The lattice parameters of pure Ti are *a*=0.295 nm & *c*=0.468 nm for the *hcp* unit cell and *a*=0.332 nm for the *bcc* at 900 ºC. The differences of the lattice parameters increase the elastic and plastic anisotropy of polycrystalline materials. *hcp* crystals have lower Young's modulus along a-axis and if loaded parallel to their *c*-axis or *a*-axis have higher yield stress. [9]

Due to the electron configuration of Ti (4 energy levels/orbitals and 4 valence electrons – $3d^2 4s^2$) [13], it can form solid solutions with substitutional metals, like Aluminium (Al), Vanadium (V) or Molybdenum (Mo), up to ± 15-20% of its size and interstitial elements, like oxygen (O), nitrogen (N) or hydrogen (H). Alloying elements operate as neutral (Sn & Zr), alpha (Al, O, N & C), or beta-isomorphous (V, Mo, W, Ta, Nb-formation of beta phase) and beta-eutectoid (H, Fe, Mn, Ni, Cu, Cr, Co & Si-formation of intermetallics) phase stabilizers, *Figure 2-2*. [9]

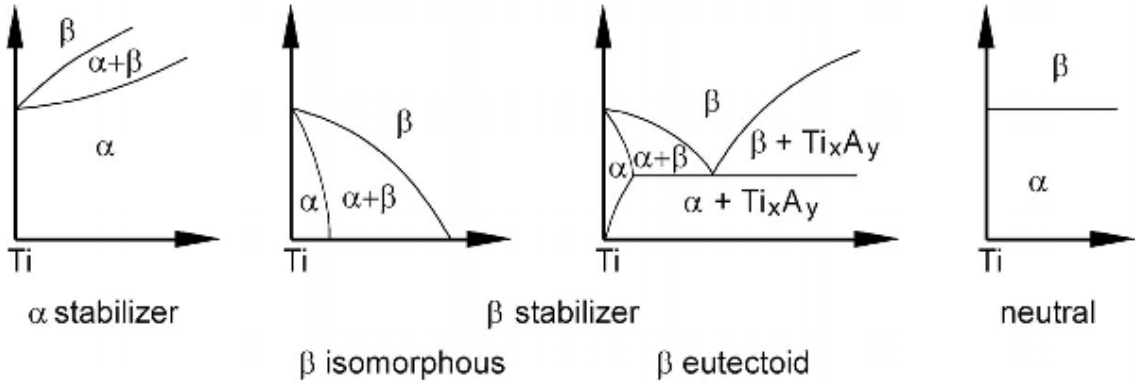

Figure 2-2 Phase diagrams of titanium alloys vs. alloying elements [8] [9] [10]

The addition of elements changes the physical properties of titanium, i.e. the allotropic temperature of Ti-6Al-4V rises to 980–1000 ºC with a melting temperature of 1604–1660 ºC and allows the development of alloys with mechanical properties and microstructure tailored to the specific application. According to the percentage of stable phases at room temperature, the alloys are categorized into *a*, near *a*, *alpha+beta*, *near b* and *b* alloys. The alloys under investigation were Grade 4 CP-Ti bar, an *a* alloy, and mill-annealed Ti-6Al-4V plate, an *alpha+beta* alloy.

Grade 4 CP-Ti correspond to the addition of 0.40% oxygen, which raises the yield stress to 480 MPa [9] and the tensile strength above 550 MPa [10] by solid solution (interstitial) strengthening. Typical production routes include a homogenization step 40-50 ºC below the beta transus (950 ºC ±15 ºC), warm (450–600 ºC or even much lower) or hot (760–815 ºC) working and static recrystallization (650–760 ºC) [14], *Figure 2-3*. Dynamic

recrystallization should be completely suppressed by the low deformation temperatures (sub-transus) or limited to small percentages depending on the deformation conditions, i.e. strain, strain rate, and temperature (and passes for multi-step process). The size of recrystallized grains can be controlled by the additions of Fe (max 0.50% in Grade CP-Ti), which precipitate out small particles of *beta* phase.

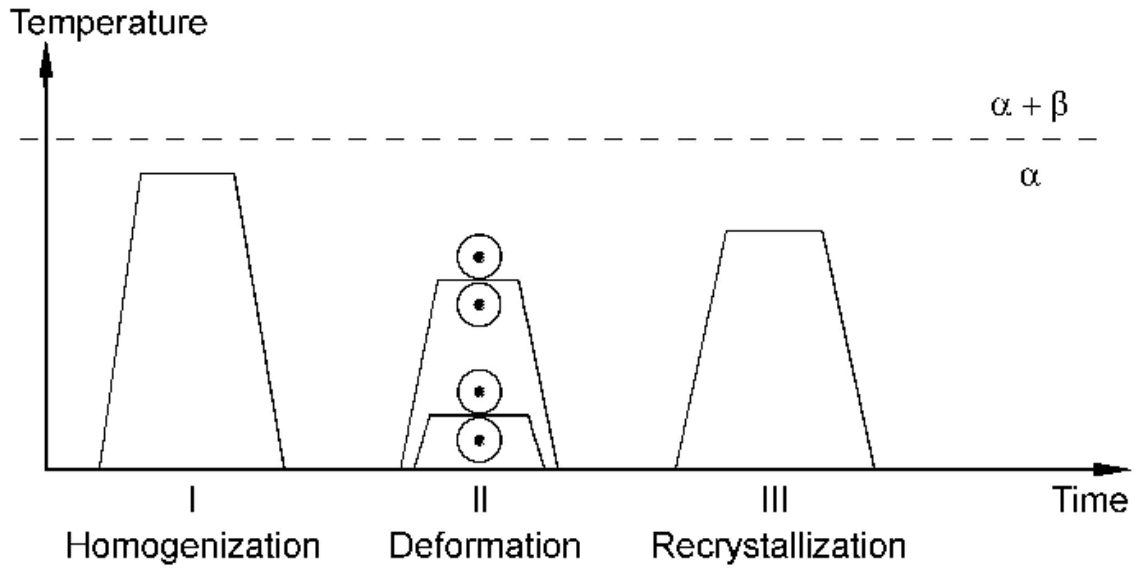

Figure 2-3 Production route of CP-Ti and a alloys [9]

Mill-annealed Ti-6Al-4V is strengthened by substitutional elements, dislocation density, and mainly grain boundary density, as the microstructure evolves during the thermo-mechanical production route. The production steps include a homogenization step 40-50 ºC above the beta transus (1000 ºC ±15 ºC), a deformation step within the *alpha+beta* region (925–980 ºC) and stress relief annealing step (from 30 min to several hours at approximately 705 ºC) [14], *Figure 2-4*, while the static recrystallization step is omitted or suppressed. Typically, dynamic recrystallization does not occur with hot deformation in the *alpha+beta* region. However, depending on the process conditions, a small volume fraction could recrystallize. Static and dynamic recrystallization can occur during slow (air/furnace) cooling from the *alpha+beta* region or between passes in sheets/plates (meta-dynamic recrystallization, i.e. static recrystallization on dynamic recrystallization nuclei). A combination of recrystallized grains and traces of the deformed microstructure during the hot working process exist in the final material, while the hydrogen pick-up is minimized. The mill-annealed condition is not standardized and microstructure can vary between batches, products and/or suppliers. If the recrystallization temperature is high (~925 ºC) and the step is complete, then fast cooling results in a bimodal microstructure with primary alpha grains at the triple points of lamellae alpha (prior beta grains). Slow cooling from the high recrystallization temperature results in fully equiaxed, coarse, alpha

grains (20-30 μm) with beta grains at the triple points of alpha phase. Lower recrystallization temperatures (800–850 ºC) result in finer, equiaxed alpha grains (~ 2 μm). [14] [2]

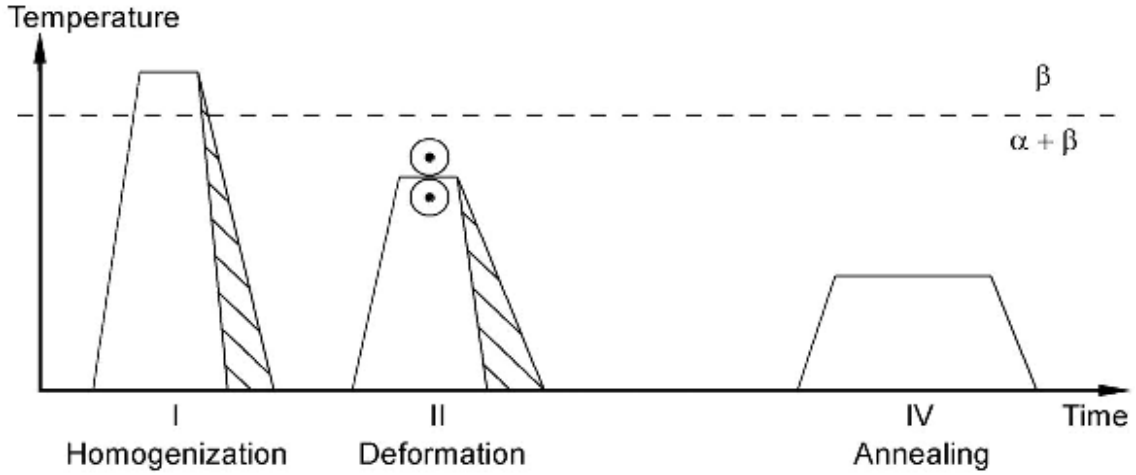

Figure 2-4 Production route of mill-annealed alpha+beta alloys

2.2 Deformation behaviour of Titanium alloys

Under deformation titanium and its alloys display a combination of slip and twinning modes in both phases, which vary according to the temperature and the alloying composition. A slip system is a combination of the planes with the larger spacing and the directions with the shorter lattice translation vector because they minimize the critical resolved shear stress and they are energetically more favorable. The planes and directions that satisfy the previous law are the planes with the highest density of atoms. Closed packed directions of alpha-Ti include the $< 1\,1\,\bar{2}\,0 >$ directions and the densely packed planes include the basal {0 0 0 1}, the prismatic {1 0 $\bar{1}$ 0} and the pyramidal {1 0 $\bar{1}$ 1} planes. Due to the reduced *c/a* ratio of alpha titanium, the prismatic planes have increased atom density and can contribute to slip [10]. The closed packed directions of beta Ti are the $< 111 >$ directions and the densely packed planes are the {1 1 0} planes. Secondary slip systems exist for both *hcp* and *bcc* crystals, *Table 2-1*. Pyramidal slip in alpha titanium is equivalent to the combination of basal and prismatic slip, hence the independent systems are only 4. The von Mises criterion of homogeneous plastic deformation in polycrystals, requires the existence of a minimum 5 independent systems and introduces the $< 1\,1\,\bar{2}\,3 > \{1\,1\,\bar{2}\,2\}$ system (<*c*+*a*>). <*c*+*a*> slip has been experimentally observed and can be verified analytically for crystals loaded parallel to the c-axis. [9] [10]

Table 2-1 Slip systems in hcp and bcc crystals. Primary systems in bold. Independent systems in brackets [9] [10]

Crystal Structure	*Slip Plane*	*Slip Direction*	*Slip Systems*
hcp	**{0 0 0 1}**	**< 1 1 $\bar{2}$ 0 >**	{1}x<3>=3 (2)
	{1 0 $\bar{1}$ 0}	**< 1 1 $\bar{2}$ 0 >**	{3}x<1>=3 (2)
	{1 0 $\bar{1}$ 1}	< 1 1 $\bar{2}$ 0 >	{6}x<1>=6 (4)
	{1 1 $\bar{2}$ 2}	< 1 1 $\bar{2}$ 3 >	{6}x<1>=6 (5)
bcc	**{1 1 0}**	**< 1 1 1 >**	{6}x<2>=12 (5)
	{2 1 1}	< 1 1 1 >	{12}x<1>=12
	{3 2 1}	< 1 1 1 >	{24}x<1>=24

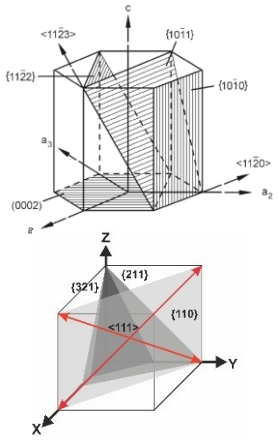

Twins generally accommodate deformation at low temperatures, when the stress is applied parallel to the c-axis and the $< 1\ 1\ \bar{2}\ 0 >$ slip directions are restricted. Tensile twins on the $\{1\ 0\ \bar{1}\ 2\}$ plane, along the $< 1\ 0\ \bar{1}\ \bar{1} >$ direction are the most frequent. Other twins are the tensile $\{1\ 1\ \bar{2}\ 1\} < 1\ 1\ \bar{2}\ 6 >$ with high shear strength, the low temperature compressive $\{1\ 1\ \bar{2}\ 2\} < 1\ 1\ \bar{2}\ \bar{3} >$ and the high temperature compressive (above 400 ºC) $\{1\ 0\ \bar{1}\ 1\} < \bar{1}\ 0\ 1\ 2 >$. Each twin system corresponds to a certain orientation relationship between the parent and the twinned part of the deformed crystal, which are described based on the angle/axis of rotation [15], *Table 2-2*. Twinning is suppressed in hcp crystals at elevated temperatures and in two-phase alloys with small alpha phase dimensions, high solute content (Al or O) or titanium precipitates. [9]

Table 2-2 Primary twin systems in alpha titanium [9] [10]

Applied Stress	*Twinning Plane*	*Shear Direction*	*Angle [degrees]*	*Rotation Axis*
Tension	{1 0 $\bar{1}$ 2}	< 1 0 $\bar{1}$ 1 >	85	< 1 1 $\bar{2}$ 0 >
Tension	{1 1 $\bar{2}$ 1}	< 1 1 $\bar{2}$ 6 >	35	< 1 $\bar{1}$ 0 0 >
Compression	{1 1 $\bar{2}$ 2}	< 1 1 $\bar{2}$ $\bar{3}$ >	65	< $\bar{1}$ 1 0 0 >
Compression	{1 0 $\bar{1}$ 1}	< $\bar{1}$ 0 1 2 >	54	< $\bar{1}$ 2 $\bar{1}$ 0 >

2.3 Machining of Titanium alloys

Titanium and its alloys have physicochemical properties that limit their machinability. The combination of the low conductivity (22.0 W/m-ºK for CP-Ti & 7.3 W/m-ºK for Ti-6Al-4V) and high chemical reactivity pose a challenge even for the most advanced cutting tools and machines. During metal cutting, the temperature can rise above 900 ºC [1], depending on the cutting conditions, due to the poor heat transfer and dissipation throughout the material. The elevated temperatures, high reactivity and strength of

titanium, and fast machining reduce the life of the cutting tool and can have a detrimental effect on the workpiece. Surface integrity is equally important to tool wear and the current practice to optimize the process involves the adjustment of the cutting speeds and the introduction of fluids for cooling and lubrication. [3] [16]

The term surface integrity is used to describe the manufacturing induced effects on the material. A more technical definition was proposed by Field and Kahles [17], where they considered the "*inherent or enhanced condition of a surface produced by machining or other surface generation operations*". Initially, surface integrity was limited to surface topography through roughness parameters examining notch effects and pre-existing flaws, but it was recognized that sub-surface alterations of the state of material should have an effect the distortion of the parts, the local mechanical properties and hence the performance of components [17] [18]. Surface integrity has been equipped with new techniques and an extended arsenal of test/inspection protocols to cope with the growing demand of high quality products with superior finish, strict dimensional tolerances and performance from difficult to machine materials [18] [19]. and it mainly consists of four primary parameters: i) surface topography; ii) strain hardening; iii) residual stresses; iv) microstructure alterations [20]. Machining conditions are directly related to the surface integrity and can affect the fatigue performance of the final components.

2.3.1 Drilling process

One of the most common cutting operations is drilling, reaching 35% of the overall machining. The standard tool for opening holes, employed in the parent study, is the twist drill with two flutes, *Figure 2-2*, from high-speed steels and carbides. Drilling is a complicated cutting process, which involves intense shear deformation from the main (lips) and secondary (chisel) cutting edges and extrusion mechanisms from the chisel faces [21]. Analytical and Finite Element models have been employed for the design of cutting tools and the investigation of the process. Early work on the geometry of the drill bit established the influence of the main cutting edges, the secondary chisel edges and the indentation zone on the associated forces and the wear zone based on simplified simple shear models [22]. Deflections and local deformations of the drill can be calculated from its geometrical features, which have established the optimum values that we see in modern tools [21]. Advancements in tools have introduced curved cutting edges at the intersection of flank and flute faces and different cutting angles (rake and relief angles), but still, a very accurate geometrical model was developed for the subsequent interpretation of cutting forces, chip shape and removal, wear and temperature [23]. The

combination of analytical representations of the tool geometry and the material removal process has provided a good approximation of cutting forces, temperature and tool wear [3] [24] [25] [26] [27]. As the computational capabilities increased, 2D and 3D FE models of drilling have provided deformation or temperature fields within the workpiece, entry/exit artifacts (burr formation) and tool forces/wear [3] [28] [29] [30] [31] [32].

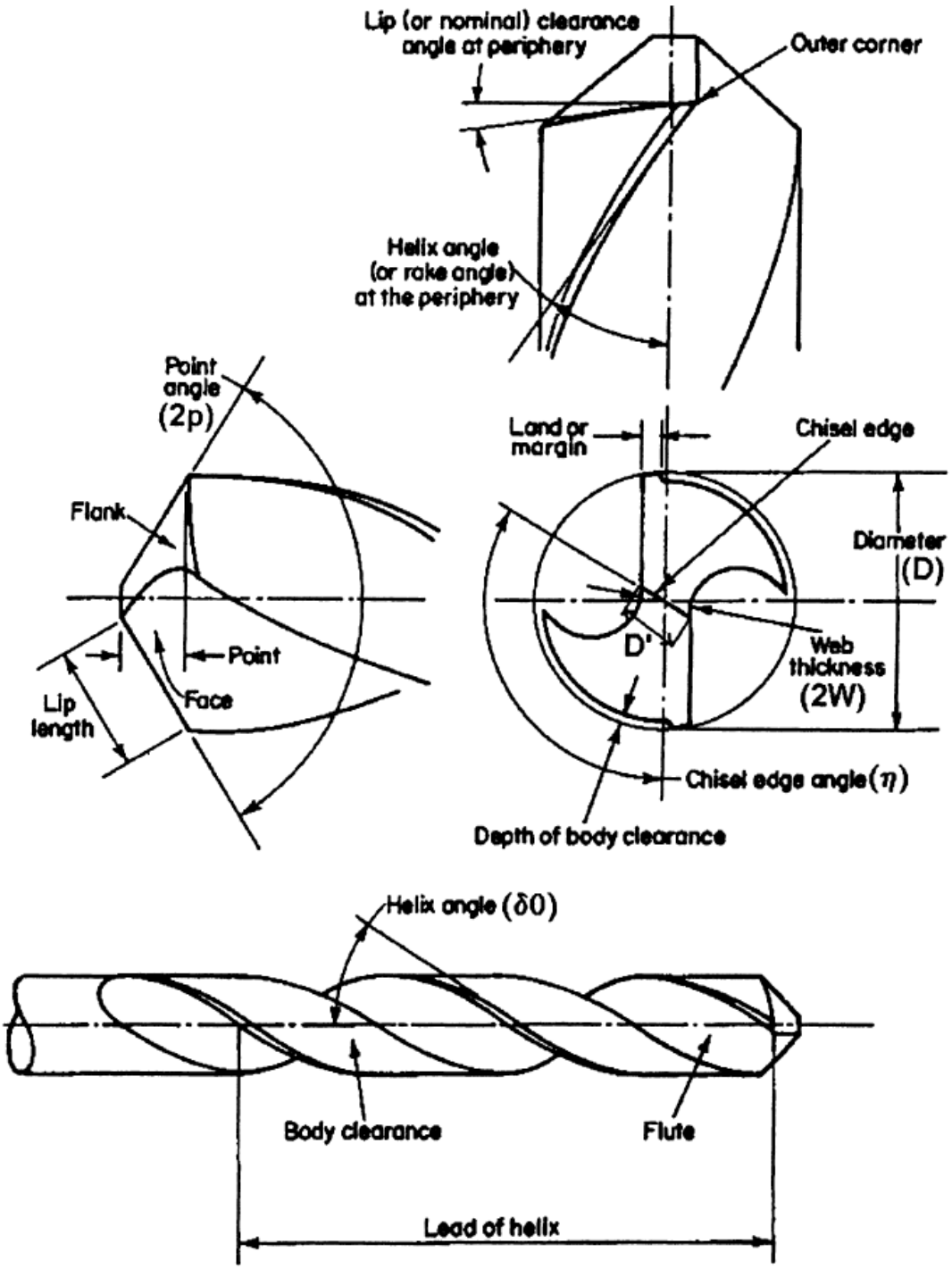

Figure 2-5 Typical twist drill geometry [25]

High-speed steels (HSS), Cemented Carbides (CC), Ceramics or Diamond tools are available for machining operations. Modern tools are designed to meet the specific requirements of the market, which include low tool wear, high rate of material removal,

versatility, good surface finish and economy. Suitable candidates are materials with a combination of high hardness, toughness, and heat resistance. HSS and CC tools were used in the parent study for the drilling trials and only HSS for the fatigue tests [1]. HSS are martensitic steels (body centered tetragonal crystal structure) with medium to high Carbon (C), Vanadium (V), Tungsten (W) and Chromium (Cr), while additions of Molybdenum (Mo) and Cobalt (Co) can also exist in certain alloys. The peak hardness of the tool is achieved by high temperature, heat treatments that lead to the precipitation of fine Mo, Cr, V, and W carbides. The main alternative to HSS tools is Tungsten carbide (WC), which allow for higher cutting speeds and better cutting performance. WC tools are inherently stronger and harder than HSS, but more brittle, with stable microstructures (hexagonal closed packed crystal structure) up to the melting point (2600 ^{o}C). Drilling is one of the metal cutting operations that more traditional types of tools have been and are being used, i.e. HSS and WC. Such rough operations require a more versatile and reliable, low-cost tool and do not have strict time constraints. HSS have proved that can still be competitive against ceramic or the more exotic ceramic/diamond tools. Coating technologies have improved the performance of HSS and CC tools. The direction of the market is aligned to the technological advances, shifting the interest between HSS and WC. [3]

2.3.2 Surface topology

A number of surface features can be generated on the workpiece from its interactions with the tool. Cutting speed, feed rate, tool geometry and wear, workpiece and tool material properties, lubrication and process characteristics introduce surface defects related to the material removal mechanisms [3] [20]. High-speed machining of titanium alloys can result in a serrated chip [33] [34], which can further affect the surface topography.

The surface features consist primarily from feed marks [35]. As the tool wear increases during the cutting process, the feed marks becomes less pronounced and intense smearing along the feed marks of the surface material occurs [36]. If the cutting speed is high, the temperature of the process rises and worn tools may introduce a chip layer on the machined surface, by melting locally or softening of the material to the extent that it can no longer separate with the chip [35]. Chip fragments can be re-deposited or embedded at the material for high cutting speed, independent of process temperature [35] [37]. It has been proposed that tearing of the machined surface can occur from the tool fragments that slide between the tool and the workpiece and penetrate its surface [35]. Less frequent surface defects are cracks and cavities from excessive levels of plastic deformation [20].

Surface roughness and other topological parameters provide an average value for the condition of the surface, heavily biased towards the dominant features, i.e. the feed marks.

An additional defect in drilling is the formation of entry and exit burrs [38] [39] [40]. A burr is any material built up, geometrical distortion or chip fragments at the edges of the hole due to material flow and removal. Typically, the burrs have to be removed by mechanical means, but it has been demonstrated that they can be avoided with the employment of vibration [41] [42]. The wobbling of the tool may also introduce some waviness at the through thickness profile of the hole [1].

2.3.3 Machining induced plasticity

The strained layer compromises from a Severe Plastic Deformation (SPD) zone immediate below the machined surface, a zone of visible distorted/sheared microstructure and a zone of low strains [43] [44] [20]. White zones have been observed in Steel [45] and Nickel [46] alloys with distinct machining-induced, microstructure features immediately below the surface and represent sub-regions of intense plastic deformation and thermal, physical or chemical alterations. The level of deformation and the depth of the machining-affected layer can be captured by micro- or nanoindentation from the sub-surface strain hardening profile. Strain softening of the material immediately below the machined surface or at a certain distance from it can exist, due to overaging from the elevated temperatures of cutting. Stress and strain localization are expected within the deformed microstructure from the anisotropy of the system. The generation and pile-up of dislocations at crystal discontinuities can form intense slip bands within the crystals from immobile dislocations. TEM is the traditional tool for the observation of dislocation structures and the interpretation of strain hardening/softening of the material. Micro-indentation suffers from resolution issues associated with the small thickness of the strained layer, whereas nano-indentation provides a localized value biased by the local crystal orientation and dislocation density.

2.3.4 Machining induced residual stresses

During cutting operations, material is removed through a shearing mechanism, which puts the deformed material into tension and generates a significant amount of heat [3]. Upon removal of the applied load, the equilibrium state depends on the thermomechanical properties of the material, the mechanisms of chip formation, microstructure alterations and the sub-surface plastic strain gradients [47] [48].

There is a wide range of residual stress profiles that have been reported. It is possible to develop fully compressive or near-surface tensile and sub-surface compressive residual

stresses, depending on the material and the process conditions [49] [50] [51]. At the immediate surface, the material can be in different states, alternating between low to high compression or tension. Compressive stresses can build up towards global maxima below the surface or dissipate immediately towards the bulk material. Similarly, surface tensile stresses can build up to local maxima and dissipate to background values or transition to compressive stresses in a predominantly compression residual stress field. Tensile stresses could appear at the end of the compressive profiles to achieve self-equilibrium. Depending on the previous state of the material, the compression to tension part of the profile can be shifted to either direction, eliminating or magnifying the residual stresses. After the equilibrium part, the stresses are building up to the original stress state of the material and prolonged compression or tension tails can exist. It should be noted that the vast majority of the measured profiles are averaged over a large area and volume, much bigger than the representative area for the chip formation or volume for the elastoplastic, in- and out-of-plane, strain gradients. Thus, they provide an overall benchmark for the cutting process, but they do not describe the local minima and maxima that can influence the crack initiation in the material.

Residual stresses in machined specimens have been measured in the past by X-ray diffraction [52] [53]. XRD averages over an area of a few millimeters, according to the size of the optics which generate the beam. The penetration of the x-rays depends on the material and it is within a few tens of microns. Advances in the area of micro-optics have enabled the use of tubes that concentrate the beam below 100 μm in diameter. Thus, only near-surface stresses can be obtained by XRD and the resolution of the method is limited. Through thickness measurements require electropolishing and a subsequent correction for the stress relaxation. Curved specimens and localized stresses pose a challenge for the method. Neutron diffraction lacks the resolution and hard x-ray diffraction is not readily available [6] [54]. [53]

Other alternatives on residual stress measurement are based on stress relaxation by mechanical means. Slitting [55] [56] and hole drilling [57] [58] [59] methods are the prevalent techniques for specimens with swallow stress profiles. The traditional application of the methods involves the installment of strain gauges, which alter the local, surface stress field and thus inevitably introduce errors 10-20 μm below the surface. Digital Image Correlation (DIC) has been utilized instead of strain gauges to improve the resolution and accuracy of the techniques. DIC can be applied either directly on the textured surface, on the decorated surface or on the pattern created by electronic speckle

interferometry (ESPI) [60] [61] [62] [63] [64]. The utilization of micro-drills, down to 100 μm, has improved the depth resolution of the hole-drilling technique at the cost of the maximum depth of the hole. Strain gauges cannot be installed on curved specimens and the cutting feature is not perfect, but DIC can provide displacement/strain fields which are corrected for the existing curvature.

A special case of slitting is the Contour method [65]. Unlike the other methods, it evaluates stresses acting normal to the cut surface from the waviness of the cut surface. The method is more appropriate for large specimens because it creates artifacts at the entry and exit edges of the specimen and is sensitive to the surface measurement procedure. A possible downscale and improvement of the method is the utilization of 3D optical profilometers for the near edge waviness if the surface of interest is oriented parallel to the direction of the cut to reduce edge artifacts.

All the traditional measurement techniques operate in the macro- or mesoscale. Thus, the stresses are averaged over a large area/volume, which is useful to describe the machining process. However, the need to correlate residual stresses with the fatigue performance of parts requires exploring local minima and maxima in the micro-scale. By definition, the underlying microstructure and the strain gradients from the cutting process would have a profound effect on the residual stress profiles, but the integration of the previous information could explain the failure mechanism under cyclic loading. Micro-machining stress relaxation [66] and Electron Back Scattered Diffraction [67] can potentially meet these requirements [54] and were further investigated in the current study.

2.3.5 Surface integrity of machined Titanium

In the parent study, the surface roughness was identical for all cutting conditions, but microstructure modifications were evident to different depths, no strain hardening was detected and residual stresses were not measured [1]. General observations on the trends of surface integrity can be established based on other cutting trials.

Sharp tools have resulted in lower levels of surface roughness, plastic shear deformation and hardening on the workpiece, than blunt tools during dry turning of Ti-6Al-4V and Ti-6Al-2Sn-4Zr-6Mo at different feed rates [68] [69]. Cutting speed (45-100 m/min) and feed rate (0.25-0.35 mm/rev) had little effect on the integrity, but the elevated temperatures of the dry cutting caused peak microhardness values immediately below the machined surface and a local minimum appeared at the edge of the plastically deformed layer, associated with over-aging, despite the short duration and scale of the heat transfer phenomena [69]. Turning of an equiaxed Ti-6Al-4V bar with two different inserts (0.15

& 0.25 mm/rev @ 80 & 120 m/min) revealed that the surface quality can be improved at low feed rates and cutting speeds for smooth inserts [70]. All conditions deformed the microstructure to a similar depth (maximum 6 μm) but displayed a reduction of micro-hardness to a depth of ~75 μm attributed to overaging [70]. In addition to the shearing of the microstructure, there were evidences of grain pull-out, recrystallized amorphous layer and material build up on the surface from smearing and embedment of chip fragments [70]. No pattern was observed for any of the previous defects. The continuation study of tool wear on surface integrity showed that worn tools increased the surface roughness, the surface compressive residual stresses and the depth of the residual stress profile, despite equivalent levels of plastic deformation [71]. The increase of feed rate resulted in an increase of the surface residual stresses and a reduction of their depth [71]. Residual stresses gradually diminished from a peak surface value, with compression-tension-compression equilibrating parts at the end of main compressive part for all conditions [71].

Milled Ti-6Al-4V to different surface conditions (Ra=12.5 μm & 1.6 μm) introduced moderate, surface compressive stresses (~300 MPa) and upon subsequent mechanical polishing with belt and bob tools the deformation layer was removed, but grinding/polishing marks and pronounced surface defects were still present or intensified for specific operation protocols [72]. High-speed machining of duplex Ti-6Al-4V resulted in a linear relationship between cutting speed (20-660 m/min @ 0.12 mm/rev) and depth of plastic deformation, but the surface residual stresses had a more complicated profile [73]. At low cutting speeds, the residual stresses were compressive and built up to a peak value at 50 m/min before transitioning to tensile stresses at 100 m/min thereafter [73]. Dry milling of Ti-6242S (100-125 m/min @ 0.15-0.20 mm/tooth) with different tools produced small variations to the surface roughness and shallow plastic deformation zones but introduced strain softening at the near surface material followed by extended strain hardening to 350 μm [35]. Milling marks, surface tearing, chip layers, and fragments were present on the machined surface [35].

Sequential dry drilling of Ti-6Al-4V (at 50 mm/min & 0.07 mm/rev) with and without air cooling of the tool after the opening of each hole was dominated by the temperature of the tool/process [38]. The elevated temperature caused tool wear, burr formation and higher roughness on the holes, while the beta phase in the SPD layer was assumed to have been transformed to alpha phase due to oxygen diffusion, despite the short duration and scale of the heat transfer phenomena. There was an obvious shearing of the microstructure

and a gradual reduction of hardness from the machined surface to the undeformed region. [38]

Plastically deformed zones in Ti alloys have been fully characterized by EBSD for high-speed milling [43], precision turning [44] and peening [74]. Persistent slip bands were identified in milled Ti-6Al-4V and Ti-834 under finishing conditions, with minimum shearing of the parent microstructure, small thickness of SPD layer and no twins [43]. Turning of Ti-834 under progressively increased cutting surface speeds produced, significantly sheared microstructures, larger SPD, higher density of tensile twins and intense slip bands [44]. Twins and slip bands extended to a larger depth for higher speeds, but a local minimum existed for intermediate speeds, due to the tool/workpiece interactions and relevant strain rates [44]. Basal, prismatic and pyramidal slip was observed below the visibly distorted microstructure [43] [44], at apparent low levels of plastic strain. Further turning experiments in Titanium alloys, ranging from near-α to near-β, verified the dependency of sub-surface deformation to alloy composition, microstructure, and the edge radius of the cutting tool [75]. Silicides were formed at the twins and slip bands of the machined Ti-834 specimens at elevated temperatures, which could reduce their fatigue resistance [44].

A reported "white layer" of intense deformation [20] in addition to the SPD layer, should be further investigated. It should not be confused with the zones observed in alloys of Steel [45] and Nickel [46] with distinct machining-induced, microstructure alterations. However, in some examples of Titanium [69] (as well as Steel [76] and Nickel [77] alloys), it could be attributed to imaging artifacts due to the loss of sharpness and detail. The combination of charging and rounding effects at the edge of the specimen from LOM/SE/BSE imaging, the contamination of the edge from environmental and not machining sources, the topography of machined surface or slight tilting of the specimen in the sample holder are common sources of such artifacts. In LOM this is typically resolved by the employment of optical filters, while in SEM, by a reduction of accelerating voltage below 5 kV or bridging of bakelite and specimen with conductive paint. It is not argued that the material at the machined surface is not highly deformed, heat affected and physically and/or chemically altered [20]. However, the extent to which the white contrast in that region should be used for a qualitative or quantitative of surface integrity, especially for different materials, could be considered debatable. TEM, nanoindentation, and FIB could provide the required resolution and level of detail based

on hard, scientific data, instead of the standard LOM, micro-hardness, and XRD which do not really describe the aforementioned layer if their thickness is below 2 μm.

The common denominator in the previous studies was that the surface quality, subsurface microstructure, and material properties can change dramatically in the machining-affected layer. However, these studies provided only a qualitative and intuitive prediction on the fatigue life of machined components. Actually, the number of studies addressing this issue is very limited.

2.4 Fatigue of machined Titanium alloys

Surface integrity depends on the machining conditions and it has been used to understand and rank them. Theoretical and practical considerations have linked surface integrity to fatigue [78]. However, there is not a clear connection of the fatigue to the machining conditions, due to the different competitive failure mechanisms and the presence of scattering or outliers. This is particularly true, for titanium alloys, which are difficult to machine and the experience in this field is limited compared to steels or aluminum.

2.4.1 General aspects of fatigue

The vast majority of mechanical failures during service is attributed to fatigue. Fluctuating stresses, with maximum values even below the yield strength of the material, but above a minimum/critical value, can lead to premature failure of the component after a number of cycles. During low cycle fatigue ($<10^4$–10^5 cycles), the material undergoes global, plastic deformation from the high applied stress and the accumulated plastic strains reduce the performance of the component. However, the design of the components is usually based on or result to elastic conditions, when the safety factors are introduced into applied loads and material properties. Components subjected to fluctuating elastic stresses can fail under high cycle fatigue ($>10^5$ cycles) conditions, because of the accumulation of localized plastic strains in the material and in the crack tip thereafter. Some materials, including titanium, exhibit an endurance, stress limit, below which the material does not provide a fatigue fracture. Fatigue can operate with other mechanisms, like corrosion (corrosion fatigue), wear (fretting fatigue), or in combination with static loads (dwell fatigue), but these are not relevant to the current study. [79] [80]

Typically, a crack is nucleated and initiated in a (sub-) region of the material, where the applied, tensile stresses reach a maximum value. In a drilled plate, the location of interest is at the surface of the hole, perpendicular to the direction of the applied load for unidirectional conditions, at the mid-thickness plane, due to stress triaxiality. Defects in

the component from the manufacturing processes can cause further, stress concentrations and strain localization in the micro- or meso-scale.

The primary defect is the topology of the finished surface, as developed by notches, indents, marks or burrs during the final production stages. Subsurface defects evolve around inclusions, porosity or precipitates and to a lesser extent to discontinuities in the crystal structure. All the previous defects can act as a pre-existing flaws in the material, crack nuclei, from where the crack then propagates. If such flaws are not present, the crack nuclei can be formed by persistent slip bands (PSBs), either from intrusions and extrusions at the surface, or microvoids at the PSBs, or cleavage at the grain or twin boundaries. The propagation of the short cracks is along the PSBs, at ~45^{o} to the direction of the applied stress. When the crack reaches a critical length, it propagates ~90^{0} to the direction of the applied stress and can accelerate by a sharpening and blunting process, described by a power law (constant growth rate – Paris equation). Different design processes have been developed to accommodate for the fatigue strength and crack propagation, aiming for an optimum solution to the modern challenges of safety vs. cost and weight reduction of components. [79] [80]

2.4.2 Cyclic deformation of Titanium alloys

Titanium alloys do not contain any microstructure defects other than crystal discontinuities because they are high purity materials and they are not precipitation strengthened. The alpha phase (*hcp*) is harder than beta phase (*bcc*) and twinning of the alpha phase has been readily observed during deformation in low temperatures. Since the beta phase has many slip systems and there are orientation relationships between the alpha and beta phases, there is an alignment of the slip systems between the two phases. Thus, crystal anisotropy of the alpha phase is the main contributor to the fatigue performance of such alloys.

Fatigue tests have been carried out in smooth specimens to examine the behaviour of single crystals and polycrystalline materials. In both cases, persistent slip bands and cyclic twins can lead to crack nucleation and initiation. Single crystals have displayed micro-cracks on basal and prismatic slip planes and twin planes [81]. Cracks have originated from holes and cavities at the PSBs, predominately on prismatic planes, as well as micro-cracks perpendicular to the bands [82] [83]. Twins also appeared to accumulate plastic deformation during cyclic loading tests and fragmented into smaller twins (twin intersections), with micro-cracks occurring along the fragmented interfaces [84] [82], at the intersections with slip bands or the interfaces with the matrix [85] [83]. It has been

reported that tensile $< 10\bar{1}2 >$twins by prior manufacturing processes have been sites for crack initiation [84] [86], while compressive $< 11\bar{2}2 >$ twins form extrusions due to compatibility with mixed slip systems [82]. In polycrystalline material, with large round grains, the interactions of grain boundaries with bands and twins are an additional source of cracks [82] [83]. TEM has provided the qualitative evidence for the strain accumulation through dislocation structures. Advanced EBSD analytical tools can quantify the cyclic strain through geometric necessary dislocations, with a high-resolution EBSD method [87]. The examination of tensile tests in CP-Ti with the previous EBSD method have verified that the interactions between slip bands and grain boundaries depend on the alignment of the slip systems/grains and quantified the stress or strain concentration which could be found in blocked bands [88]. Deformation twins and dislocation structures have been evaluated at strain controlled fatigue tests, above yield, on commercial pure Titanium, where the twin density at fracture was significantly reduced for small strain amplitudes [89]. However, the dominant mechanism depends also on the type of the microstructure.

In fully lamellar microstructures, slip can occur through the whole colony and cracks have originated at the persistent slip bands of the colony or at the intersection of slip bands of one colony with other colonies. In acicular (martensitic) microstructures, the crack is suggested to be formed predominately at the slip bands of the coarser alpha plate, rather than the phase or grain boundaries. Micro-cracks in lamellar Ti-6Al-4V are accelerated by the persistent slip bands and propagate faster than macro-cracks because they do not have any (microstructure) obstacles in their path. Coarser microstructures have inevitable lower fatigue life than finer ones. In bi-modal microstructures subjected to low/medium stresses, the cracks are originating in the lamellar grains under the same mechanism of persistent slip bands, because they are softer than the primary alpha grains. Aging/Annealing result in partitioning of the alpha stabilizing elements (Oxygen, Aluminium) in the primary alpha grains and depletion of the transformed beta (lamellar) grains. Hence lamellar grains are softer than primary alpha grains. The fatigue life of bi-modal alloys decreased for higher volume fraction of primary alpha, due to the preferential partitioning of the solute elements, despite the reduction of the slip length in lamellar grains. At elevated stress, the fatigue performance of the bi-modal alloys is dominated by the size of the primary alpha grains, i.e. the slip length. Fully equiaxed or bi-modal (with interconnected alpha grains) microstructures tend to fail due to the dislocation pile-up in persistent slip bands of the alpha grains. The size of the alpha grains

dictates their fatigue performance. Larger grains have a longer slip length and that results in a significant increase in stress and strain reducing the fatigue life of the alloy. The opposite is also true. It is common that equiaxed microstructures have a specific texture directly related to the manufacturing processes. Texture increases the slip length, beyond that of the alpha grains and further reduces the fatigue performance. Small grain sizes reduce the propagation rate of micro-cracks in equiaxed alloys but slightly increase that of macro-cracks. [9] [10]

An as-forged, bimodal Ti-6Al-4V with macrozones, failed due to basal and prismatic slip coalescence of microcracks along the bands under fully reversible loads [90]. Internal failures were found for lower stress levels in bi-modal and basketwave microstructures, whereas surface failures for higher stresses, without a clear evidence of the reason and some notable scattering for ultra-high cycle fatigue (tension-tension regime) [91]. The dominant stage in the fatigue life of the previous microstructures was the crack initiation one and basketwave microstructures outperformed the bimodal ones during the crack propagation stage [91]. In another micro-textured, bi-modal Ti-6Al-4V subjected to high cycle fatigue (tension-tension regime), the crack initiation appeared near the surface and occurred at facets associated with basal slip [92] [93], while the crack propagation was promoted by the prismatic slip and retarded by cross (mixed mode) slip [94]. The differences in the behaviour of local microstructures have been further examined and verified in fully reversible fatigue tests, where the size of the primary alpha grain and their connectivity were the dominant factor [95]. During high frequency, fully reversible, cyclic ultrasonic tests on equiaxed Ti6Al4V, the crack initiation site shifted from the surface to the interior for stresses below ~645 MPa and the crack apparently occurred at the boundaries of the primary alpha grains, despite cyclic twins and subgrain formation [96].

It is assumed that under high cycle fatigue loads when the ratio of the applied minimum and maximum stresses is positive, the tension-tension cyclic loading creates a compressive residual stress layer near the surface, hence the material fails internally [9] [10]. Similarly, the fatigue life increases as the stress ratio increases, but the two observations have not been fully described [9] [10]. Accumulated cyclic plastic deformation could be the underlying mechanism that triggers the aforementioned behaviour. SEM and TEM could provide information on the crack nucleation, initiation, and propagation that consist the overall fatigue live.

2.4.3 Roughness and surface treatments of alloys vs. fatigue

All the surface defects are described through roughness parameters, either average or maximum peak/valley values, and these have been to the fatigue life of specimens to different surface conditions. Roughness is considered as a pre-existing defect, which causes local stress concentration and accelerates crack initiation and propagation. In a low cycle fatigue test of type 304 stainless steel, the cycles to failure reduced dramatically with the increase of surface roughness, which was associated with the reduction of the number of cycles for crack nucleation and initiation [97]. Different surface conditions were tested in steel samples, where the residual stresses were removed by heat treatment, and displayed a reduction of the fatigue performance with increased surface roughness [98]. The same result was obtained for steel specimens machined with a waterjet [99]. Milling operations on aluminum were ranked according to surface roughness and residual stresses and their fatigue performance appeared to follow the roughness ranking, though the crack initiation point was located near the machined surface at intermetallic inclusions and porosity [100]. Laser and traditional machining of aluminum plates reduced the fatigue life of the parent material, because of the apparent increase of the roughness, though it was still above the tight aerospace requirements [101]. Turning of aluminum under higher rake angle (10-30 degrees) and cutting speed (0.51-1.27 mm/sec) increased the number of cycles to failure, which was directly correlated to the decrease of the surface roughness [102]. None of the previous studies specified the exact crack initiation site or identified the critical surface defect, which acted as the crack nuclei.

Surface treatments aim to improve the fatigue life of is service components by introducing a work hardened sub-surface layer with compressive residual stresses. Such processes also alter the roughness of the surface and the underlying microstructure. In a macroscopic level, residual stresses are superimposed with the applied stresses and compressive ones reduce the applied tensile stresses locally, hence cyclic deformation and crack nucleation or initiation [79] [103]. Additionally, the work hardened layer, with the finer, deformed microstructure, enhances the fatigue strength of the material [104]. In the microscale, the stress localization in slip bands, twins and grain boundaries should be reduced by residual stresses. Thus, they can suppress the mechanism of slip band intrusion/extrusion failure at the surface. If the surface does not contain major defects, persistent slip bands should develop more easily inside the material, beyond the compressive residual stress field, and cause internal cracking [105]. Internal cracks grow slower, because of the smaller crack opening width, the propagation within the compressive layer and the four directions of the crack propagation. The stress field ahead

of the crack tip for micro- and macro-cracks is also altered by the existing residual stresses and in conjunction to the dislocation pile-up (with their individual strain and stress fields) decelerate the crack [106].

High cycle fatigue in peened aluminum specimens was dominated by the crack nucleation and initiation stages [106]. Such improvements were acquired only for peening of notched specimens and not for smooth in titanium, due to the elimination of surface defects [107]. The crack propagation rate was reduced for increased depth and magnitude of residual stresses in peened aluminum and titanium [107] [108]. However, improvements in both the smooth and notched condition were obtained for peened, roller burnishing and deep rolling titanium alloys [105]. A similar outcome was obtained for a number of un-notched, titanium alloys in the electro-polished, shot peening, laser peening and ball burnishing conditions, where all failures of the surface treated specimens were internal and the high roughness of the laser peening was not a limiting factor for the fatigue life [109]. The crack initiation point has moved away from the surface for the vast majority of peened steel compared to the ground only specimens [110]. Residual stresses represent an internal equilibrium state of the material. Subsequent static and cyclic deformation can alter the existing residual stresses, reducing their effect to fatigue [111] [112].

It is unclear if the main increase in the fatigue life of surface treated parts is due to the compressive residual stresses or the work hardening. High and low cycle fatigue of bi-modal Ti-6Al-4V at room and elevated temperatures displayed that work hardening plays an important role in crack nucleation and initiation [104]. A key element of the previous experiments was that the crack initiation site was located on the surface for all conditions. Typically, peened specimens would fail internally, at the depth where compressive stresses dissipate and even transition to tensile ones. The discrepancy in the laser peened and deep rolled material was apparently due to the surface roughness in the as machined specimens as evolved by the surface treatments. Deep rolling reduced the surface roughness of the as machined specimens, but the crack initiation site was still located on the surface. Thus, surface defects dominated the fatigue performance, suppressing the crack nucleation and initiation stages. No microstructures of the surface treated material were provided to evaluate subsurface deformed microstructures and possible cracking from the manufacturing steps. [104]

There is not consistency in the effects of surface treatments to fatigue life and the variations are very loosely attributed to the surface condition because there are not clear links between certain surface features and crack initiation. Machining has a similar effect

to surface treatments on surface roughness and sub-surface deformation. The question is which one becomes dominant and under which machining conditions is it possible to maximize fatigue life.

2.4.4 Fatigue considerations of machined components

Drilling introduces surface defects, shears the parent microstructure, generates twins and slip bands, and develops a tension/compression, residual stress field. All the previous factors can act as a pre-existing crack nuclei that accelerate the failure of machined parts under cyclic loading.

Slip bands and tensile twins observed at the machined specimens represent low levels of plastic strain, evident by their location and process characteristics, but they could still serve as a pre-existing microstructural defect. These defects have been developed by shearing deformation and under cyclic tension/compression they could intensify or cause additional strain incompatibility and lead to cracking. However, slip bands have been identified from the early stages of the fatigue test (a few thousand cycles) and even below the fatigue limit, without causing cracking [79]. The key characteristic of the slip bands appears to be the accumulated strain, which is much higher in cyclic vs static/dynamic loads [79]. It would be interesting to establish the levels of strain at the slip bands after machining and the onset of cracking by TEM and nano-indentation. However, it is not anticipated that the pre-existing slip bands could cause such vast differences in the fatigue lives of the parent study, especially since the slip bands and tensile twins should exist in all specimens, though to a different depth [1]. Tensile residual stresses may be part of the predominately compressive residual stress profile, at the near surface region or at the end of the profile equilibrating the compressive ones [113] [114], causing a crack at the aforementioned locations and could dictate the failure mechanism.

Research on machining conditions and their links to fatigue of titanium alloys is limited. Thus, the literature review was expanded in other alloys to provide information on potential trends and crack initiation/propagation characteristics. It should be noted that drilling is a more aggressive cutting operation compared to the high-speed milling or turning because the later are typically evaluated on finishing conditions. Thus, the parent and current studies can involve different failure mechanisms to the reported cases and the literature should only be a guide for the subsequent analysis, rather than a benchmark of the process or performance.

2.4.4.1 Steel alloys

Fine turning of spring steel caused early failures on surface defects while grinding and polishing had higher fatigue lives with cracks initiated in inclusions for all machined-annealed (residual stress relaxation) specimens [115]. Grinding of AISI 316L steel reduced its fatigue performance compared to the polished specimens, causing crack initiation at the machined surface, which could have been assisted by the tensile residual stresses [116]. Residual stresses evolved during the fatigue tests for both cases and their final profile was descriptive of the nature of the tests [116]. Turning of bearing steel with different tools was compared against grinding and the reduced surface roughness of turning appeared to improve the fatigue lives for all stress levels, although there was a notable increase in the hardness and a beneficial compressive residual stress field [117]. The utilization of a chamfered tool at low feed rates on a low carbon steel, resulted in lower surface roughness and deeper plastic and elastic strain fields, which increased the fatigue life of the parent material [118]. Small corner radius introduced more roughness, but the subsequent increase in sub-surface hardening and beneficial compressive stresses increased the fatigue live of specimens [119] [118]. Dry hard milling of H13 steel with sharp and worn tools under different cutting speeds (100-300 mm/min) and feed rates (0.05-0.2 mm/tooth), kept the surface roughness below $Ra<0.6$ μm and increased the compressive residual stresses and micro-hardness for low feed rates and worn tools, leading to high cycle fatigue failure at the machined surface [120].

2.4.4.2 Aluminium alloys

Drilling of Aluminium plates under various strategies, i.e. with or without pilot holes and new versus worn tools, indicated that the surface roughness was more dominant than the compressive residual stresses for the fatigue life based on as machined and fully polished machined specimens [121]. The holes opened under smaller loads outperformed the others and the pilot holes had a positive contribution to the fatigue lives. Polished machined specimens had considerable scattering, which could be attributed to the partial polishing of the machined surface and removal of the strained layer. New and old tools had similar performance because the negative effects of surface roughness with the old tool were canceled out by beneficial compressive residual stresses [121].

2.4.4.3 Titanium intermetallics

Turning of gamma titanium aluminide under different cutting speeds and feed rates had considerably different surface roughness and distinct surface features, but when compared to the polished material there was not a clear trend in the fatigue performance, indicating that the failure mechanism was more complicated [122]. Instead, a notable

increase in fatigue life was obtained for high speed milled specimens against polished ones, which was related to the beneficial compressive stresses, despite the surface cracking of some specimens [122] [123] [124]. A comparison of turning, electro-chemical machining and electro-discharge texturing on gamma titanium aluminide indicated that the compressive stresses, the lower roughness and the shallower surface cracking of turning increased the number of cycles to failure [125].

2.4.4.4 Nickel alloys

Turning of Nickel superalloys to different surface roughness resulted in a notable increase of fatigue life for fine conditions, but all conditions (rough, smooth and fine) introduced tensile surface residual stresses, which diminished from rough to smooth and slightly increased for fine conditions [126]. Low cycle fatigue was similar for rough and smooth specimens and higher for fine specimens, but high cycle fatigue was 57% more for smooth specimens compared to rough ones. Thus, the high cycle fatigue was affected by residual stresses, whereas the low cycle fatigue not.

2.4.4.5 Titanium alloys

Electro-discharge machined (EDM) Ti-6Al-4V specimens tested under tension-compression and tension-tension, cyclic conditions, displayed a significantly lower fatigue performance in comparison to the parent material [127]. All specimens apparently failed at the relatively rough surface, although there was a white (re-cast/amorphous) sub-surface layer [127]. Due to the small thickness of the EDM layer, it is not possible to differentiate between the effects of the white layer and the rough surface. In a closer inspection, micro-cracks and surface texture were present on the EDM surfaces and some cracks originated from what was thought of as a void in the re-cast layer [128]. The re-cast layer can be thought of as an SPD layer for the conventional machined specimens, without any other significant microstructure alteration. However, even in this simplified case, there is significant ambiguity about the mechanisms of fatigue failure.

Low and high cycle fatigue tests on Ti-6Al-4V specimens prepared under different machining conditions as well as shot peening, indicated that surface topography is critical for the performance of the specimens, but sub-surface residual stresses can control the crack initiation and short crack propagation, despite the stress relaxation during the tests [129]. Notches on the surface can act as crack concentrations, but their geometry could contribute to variations of fatigue lives, as it has been displayed for large notches on the Ti-6Al-4V bar [130].

The effects of high-speed milling on the fatigue performance of TB6 have been assessed through the surface roughness of the specimens (Ra=0.67-1.93 μm), without any further investigation of the deformed microstructures or residual stresses [131]. In that study, milling marks were parallel to the applied, uniaxial, cyclic load (tension-tension regime) and the crack initiation point was located at the corner of the flat specimen with rectangular cross section, in an area close to or on the machined surface. Due to the direction of the applied stress, the marks should not be significant stress risers, while stress triaxiality does not favor a specific location. Despite that, there was a slight increase in fatigue lives of specimens with lower surface roughness. Specimen miss-alignment and high plastic strains in the corners of the orthogonal faces could have contributed to these failures.

High speed machining of different Ti-6Al-4V microstructures and grades resulted in identical surface finishes (Ra<0.4 μm) for cutting speeds in the range of 50 -150 m/min (finishing conditions) and very small sub-surface deformation, indicating that the roughness did not contribute to the fatigue performance in the subsequent uniaxial cyclic loading test [132]. The crack initiation point was not disclosed, but the finer microstructure in the mill-annealed condition, compared to the coarse beta-annealed one, reached fatigue lives more than 10^6 cycles.

2.5 Summary

A number of machined induced defects have been identified, which could accelerate the crack nucleation, initiation and propagation stages in Titanium alloys. The mechanisms of fatigue failure were examined by extended cyclic loading tests in smooth and rough specimens. The majority of the tests were conducted in un-deformed microstructures and have displayed that the generation of slip bands, twins and the interactions between each other and the grain boundaries can lead to micro-cracks. Peening and other surface treatments have improved the fatigue resistance of materials due to strain hardening and beneficial, compressive residual stresses. High fatigue lives were achieved for surface processes that reduce the surface roughness and move the crack initiation point deeper into the material. In machined specimens, the fatigue behaviour has been linked to the surface quality, since the crack initiation point was located close to the surface. However, the exact failure mechanism has not been satisfactory explained, because sub-surface plastic and elastic strain fields have been ignored. There was no clear crack initiation location and no evidence of how the deformed layers affected crack initiation and propagation. Moreover, there was no explanation of why peening has a beneficial effect

on fatigue, while machining has a detrimental effect for similar surface roughness and/or sub-surface strain fields. The key limitation of the previous studies is that there have not been conducted comparisons on the fatigue performance of smooth specimens (polished to Ra=0.1-0.2 μm) vs peened smooth vs machined vs smooth machined (polished to remove only the roughness of the machined surface) to describe the behaviour of the material under different surface and sub-surface conditions. All experiments have been conducted on a need-to-know basis for specific sets of loads and materials, which cannot be integrated into a unified theory.

Sub-surface plastic and elastic strain fields, deformed microstructures, and surface topology consist a very complicated system for the drilled Ti-6Al-4V plates, with competitive failure mechanisms. All factors can contribute to the fatigue performance and must be thoroughly examined to fully appreciate the effects of the varying machining conditions on fatigue. The close examination of fracture surfaces is the only tool that can provide information about the dominant failure mechanism. Typically, only the crack propagation stage is considered in machined specimens, due to the pre-existing (mostly surface) defects. This was not the case for the drilled plates of the parent and the current study, where large differences in fatigue performance occurred in specimens with seemingly identical surfaces roughness (below 1 μm) and moderate variation of the subsurface plastic deformation (ranging 20-80 μm).

Chapter 3. Background Information & Preliminary Work

A preliminary analysis was conducted to categorize the available specimens and prepare the experimental work of microstructural characterization and measurement of residual stresses. The information collected from:

i. LOM images of the material, in both the deformed and the undeformed state;

ii. SEM images of the material, in both the deformed and the undeformed state;

iii. Surface roughness of the drilled specimens;

iv. Micro-hardness mapping of deformed regions.

These data were compared against the fatigue lives of the specimens and the drilling conditions, which have been described extensively in the parent study [1] and they were included in the current chapter for completeness.

3.1 General Information

The material under investigation was ASTM Grade 5, Ti-6Al-4V annealed plates, 8 mm and 10 mm in thickness, in accordance with the aerospace standard AMS 4911H, [133], *Table 3-1 & Table 3-2*.

Table 3-1 Typical chemistry and properties of Ti-6Al-4V mill annealed plates to AMS 4911H [133]

Ti	Al	V	O	Fe	C	N	Others	
							each	total
balance	5.5-6.75	3.5-4.5	max 0.2	max 0.3	max 0.08	max 0.05	max 0.1	max 0.4

Thickness [mm]	Tensile Strength [MPa]	Yield Strength at 0.2% Offset [MPa]
1.60-4.76	920	866
4.76-101.6	893	823

Table 3-2 Typical properties of Ti-6Al-4V[2]

Density [g/cc]	4.43
Hardness Vickers	349
Modulus of Elasticity [GPa]	113.8
Ultimate Tensile Strength [MPa]	950
Tensile Yield Strength [MPa]	880
Compressive Yield Strength [MPa]	970
Fatigue Strength (notched @ stress concentration factor 3.3) [MPa]	240
Fatigue Strength (unnotched) [MPa]	510
Fracture Toughness [MPa-$m^{1/2}$]	75
Specific Heat Capacity [J/g-ºC]	0.5263
Thermal Conductivity [W/m-K]	6.7
Coefficient of Thermal Expansion @ 20 ºC [µm/m-ºC]	8.6
Solidus [ºC]	1604
Liquidus [ºC]	1660
Beta transus [ºC]	980

[2] http://asm.matweb.com/search/SpecificMaterial.asp?bassnum=MTP641

The 10 mm plates were cut in strips of 355 mm x 25.40 mm, while the 8 mm plates in strips of 355 mm x 32 mm and seven (7) holes were opened in each strip, *Figure 3-1*. The diameter of the holes was 7 mm for the 10 mm plates and 8 mm for the 8 mm plates. Different drilling conditions were used for each set of holes.

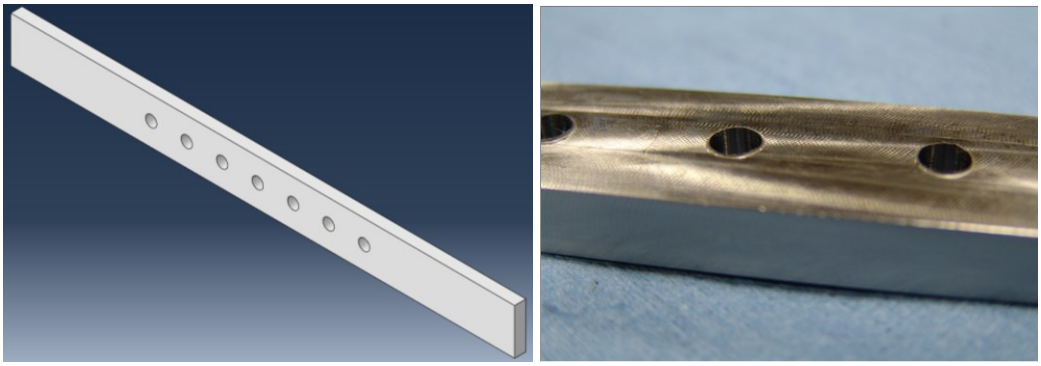

Figure 3-1 Geometry of fatigue test coupons [1]

The parent study mainly investigated the 10 mm plates and provided the basis for the design of the fatigue tests of the 8 mm plates. The current study investigated mainly the 8 mm plates after the fatigue test and the area of interest was primarily around the location of the maximum applied stresses during the fatigue test since the majority of the cracks were originated in that area [1].

3.2 Bulk Microstructure

The 8 mm plate had a layered microstructure, consisting of globular grains and macrozones, whereas the 10 mm plate had limited macrozones and mostly globular grains, *Figure 3-2* & *Figure 3-3.* A supplementary complete set of images can be found in *Figure AP- 1*.

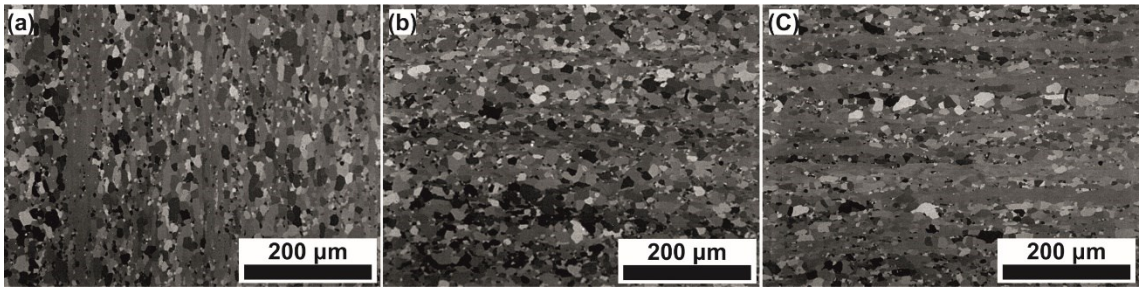

Figure 3-2 Ti-6Al-4V 8 mm plates, 3D microstructure, LOM images; a) XZ plane; b) XY plane; c) YZ plane

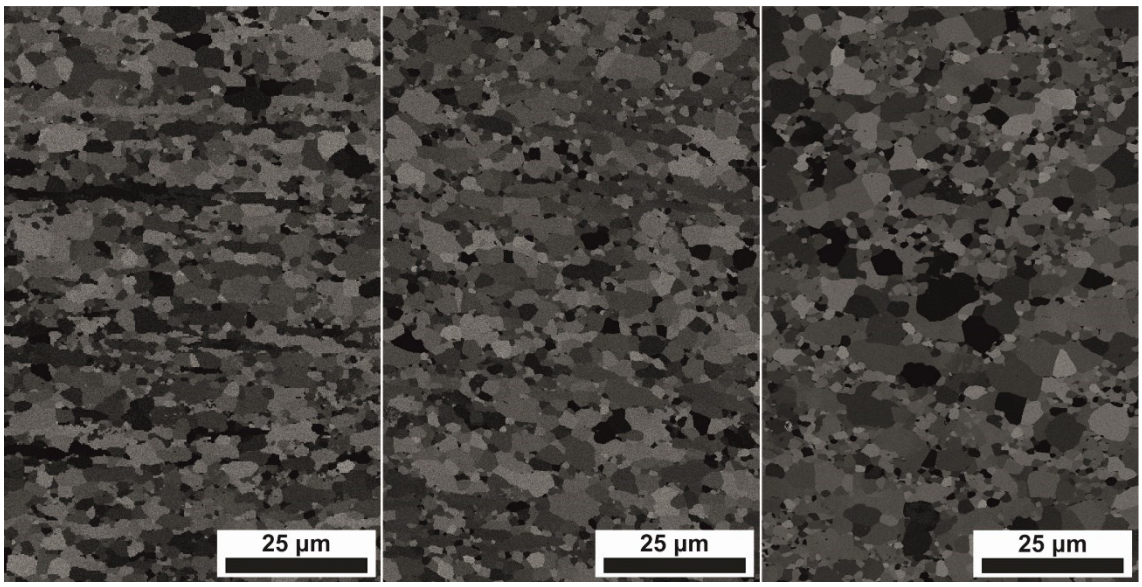

Figure 3-3 Ti-6Al-4V 10 mm plates, 3D microstructure, EBSD images; a) XZ plane; b) YZ plane; c) XY plane

The existence of the macrozones was not reported in the parent study of the 10 mm plates and was not identified prior to the fatigue experiments of the 8 mm plates. Such zones were considered as microstructural defects because they were a deviation from the desired microstructure and could affect the fatigue life, since they may have a different behaviour during machining or later during the cyclic loading test. Different microstructures could act as crack initiation sites due to their incompatibility during deformation and could further affect the short and long crack propagation path and growth rate.

3.3 Drilling Conditions

The drilling conditions for the fatigue tests were selected in the parent study [1] and they were a subset of more extended analysis based on thermal and metallographic ratings of test holes, *Table 3-3* & *Table 3-4*.

Table 3-3 Experimental drilling conditions (full set)

Drill bit	**Tool Wear**		**Medium**
Type S	Sharp	51 µm	Lubricant
Type U	Dull	100 µm	Coolant
Speed	458 rpm	917 rpm	1375 rpm
	Feed rate	51 µm/rev	

Table 3-4 Drilling conditions and grouping for fatigue tests

Type S	**Group**	**Tool Wear**	**Medium**
Speed	A	Dull	Lubricant
458 rpm	B	Sharp	Lubricant
Feed Rate	C	Dull	Coolant
0.051 mm/rev	D	Sharp	Coolant

Statistically, all parameters of the parent study were important drivers for the hole quality matrix. But the parameters selected for the fatigue tests were limited to the level of the tool wear and the type of medium used during drilling because they were showing more consistent results compared to the cutting speed and there was a need to reduce the number of tests.

3.4 Fatigue Test

The open hole, plate strip, specimens were tested under load control at room temperature according to the relevant standard, ASTM E466-07 [134]. In the parent study [1], each specimen had seven holes centered along the strip, at two diameters center to edge distance and four diameters center to center spacing. That configuration increased the stress concentration factor (kt) at the first and seventh hole to 3.34 from the theoretical value of 3.0 and the rest of the holes were approximately at 3.29. The specimens were subjected to constant amplitude testing, with the majority of them at a peak net stress of 221 MPa (kt*221 MPa of 724 MPa) and a few at a peak net stress of 200 MPa (kt*200 MPa of 655 MPa), stress ratio of R=-0.2 at a frequency of 10 hertz. Since the fatigue limit is around 510 MPa, the tensile yield stress is around 880 MPa and a significant decrease in performance has been observed for stresses higher than 650 MPa [9], the cyclic load should be considered relatively high.

The 10 mm plate specimens had significant variation and scattering even within the same grouping of *Report 0-66424*, *Table 3-5* & *Figure 3-4*. A statistical analysis from the parent study [1] indicated that the use of dull drill bits was beneficial for the fatigue life, which could be further increased by the use of lubricant instead of coolant, Groups A & C. The drilling conditions of *Report 9-39096* were not disclosed, but the range of fatigue lives was wider and a limited number of specimens reached the high cycle regime, *Table 3-5 & Figure 3-5*.

Table 3-5 Machining and fatigue data for the 10 mm plates

Specimen	Cycles to failure	Specimen	Cycles to failure	Group
1-1	3165947	1-1	196095	A-2
1-2	78291	1-2	224239	B-3
1-3	64916	1-3	140214	A-3
1-4	2690063	1-4	147742	C-1
2-1	43755	1-5	110103	C-3
2-2	36807	1-6	204420	-
2-3	33750	1-7	137550	B-2
2-4	32135	1-8	230388	C-2
3-1	620422	1-9	133954	D-2
3-2	137156	1-10	322505	D-4
3-3	91187	2-1	139552	A-4
3-4	123795	2-2	165872	B-4
4-1	42377	2-3	227132	C-4
4-2	44265	2-4	154758	B-1
4-3	38189	2-5	182773	D-1
4-4	25871	2-6	160930	A-1
Report	*Test Log*	*Report*	*Test Log*	*Report*
9-39096	L14771-86	0-66424	M55980-95	0-66424

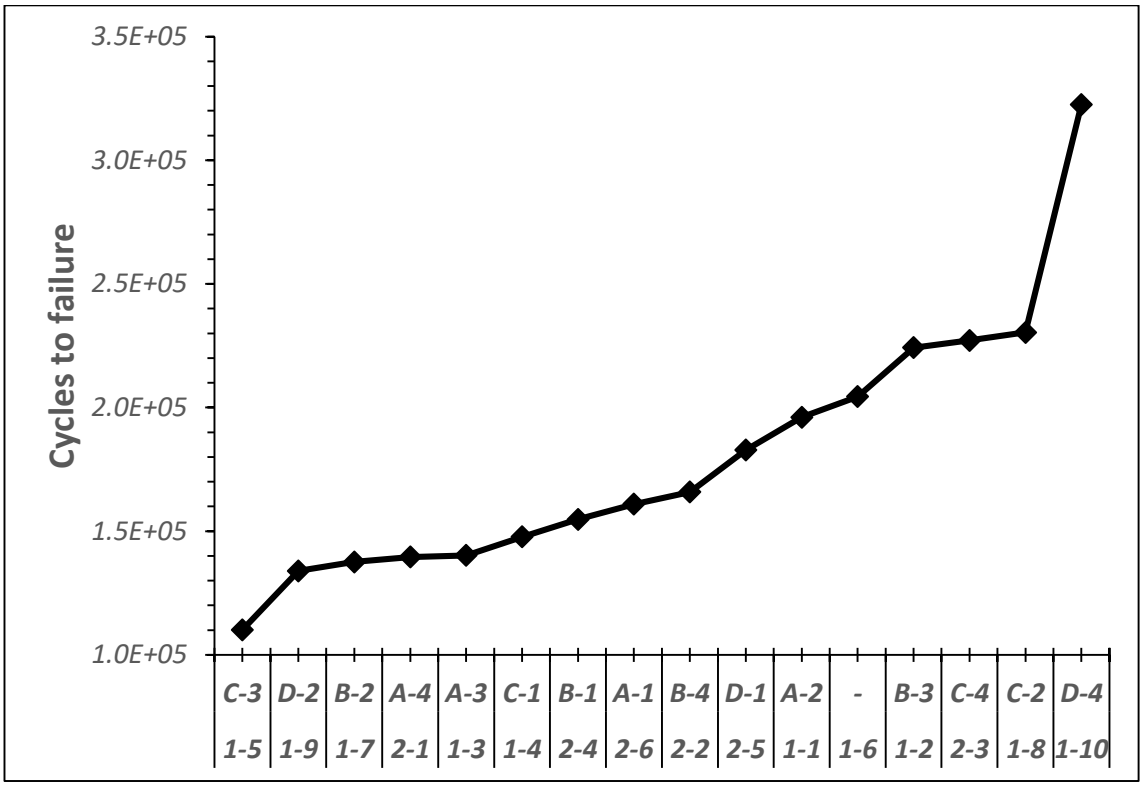

Figure 3-4 Fatigue life vs. machining conditions, 10 mm plates Report 0-66424

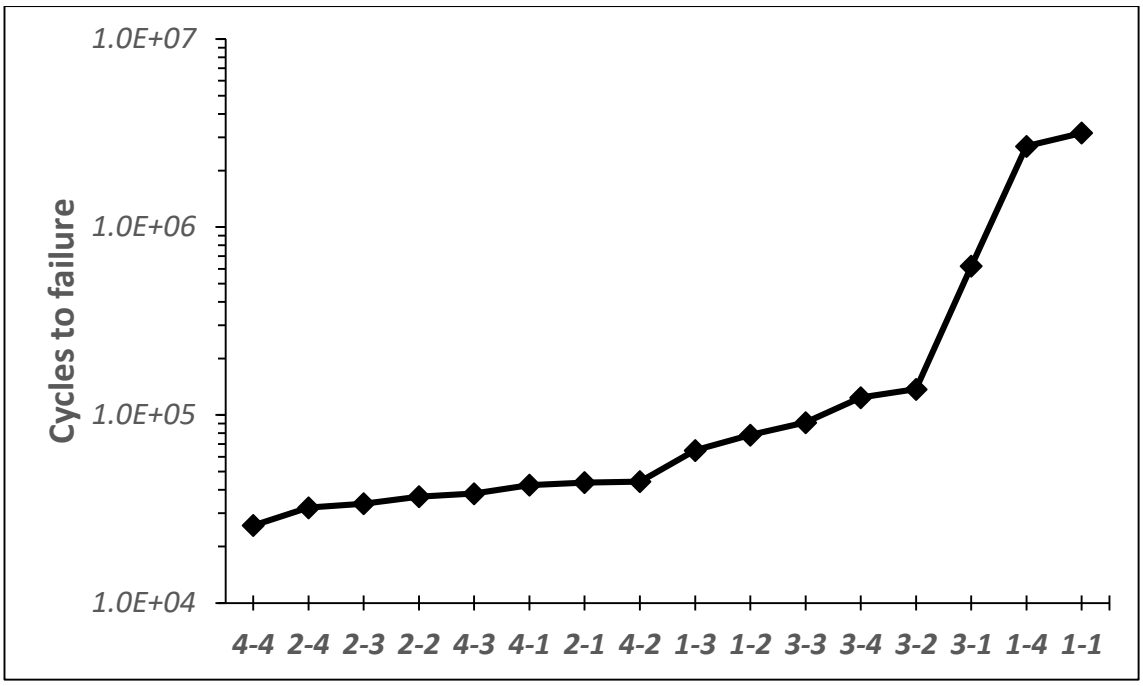

Figure 3-5 Fatigue life vs. machining conditions, 10 mm plates Report 9-39096

The 8 mm plates were a selected subset of drilling conditions from the subset of the 10 mm plates tested in fatigue, hence they showed a clear increase in the fatigue life of specimens in Group C, *Table 3-6* & *Figure 3-6*. Group C corresponded to the set of drilling conditions where the holes had been opened with a dull tool and the aid of coolant rather than lubricant. There was significant less scattering due to the relatively small number of the specimens examined.

Table 3-6 Machining and fatigue data for 8 mm plates

Specimen #	Designation	Group	Cycles to failure
1	HSC-5	D	127836
2	SD-4	B	72559
3	SD-2	B	100113
4	HSC-1	D	181525
5	NSC-5	C	1238187
6	BL-13	A	142887
7	BL-14	A	135770
8	NSC-6	C	945223

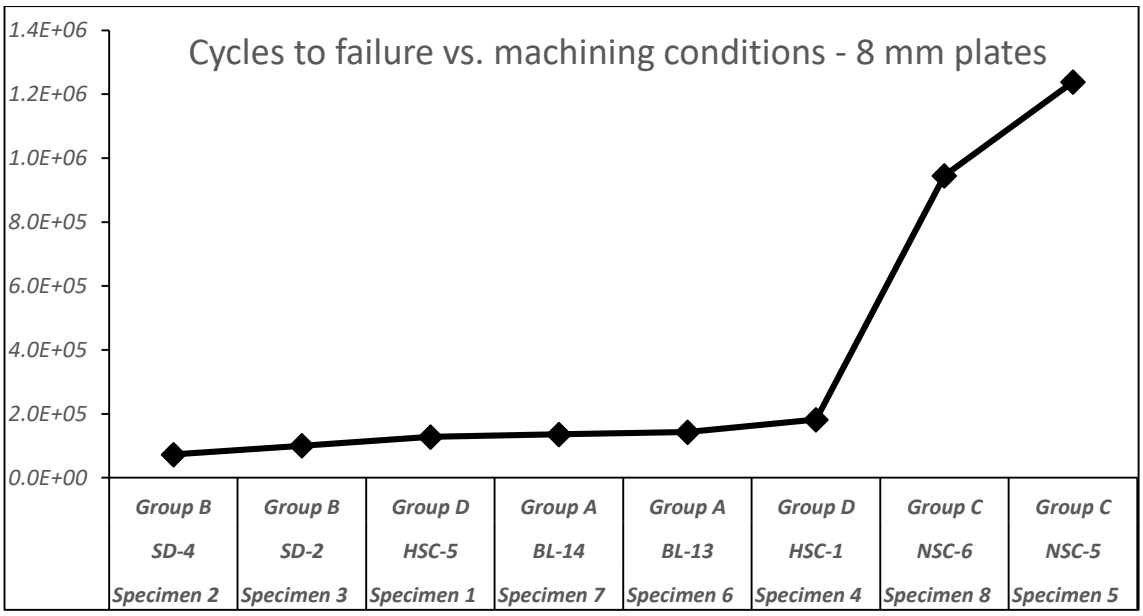

Figure 3-6 Fatigue life vs. machining conditions, 8 mm plates

3.5 Surface Roughness in Drilled Specimens

All the 8.0 mm plate specimens were examined by a 3D optical microscope, Bruker ContourGT-I[3] under the Vertical Scanning Interferometry (VSI) mode and at the three available magnifications, i.e. 5X, 10X & 50X. VSI was the standard scanning mode, where the height of each pixel is determined by the height of internal translator at maximum modulation as the surface comes in and out of focus according to the backscan and length of scan settings [135]. Partial and full depth scans were performed on the drilled surface at the location of maximum stress applied during the fatigue tests.

The raw data were initially corrected with the cylindrical and plane fit algorithms of the accompanying Vision64^{TM} software[4] to accommodate the shape of the hole surface and possible tilt of the specimen. Basic surface R-parameters, *Table 3-7*, and three-dimensional S-parameters, *Table 3-8*, of the profile were acquired for the height deviations from the mean plane. These corrections were appropriate for small/local area scans at 10X & 50X, *Figure 3-7, Figure AP- 3 and Figure AP- 4*.

[3] https://www.bruker.com/products/surface-and-dimensional-analysis/3d-optical-microscopes/contourgt-i/overview.html

[4] https://www.bruker.com/products/surface-and-dimensional-analysis/3d-optical-microscopes/surface-optical-metrology-accessories/vision64-map-software.html

Table 3-7 2D Surface R-parameters [135]

Ra	Average Roughness	$\frac{1}{N}\sum_{j=1}^{N}\lvert Z_j\rvert$
Rp	Max Peak Height	Rp=max(Z)
Rq	Root Mean Square Roughness	$\sqrt{\frac{\sum_{i=1}^{N} {Z_i}^2}{N}}$
Rv	Max Valley Depth	min(Z(x,y))
Rt	Maximum Height	Rp-Rv

Table 3-8 3D Surface S-parameters [135]

Sa	Average Roughness	$\iint_a \lvert Z(x,y)\rvert dxdy$
Sku	Kurtosis	$\frac{1}{Sq^4}\iint_a (Z(x,y))^4 dxdy$
Sp	Max Peak Height	max(Z(x,y))
Sq	Root Mean Square Roughness	$\sqrt{\iint_a (Z(x,y))^2 dxdy}$
Ssk	Skewness	$\frac{1}{Sq^3}\iint_a (Z(x,y))^3 dxdy$
Sv	Max Valley Depth	min(Z(x,y))
Sz	Ten Point Height	$\frac{\sum_1^5 \lvert PeakHeights\rvert + \sum_1^5 \lvert Valeydepths\rvert}{5}$

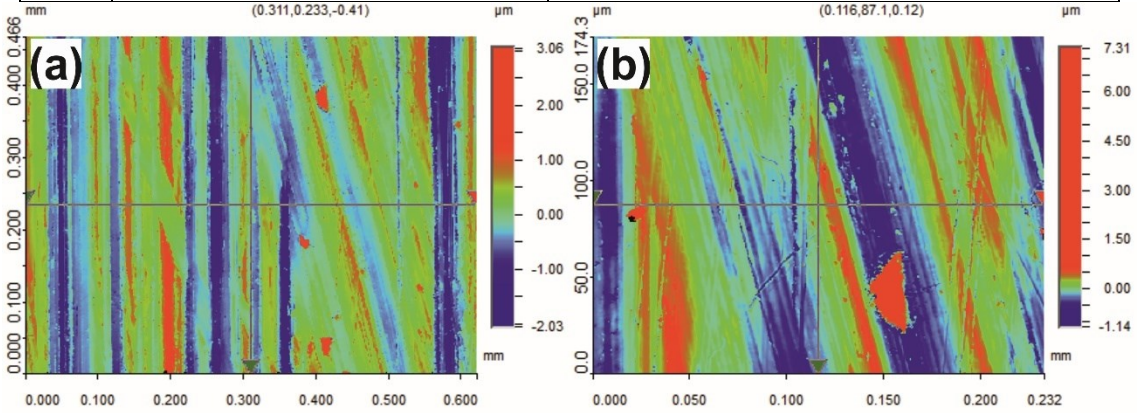

Figure 3-7 Localized surface profile measurements of the hole at the half thickness in Specimen 3 @ 100113 cycles; a) 10X; b) 50X.

However, the surface profiles maintained some waviness introduced by the wobbling of the tool, non-uniform material removal, and relevant artifacts during drilling, especially in full or half depth hole scans, *Figure AP- 5*. Thus, the Fourier filter was a more suitable correction setting within the Vision64™ software to capture the roughness of the profiles,

with a low-frequency cut-off, either after cylindrical and tilt fit (*CTF*) or directly applied to the raw profile (*F*). Then it was possible to relate the roughness of the surface profile with its quality and examine its effect on the fatigue life.

All specimens had (average) surface roughness values (*Sa*) below 1.0 µm, Figure 3-8. Full (un-sectioned plates) and half-length (sectioned plates) profiles provided a more accurate representation of the surface profile rather than local measurements, although the values did not differ significantly.

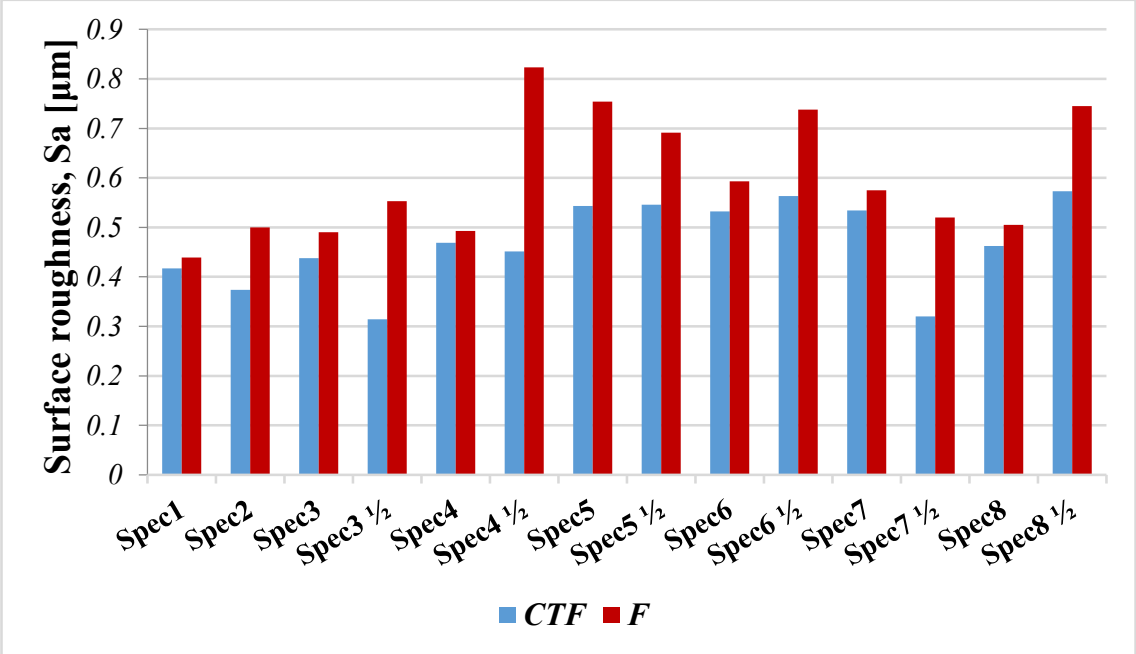

Figure 3-8 Full and half-length hole surface roughness of drilled 8.0 mm plates

It is generally accepted that titanium specimens with Ra values below 1.0 – 2.0 µm have a good surface quality, which should not significantly affect the fatigue life since they evidently have similar fatigue endurance limit [78]. This hypothesis was not verified due to the scattering of results from the fatigue tests, *Figure 3-9*, indicating that the surface quality of the hole was not the parameter linking the drilling conditions to fatigue lives.

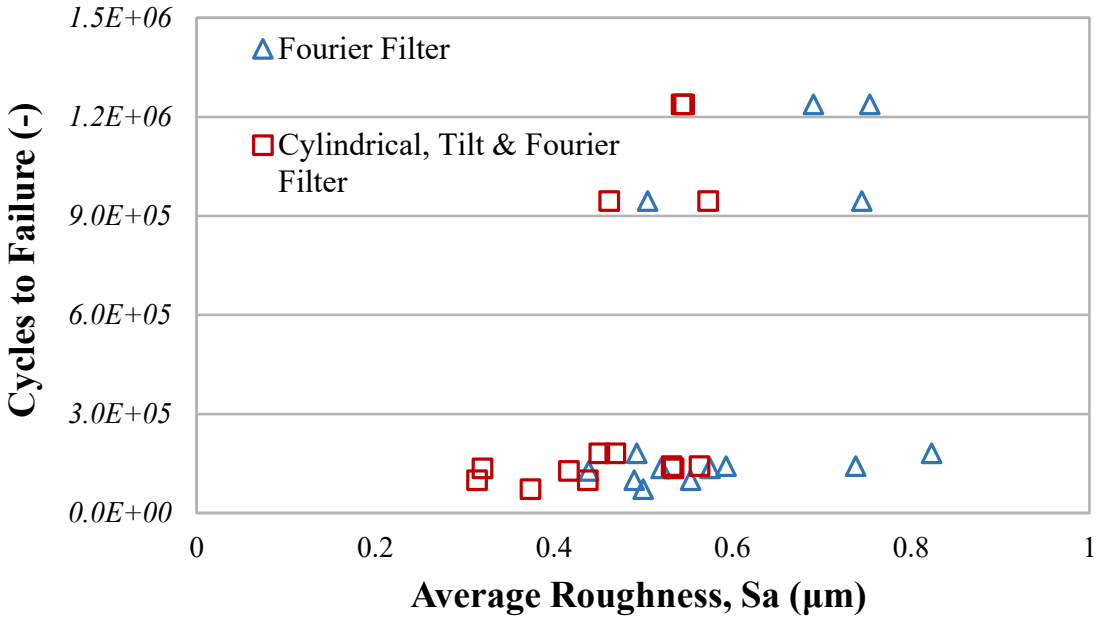

Figure 3-9 Full and half depth (average) surface roughness vs. Fatigue life, 8 mm plates

Traditionally the average roughness has been used for lifing assessments because it is an average of the absolute values of the surface heights, *Table 3-7* & *Table 3-8*, in either or both directions (*Ra* vs. *Sa).* However, in drilling the feed marks were the dominant features captured by surface profilometry and developed over the hoop direction creating a significantly rougher profile in the axial rather than the hoop direction, *Figure 3-7* & *Figure AP- 5*. Thus, the 2D roughness (*Sa*) is further averaged and lowered in comparison to the 1D roughness (*Ra*) over the axial direction. The most appropriate parameters for surface quality in terms of fatigue are the max valley/depth and their distributions but they should be evaluated with respect to the direction of the applied cyclic load.

The majority of the drilling marks on the machined surface were along the hoop direction which was parallel to the orientation of the applied cyclic load at the locations of the fatigue cracks. Since the feed marks could be considered as notches loaded parallel to their length and not perpendicular to it, these dominant surface features could not act as stress concentration sites or pre-existing defects leading to premature failure due to early crack initiation. Some drilling marks have different orientations, reaching even 45 degrees, and their role should be clarified by the examination of fractured surfaces.

Other local surface defects were chip fragments embedded on the surface, detected as peaks in the profiles of roughness, i.e. red “islands” in *Figure 3-7*. These sites did not affect the overall surface roughness because they were masked behind the numerous drilling marks of the hole. Only max peak values and additional filtering options on transition and average values around the area of interest could reveal the presence of chip fragments. Their occurrence had a strong statistical/probability element, which would not

necessarily be captured by these measurements. Ultimately, their importance in the fatigue life was questionable and similar to the orientation effect of drilling marks, their role should be clarified by the examination of fractured surfaces.

3.6 Deformed Microstructures

The 8 mm drilled plate specimens were sectioned through the half thickness plane, prepared with the standard techniques and the deformed microstructures were characterized by LOM in a Nikon Eclipse LV100 Polarizing light optical microscope and SEM in a FEI FEG/SEM InspectF. LOM under polarized light clearly described the deformed microstructure, including twins, whereas the SEM provided additional information about the SPD layer, the presence of beta phase near the machined edge, slip bands, the distortion of the grain structure and strain localization.

The LOM images, *Figure 3-10* & *Figure AP- 2*, indicated that the specimens had different levels of sub-surface deformation. More aggressive drilling conditions resulted in a higher depth of the deformed layer, but all specimens had the same microstructural features.

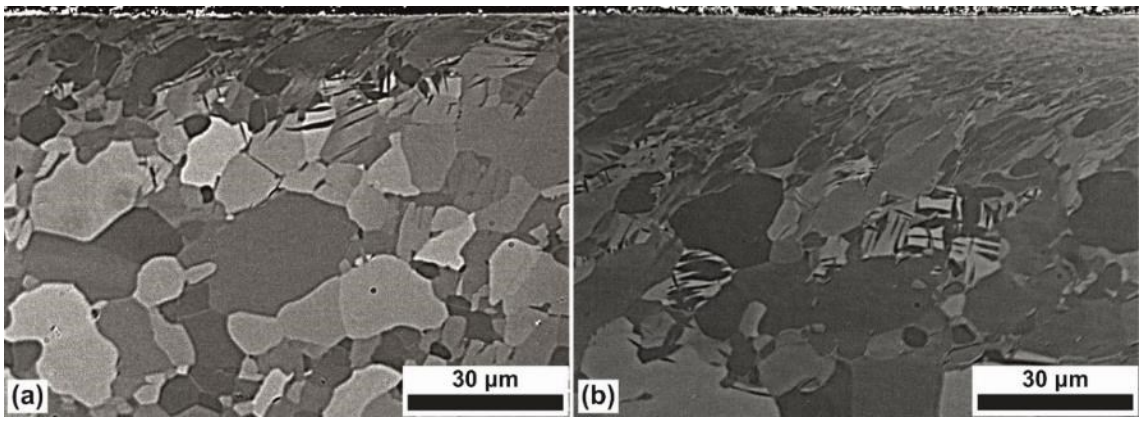

Figure 3-10 Deformed microstructures – LOM; a) Specimen 5 @ 1238187 cycles (max); b) Specimen 2 @ 72559 cycles (min)

Starting from the edge of the hole, there was a Severely Plastically Deformed (SPD) layer where the microstructure was completely sheared, with few traces of the pre-existing microstructure. Below the SPD layer, extensive twinning was observed within the alpha phase grains in the Intermediate Plastic Strains and Twinning (IPST) zone, but there was significant variation, even between neighboring grains of the same specimen. Typically, the twins introduced the highest variation in the depth of the deformed layer, thus three different depth levels were recorded in an attempt to cope with that issue:

i. average SPD depth – high plastic strains region;

ii. average depth of visibly distorted alpha phase– severely plastically deformed region;

iii. maximum depth of twins – low plastic strains regions.

The subsurface deformation was directly related to the drilling conditions and subsequently to the fatigue lives, *Figure 3-11*. Specimens from Group C had the smallest sub-surface deformation and the highest fatigue lives. There was also one outlier, Specimen 4 – Group D, which had a small deformed region, but also a low fatigue life. The transition from low to high fatigue lives was very abrupt and the specimen with the highest fatigue life had the third lowest deformation layer. Those inconsistencies could be explained by the fact that the measurements were based on an averaging, qualitative approach on a single plane. Specimens 1, 5 & 7 had higher twin density, but that did not have a notable effect on the fatigue life, possibly for the same reason.

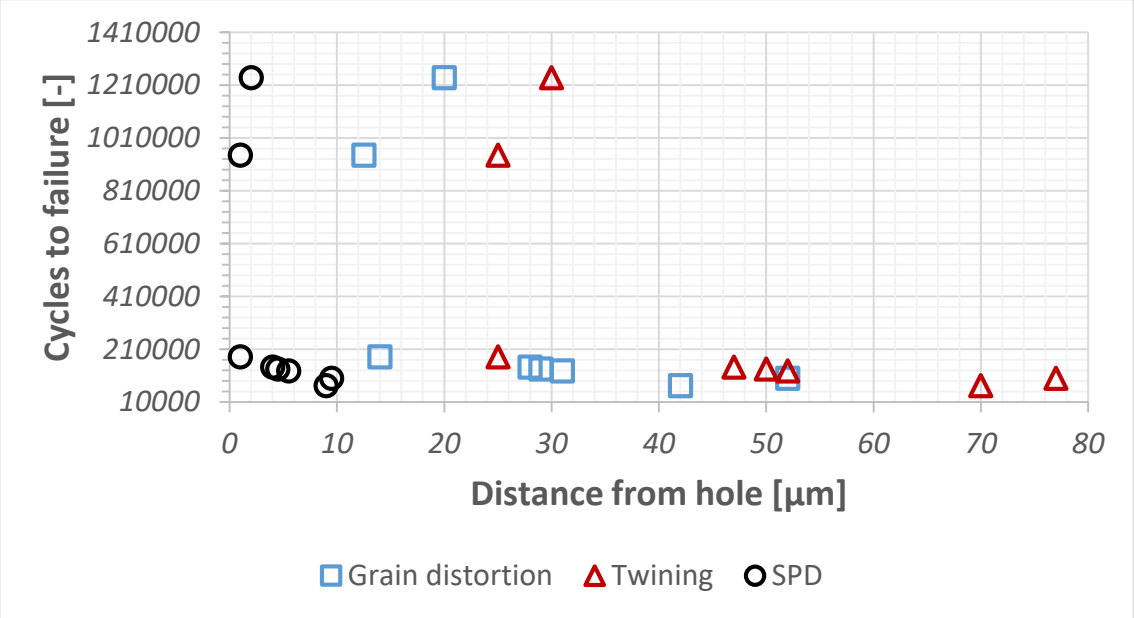

Figure 3-11 Characteristic deformation depth levels vs. fatigue life of specimens (LOM)

Higher strains appeared to exist in regions with smaller grains, breaking them up into sub-grains and cells, while larger grains were apparently more capable of accommodating the shearing. Due to the low magnification, it was not possible to evaluate accurately the SPD layer and the distorted beta phase in less deformed specimens and SEM was used instead.

The SEM images provided more detail inside the deformed region, *Figure 3-12 & Figure AP- 7*. The beta phase (bright contrast in *Figure 3-12*) was still present close to the hole for all specimens. Oxygen diffusion should be promoted due to the high temperatures and the deformed microstructure during drilling [38], but beta phase depletion (alpha phase stabilization) were not apparent, probably due to the low duration of the cutting process and the use of cutting fluids. Bright contrast at the edges could be considered as white layers [20], but under different imaging conditions such features were suppressed. The

severe plastic deformation zone, clearly visible in *Figure 3-12*, should have higher oxygen content, particularly towards the edge. No measurements of oxygen were carried out because there was not sufficient drive at any point during the research project with respect to the main research question. Both phases were significantly distorted and especially beta phase was elongated and thinned. Measurements of the deformed layer by SEM followed exactly the ones from LOM.

SEM and LOM images indicated the strong rolling texture was influencing the depth of the deformed layer and the twin density around the hole in a similar way to texture and cutting forces [136]. Since the cracks originated in the maximum stress area of the hole, no further examination was carried out.

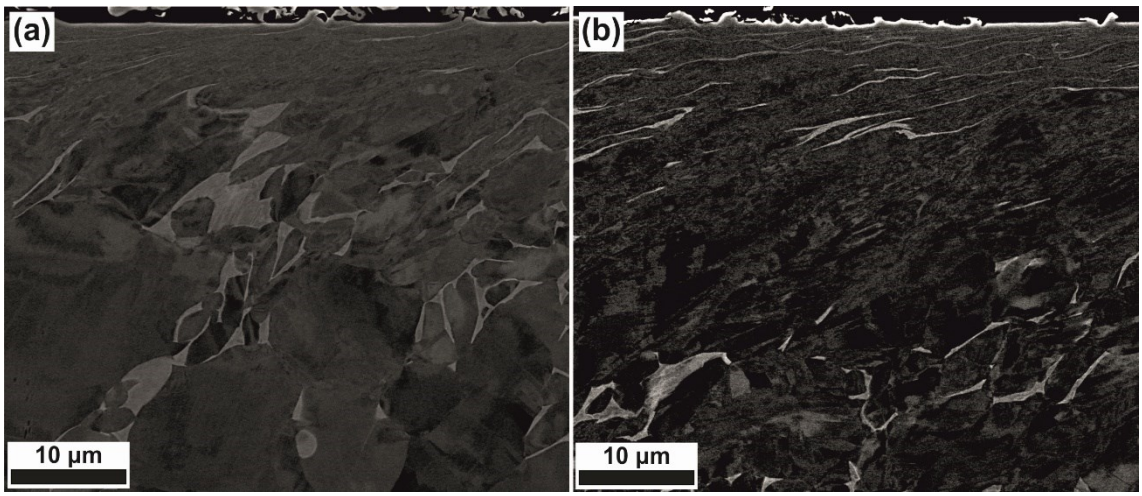

Figure 3-12 Deformed microstructures - SEM; a) Specimen 5 @ 1238187 cycles (max); b) Specimen 2 @ 72559 cycles (min)

3.7 Micro-hardness in Drilled Specimens

Micro-hardness has been used in the past to assess the mechanical properties of the deformed layer as part of the integrity analysis. This method was successfully applied in a number of materials including peened commercial pure Titanium (CP-Ti) [7], but it has not provided clear profiles or trends in machined Ti-6Al-4V [78] and the parent analysis [1]. Potentially, this technique could provide the depth of the deformed region, the strain hardening profile through the deformed region and an association between microstructure features and hardness values.

Thus, the 8 mm Ti-6Al-4V drilled plates were examined on a Struers DuraScan-70 G5[5]. The micro-hardness testing equipment had the ability to measure both Vickers and Knoop hardness under low loads, 10 – 100 gcf. Beyond that range, the indent size was too large

[5] http://www.struers.com/Products/Hardness-testing/Hardness-testing-equipment/DuraScan-G5#durascan-g5-facts

to provide the required level of detail. The measurements were conducted in accordance to the ASTM E384-11 standard [137]. An initial study was conducted to establish the approximate size of the indents for the construction of the test matrix, *Table 3-9*.

Table 3-9 Indicative sizes of Vickers and Knoop indents for the 8 mm Ti-6Al-4V plates

Load [gcf]	**Vickers Indent**	**Knoop Indent**	
	mean Diagonal [μm]	*Diagonal [μm]*	*Width [μm]*
10	7.5	19.5	4
25	11	35	5.5
50	15.5	53	7
100	20	71	8.5

Knoop indentation had better spatial resolution compared to Vickers and more bias towards each depth level even at larger loads, which could eliminate local microstructure variations and capture the average hardness gradient through the strained layer. The spacing of the indents was kept according to the relevant standard, at two indents between successive indents and edge to indent distance to avoid any kind of interferences. Due to the low testing loads, manual measurement was employed with the Nikon Eclipse LV100 Polarizing light optical microscope to avoid imprecision errors during the measurement of the diagonals. Furthermore, since the deformation zone in the drilled specimens was relatively small (20-60 μm), the indentation was performed in a high tilt angle.

As a first approach, a part of the sectioned plate of specimen 7 was used containing a non-critical, low stress, region of the hole, tilted at ~30 degrees, *Figure 3-13*. The results showed a significant scattering and there was not any notable trend, except to the apparent reduction of the scattering at the first 100 μm from the hole, in line with similar studies [1] [78] and despite the visible microstructure changes and strain gradients. Similar results were obtained from the rest of the test conditions with the Knoop indenter.

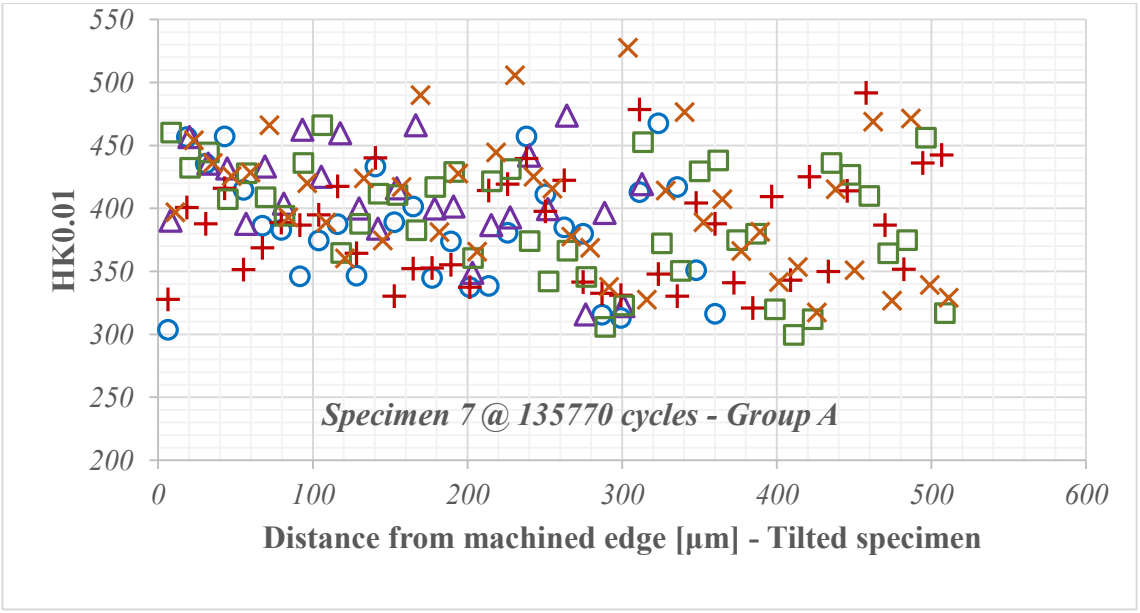

Figure 3-13 Specimen 7 @ 135770 cycles – microhardness evaluation

Only the Vickers indenter at 25 & 50 gcf showed some consistency with LOM and SEM observations, *Figure 3-14*. In fact, the obtained curves were a very close match in the first 150 µm, where the highest plastic strains exist, from the SPD to the IST zone, *Figure 3-15*. Some inconsistencies started to appear at the twinning zone, possibly as a result of different strains within grains, variations of grain size, twinning, orientation and the presence of macrozones inside a 3D volume. The 10 gcf Vickers indents had significant variation and scattering, similar to that of the Knoop indents, probably due to the small load.

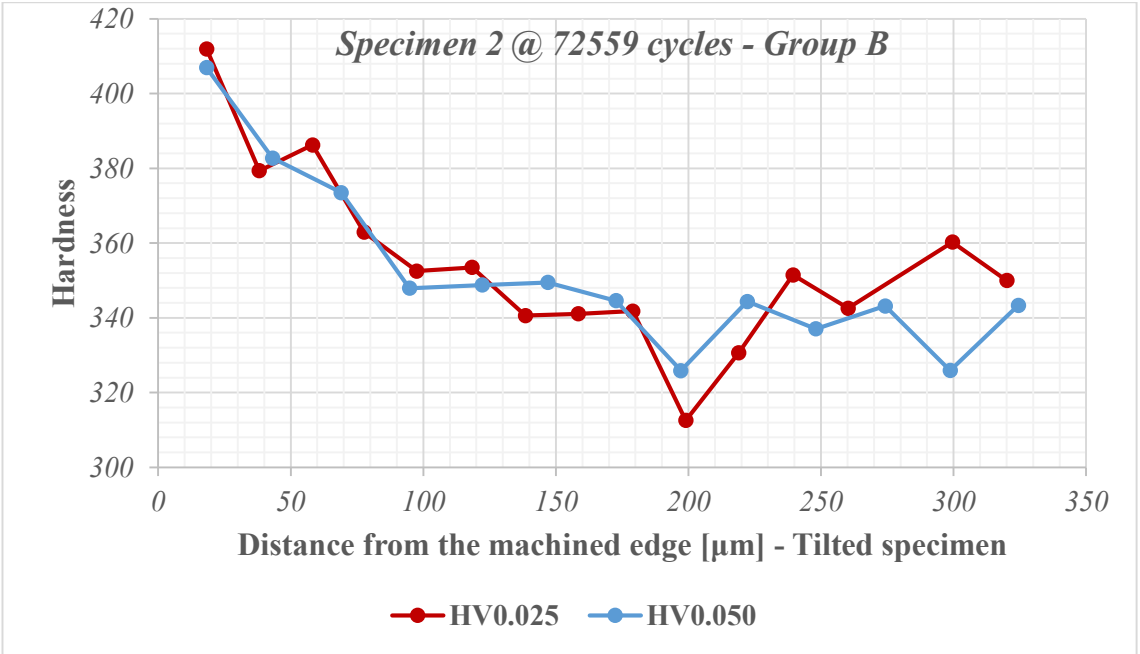

Figure 3-14 Microhardness measurements through the deformed zone of a tilted Specimen 2

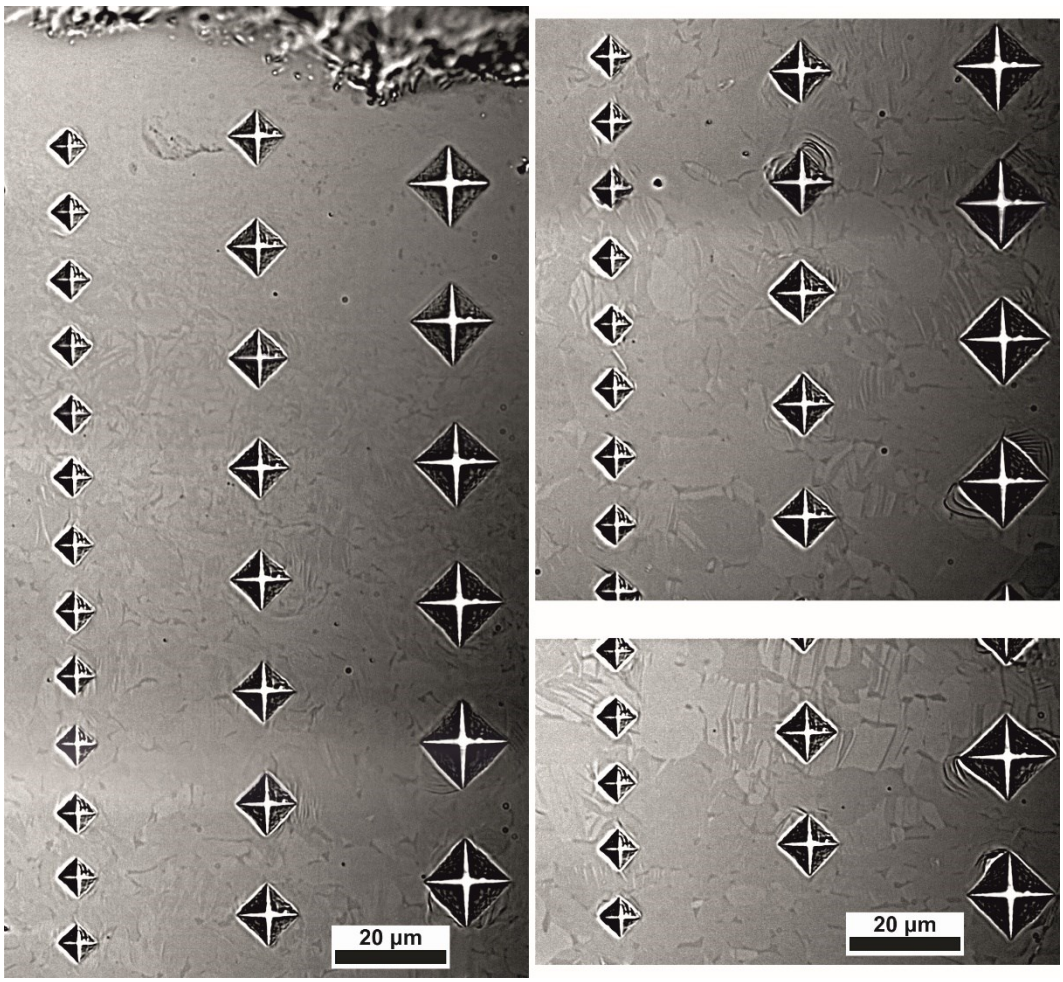

Figure 3-15 Vickers Indentation at a tilted specimen 2; 10, 25 & 50 gcf indents vs microstructure features

The Vickers indents were not carried out according to the standard in terms of spacing because the loads were small and there was not any significant interference between idents, *Figure 3-15*. Besides, it was more important to acquire a trend rather than absolute values and the spacing would only provide a systematic error, not affecting the overall trend.

The incremental grinding/polishing and direct indentation of the machined surface under higher loads could have reduced the variation and provide more useful information. In this case, the depth of the indenter should be kept within a maximum of 5-10 µm and use only the Vicker indenter to avoid any direction bias. The main problems of this approach were that it was a catastrophic technique (critical for the limited number of specimens at the regions of the maximum applied stress), the preparation of the machined surface because of its curvature and subsequently the alignment of the specimen.

Definitely, the small loads were the major issue with the micro-hardness work. The Knoop indenter was not very selective and efficient as an averaging operator for each depth lever. Small loads made the measurement of the diagonal(s) very challenging and

quite often led to badly shaped indents, especially for the Knoop indenter. This indicated possible miss-alignment errors with the Knoop indenter. In any case, the use of the Vickers indenter, provide a clear strain hardening profile. The microhardness was decreasing with the increase of the depth from the machined edge following the plastic strain gradient. This was directly in line with the work carried out in peened CP-Ti [7] and was in accordance to the underlying mechanics of the system, even if the mode of deformation was more complicated due to the drilling.

The microhardness could probably describe the drilling conditions and provide an additional alternative to categorize specimens. Since the specimens had identical microstructural characteristics within the deformed regions, there would not be any additional information regarding the main research question. It should be noted that microhardness measurements are affected by the presence of residual stresses and pure strain hardening effects can be investigated with other techniques, namely EBSD.

3.8 Testing material - shot peened CP-Ti

A well investigated and simpler material was used for the development and validation of experimental and analytical techniques. That was commercial purity titanium (CP-Ti ASTM II) peened with steel shots to 200% coverage and 9A Almen target intensity at different temperature [7]. Each specimen had a characteristic sub-surface, hardness and twin line profile due to the different level of subsurface plastic deformation and twinning, *Figure 3-16*.

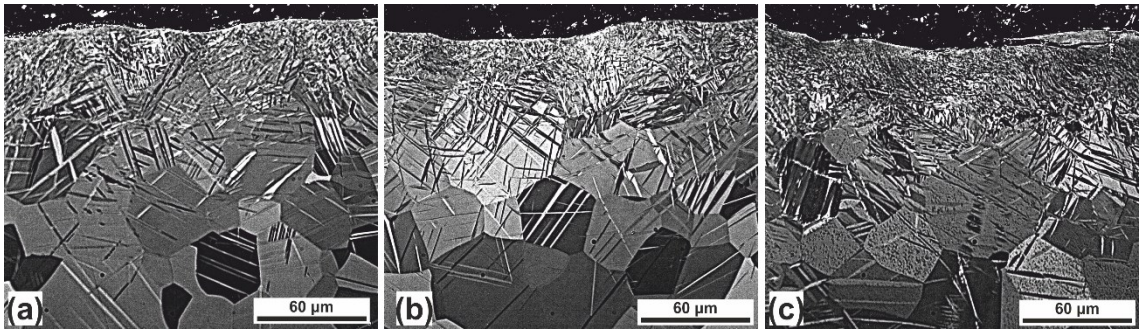

Figure 3-16 Shot peened CP-Ti; a) T=-196 ºC; b) T=25 ºC; c) T=280 ºC.

3.9 Summary

The preliminary analysis established the facts and formed the basis for the further examination of the drilled specimens. LOM and SEM images were directly correlated with each other, but SEM described additionally the SPD zone and the deformation of the two-phase material. The level of deformation and the local hardening of the material throughout the strained region was, ultimately, verified through micro-indentation studies. At this point, it was made clear that the drilling conditions were directly related

to the deformed microstructures and established them as a dominant factor for the fatigue life of the specimens. Generally, specimens with low levels of plastic deformation (evident from the depth of the deformed region) had significantly higher fatigue lives. That was achieved when a dull tool was used with the aid of coolant.

Roughness measurements of the drilled surfaces did not provide a clear trend as a function of the drilling conditions and the fatigue life. Furthermore, all roughness values were lower than a proposed critical Ra value of Ra=2.0 [78], which could be considered a threshold value for correlating the quality of the machined surface with the fatigue performance of the specimens.

During the preliminary analysis, it was not possible to specify the mechanism of the early failure of the drilled plates. LOM and SEM images indicated that all the specimens had the same microstructural features and only the depth of each deformed layer was changing. The fatigue lives of specimens with low levels of plastic deformation were significantly higher and a moderate to low threshold value appeared to exist. Strain localization, strain gradients, twins, brittle SPD layers and other misfits could serve as crack initiation points. Thus, the specimens were further examined with advanced characterization techniques, namely Electron Back Scatter Diffraction (EBSD). EBSD provided a scientific, semi-qualitative tool for the evaluation of plastic strains with excellent spatial resolution and could have been further evolved to provide elastic strain maps.

Chapter 4. Advanced Material Characterization with Electron Backscatter Diffraction

Deformed microstructures and plastic strains have been assessed in the past by advanced characterization techniques, like SEM and EBSD, because they can provide the required level of detail and spatial resolution. SEM images provide a qualitative approach, but raw and post-processed EBSD data can be transformed into semi or fully quantitative deformation tools for a more rigorous analysis.

Peened CP-Ti material was used to evaluate some of the available tools. Then, the drilled Ti-6Al-4V plates were examined through deformation maps and plots to reveal the plastically strained layer and its sub-regions. Strain gradients and localization, as well as microstructural defects, misfits, microcracks and voids were of particular interest for their contribution to the fatigue performance of the specimens.

The acquired information formed the basis of interpretation of differences in fatigue lives of the drilled plates and contributed towards the identification of the optimum process conditions for drilling Ti-6Al-4V plates.

4.1 EBSD Background

EBSD is an advanced characterization technique that provides crystal orientation information about the microstructure of the examined material. EBSD is carried out in a Scanning Electron Microscope, where the electron beam hits a highly tilted specimen and the diffracted electrons form a characteristic Electron Backscatter Diffraction Pattern (EBSP) on the fluorescent screen of the detector. EBSPs consist of bands intersecting at the zone axes and follow Bragg's law [52], $n\lambda=2dsin\theta$ *Equation 4-1*, linking EBSPs to the crystal structure and orientation.

$n\lambda = 2dsin\theta$ *Equation 4-1 Bragg's Law*

where ***n*** *is an integer,* $\boldsymbol{\lambda}$ *is the wavelength of the electron beam,* ***d*** *is the spacing of the diffracting plane, and* $\boldsymbol{\theta}$ *the angle of incidence of the electron beam on the diffracting plane.*

The matter and the electrons of the beam undergo elastic and inelastic interactions over a volume which depends on to the size and intensity of the beam and the material properties. Some of the electrons are absorbed, while others are emitted as Auger electrons, Secondary electrons, Backscatter electrons, and X-rays. If the specimen is thin then there will also be emissions of Elastically and Inelastically scattered electrons and Transmitted electrons, which will travel through the entire thickness of the specimen. [15]

EBSD utilizes the backscattered electrons which are considered to be elastically diffracted from a depth 20-100 nm. The (thick) specimen is positioned typically at 70^{o} degrees to increase the scattering of the electrons of the beam by reducing their travel length within the interaction volume. The incident beam spreads in all directions within the interaction volume due to small losses of energy from the electrons during their interactions with atoms of the material. Since some of the new trajectories are incident to crystal planes at an angle that satisfies the Bragg's law, then these electrons are scattered into two cones, mirror image to each other about the diffracted plane, with the cone axes normal to the diffracted plane. At an accelerating voltage of 20 kV the electron beam wavelength is 0.0087 nm, resulting in a Bragg angle below 2 degrees for most materials (based on typical unit cell dimensions). Hence the large angle cones are intercepted by the phosphor screen as almost straight bands. [15] [5]

The generated EBSPs are post-processed to identify the bands through the Hough transformation (converting bands to points) [138], and compared against databases of simulated, strain free, diffraction patterns to identify the crystal orientation of the phase(s) under examination [139]. During the EBSD scan topological information of phase, crystal orientation in terms of Euler angles, bands, error, EBSP image quality factors (Band Contrast – BC and Band Slope – BS) and goodness of solution (Mean Angular Deviation – MAD) are collected. Euler angles are three sequential rotations that transform the specimen coordinate system to the crystal coordinate system [15]. The first angle introduces a rotation about the Normal Direction (ND); the second a rotation about the new Rolling Direction; and the third a rotation about the new ND.

The characterization and texture analysis operations have been further extended with appropriate post-processing tools to include parameters that describe the level of deformation of the material. Elastic and plastic strain mapping features with EBSD have a lot of practical application in machined/peened specimens, where strain localization and steep gradients exist.

4.2 EBSD deformation parameters

Residual elastic strains and plastic strains coexist within the materials and are linked to the manufacturing process. Non-uniform plastic deformation from the thermal, mechanical or thermo-mechanical loads, microstructural variations, and other misfits generate residual stress fields [48]. Elastic strains can be inferred from the changes in the interplanar angles of the crystal lattice, which cause changes in the band widths and angles of the EBSPs and shift of the zone axes. Plastic strains are linked to the presence of

dislocations, which cause lattice rotation/curvature and additional shift of the zone axes [140].

As a material yields and deforms plastically, lattice imperfections in the form of dislocations move, accumulate and (re-)arrange themselves in networks, creating sub-grains and cells within the deformed grain structure. Dislocations are typically categorized into Statically Stored Dislocations (SSD) and Geometrically Necessary Dislocations (GND). SSDs have zero net Burgers vector (direction and magnitude of the distortion that occurs from the movement of a dislocation) canceling each other out, while GNDs have a nonzero vector and introduce a small orientation change or lattice curvature across the grain, i.e. the low angle grain boundaries of sub-grains/cells.

Plastic strains have been traditionally investigated through the image quality numbers of the EBSPs and/or the orientation gradients within the crystals of the deformed material with a number of qualitative and quantitative tools. In recent years, a step forward has been made with the mapping of elastic and plastic strains through cross-correlation of EBSPs.

4.2.1 Image quality factors

The presence of dislocations within the diffracted volume causes the degradation of the EBSPs, reducing their contrast and sharpness [5] [141]. Two default EBSP image quality factors exist, the Band Contrast (BC) and the Band Slope (BS), which are derived from the Hough transform. BC corresponds to the average intensity of the Kikuchi bands with respect to the overall intensity within the EBSP, whereas BS to the maximum intensity gradient at the margins of the Kikuchi bands in an EBSP [142]. Some bands can appear more diffuse than others, due to specific orientation relationships to the Burger's vectors of the GND's [143], but it is not possible to distinguish the effects of SSDs and GNDs in the pattern quality. Thus, image quality factors represent the overall imperfection of the crystal structure and are representative of the entire dislocation content. Grain boundaries are high angle boundaries, in locations where there is a significant change of crystallographic orientation. Hence the overall pattern in a boundary is a combination of two patterns increasing the blurriness of the image and reducing significantly its quality. BC and BS are recorded for each point of the scanned area, irrespective of the successful identification of the crystal structure and have been used in the past for deformation studies.

4.2.2 Orientation gradients

The spatial distribution and accumulation of GNDs within the crystals cause orientation gradients, which can be deduced from suitable post-processing of the Euler angles after an EBSD scan. Different parameters have been proposed in the past, but all of them are based on the calculation of misorientation, either as a point to point or an average value of the (sub)grain [5] [141].

If a point has Euler angles φ_1, Φ and φ_2 (Bunge definition), the orientation matrix, g, is given by the product of the rotation matrices of the Euler angles, $g_{\varphi 1}$, g_{Φ} and $g_{\varphi 2}$, *Equation 4-2 – Equation 4-5*. For two points with orientation matrices g_a and g_b, a misorientation matrix, Δg_m, can be constructed, *Equation 4-6*. Then the misorientation angle, θ_m, is calculated from the trace of Δg, *Equation 4-7*, while the rotation axis vector, r_m, from the rest of the elements of Δg_m, Equations 4-8 & 4-9 [15].

$$g_{\varphi 1} = \begin{pmatrix} cos\varphi_1 & sin\varphi_1 & 0 \\ -sin\varphi_1 & cos\varphi_1 & 0 \\ 0 & 0 & 1 \end{pmatrix} \quad \textit{Equation 4- 2}$$

$$g_{\Phi} = \begin{pmatrix} 1 & 0 & 0 \\ 0 & cos\Phi & sin\Phi \\ 0 & -sin\Phi & cos\Phi \end{pmatrix} \quad \textit{Equation 4- 3}$$

$$g_{\varphi 2} = \begin{pmatrix} cos\varphi_2 & sin\varphi_2 & 0 \\ -sin\varphi_2 & cos\varphi_2 & 0 \\ 0 & 0 & 1 \end{pmatrix} \quad \textit{Equation 4- 4}$$

$$g = g_{\varphi 1} * g_{\Phi} * g_{\varphi 2} \quad \textit{Equation 4- 5}$$

$$\Delta g_m = g_a * g_b^{-1} \quad \textit{Equation 4- 6}$$

$$cos\,\theta_m = \frac{(\Delta g_{11} + \Delta g_{22} + \Delta g_{33} - 1)}{2} \quad \textit{Equation 4- 7}$$

$$r_m = \left[\frac{(\Delta g_{23} - \Delta g_{32})}{2\,sin\,\theta_m} \quad \frac{(\Delta g_{31} - \Delta g_{13})}{2\,sin\,\theta_m} \quad \frac{(\Delta g_{12} - \Delta g_{21})}{2\,sin\,\theta_m}\right] \quad \textit{Equation 4- 8}$$

if θ_m is 0 or 180 degrees then r_m is simplified

$$r_m = \left[\left(\frac{\Delta g_{11}+1}{2}\right)^{1/2} \quad \left(\frac{\Delta g_{22}+1}{2}\right)^{1/2} \quad \left(\frac{\Delta g_{33}+1}{2}\right)^{1/2}\right] \quad \textit{Equation 4- 9}$$

Each crystal structure has a number of equivalent arrangement of atoms, which result in crystal symmetry. When these symmetry operators (O_c) are applied to the misorientation, a single, minimum value can be calculated termed disorientation (Δgd), which represents the real misorientation between two points [15]. These terms have been used loosely in commercial software and previous research work [5] [141].

$$\Delta gd = (O_{c,a} * g_a) * (O_{c,b} * g_b)^{-1} \quad \textit{Equation 4- 10}$$

Kernel Average Misorientation (KAM) is an example of a local misorientation component calculated from a point within a grid which contains up to its 1st, 2nd or 3rd neighbors. If the KAM values are averaged within the (sub) grain area, then the Grain Average Misorientation (GAM) [141] parameter is constructed, also called Integrated Angular Misorientation Density (IMD) [4]. Such parameters represent the real misorientation, but the level of detail depends on the scan step since the number of points

within the grain can be insufficient to describe the complete dislocation network and they often have high levels of noise. A possible modification is to divide the KAM with the scan step to acquire orientation gradients rather than differences.

Another approach is to calculate the misorientation of each point of the (sub)grain with reference to either the average orientation or the minimum cumulative misorientation of the (sub)grain and then average them over the (sub)grain area to form the Grain Orientation Spread (GOS) [141], also called Average Intragrain Misorientation (AMIS) [144], or Crystal Deformation (CD) [145] parameters respectively. Certain variations of the GOS parameter exist with regard to the calculation of the reference orientation, like the most probable orientation from a distribution function and the minimum 1^{st} neighbor KAM. GOS and CD do not depend on the scan step since the misorientation of a point is calculated against a reference orientation, but the choice of the reference misorientation is not necessarily representative of the grain and its deformation. The most suitable value would be that of the initial orientation of the (sub)grain, i.e. prior to the deformation. In absence of such information, selecting a reference orientation based on the minimum summation of misorientations from a point of the (sub)grain to all the other points of the (sub)grain maximizes the orientation differences and is physically more representative of the deformation in terms of GNDs and subgrain formation.

Global strains are calculated by averaging the parameters over the entire map [144] [146] or employ distribution functions [147], while the grain detection is based on high angle grain boundaries. For localized strain and strain gradients within an area, the averaging is limited to each depth level and low angle grain boundaries are used to increase the spatial resolution [148]. In the latter case, the method becomes sensitive to the scan step. When subgrains are detected rather than grains, GOS, GAM and CD provide similar results, due to the discretization of the grain area.

The arrangement of GNDs in dislocation networks to form subgrains, allow the direct detection of plastic strain by low angle grain boundary (LGB) detection in deformed [144] and aged [149] samples. This type of analysis is performed through a kernel misorientation analysis with a critical angle below 10-15 degrees. Strain localization can be captured by the local density of low angle boundaries, while global stains by the average density of low angle boundaries. Similar to KAM, low angle grain boundary density is dependent on the scan step. The number of subgrains detected by the closed loops of low angle grain boundaries is a metric by itself for the GNDs and the increased number of high grain boundaries is an indication of excessively high strains.

The accurate determination of strain in a deformed material requires the collection of high-quality diffraction patterns. Any orientation error can introduce significant noise to the misorientation analysis, especially for low strain specimens. The orientation error in modern EBSD systems is 0.5-1.0 degrees with the standard band detection methods and the resulting misorientation error is 0.2-0.5 degrees [150].

4.2.3 Elastic and plastic strain mapping with cross-correlation methods

The elastic and plastic strain fields can also be built through the successive comparison of diffraction patterns [140] [67] [151] [152]. Digital Image Correlation (DIC) is carried out between sub-regions of one pattern and the reference pattern within each grain of the EBSD map. Typically, two maps of the same area are required to make comparisons so that each point on the deformed map can be matched with a point on the un-deformed map, which serves as the reference map. Otherwise, the reference patterns are selected within the grains based on a minimum deformation criterion (MAD for example) or the center of gravity, although they may not represent the strain-free condition [151] [152].

Shifts of zone axes and bands provide the deformation gradient tensor through the combination of a geometric relationship for the pattern shift on the phosphor screen and a zero normal stress condition. Then the tensor is linearly decomposed by small deformation theory to obtain displacements and eventually strains. [152]

The method requires high-quality patterns and despite the relatively large area of the subregions in comparison to the detected and/or reference pattern, the proposed methodology has provided the full strain tensor even in cases of high lattice rotations [152]. Cross-correlation of EBSPs has reduced the misorientation error to 0.01-0.02 degrees [150] and even further to ~0.006 degrees [67].

4.2.4 Misfit of detected and simulated patterns

The deviation of the detected from the simulated, strain free, patterns is assessed by the Mean Angular Deviation (MAD) through the average angular misfit, in degrees. By definition, MAD should be capturing elastic distortions in regions of low plastic strains, where the corresponding error from the image quality and zone axes shifts can be neglected. Higher dislocation density will increase the misfit between the detected and reference patterns and mask the elastic distortion behind the lattice rotation. MAD is a parameter recorded only when a point is matched against a reference pattern, limiting its use as a plastic deformation indicator in severely deformed regions.

4.3 Plastic Strain Mapping with EBSD – Method development

EBSD data were transformed into semi-quantitative deformation parameters, exploiting the gradient of plastic strain. Alloy composition, processing route, sample preparation, crystal orientation and EBSD scan settings provided an average, background value for the deformation parameters in the bulk material. Subsequent machining produced a deformation gradient from the machining edge towards the bulk material, which was accurately captured by EBSD employing depth averaged BC, BS, MAD profiles and spatial GOS scatter plots. Low angle boundary density, MCD, GAM and KAM are based on the same principles as GOS and would not provide any additional information. GAM and KAM parameters, in particular, would only increase the noise in the results.

In regions of plastic strain, the pattern quality degraded due to the presence of dislocations, and the BC and BS had lower values, while the elastic distortion of the crystals was partially captured by higher MAD values. Strained grains and/or subgrains were additionally identified by the increased GOS values. BC and BS were available for all points, whereas GOS and MAD could only be developed for indexed points.

Cells and sub-grains were typically detected by low angle grain boundaries, i.e. a critical misorientation angle below 10 degrees. The option of grain completion was also employed to cope with incomplete boundaries, by tracing them down to a lower critical angle obtained by a grain boundary analysis. Cells and sub-grains were detected with the standard algorithm of the accompanying EBSD Channel5 software, where the misorientation between neighboring points was compared against the critical value to form the low angle boundaries. The GOS component is defined as Mean Grain Misorientation (MGM) within the Channel 5 software and this term was used for the analysis to link the grain detection algorithm to the final value. One limiting factor of the grain detection algorithm was its inability to skip non-indexed points and compare the current point with second or higher order neighbors during the grain detection.

A modification of the MGM was to divide its value with the area of the (sub)grain to obtain a weighted MGM (wMGM). This non-uniform scaling of the misorientation aimed to address the issue with the large number of detected grains in heavily deformed regions where the hit rate was small and the misorientation within the small cluster of points was low. Another positive effect was the elimination of noisy MGM results from low angle boundaries in traces of macrozones. The alternative to data cleaning and interpolating would alter significantly the maps close to the peened and machined surfaces, rendering them inappropriate for this application.

Thus BC and BS could build a more representative profile of plastic strains within the highly sheared region, based on the entire data range and not the reduced number of the indexed points. The presence of twin, high angle, and/or low angle boundaries was captured by the image quality numbers and they were indirectly incorporated into the analysis. On the downside, high angle grain boundaries would also be introduced into the analysis, but their effect would be smoothed out by the averaging procedures at each depth level.

The exclusion of the twins from the analysis using a typical deviation of 5 degrees resulted in erroneous grain boundary identification, while the typical deviation of 1 degrees resulted in identifying the twins as grains. Since orientation gradients existed even within the twins the most appropriate approach was to include them in the grain identification. No limiting number on the size of grain was applied to enable MGM to operate in highly deformed regions (where the hit rate of the scan was extremely low) both as a misorientation value and subgrain number deformation metric.

EBSD scans were performed in an FEI Sirion Field Emission Gun scanning electron microscope (FEG/SEM) at the Sorby Centre for Electron Microscopy and Microanalysis of the Department of Materials Science and Engineering of the University of Sheffield. The set-up of the scans and post-processing of data were carried out by the accompanying HKL Channel 5 software package[6], which compromises of the following modules:

- Twist for the generation of simulated diffraction data;
    - kinematic electron diffraction model of band intensity;
- Flamenco for the EBSD setup and data acquisition;
    - Euler angles follow Bunge convention;
    - band center vs. band edges detection, simple vs. enhanced adaptive algorithms;
- Tango for the mapping and post-processing of orientation data;
    - data cleaning & grain detection;
    - orientation maps & relationships;
    - misorientation profiles and boundaries;
- Mambo for pole and inverse pole figures;
- Salsa for orientation distribution functions.

[6] Version: 5.10.50315.0, Release Date: 15/3/2010

Standard scan settings were employed, i.e. 20 kV and spot size 5, under a working distance of ~14 mm. Deformed materials typically require more sensitive settings, i.e. 15 kV and spot size 3, but the overall speed of the system did not allow it. Additionally, 4x4 binning was used, with a limited level of gain and noise reduction filters. The diffraction patterns were reduced in size by employing 4x4 binning, so as to increase the speed of EBSP acquisition and post-processing. A limited number of scans were performed with zero binning for higher accuracy results.

Ti-6Al-4V drilled plates were a relatively complex system to analyze due to the severe shearing of the microstructure, the existence of two phases, the variability of the grain size and orientation, and the slip and twinning systems of the crystals. Instead, CP-Ti material shot peened at 25 ^{o}C was used for the development and validation of the plastic strain mapping methodology, before of its application on the Ti-6Al-4V drilled plates. The developed methodology followed the one for peened nickel alloys [148].

CP-Ti was selected based on the previous work and knowledge on the material, particularly microhardness, twin line densities, uniform grain size, single phase and simpler microstructure. Peening is a completely different deformation mode to machining, however both systems had certain similarities like the presence of twins, a near-surface region of high plastic strains and deformation was limited to a sub-surface region with comparable size. Other processes, like rolling, which would introduce global strains and stresses in the cross section would not be as useful. Peened CP-Ti was also a good candidate material for the continuation work on residual stress measurements with FIB. Other less intense sliding processes, like stress rolling (surface, ball or deep) would be a more appropriate benchmark for plastic strains and deformation modes but would not simplify the problem for the residual stresses.

4.3.1 EBSD analysis of peened CP-Ti

A specimen of the CP-Ti peened at room temperature was prepared with the standard sample preparation methods for EBSD. Peening introduces compressive strains, which diminish with depth. The collected maps captured the deformation zone with sufficient quality, *Figure 4-1*. An SPD zone of 5 μm mean depth was clearly visible at the top of the specimen, due to the high level of plastic deformation. There was not significant distortion of the grains because the material had a high number of compression and tension twins, which accommodated the plastic deformation. The density of the twins was reducing with the increase of depth and no visible strain localization existed.

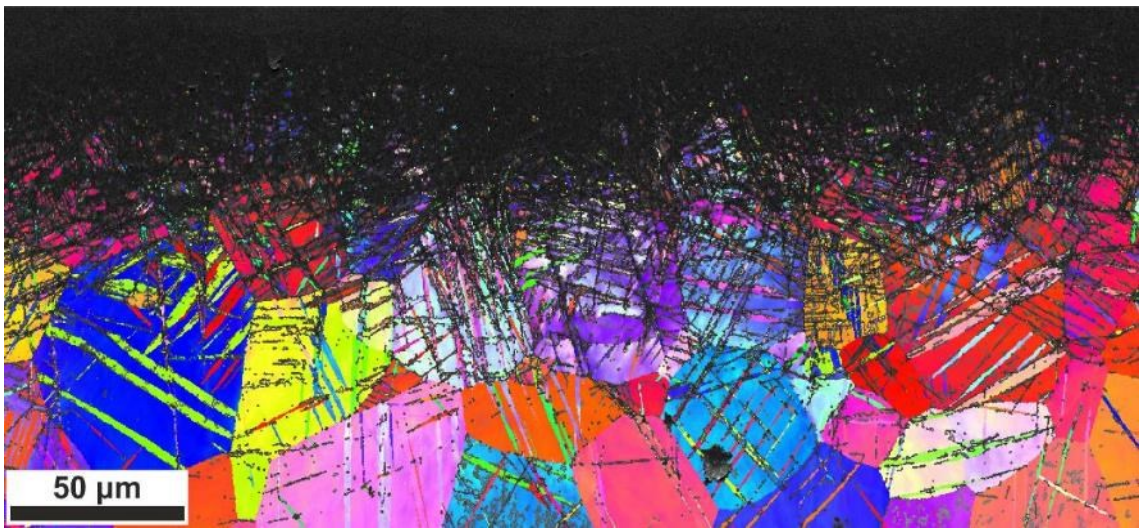

Figure 4-1 EBSD map of Cp-Ti peened @ RT; Band Contrast & Inverse Pole Figure map (Coordinate System: Sample Primary; Direction: Sample X)

The raw plots of the depth-averaged deformation parameters BC and MAD clearly captured the strain gradients throughout the material, *Figure 4-2 (a)*. BS was not available because the detection mode was based on band centers rather than edges. BC values of non-indexed points displayed a clear transition profile which was following the plastic strain gradient. MAD also captured the profile, but the number of available points in the heavily deformed region was limited and had considerable scattering. Rescaling the BC and MAD maps revealed regions of higher strains, but the gradients were not directly visible, *Figure 4-2 (b) & (c)*. MAD values were highly affected by the plastic strain and did not show any bias towards elastic strains, reducing to a background value at the limit of the plastically deformed region.

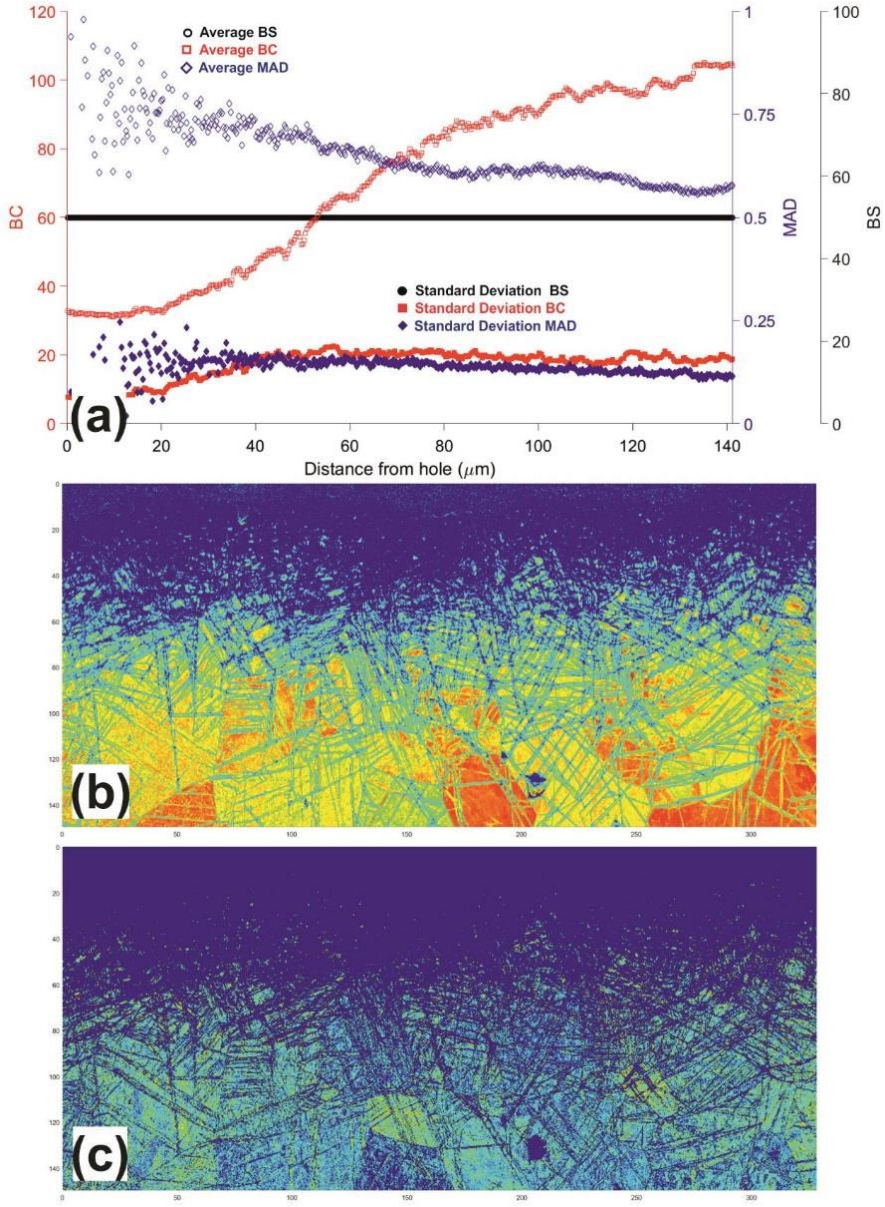

Figure 4-2 Deformation plots of CP-Ti; a) Average & Standard Deviation of BS, BC, and MAD; b) BC scaled map; c) MAD scaled map. NOTE: BS data not available.

Prior to the misorientation analysis, grain boundaries were detected and categorized to prove the validity of the method and establish the optimum value of the minimum critical angle of the boundary completion option, *Figure 4-3*. The vast majority of boundaries were below 2.0 degrees and significant noise existed up to 0.5 degrees. Higher values were located along the twins. A low grain boundary structure could be identified with 1.0 degree boundaries, which required a 0.4-0.5 degrees completion criterion. Although that was the assumed level of the EBSD accuracy, the map was displaying good consistency with the deformation mode. The number of low angle boundaries, their density (regarding the indexed points), and their absolute values were increasing towards the hole, due to the severe plastic strains. Thus, LGB detected all the different strain levels within the

deformed region. It was also evident that a large number of pixel sized subgrains would be detected. The exclusion of small clusters would result in loss of information because the clusters would not be incorporated into the neighboring grain(s).

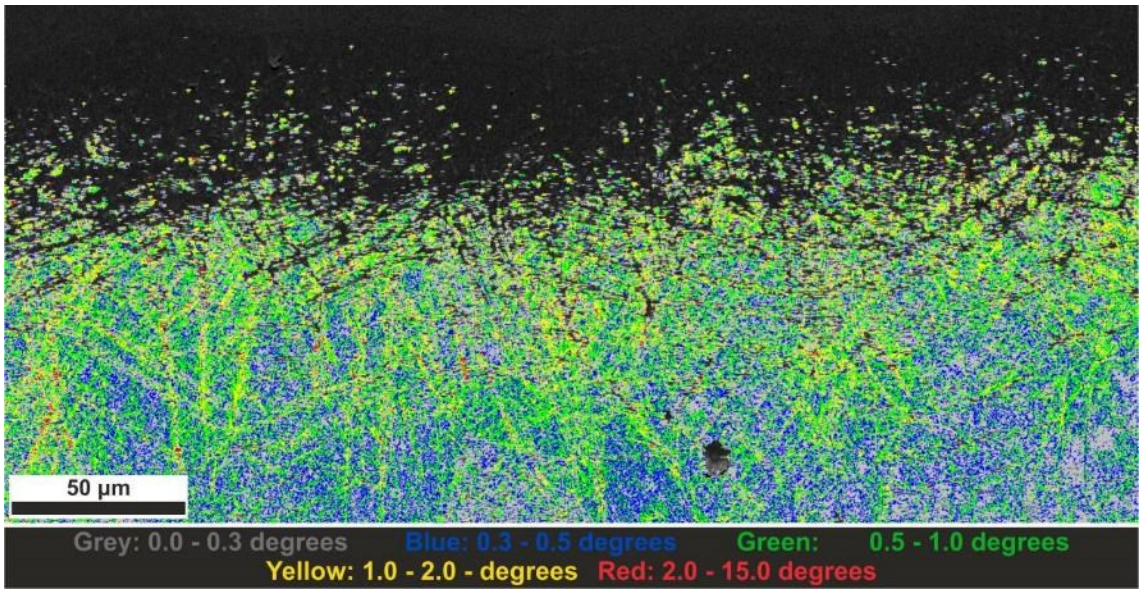

Figure 4-3 Grain boundary analysis of peened CP-Ti.

MGM plots displayed similar subsurface deformation profiles to the ones of BC and MAD, *Figure 4-4*. Background MGM values of 0.5-1.0 degrees were recorded, as expected due to the typical capabilities of EBSD systems. Significant scattering existed within the heavily strained region, which was more pronounced for grain detection with low critical misorientation angles (i.e. 1.0 degrees). This was a direct result of the number of subgrains detected and their small size. Higher critical angles, 2.5-10.0 degrees, did not capture the subgrain structure. Instead, the grains were detected from the high angle grain and twin boundaries and the lines of non-indexed pixels along high angle grain and twin boundaries and heavily deformed regions. Further cleaning and extrapolation of the raw EBSD data changed the map introducing features that did not exist. The fact that the location of the subgrain is based on its center of gravity contributed to the scattering.

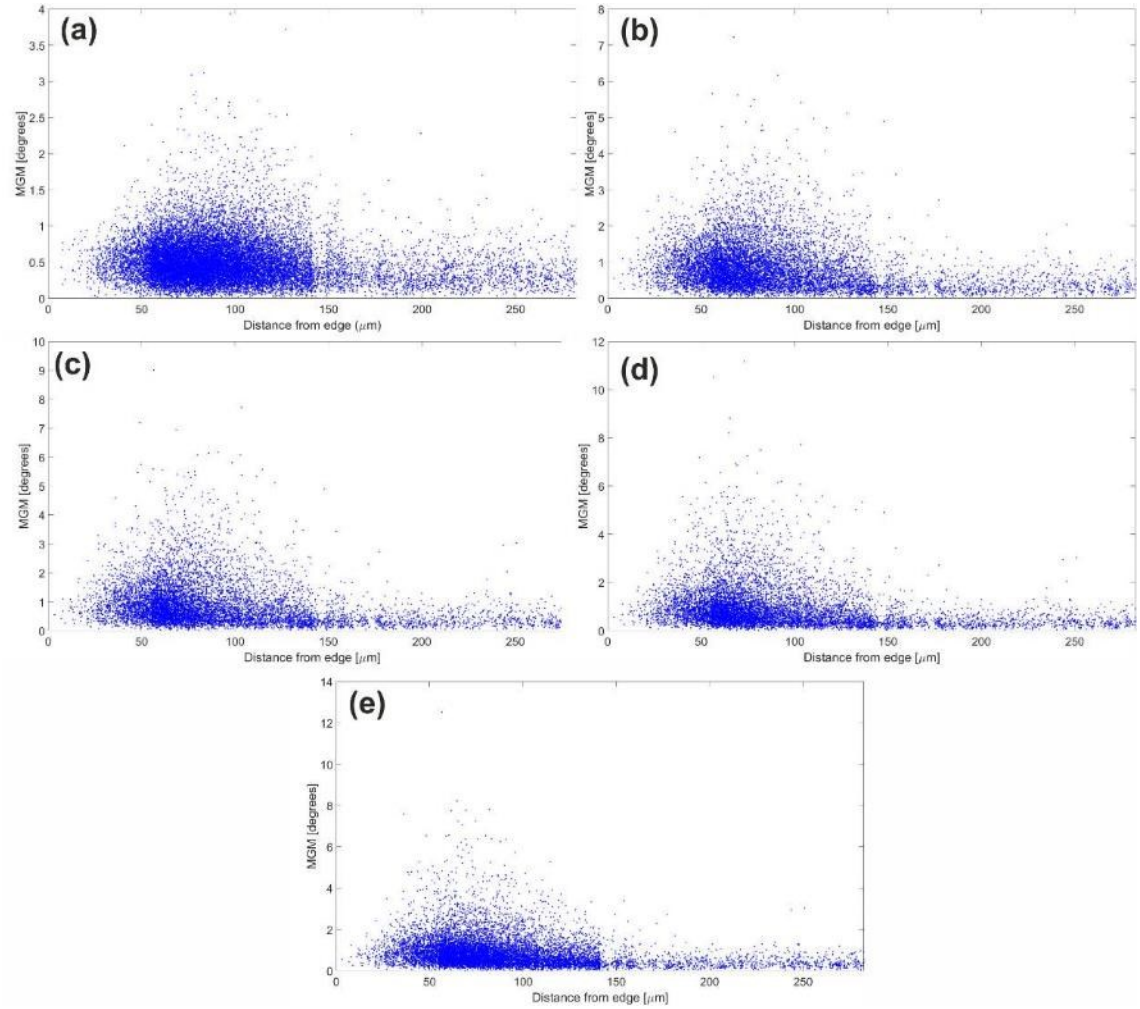

Figure 4-4 MGM plots of CP-Ti peened @ RT; a) Grain detection @ 1.0 degree; b) Grain detection @ 2.5 degrees; c) Grain detection @ 5.0 degrees; d) Grain detection @ 7.5 degrees; e) Grain detection @ 10.0 degrees.

The wMGM parameter improved the resolution within the deformed region but introduced significant scattering in low strain regions, *Figure 4-5*. In the first 50-60 μm, there were pixel sized subgrains and created a discontinuity in the graphs due to the area scaling, more pronounced in low critical angles of grain detection. However, the result was still the same and the subsurface deformation was found to extend 150 μm from the peened surface.

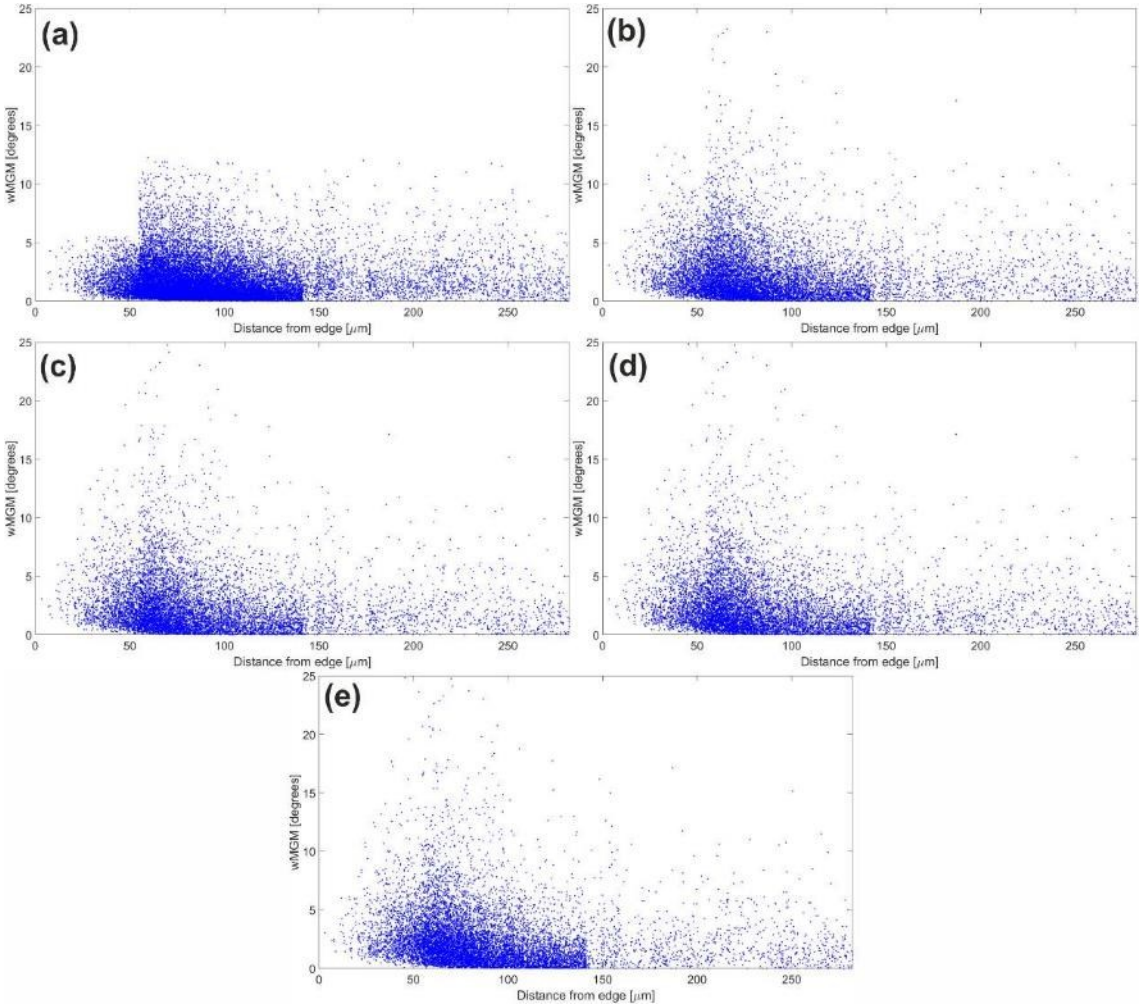

Figure 4-5 wMGM plots of CP-Ti peened @ RT; a) Grain detection @ 1.0 degree; b) Grain detection @ 2.5 degrees; c) Grain detection @ 5.0 degrees; d) Grain detection @ 7.5 degrees; e) Grain detection @ 10.0 degrees.

The EBSD semi-quantitative tools of plastic deformation detected with a high level of confidence the depth of deformation zone. SPD and IST zones were clearly visible in the EBSD maps and especially the SPD was accurately identified by the small hit rate. The number of subgrains was misleading due to the high level of twinning, which introduced a high density of boundaries and unidentified points, isolating small clusters of points. However, it did not change the outcome, because their existence was a direct consequence of the high levels of deformation. BC outperformed MAD, MGM, and wMGM, displaying excellent sensitivity to the strain gradients throughout the scanned region.

4.4.2 EBSD analysis of Ti-6Al-4V drilled plates

4.4.2.1 Characterization maps

The drilled plates were examined with EBSD following the procedure outlined in Section 4.3 and implemented on the peened CP-Ti in Section 4.3.1. Drilling of mill annealed Ti-6Al-4V is a more complex system in terms of deformation mode and parent microstructure than peening of CP-Ti, but the sub-surface deformation was still accurately assessed with evidence of strain localization and relevant misfits.

The various deformation zones, SPD, IST, and LT, were clearly identified according to their individual features, but with a higher level of details and accuracy than SEM and LOM images. For example *Figure 4-6* of the most heavily deformed specimen 3. EBSD was not able to detect any beta phase close to the machined edge because of the high levels of deformation. Instead, within the SPD layer, there was almost a zero hit rate, without any microstructure features in any EBSD map. LOM and SEM micrographs captured more information and details in the SPD zone. No evidence of white layers were observed with EBSD. This was another indication of the brittle nature of the SPD layer and its potential as a crack initiation area. Despite that, there was a smooth transition to lower strained and less brittle regions, more evident from SEM, reducing misfit strains between SPD and IST.

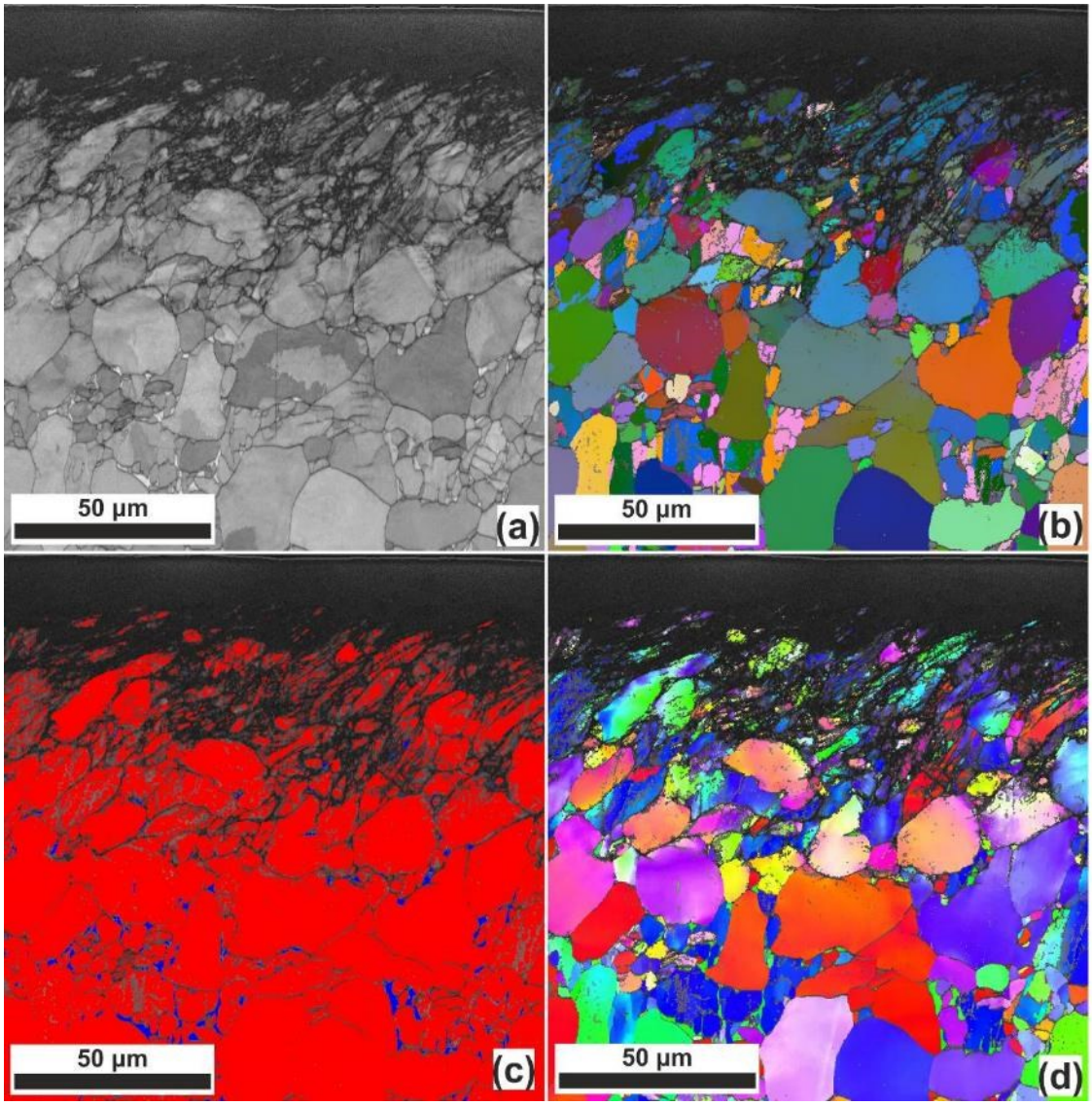

Figure 4-6 EBSD maps Specimen 3; a) BC map; b) Euler map; c) Phase map; d) IPF @ x map.

The progressive removal of material during drilling caused shearing of the parent the microstructure. Grains were significantly distorted and twinned according to the direction

of drilling (counter clockwise for *Figure 4-6*). Only tensile and compressive twins were detected, the majority of which were tensile. As the process continued, both the twins and the original crystals were further deformed. Larger grains were more capable of accommodating the deformation than smaller grains, through long range distortion.

In regions with smaller grains, the twinning and the increased dislocation density appeared to introduce a large number of low and high angle boundaries, *Figure 4-7*, aligned according to the machining process. This strain localization could become a significant misfit and act as a crack initiation area.

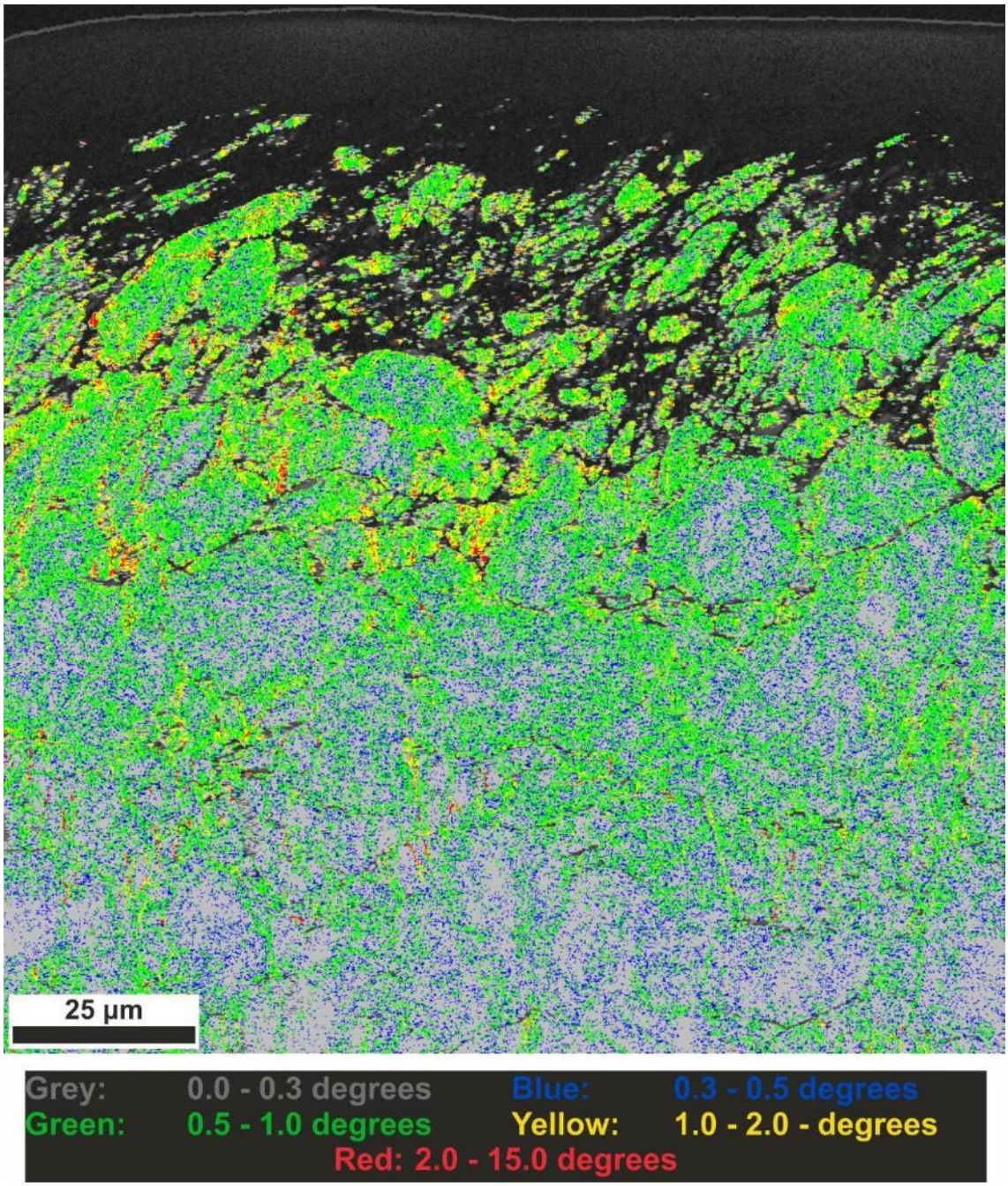

Figure 4-7 Grain boundary analysis of drilled Ti-6Al-4V plate – Specimen 3.

4.4.2.2 Plastic strain mapping

Strain gradients and depth of sub-surface deformation were revealed in more detail by the rescaling of BC, BS and MAD maps and raw plots of their depth averaged values, *Figure 4-8*. BS displayed the highest sensitivity to plastic strain compared to BC and MAD, with lower values in the deformed region and a constant background value. BC had a similar profile to BS, but there was still some variation in the background values due to traces of the macrozones, the number of grain boundaries and crystal orientations. MAD values were excessively high for severely deformed crystals and they reduced to a background value well after BS and BC, possibly because of the residual elastic strains which exist below the deformed region.

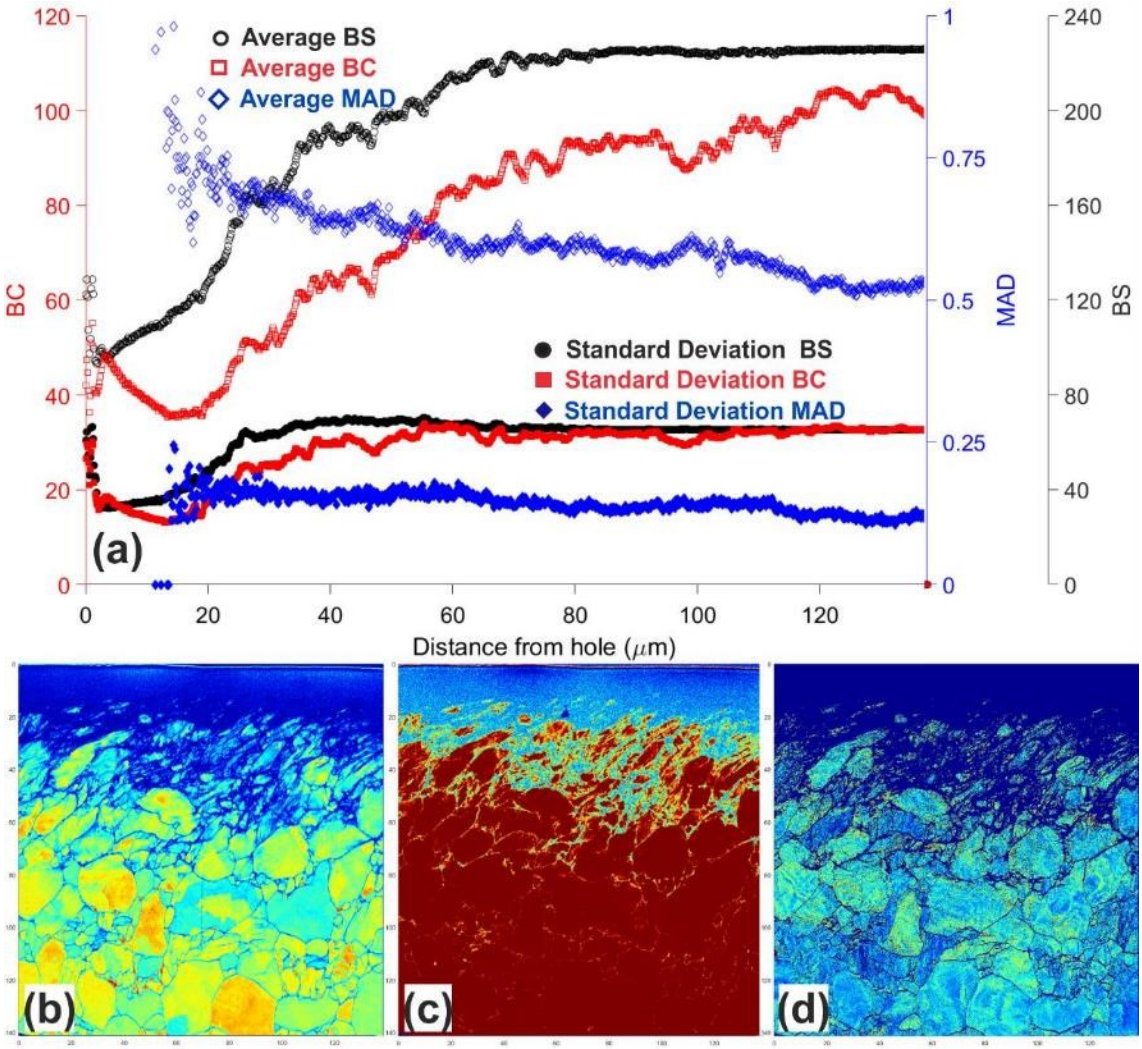

Figure 4-8 Subsurface plastic deformation mapping Specimen 3; a) Depth averaged BC, BS & MAD; b) BC map; c) BS map d) MAD map.

The drilled Ti-6Al-4V plates had similar MGM and wMGM profiles, *Figure 4-9 & Figure 4-10*, to the peened CP-TI, *Figure 4-4 & Figure 4-5*. For low critical misorientation angle, i.e. 1.0 degrees, the subgrain detection algorithm identified large numbers of pixel sized clusters with small MGM values, resulting in significant

scattering. Increasing the critical angle value to 2.5 degrees reduced the number of the detected subgrains and start displaying a profile along the depth, with MGM values above the error threshold of 1.0 degrees. Low angle grain boundaries from macrozones traces were contributing to the scattering of MGM in higher depths.

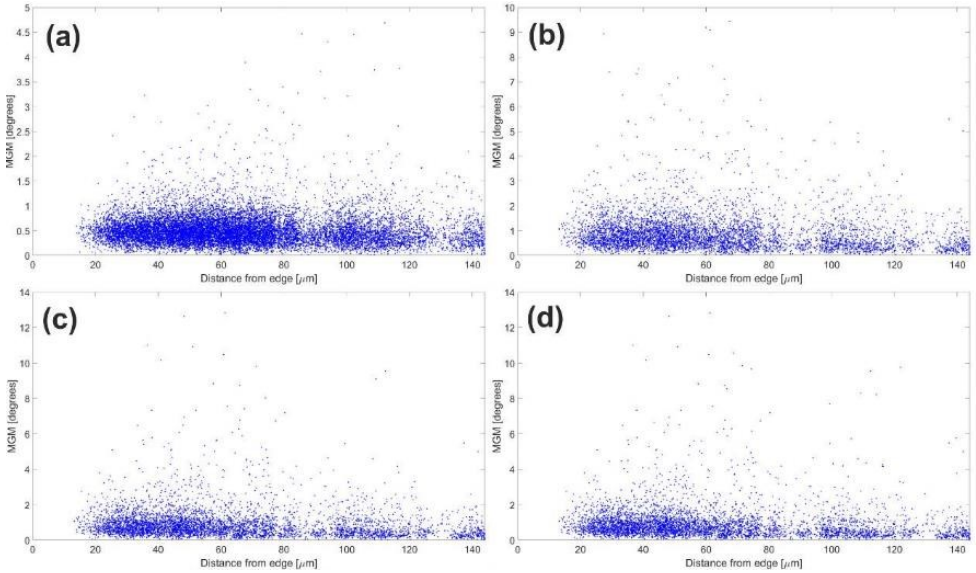

Figure 4-9 Subgrain misorientation plots Specimen 3, MGM component; a) critical angle 1.0 degrees; b) critical angle 2.5 degrees; c) critical angle 7.5 degrees; d) critical angle 10.0 degrees.

The wMGM at low critical angle had the same problem with grain detection and scattering to MGM, *Figure 4-10*. But for higher critical angles a more clear profile was formed, due to the elimination of the macrozones effect and the inclusion of pixel sized grains to larger clusters, though the accuracy and resolution within the deformed region were still an issue.

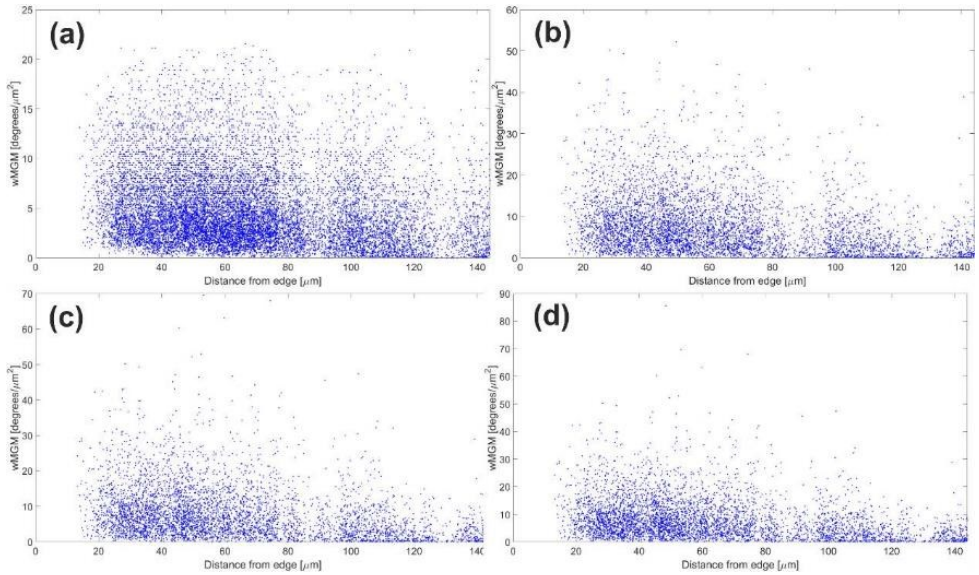

Figure 4-10 Subgrain misorientation plots Specimen 3, wMGM component; a) critical angle 1.0 degrees; b) critical angle 2.5 degrees; c) critical angle 7.5 degrees; d) critical angle 10.0 degrees

A limited number of strip maps was collected with zero binning to increase the accuracy and sensitivity of the tools, *Figure 4-11 & Figure 4-12*. BC and MAD results were virtually identical between zero and 4x4 binning strain mapping, *Figure 4-15 (a), (b) & (d)*. The most important difference was on the BS values, which introduced a higher level of sensitivity in low strained regions, *Figure 4-15 (a) & (c)*. Furthermore, wMGM was still performing better than MGM, *Figure 4-14* (a) & (b) and the plots contained less noise because of the improved accuracy and the presence of larger grains (and high angle grain boundaries) at the low strain region.

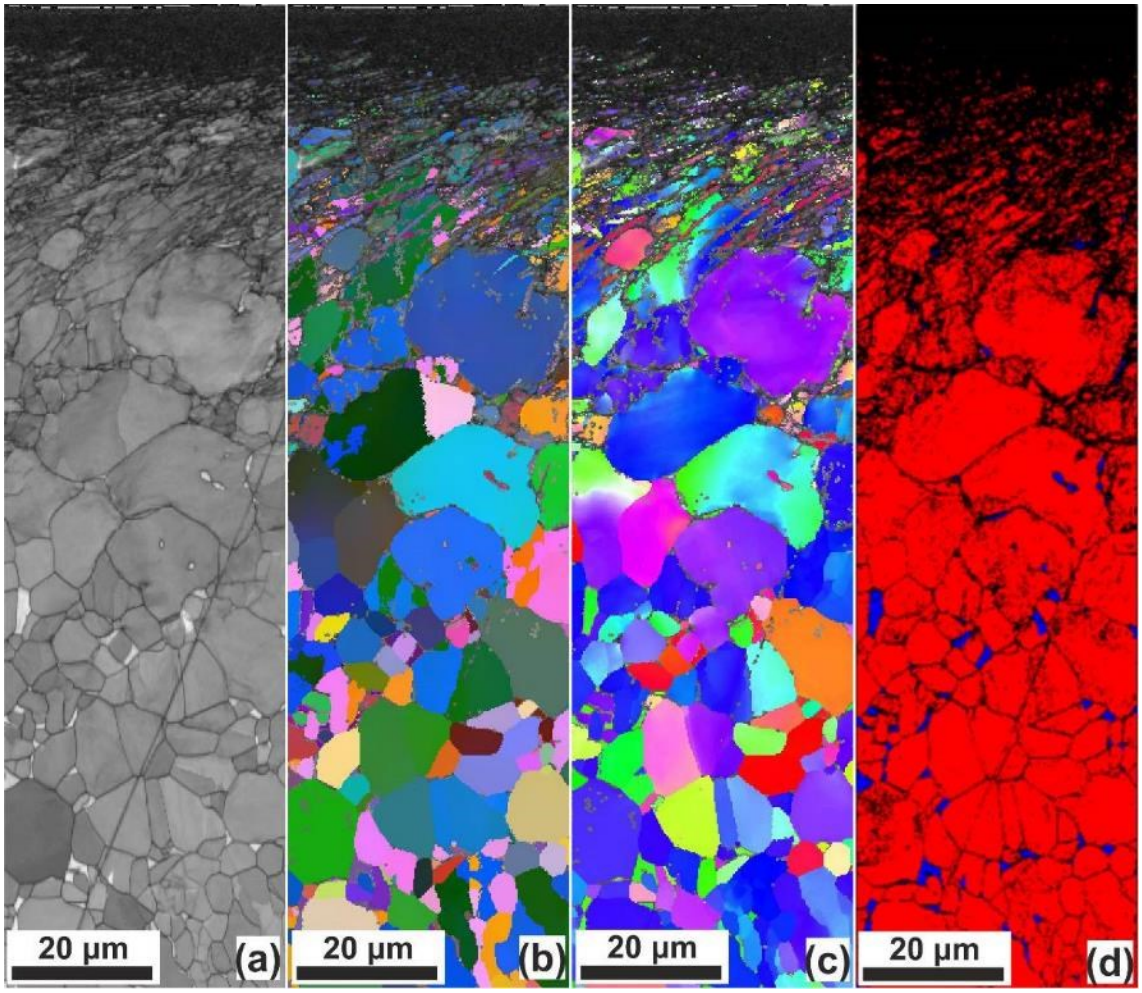

Figure 4-11 EBSD maps Specimen 3 – Zero binning; a) BC map; b) Euler map; c) Phase map; d) IPF @ x map.

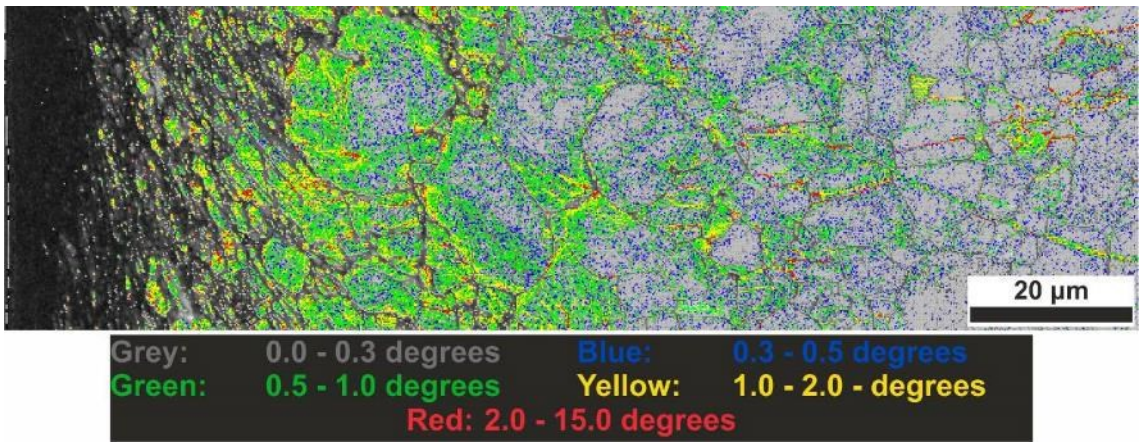

Figure 4-12 Grain boundary analysis of drilled Ti-6Al-4V plate – Specimen 3 – Zero binning.

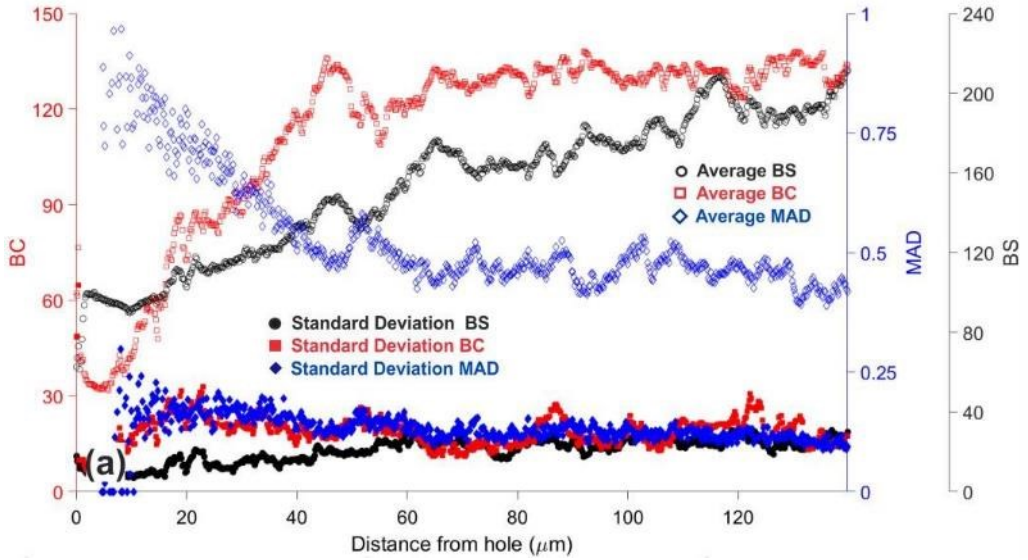

Figure 4-13 Subsurface plastic deformation mapping Specimen 3 – Zero binning; a) Depth averaged BC, BS & MAD

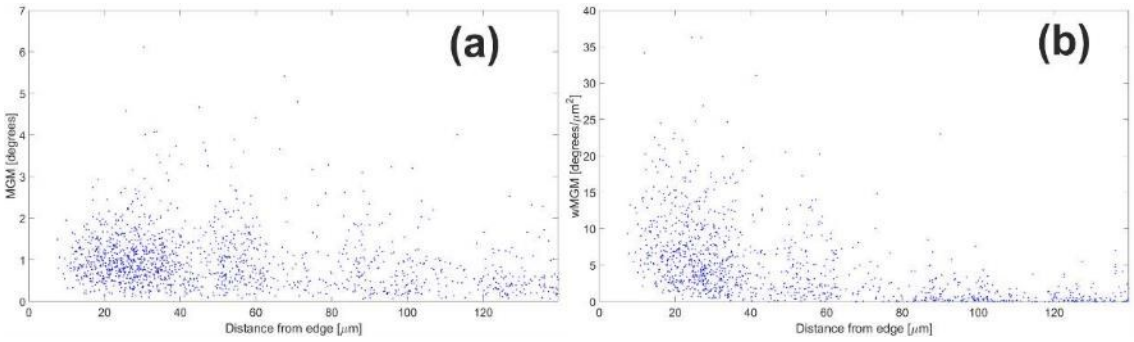

Figure 4-14 Subgrain misorientation plots Specimen 3 vs. depth; a) MGM component, critical angle 2.5 degrees; b) wMGM component critical angle 2.5 degrees.

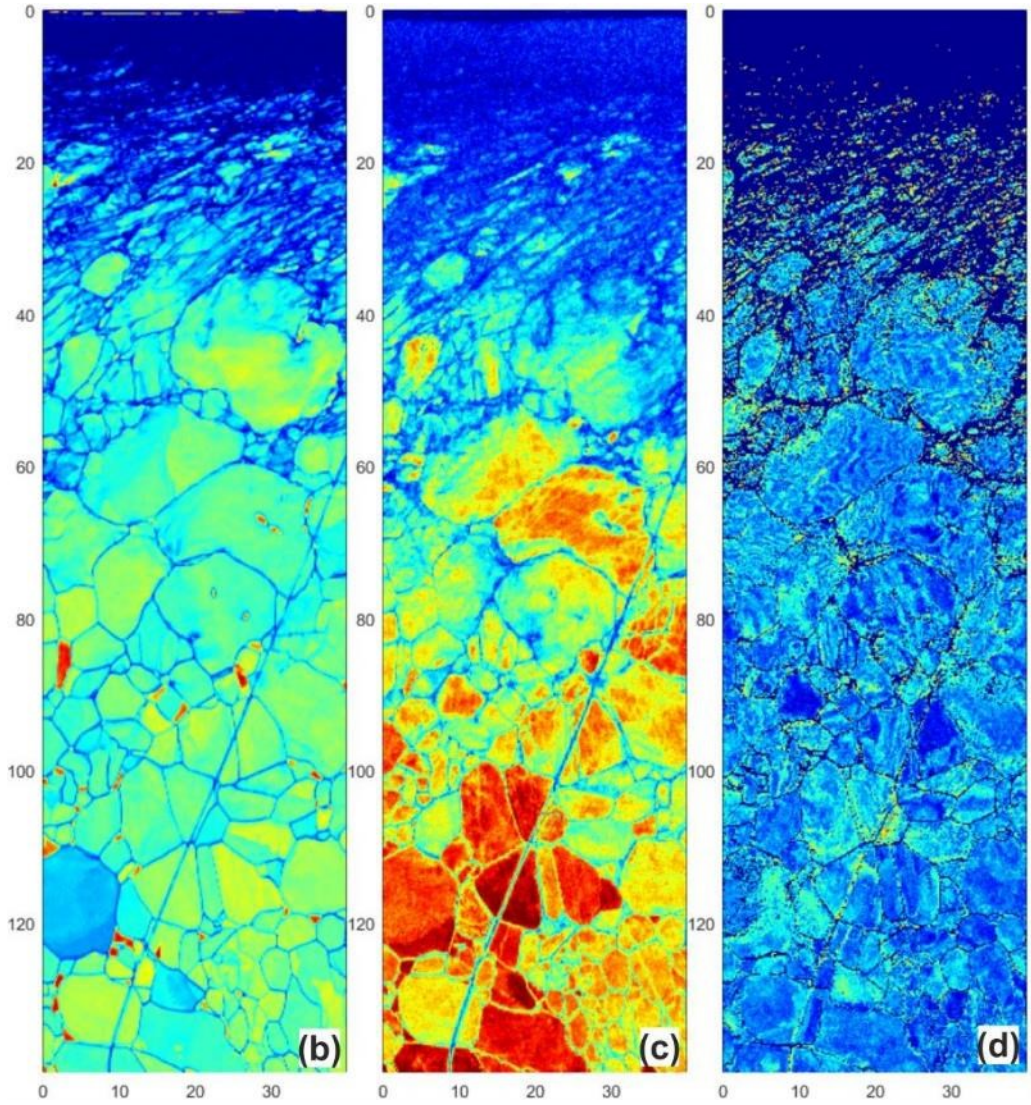

Figure 4-15 Subsurface plastic deformation mapping Specimen 3 – Zero binning; b) BC map; c) BS map d) MAD map.

The steep strain gradients within the deformed region and the variable grain size did not allow MGM and wMGM to perform as expected. Subgrains were identified for angles between 1.0 - 2.0 degrees, but the misorientation analysis contained a lot of noise. Rather than sub-grains, it was more suitable to operate on the main grains and accommodate macrozones by the grain area weights and a critical grain boundary detection angle above 2.0 degrees. There was still noise within the results arising from the small clusters of pixels within the heavily deformed region, but their number served as another metric for the transition from high to low strain regions. LGB, BS, and BC were the most sensitive parameter of low plastic strain mapping. The grain boundary detection algorithm required an upgrade, but this was beyond the scope of the research because the plastic strain was sufficiently described.

4.4.2.3 Slip Bands

Drilling is a very complicated deformation process which subjects the material in shear and compression. The chip is formed by a shearing mechanism in a zone that is primarily located at a certain angle from the tool tip to the free surface of the material as illustrated in the orthogonal cutting sketch, *Figure 4-16 (a)*, but actually extends ahead and below to tool. However, for the workpiece the trace of the shear plane (zone) lies on the machined surface and the tool that comes into contact with the newly formed surface of the workpiece introduces a secondary deformation zone through friction. As a practical simplification, a pure shear stress is assumed parallel and opposite to the cutting direction along the finished surface on the workpiece [43] [44]. Single shear would be a more appropriate deformation mode but the shear plane for the workpiece would remain similar to pure shear. Single shear would also introduce a complicated stress tensor with different stress components and further uncertainties for the principal stresses and their directions. During the slip trace analysis both loading directions are considered and single shear would be biased towards one direction contrary to pure shear. Without a knowledge of the actual drilling forces and the stress state of the material on the workpiece, it is difficult to describe the simple shear condition. Finite Elements (FE) could provide a more representative stress state but the quality of the simulations never reached the appropriate level and a more rigorous analysis was omitted.

Assuming that drilling subjects the material into a condition of simple shear, then the shear plane is tangential to the hole surface, *Figure 4-16 (a)*, with respect to the workpiece (finished machined surface). The shear stress is resolved to the principal, compressive and tensile stresses acting at orthogonal axes to the shear plane, at ±45 degrees to the cutting direction, *Figure 4-16 (b)*. Sectioning the machined surface along the cutting direction reveals the slip bands due to machining, *Figure 4-16 (c)*. The angle of the slip bands with regard to the sample reference system can provide the slip plane. First, the slip plane indices must be transformed from the crystal to the sample reference system. Then, the angle of the intersection direction between the slip plane under examination and the sectioning plane ({0 0 0 1} in sample reference system) can be calculated and compared to the measured value. A more rigorous analysis has been implemented in the past, based on a cumulative tension-compression Schmidt factor [43] [44] [136].

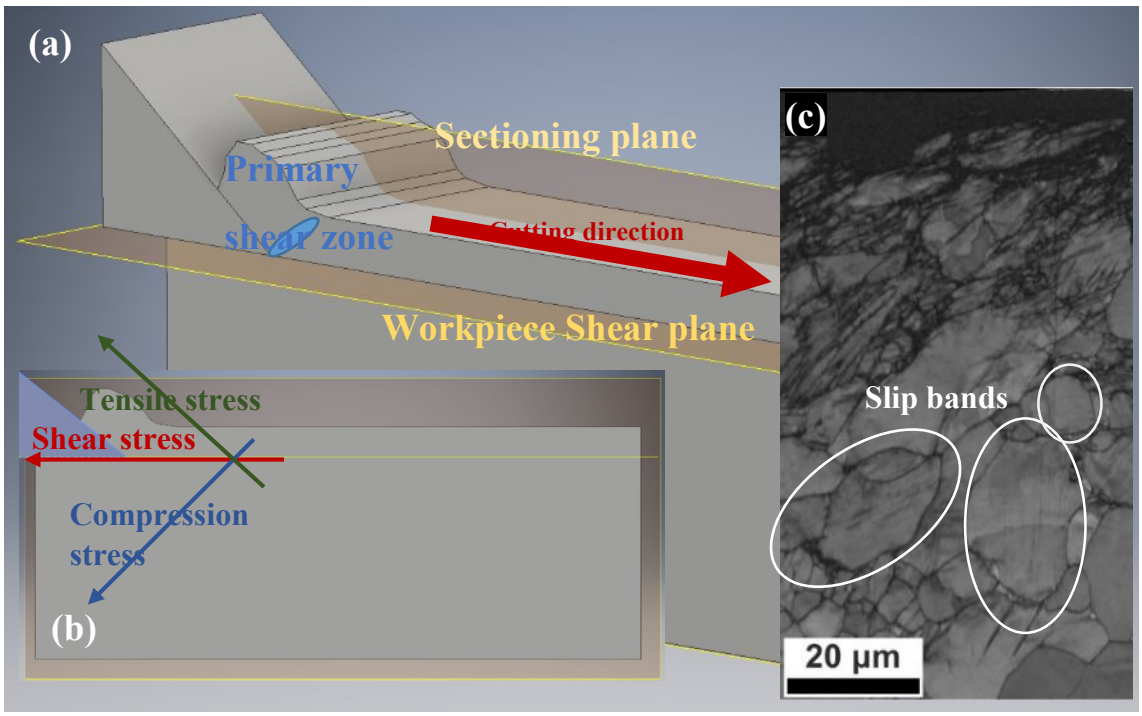

Figure 4-16 Graphical representation of machining and slip band identification. a) 3D orthogonal cutting; b) 2D analysis of shear and principal normal stresses; c) BC map of Specimen #3 with slip bands

The slip bands observed in the drilled plates belonged mostly to prismatic and basal planes. Schmidt factors for <a> slip at those planes are higher. Intense slip bands represent lower levels of plastic deformation. The depth of the slip bands was not consistent and was a function of the orientation, size, and location of the crystals. In some cases, slip bands were completely absent. Since the cut is through the half-thickness plane and not through the thickness of the plane the global minimum and maximum depths of slip bands could not be identified. Thus, on average the depth of slip bands was reduced to that of the twinning zone. Their effect on the fatigue life can only be verified by the examination of crack initiation locations, but their proximity to the IST zone could make them difficult to distinguish from twins.

4.4.3 Ti-6Al-4V Drilled Plates Results

Each specimen and particularly group had different deformation profiles, but they had exactly the same features and defects. The complete set of the EBSD maps and plots can be found in *Figure AP- 8 & Figure AP- 9*. The EBSD results as expected followed the ones from LOM and SEM, *Figure 4-17*. However, the depth of the SPD, IST, and LT layers were calculated with a combination of qualitative and quantitative properties of the EBSD data and averaged over the width of the maps to produce a more realistic and representative deformation profile.

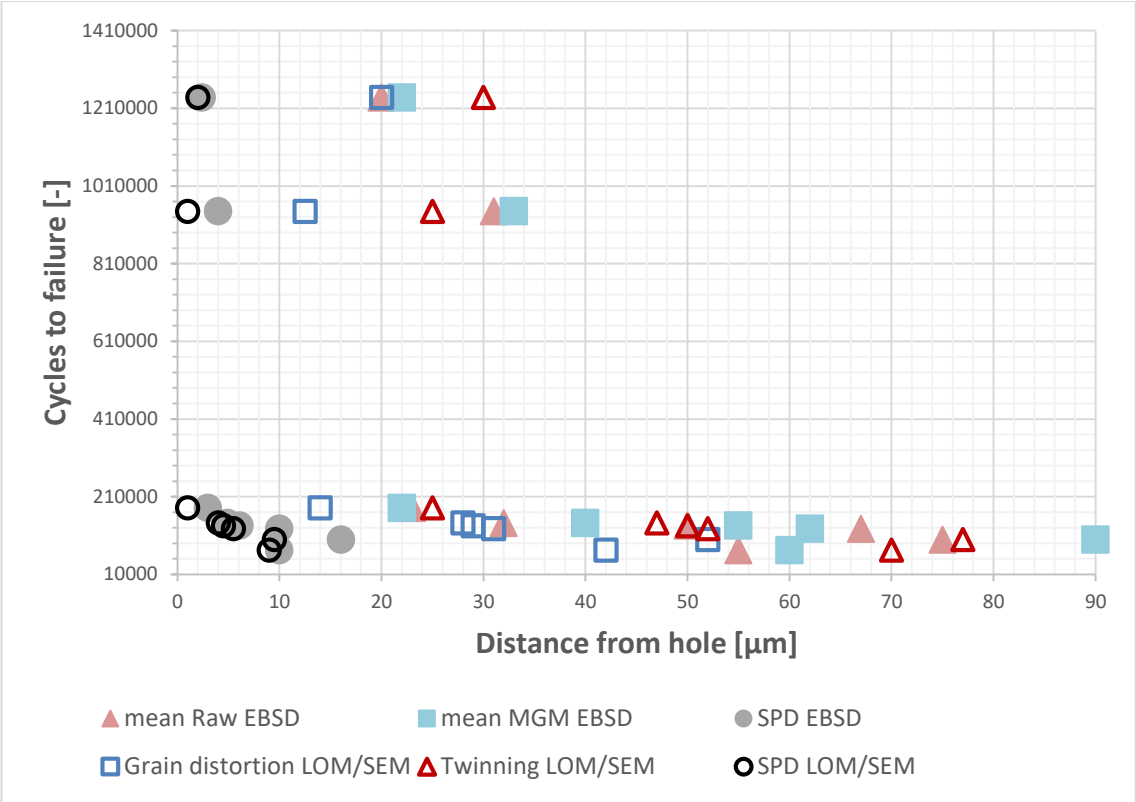

Figure 4-17 Fatigue performance of Ti-6Al-4V drilled plates as a function of deformation – EBSD vs LOM/SEM.

At this point, it was obvious that there were variations of the deformation profile over the cylindrical surface of the hole from the underlying texture and the machining effects (wobbling of the tool, grinding and re-grinding of the surface, and tool marks/scratches). Such variations occurred even in the same datasets at the same locations around the hole. The assessment of the deformation from a plane parallel to the feed marks had limited value compared to a through thickness mapping. However, it was more feasible for practical reasons, i.e. maintaining the central region of interest of the hole, where the cracks originated.

Through EBSD it was verified that specimens with lower sub-surface deformation had superior fatigue performance. One outlier existed in the dataset, Specimen #4, where all the metrics indicated that it should have a higher fatigue life. Nothing from the EBSD maps revealed a particular microstructural defect or other misfits. No cracks were detected, but severe strain localization was observed in twins. The main concern was that all the specimens displayed identical microstructure features, though to a different depth.

4.5 Elastic Strain Mapping with EBSD – Method development

There was an attempt to quantify elastic (and plastic) strain through DIC of EBSPs based on previously published work [152]. For the machined specimens, the strain profile was

built from the bulk towards the deformed region, similar to the application on a semiconductor with an epilayer of SiGe grown on Si [140]. The reference pattern was updated either at every step or when a phase or grain boundary was reached, *Figure 4-18*. Strain continuity between grains and phases was carried out by averaging the strain gradients before and after the discontinuity. Nine sub-regions of the current pattern were compared to the reference pattern in a Matlab[7]-based code, *Figure 4-19*. DIC was performed with the command *cpcorr* [153]. The elastic properties of each grain were introduced by the relevant, tensors based on the phase and orientation of each point [154] [155] [156]. An average elastic property was assigned in heavily deformed regions, were non-indexed points existed, but a pattern was still present. The limit of this method was in such regions, because of the non-indexed points and the subsequent problems with the update of the reference pattern.

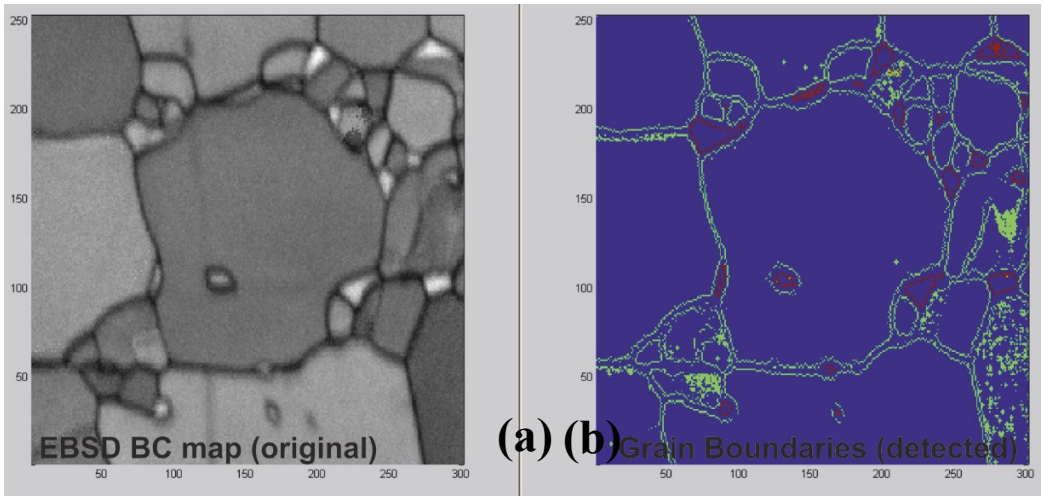

Figure 4-18 Grain and phase boundaries; a) EBSD BC map; b) Boundaries map.

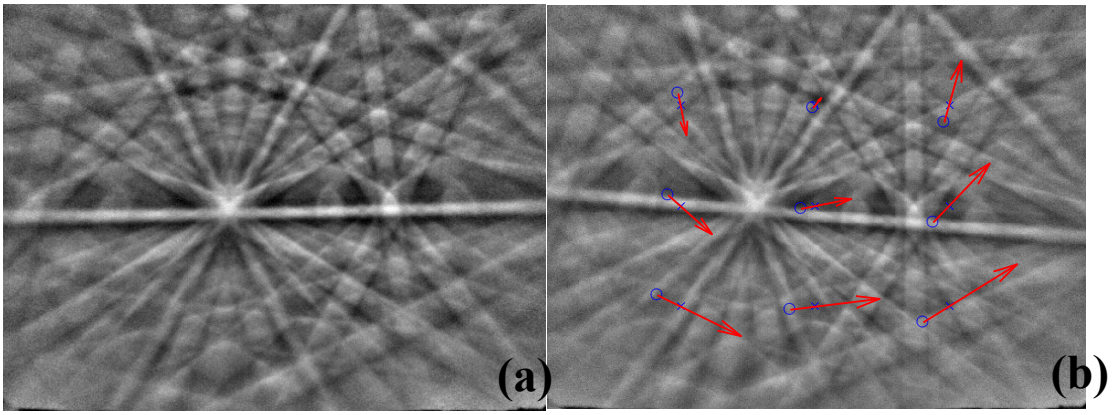

Figure 4-19 DIC on detected patterns; a) Reference pattern; b) Current pattern (with displacement vectors).

[7] https://uk.mathworks.com/products/matlab.html

The method failed to yield meaningful results and was replaced with a micro-machining method, which could operate in regions with high strains (SPD) and could produce more accurate results. Accumulated errors from the DIC process and the continuation rules were their primary reasons for the poor results. The method should at least provide a reasonable profile, as it has been demonstrated in other applications and failure to do so indicated that there were mistakes in the code.

4.6 Bulk Texture Analysis

EBSD revealed a rolling-transverse texture within the 8.0 mm plates, *Figure 4-20 & Figure 4-21*, in regions with globular grains. The transverse component was stronger than the rolling one. Rolling components could be present prior to the final rolling operation, the rolling may have been carried out above the beta transus or the rollng components are traces of the hot deformation due to the partial recrystallization from the mill annealing [5] [2]. The crack(s) propagated on the y-z planes, where the texture was transformed to basal-transverse, with stronger transverse components.

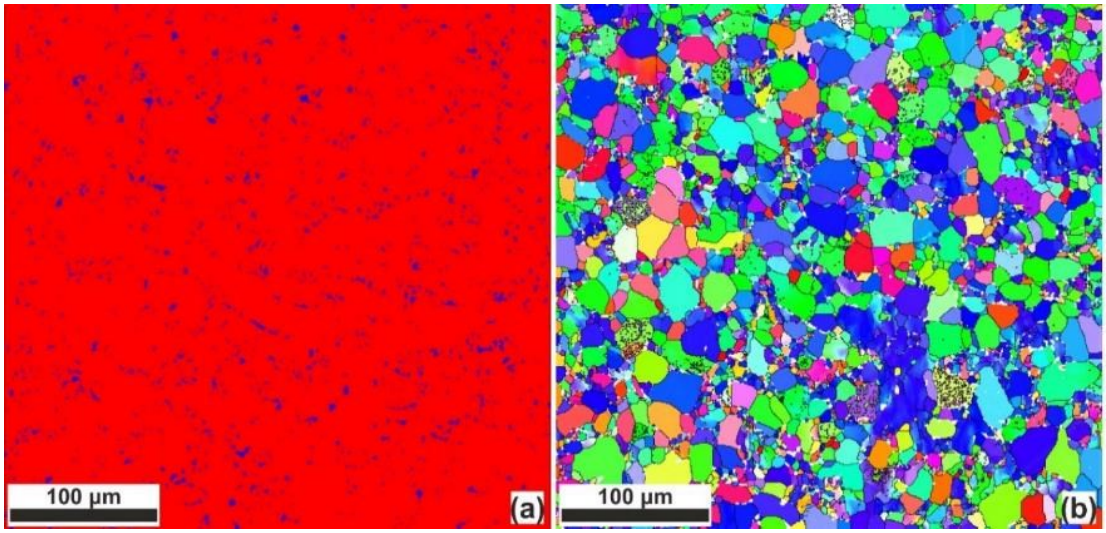

Figure 4-20 EBSD maps of the bulk Ti-6Al-4V 8.0 mm plates; a) Phase map; b) IPF map.

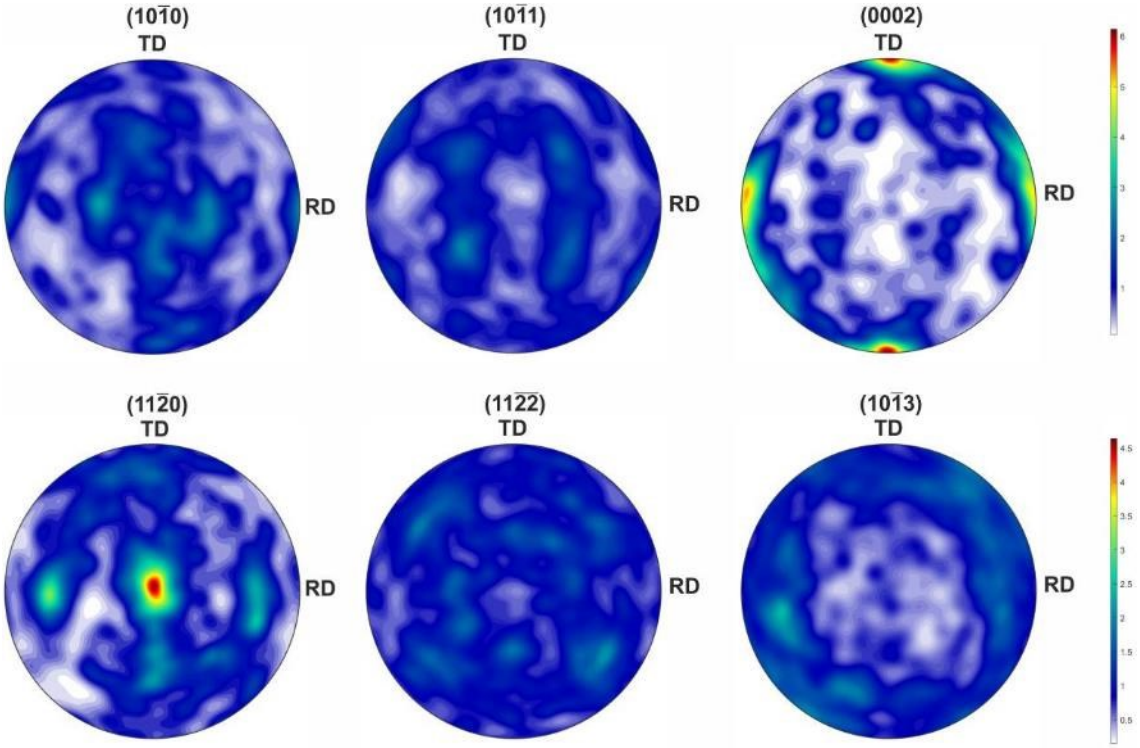

Figure 4-21 Pole figures of the EBSD maps from Figure 4-20.

The 8.0 mm plates contained macrozones with strong transverse components. Rolling components were still present, but they were weak compared to the transverse ones. Due to the macrozones, the texture changes through the thickness could not be investigated in the 8.0 mm plates, *Figure 4-22*. Additional maps at the mid-thickness XY plane with globular grains and macrozones can be found in Appendix IV-EBSD.

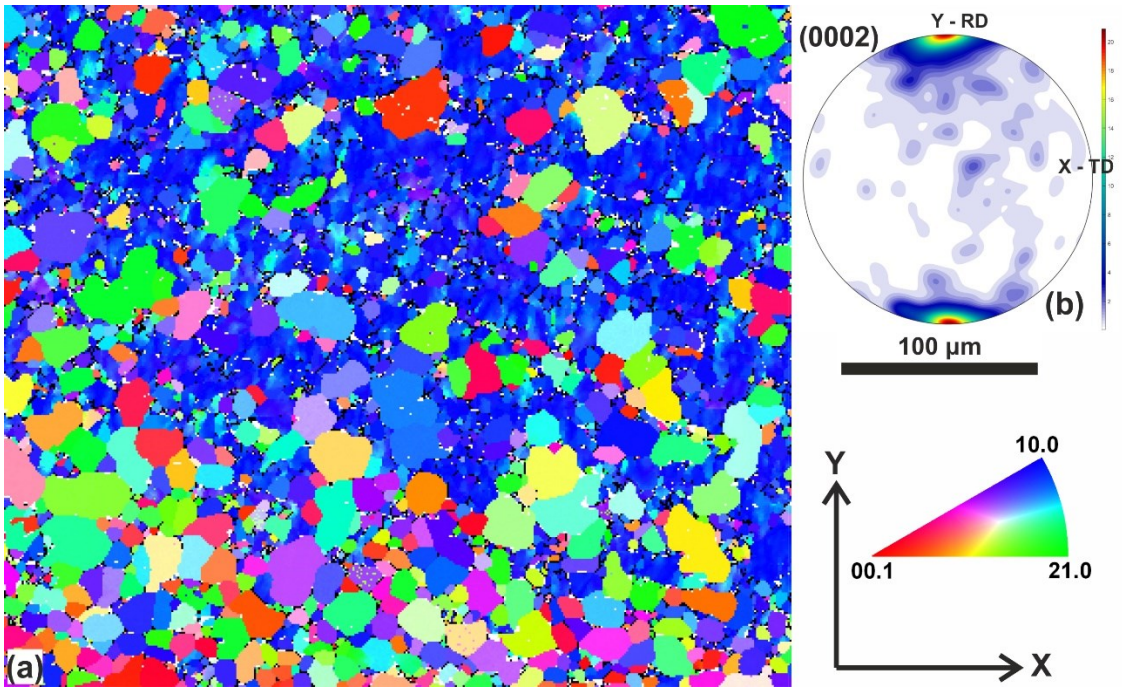

Figure 4-22 Rolling plane texture with macrozones, 8.0 mm plates; a) IPF map; b) Pole figure (transverse components).

The 10.0 mm plates had the same rolling-transverse texture with the 8.0 mm plates, except to the macrozones, *Figure 4-23*. Similar texture was found between the rolling (XY) plane and the transverse (XZ) plane, *Figure 4-24*. Stronger transverse and weaker rolling components were expected on the rolling plane, but the size of the relevant map may have introduced an error.

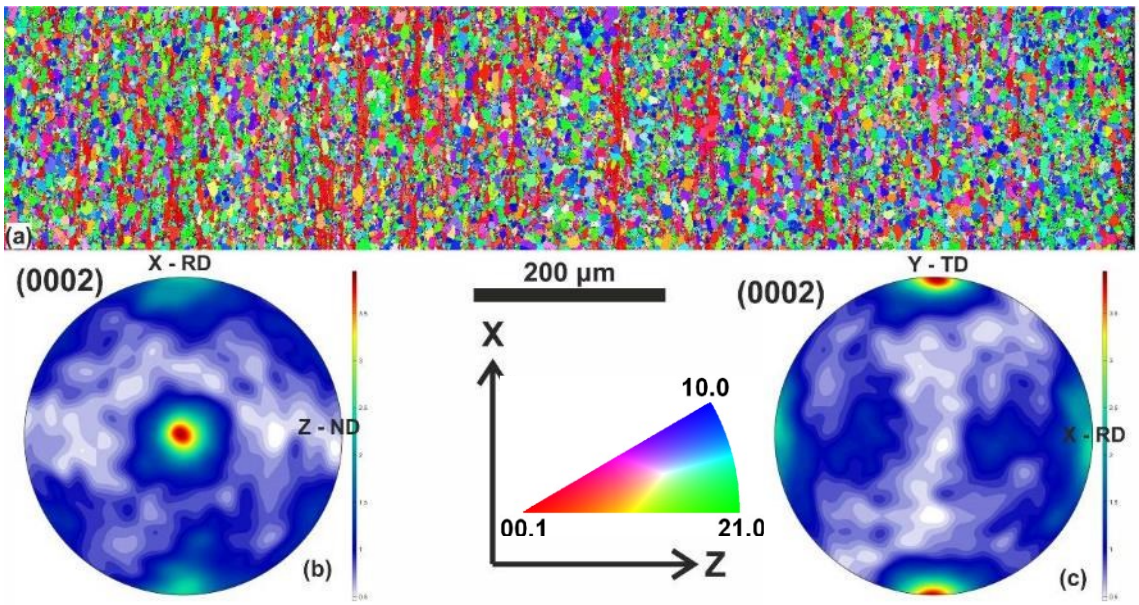

Figure 4-23 Through thickness texture 10.0 mm plates; a) IPF map; b) Pole figure (basal & rolling components); c) Rotated pole figure (transverse & rolling components).

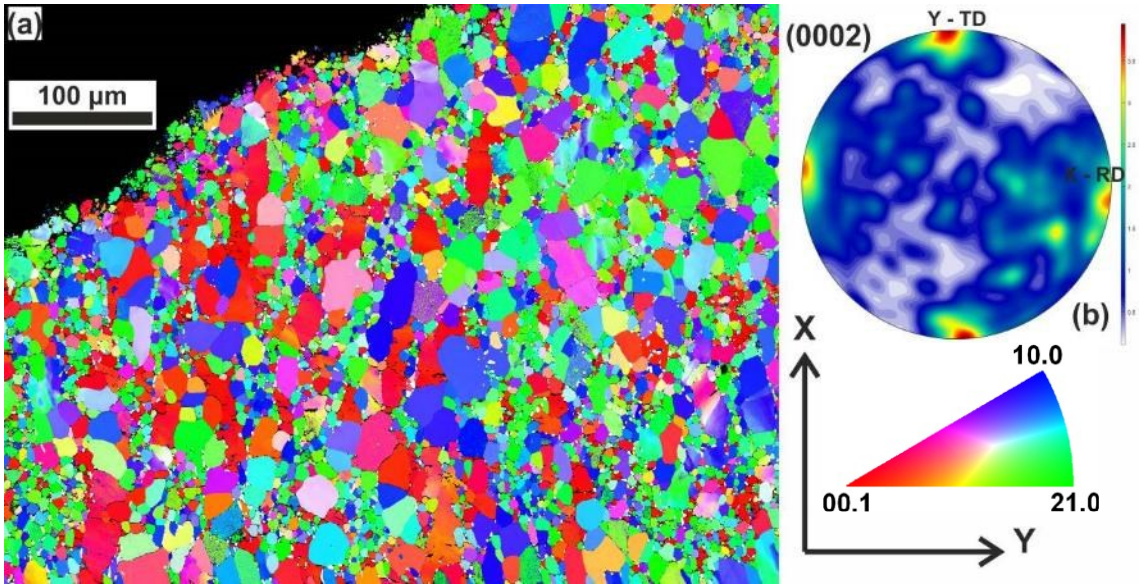

Figure 4-24 Rolling plane texture 10.0 mm plates; a) IPF map; b) Pole figure (transverse-rolling components).

4.7 Summary

EBSD was applied in peened CP-Ti and drilled Ti-6Al-4V plates. Strain localization, microstructural defects, and misfits were identified from the detailed characterization maps. Regions with smaller grains acted as strain concentrator sites with a large density

of dislocations, while larger grains deformed and twinned, accommodating the plastic strain more efficiently. All Ti-6Al-4V drilled specimens had the same features and only the depth of the subsurface deformed layer and its subregions (SPD, IST, and LT) were varying. The machining conditions were directly related to the subsurface deformation, as with LOM and SEM, but with a higher accuracy, especially for the SPD layer.

The texture was fairly consistent through the thickness of the 10.0 mm plates, with mainly stronger transverse and weaker rolling components in the relevant directions. In the 8.0 mm plates, the presence of macrozones introduced very strong transverse components and a through thickness analysis on such a layered microstructure was rendered inadequate.

The EBSD technique proved to be a very effective and powerful tool for strain mapping. A number of semi-quantitative tools were examined and all of them captured the subsurface, plastic strain gradient, though to a different level of sensitivity. Depth averaged EBSP image quality and low angle boundaries (0.5 – 1.0 degrees) parameters outperformed subgrain misorientation and pattern misfit. Band slope and low angle grain boundaries further revealed low strained regions. Misorientation tools were not as effective as in literature for the drilled plates due to the nature of the material, i.e. macrozones, with low angle boundaries and subgrains, two phases, variable grain size, layered microstructure, twins and steep strain gradients.

More severely deformed specimens displayed a higher thickness of SPD layer, larger and longer “channels” of low and high angle boundaries aligned with the drilling direction and twins deeper into the material. The previous defects and features could potentially act crack initiation sites and as verified by the fatigue data, specimens with lower levels of subsurface deformation had higher fatigue lives.

At the same time, all specimens had the same features and if the mechanism was based on the microstructural defects it should act to all of them. However, specimens with lower levels of deformation had significantly higher fatigue lives. This variation of fatigue lives was unlikely to be an effect of the crack propagation within the deformed microstructure and the elastic and plastic strain fields. It was rather a crack initiation problem for which the transition from low to high fatigue lives was caused abruptly when crossing from a threshold subsurface deformation value. A definite answer for the prevalent crack initiation mechanism could only be derived by the detailed examination of the fracture surfaces, since these features exist at different depths, although its actual identification could be challenging due to their small length scale.

The elastic strain mapping was not successful with EBSD and the effect of subsurface residual stress profiles on the fatigue life, was not been investigated. Depending on the machining conditions the residual stress could be either compressive or tensile close to the machined surface and should have an extended, mainly compressive profile deeper into the material proportional to the plastic strain field. The overlapping of the residual stresses, plastic strains, and microstructural defects could further alter the prevailing failure mechanism and change the fatigue performance.

A number of techniques are available for measuring residual stresses, but the curvature of the cylindrical surface of the hole, the required resolution and the availability of equipment pointed towards the direction of the stress relaxation, micro-machining methods with the Focused Ion Beam in an FEG/SEM microscope. This technique was developed in the peened CP-Ti specimens and applied to the Ti-6Al-4V drilled plates to complete the characterization of the plates.

Chapter 5. Residual Stress Mapping with Focused Ion Beam Micromachining & Finite Element Models

LOM, SEM and EBSD images revealed the presence of a plastic strain (PE) gradient through the deformed region and potential strain localization sites. Non-uniform deformation, temperature gradients and any other type of misfit, including microstructural features, could introduce residual stresses (RS), which could extend beyond the plastically deformed layer. The shape, peak stress location and overall depth of the residual stresses profile depend on the previous parameters, and hence the machining conditions. More aggressive drilling conditions could lead to deeper RS profiles and/or introduce tensile stresses close to the surface of the hole.

Due to the cylindrical surface of the hole, the measurement of residual stresses with traditional techniques was challenging. Additional limitations were imposed from the shallow residual stresses expected and the need for a semi-destructive, localized measurement technique with high spatial resolution. One potential method was the cross-correlation of EBSPs, but its application was not successful and there was an inherent limitation on obtaining results within the SPD and other heavily deformed areas. A more promising alternative was the downscaling of stress-relaxation methods with a Focused Ion Beam (FIB) FEG/SEM microscope.

The FIB method was applied successfully in peened CP-Ti and spring steel specimens, which posed a simpler problem, before transferring it to the drilled Ti-6Al-4V plate specimens. Residual stress profiles were compared against plastic strain through LOM images, in an attempt to correlate sub-surface profiles to microstructural features. RS and PE had significant variations, which were ultimately correlated to the cutting process through simplified, 2D finite element (FE) models. The combined information of surface roughness, hardening, plastic strains, residual stresses and deformed microstructure provided some explanation on the potential failure mechanisms and indicated the next step in the experimental work.

5.1 Review of FIB technology and applications

A FIB FEG/SEM is an extension of the traditional FEG/SEM microscope. In addition to the standard electron beam set up, there is an ion beam operating at 45°–55° to the electron beam and a gas injection system. The capabilities of the specific microscopes include imaging with secondary ion/electron and backscatter electron detectors, chemical and

mass analysis, ion beam milling assisted by gas, metal/carbon gas deposition and sequential milling and chemical analysis/EBSD.

Typically, the source of the ion beam is liquid Gallium (Ga), which flows down a Tungsten (W) needle to form a cone and is ionized by the applied electric field at the tip of the needle. Ga is more suitable for the specific application, due to its chemical, electrical and thermal properties, i.e. low melting point, volatility, surface free energy, vapor pressure and good emissivity characteristics. The emitted Ga^+ ions are concentrated and accelerated (5 kV–50 kV) along the column to produce beams of various intensities (1 pA–5 nA) and diameters (5 nm–0.5μm). Ga^+ beams cause sputtering of ions and atoms from the specimen under examination, while Ga^+ are implanted into it (penetration depth is ~20 nm at 25 kV). Higher intensity beams, >100 pA, are used for milling operations on specimens and low intensity ones for imaging. [157] [158]

The sputtering mechanism involves elastic and inelastic interactions between Ga^+ and the immediate surface of the examined material. Elastic ion-matter collisions result in the emission of (secondary) atoms (SA) and if they become ionized (SI), they can provide an image or location specific, mass information. Inelastic collisions result in the emission of secondary electrons (SE) and quasiparticles from plasma oscillations and mechanical vibrations. SI and SE are both suitable for imaging, but the standard mode is SE either by electron or ion beams. The advantage of the ion beam, SE imaging is that it provides an excellent surface topology and an enhanced contrast. [157] [158]

FIB has been used for a variety of applications including engineering of semiconductors [159] [160] [161], preparation of samples for TEM [158] [162] and atom probe tomography [163] [164], cross-sectional analysis of materials microstructure [165] and sub-surface cracks [166], machining of features for micromechanical testing of miniature beams under bending [167] or pillars under compression [168] in a nanoindentation tester, and measurement of surface residual stresses in the micro-scale [48] [66].

The FIB RS application was of particular interest for the current research work. A localized, site specific, technique for the measurement of residual stresses in a scale comparable to the existing microstructure, is a very powerful analytical tool. It could capture the short and/or long range RS profile of the previously applied thermo-mechanical processes and potentially link everything to particular microstructural features. Under the strict definition of residual stresses which involves their characteristic length, i.e. “scale over which they equilibrate” [6] [47] [48], FIB RS should be considered as Type II or intergranular stresses [6] [47] because they arise from measurements in the

microscale and should equilibrate within the grain scale, 3-10xgrain size [47] to provide the macroscopic stress (Type I). For peening and machining processes only the horizontal and the transverse directions can directly equilibrate to a uniform, average, macroscopic stress for all of its components because in the other direction, depth-wise, the stresses develop a certain profile in a narrow sub-surface region of a few hundreds of microns. Local microstructure will affect the residual stress profile, but since the characteristic length of the macroscopic stress/process is similar to that of the microstructure, the residual stress profile should maintain most of its features, though absolute magnitudes would change. Thus, the FIB technique in these applications should provide Type II stresses representative of the Type I stresses at the specific locations as developed by the combine effect of the process and the local microstructure, providing upper and lower bound limits to the stress field.

The first FIB RS techniques were developed to capture the average, residual stresses associated with the deposition of thin films, based on the deflection of micro-cantilevers pre-milled on the substrate [169] or post-milled on the coating [170]. Finite element and analytical solutions were used to solve the inverse problem. Such methods are limited by the high milling time and the need to employ a surface measurement equipment with a high resolution, i.e. the Atomic Force Microscope (AFM). The size and imperfections of the milled features could introduce some variation on the deflection profile, as the beam deflects during milling under the presence of residual stresses. A different approach is to mill a pattern of lines on the cantilever and use the Moire interferometry method for the in-plane displacement field [171]. Work on coatings was driving the evolution of the FIB micromachining, stress relaxation methods. Slot milling directly on the coating surface and SE imaging of the surrounding area before and after milling reduced the milling and measuring time for the RS calculation [172]. The SE images were post-processed by Digital Image Correlation (DIC) operations with commercial and customized codes and the measured, filtered/unfiltered, 1-D field was incorporated into analytical and FE solutions for the calculation of the existing, uniform stress [172] [173]. A 2-D solution became available by changing the milled geometry from the slot to hole [174] or ring [175]. In all cases, the length, width and particularly depth of the milled feature were required for the calculations. DIC was also applied to the cantilever system in coatings and it allowed the calculation of residual stress through the thickness of the layer with progressive milling of the underside of the beam and imaging of the topside [176]. If the surface of the coating has poor surface details, then it was proposed to mill a regular array

of nanoscale holes [175] [177]. Milling of cantilevers is a relatively laborious task, which involves a number of roughing and finishing passes.

Advancements on the FIB method occurred with the work on engineering materials. Sub-surface RS were measured in peened, amorphous materials with slots [178] and holes [179]. Complete profiles were built by measurements at different depths from the peened surface, and they were used for the validation of FE models and evaluation of the peening process. For the purposes of that work, the (electro-) polished surface was decorated with Yttria-Stabilized Zirconia (YSZ) with a diameter in the range of a few tens of nm and then the surface was carbon coated to protect it from the Ga^{+} implantation or potential damage of the details from the ion beam [178]. Further improvements were introduced with the incremental milling of the slot [180] and holes [179]. The solution algorithm was modified to incorporate the sequential processing of images, incremental built up of the displacements and filtering operations of the associated DIC errors [181]. YSZ are a good and cheap alternative for the surface decoration of featureless samples, but more efficient methods exist with the deposition of Platinum (Pt) on the surface with Focused Electron or Ion Beams (FEB- FIB) [182]. The decoration techniques yield equivalent results only under ideal conditions. YSZ are sharp and can create small agglomerates, but there is no control on the coverage and sometimes they can form large agglomerates with low spatial distribution. Instead, Pt dots and milled details are excellent candidates for the FIB RS technique, at the expense of time on the microscope. FIB slot and hole milling were carried out in peened Al-7075-T651 notched specimens, both on the peened surface and on the cross-section to establish surface and sub-surface RS profiles [183] [184]. Despite the relatively large standard deviation errors the shape, magnitude, and depth of profiles were verified by micro-XRD measurements and partially linked to the deformed microstructures.

DIC operations require a high-quality image. Changes in brightness and contrast can result in relatively large errors due to the small sub-pixel displacements. The recommended method for imaging involves BSE with integration filters for sharpness, detail preservation and low image shifting [182]. No work has been carried on the image resolution and its effects on the accuracy, which can become a very important factor since the displacement calculations require sub-pixel accuracy. In any case, the imaging capabilities of SE and BSE modes should be tested for each microscope prior to the actual experiment. The patch size during DIC also contributes to the variations and can have an averaging/smoothening effect on the results. Commercial software typically employ large

patches in comparison to the size and distribution of the decoration details in DIC [178] [182], which should be avoided.

Surface damage and modification of the elastic properties can occur by the ion implantation [158] [157]. That was evident from a qualitative examination of TEM samples prepared with FIB [185] [186]. In most FIB RS applications damage was neglected based on the reasoning that these are second order effects and they have limited influence on surface material properties and displacements. After all, the milled region is not included in the analysis, unlike TEM samples. A preventive system is to apply a carbon layer prior to milling to protect the surface and the deposited details [178].

The localized nature of the RS measurement with the FIB imposes limitations on the comparison of results with other well established, area average methods, like XRD and hole drilling [54]. Basic information on RS and PE can be obtained by FE simulations of drilling. A full analysis of any machining operation is computationally expensive, time consuming, and may not retain the required level of detail in the regions of interest [187]. Simplified, 2D, orthogonal cutting models have been used in the past to capture the key characteristics of the process, i.e. material behaviour [188] [189], chip morphology [190] [189], machining forces, temperature distribution [191] and tool performance [192]. Elasto-plastic, plain strain models have additionally provided the required information regarding the depth of plastic deformation and RS fields [193]. Hence, 2D FE models of orthogonal cutting could provide the plastic and elastic strain fields along and across the machined surface and serve as benchmarks for the FIB RS technique. The magnitudes from the FE model and depth of profiles should be quite different, but the shape of profiles and any variations during the process should still be present.

5.2 Method development

The developed methodology was a direct application of the work carried out in amorphous peened material (bulk metallic glasses) [178]. Surface displacements were calculated through Digital Image Correlation (DIC) on the decoration details of the SE/SI images, before and after milling. The actual, residual stress value was calculated based on a 3D, Finite Element (FE) model of a slot, with a pre-defined, uniform stress. An underlying assumption was that the stress relaxation problem was linear, elastic. As a result, the reference, uniform stress could be scaled according to the ratio of the reference to the measured displacement field to provide the applied, uniform, average stress normal to the slot.

5.2.1 Milling and imaging conditions

FIB work was mainly performed in an FEI Quanta 200 3D thermal emission (tungsten filament) scanning electron microscope (FIB/SEM) at the Sorby Centre for Electron Microscopy and Microanalysis of the Department of Materials Science and Engineering of the University of Sheffield. Due to an ongoing problem with the tungsten filament electron source, SE imaging was poor compared to SI imaging. Additional operational limitations existed regarding the recommended operation settings. A limited number of experiments were carried out at the Culham Centre for Fusion Energy (CCFE), in an FEI Helios NanoLab 600i, FIB/SEM. The quality of milling and imaging was far superior at Helios compared to Quanta.

Slots [178] were selected instead of holes [179], because of mainly two reasons. Firstly, slots could be placed in closer proximity to each other and to the specimen edge, since they release stresses mainly perpendicular to the long dimension. Holes would release stresses in all directions around the hole causing resolution problems with the vertical offset of holes. Secondly, slots were smaller features than holes, thus the imaging area was maximized and the milling time was reduced.

Slots were opened on the cross-sectioned specimens (through thickness cut) to examine the subsurface profile of stresses in different depths/locations. No incremental milling and imaging [180] were conducted to reduce imaging time, post-processing cost, avoid accumulation of errors associated with low intermediate displacements, and simplify the process. Incremental milling would more suitable in cases where there was a stress/strain gradient with depth and/or high resolution/accuracy was required in the first few microns of the machining surface, in which case milling would be conducted directly on the machining surface.

The surface under investigation was decorated with Yttria Stabilized Zirconium (YSZ) particles [178] [182] and regular, milled details (MD) [175] [177]. Platinum (PT) deposition [182] operations were not available on the available microscopes. YSZ reduced the milling time in the microscope for the surface preparation and allowed the application of a protective carbon coating layer on the surface, but there was little control of the spacing/size of agglomerates and selection of specific location/feature to examine. MD could be placed anywhere on the surface based on SEM/BSE images to an appropriate size and resolution, which was an attractive alternative for specific regions of interest, like (plastic) strain localization sites, twins and transition zones. High

magnifications and milling details were employed for specimens with reduced levels of deformation to increase the spatial resolution.

Due to an ongoing problem with the Quanta equipment, the imaging was conducting with the Ion beam, rather than the recommended Electron beam [182]. The Ion beam was operated at 30 kV, and a working distance of approximately 30 mm. Imaging was conducted at 10 pA because at 1 pA (minimum available) the beam was considerably unstable. Integration filters were applied to improve the quality of the image and cope with the beam drift at slow scans [178] [182]. The energy of the ion beam damaged the surface details in high magnifications because it was concentrating in a smaller area. Thus practical limits were imposed in the FIB work. YSZ were the preferred technique for lower magnifications, 2kX-10kX, whereas MLD was more suitable for 15kX-30kX magnifications, *Figure 5-1*. All images were taken at 1024x884 pixels; higher resolution images could increase accuracy and should be recommended, but the ion beam damaged the surface details in previous test runs.

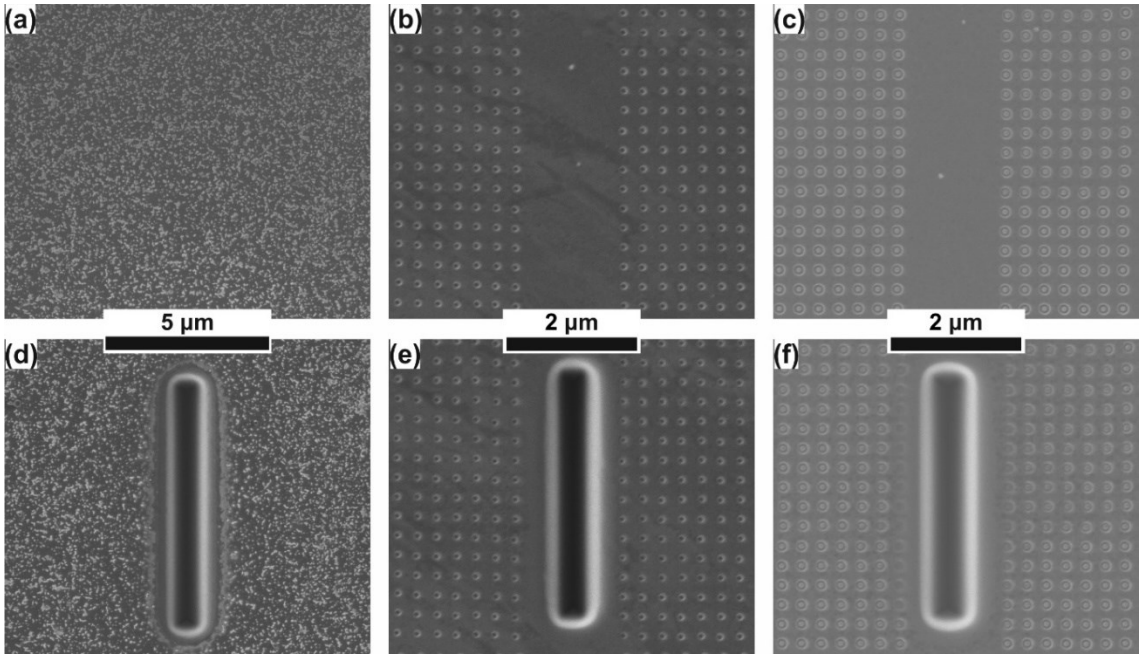

Figure 5-1 Examples of surface decoration. a) & d) YSZ; b) & e) MLD holes; c) & f) MLD rings.

Decoration details were milled at 10 pA and slots were milled at 0.3-1.0 nA, at 30 kV and 30 mm working distance. Higher currents reduced the milling time and increased the depth at the cost of feature sharpness and ion implantation. No study was conducted for the effects of the ion implantation. The milled settings were selected on previous applications and a limited, optimization study carried out to reduce the process duration. The depth of the milled slot was revealed by images of the slot at a tilted position through end trenches and/or images of the end face with the ion and electron beams, *Figure 5-2*.

End face calculations require a small correction due to the slope of the face by half slot width over the slot depth.

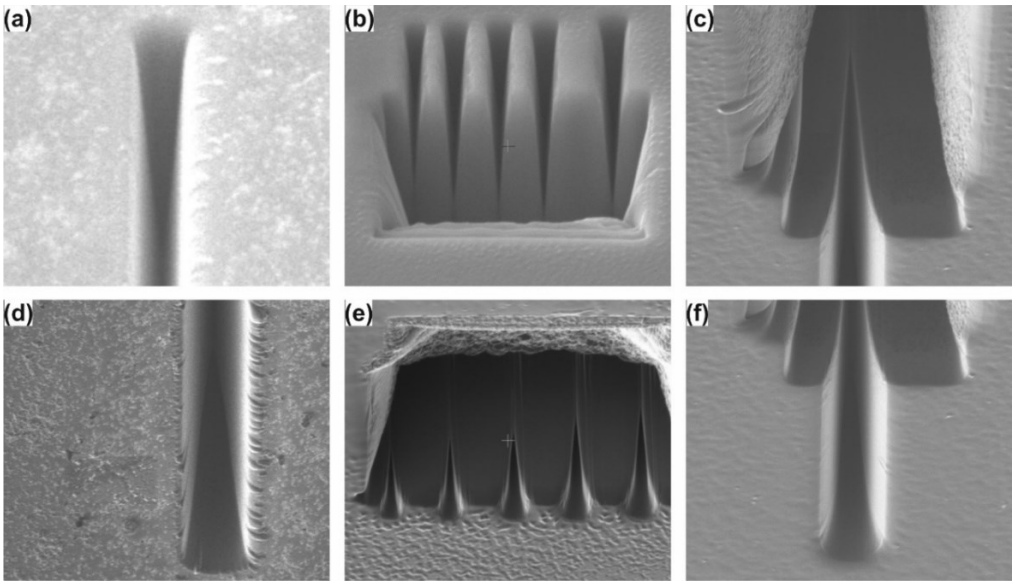

Figure 5-2 Depth measurement of slots. a) E-beam @ tilted end face; b) E-beam @ end trench; c) I-beam @ end trench; d) I-beam @ tilted end face; e) I-beam @ end trench; f) I-beam @ end face.

5.2.2 The FE model of the slots

The stress relaxation due to the milling of the slot was simulated in the commercial, FE software ABAQUS, *Figure 5-3*. A finite volume containing the slot was pre-loaded with a uniform stress field acting perpendicular to the direction of the slot. Fixed boundary conditions were applied at the outer and bottom faces. Quarter symmetry was used to reduce the size of the problem. The volume of the model was selected according to the size of the slot, by examining when the edge effects would dissipate. Typically, the length of the (quarter symmetry) volume would be 4xslot length, the width 2xslot length, and the depth 3xslot depth. A linear-elastic solution algorithm was used for the calculation of the surface displacements, as the unconstrained faces of the slot moved under the presence of the uniform stress. The uniform stress reduced progressively from the bulk material towards the slot.

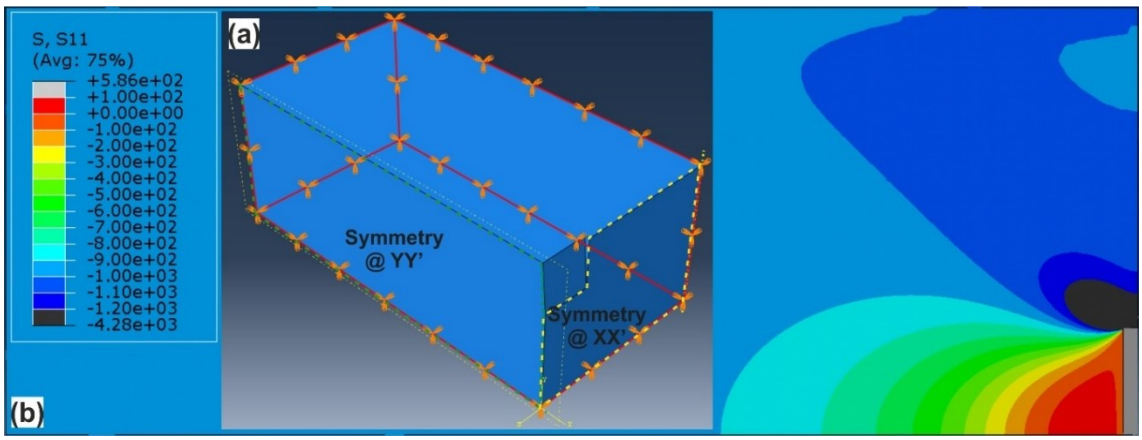

Figure 5-3 FE model of the slot in CP-Ti. a) Quarter volume of the slot with symmetry planes (doted outlines) and encaste conditions (planes with red outlines); b) RS field of a 10x1x5 slot @ uniform compression of 1000 MPa.

The stress localization at the slot could introduce some plasticity to the model, which only affect results at very high stresses, *Figure 5-4*.

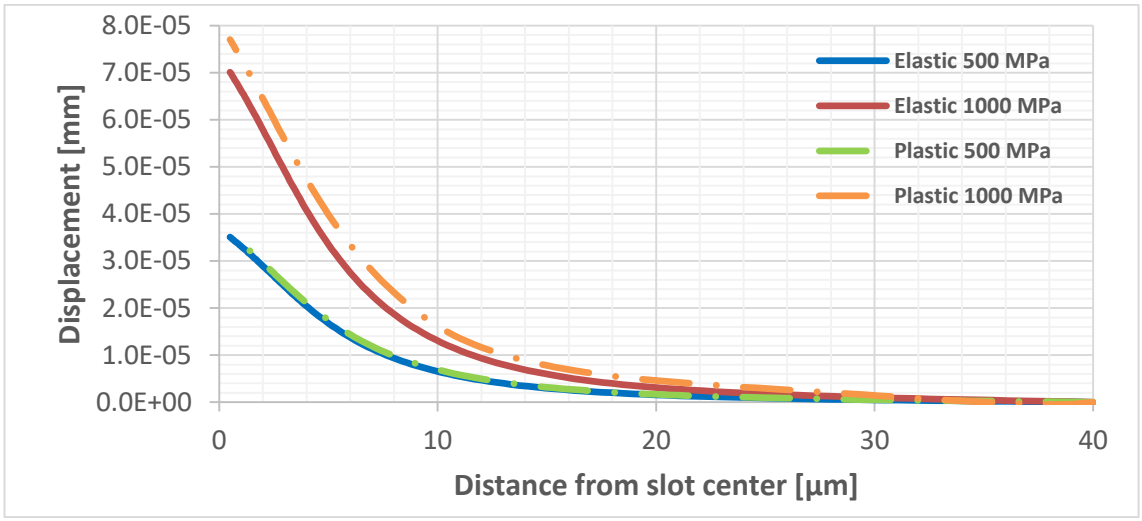

Figure 5-4 FE displacement results for elastic and elastoplastic FE models in CP-Ti.

Typically the volume of the material would not be under a constant stress value. Instead, a gradient should exist along the slot. Thus the net effect of milling a slot would be an asymmetric displacement field, not scalable for all practical reasons. Corrections could only be possible after the first run with a uniform stress approach. Then, the second run with location specific gradients from the first run, at a significant expense of time. Additional complexity to the FE model could be introduced by location depended on elastic properties based on orientation data from EBSD scans.

Due to accumulated errors from the imaging, DIC, microstructure, texture, anisotropy, and the existing stress gradients, it was more important to calculate an approximate stress profile. To this end, a uniform stress field was used in an FE model with isotropic elastic properties. The small size of the slot and the reduced stress calculations at the middle of

the slot ensured that the simplification would not affect the accuracy and validity of results.

5.2.3 Post-processing tool

The images before and after milling were analyzed with a custom made code, developed with the programming software MATLAB[8] [153]. DIC operations were applied at the locations of the decoration details through the command *cpcorr*. As an example, the method was applied on the CP-Ti, peened at room temperature. The slot and the image scale were located on the milled image manually with the command *getrect*, *Figure 5-5*, while the details were detected by the command *regionprops* on an auto-thresholded binary image, *Figure 5-6*.

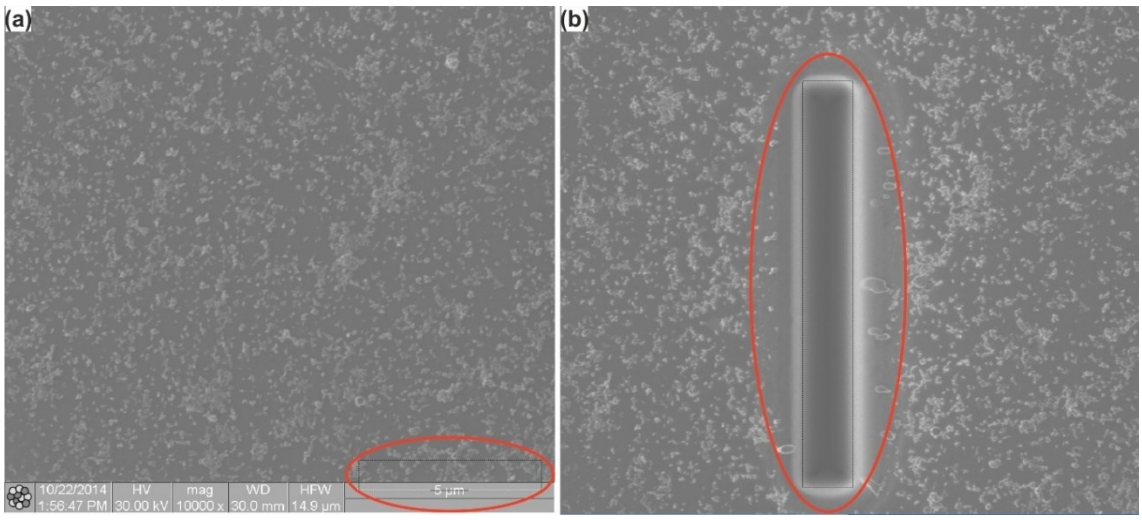

Figure 5-5 Detection of image features. a) Scale length; b) Slot length and location.

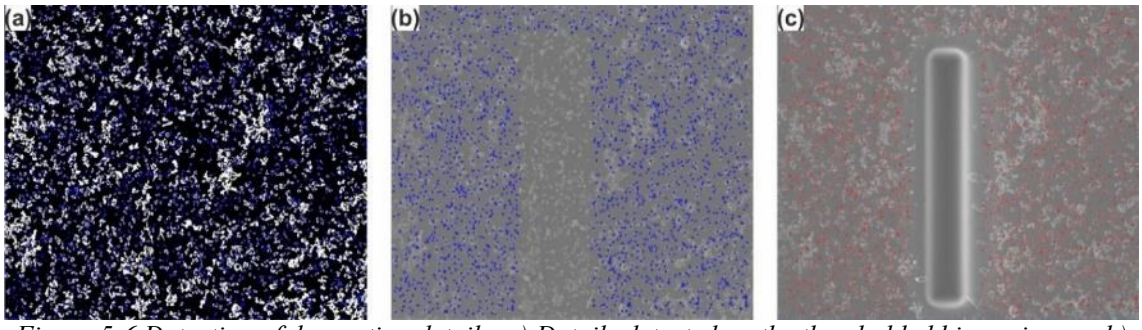

Figure 5-6 Detection of decoration details. a) Details detected on the thresholded binary image; b) DIC locations on the original image; c) DIC locations on milled image.

Image shift, due to beam drift after imaging and stage movement, were corrected by manual selection of control points on both images (typically at the corners of the images) with the command *cpselect, Figure 5-7*. The control points were further auto-corrected by *cpcorr*.

[8] https://uk.mathworks.com/products/matlab.html

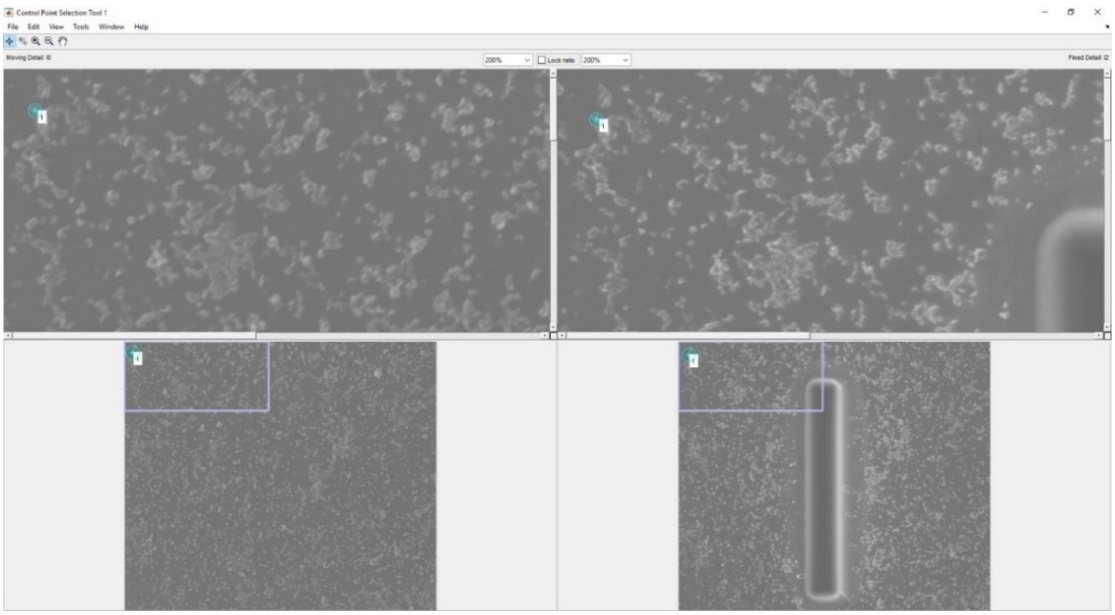

Figure 5-7 Selection of control points.

DIC provided the displacement field around the slot(s) and the origin was placed in the middle of the slot, *Figure 5-8 (a)*. Then the displacement field from the Finite Element (FE) analysis of the equivalent 3D problem at a predefined stress was interpolated into the DIC locations by the command *griddata, Figure 5-8 (b)*. The displacements were not always centered, because there were DIC errors on the control point(s), a limited number of control points (i.e. a single control point) and/or small displacements at the corners. Global displacements were only a few pixels, thus such problems did occur.

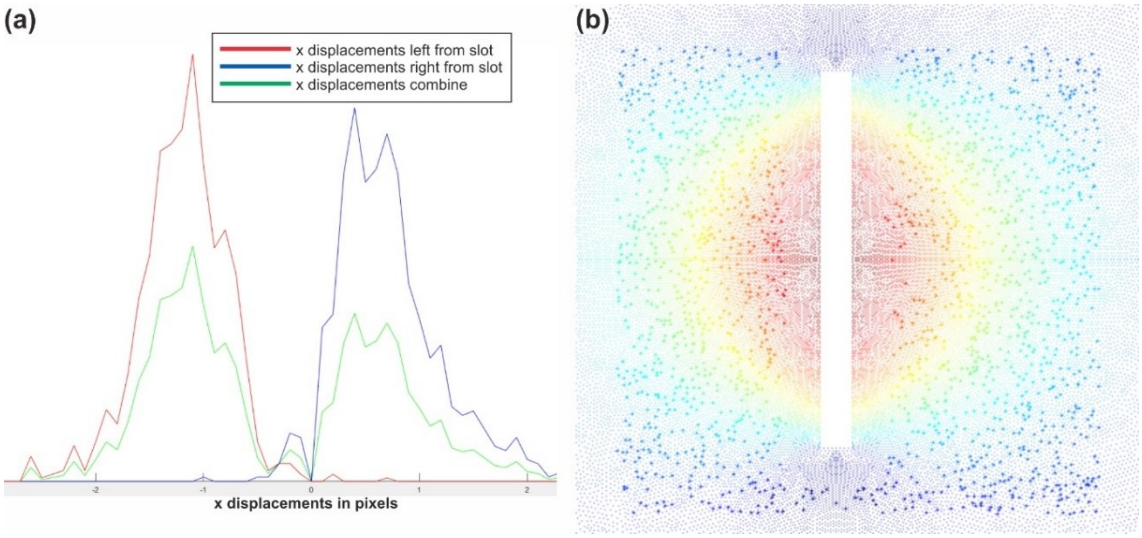

Figure 5-8 Distribution of DIC displacements along the slot; b) Interpolation of DIC locations on FEM model of the slot.

Finally, the actual stress was calculated by linear interpolation of the DIC vs. FEM displacement fields for the uniform, FEM stress, *Figure 5-9 (a)*. Alternatively, the reference stress was scaled to the appropriate magnitude according to the ratio of displacements at each location and both the average and the standard deviation were

calculated, *Figure 5-9 (b)*. In either case, the calculated error corresponded to the cumulative error from the DIC, the stress variation along the slot and the scattering of results.

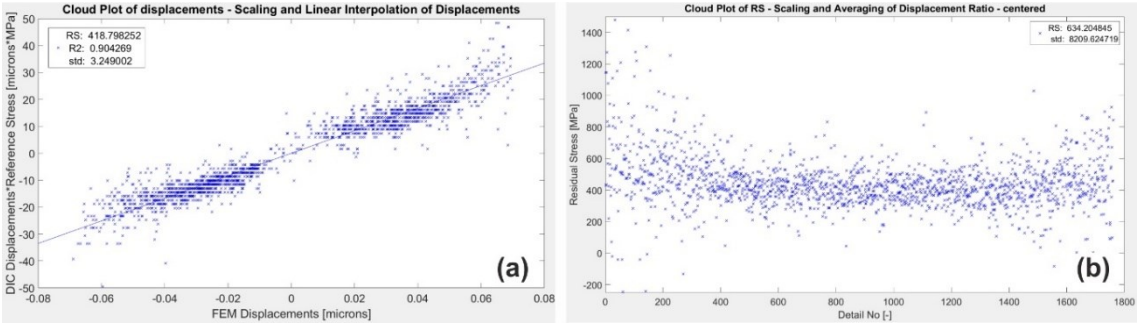

Figure 5-9 Stress calculation plots. a) Linear interpolation; b) Average and standard deviation of cloud plot.

Linear interpolation was superior to the simple, averaging algorithm. Close to the edges of the slot the scattering of the results increased and the mean could not produce accurate results. The origin of the scattering could be traced back to the non-uniform residual stress field along the slot, errors in the DIC and stress concentration effects at the slot.

The code was tested on un-milled images, *Figure 5-10*, and milled images taken at the bulk of the specimens, *Figure 5-11*. Displacement vectors had very low values at either side of the slot and an overall very low average value of stress with higher error than the absolute stress value. Some scattering of the results was still present and it was the evidence of relatively poor imaging conditions and the effect of brightness/contrast changes with imaging/milling, especially on the milled images.

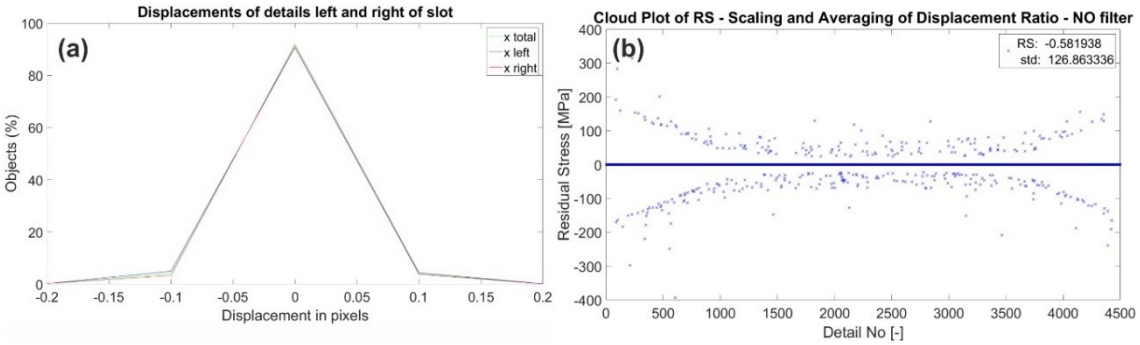

Figure 5-10 DIC code test on un-milled images; a) Displacement distribution at either side of the (imaginary) slot; b) Average stress calculation (note the high number of zero stress points and high error).

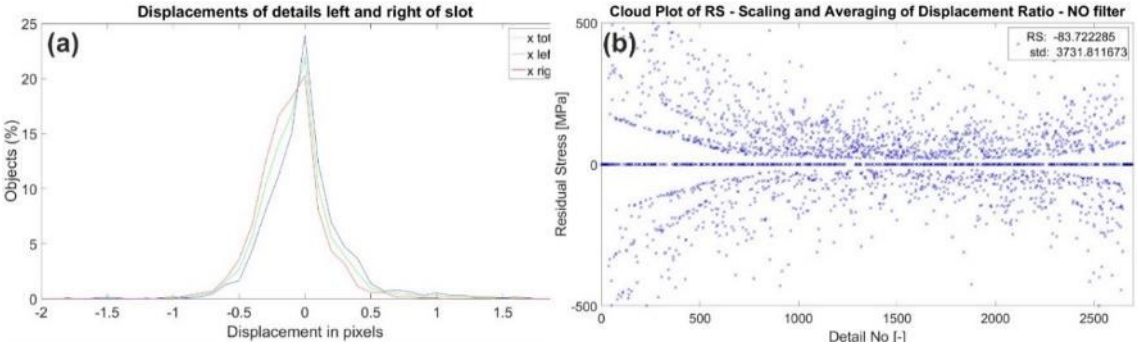

Figure 5-11 DIC code test on milled images at the bulk; a) Displacement distribution at either side of the (imaginary) slot; b) Average stress calculation (note the high scattering of stresses at the ends of the slot, the high full slot length error and the low average value).

5.2.4 Cut effects and stress relaxation

The sectioning of the drilled plates was conducted by Electrical Discharge Machining (EDM). The cut should have released completely the stresses acting normal to the plane of the cut. However, stresses acting on the plane of the cut should be retained close to the free surfaces of the specimens. EDM is considered a stress free cut, an assumption typically employed in the contour method of residual stress measurement [55].

As a first example, the well-documented and investigated system of quenching a solid aluminum block. A solid block with rectangular cross-section, 1270x406x254 mm, was quenched in water at 70 ºC. Reference material data and heat transfer coefficients were applied to generate a residual stress field within the block through the FE software Abaqus[9], [194]. Then the symmetry boundary condition on the XY plane was suppressed to simulate the stress-free cut by EDM and the subsequent stress relaxation, *Figure 5-12*.

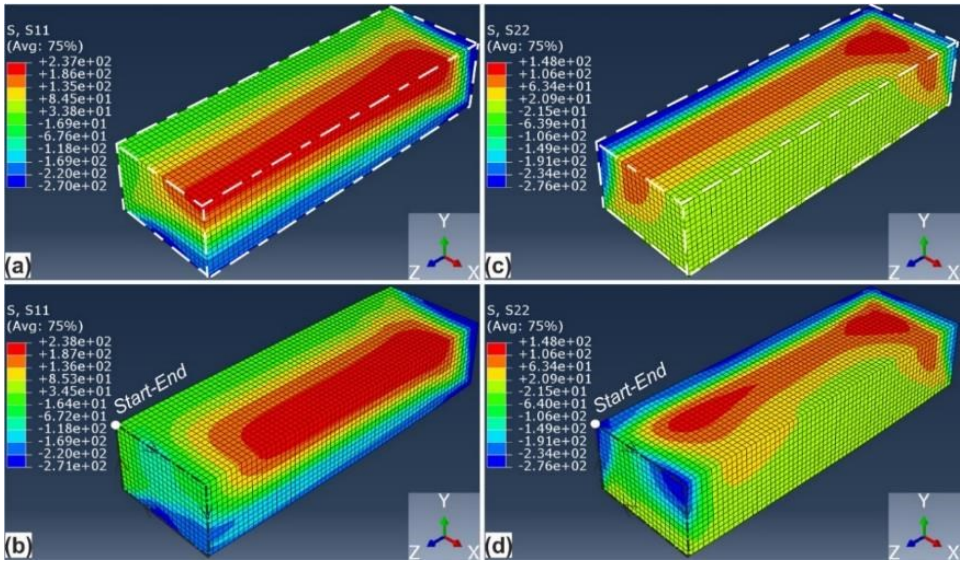

Figure 5-12 FE model of stress relaxation in quenching induced stresses in an aluminum block. a) & b) Stresses in the x & y direction before cut; c) & d) Stresses in the x & y direction after cut

- Note 1: Block is 1/8th due to symmetry;

[9] https://www.3ds.com/products-services/simulia/products/abaqus/

- Note 2: Symmetry planes are the front planes outlined with the dashed white line;
- Note 3: Path #01 is outlined in (b) & (d) with the black dotted-dashed line.

In more detail the stresses along the path #01, *Figure 5-12 (b) & (d)*, which were acting normal to plane of the cut completely relaxed after the cut, but the stresses acting on plane of the cut were retained along the exterior faces (after 406/2+254/2=330 mm), *Figure 5-13*.

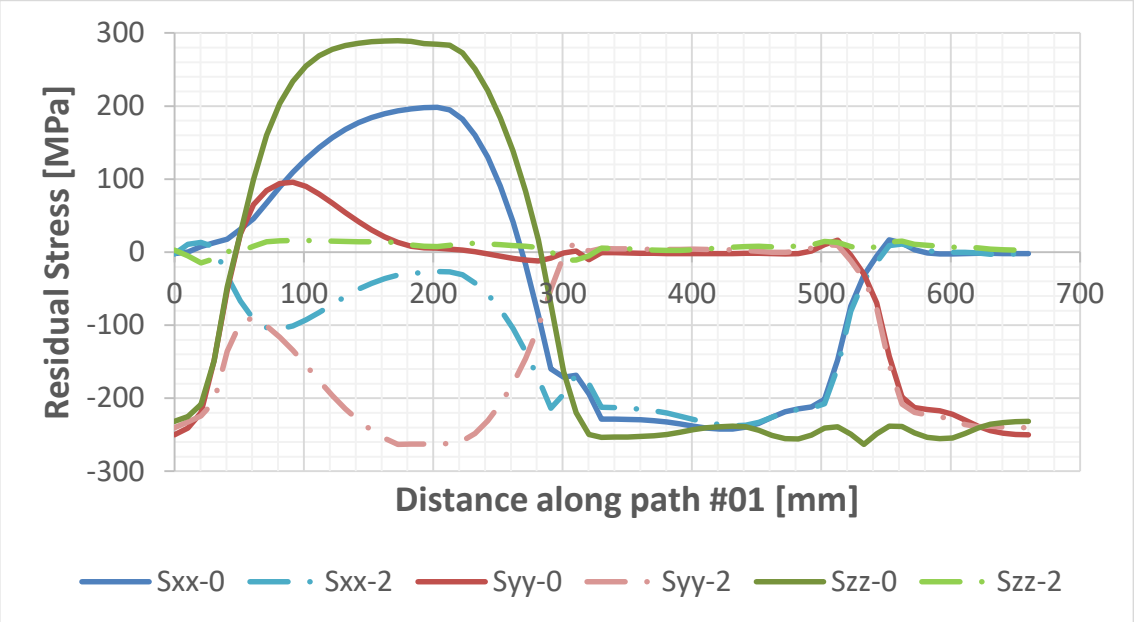

Figure 5-13 Plot of stresses before (Sij-0) and after (Sij-2) the cut at the three principal directions along the Path #01.

A second example, closer to the scale and nature of peened and machined specimens, the subsurface residual stress generation and relaxation in a solid block (0.5 mm x 0.5 mm x 1.0 mm), *Figure 5-14*. The simulation was created through the FE software *SFTC DEFORM 3D*[10] and the use of coating layers [195]. RS were generated in x and y directions as a function of depth at the top *xy* plane. Symmetry conditions were applied on the front *xz* and *yz* planes, whereas the bottom *xy* plane was fixed. Upon suppression of the symmetry condition on the *xz* plane, the stresses on the *y* direction were released, but there was little effect on the stresses acting on the x direction, *Figure 5-15 & Figure 5-16*. The average drop of stresses in the *x* and *y* directions were due to the geometry of the coating mesh, which had reduced thickness at the corners of the block. Note that the small dimensions of the volume under investigation contributed to the average stress reduction.

[10] http://www.deform.com/

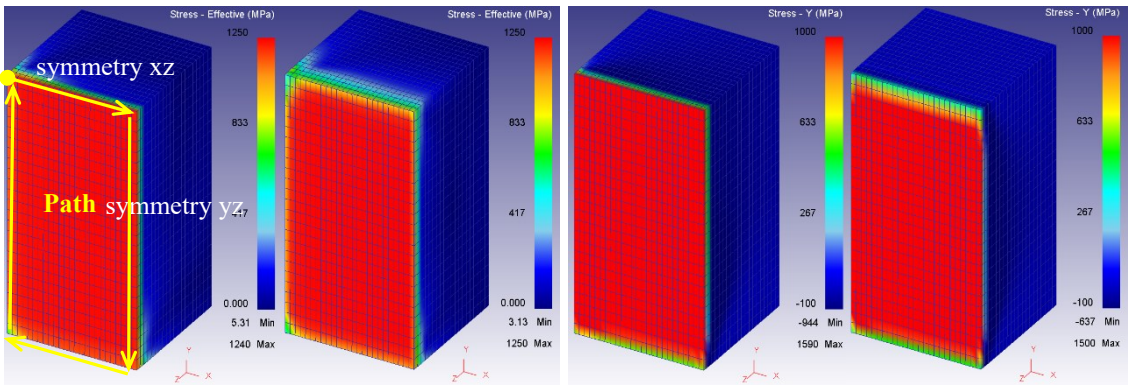

Figure 5-14 Stress relaxation; effective and Syy stresses

Figure 5-15 Residual stress relaxation along path – Sxx

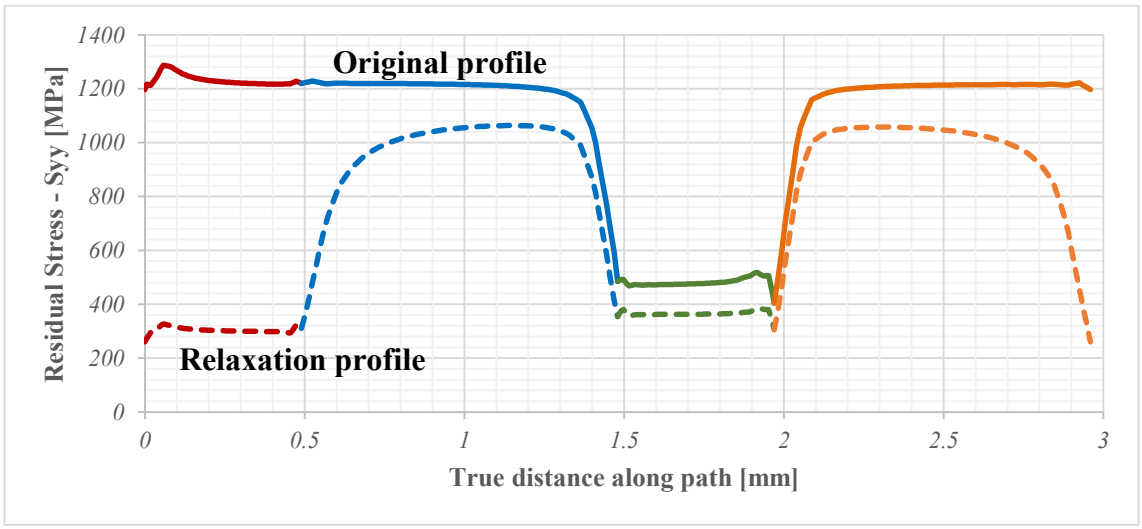

Figure 5-16 Residual stress relaxation along path – Syy

The drilled plates were a more complicated system, where residual stresses were developed predominately from the high plastic strain gradients. Typically, stresses extend about 100-200 µm beneath the machined surface. Due to the proximity of the stresses to

the exterior surface and their origin, it was expected that they would also be retained on the plane of the cut.

5.3 Application in peened material

The CP-Ti material peened at different temperatures [7] was examined with the FIB micromachining, stress relaxation method. Slots, 5-20 μm in length, 0.5-1.0 μm in width and 4.5-7.5 μm in depth were opened on the sectioned specimens, which were decorated with YSZ. Specimens were prepared by standard metallographic techniques and electro-polishing. Error values were well below ±50 MPa for the linear fitting algorithm and ±100 MPa for the averaging one. Bulk residual stresses were measured at the CP-Ti with XRD at the Advanced Forming Research Center (AFRC) to an average, compressive value of 50 MPa. Sub-surface residual stresses were measured with the ESPI hole drilling technique at the Advanced Forming Research Center (AFRC) at the CP-Ti peened at room temperature. ESPI and XRD provide macroscopic area and depth averaged RS values indicative of the state, magnitude and variation of stresses. To that extend ESPI and XRD can provide an indication of the existing stress state and allow for qualitative comparisons to the proposed technique. FIB RS are measurements performed in the microscale (Type II stresses) and the length of the slot was similar to the grain size of the materials examined considering the grain size variation. However, the operations under investigation introduce macroscopic stresses in the same scale and that overlap of the characteristic length of process and RS profile could allow FIB to capture a representative RS profile with depth and be compared to XRD and ESPI results.

5.3.1 CP-Ti Peened @ low temperature

The low-temperature specimen provided similar peak values and location of peak values in the four RS profiles of *Figure 5-18*, for the four different locations of *Figure 5-17*. However, the near edge/surface stresses and the depth of the profiles varied considerably. Higher near-surface values were observed for hills, profile *(a)*, and valleys on the peened surface, profile *(d)*. Profiles *(b) & (c)* were typical compressive stress fields for peened material. The depth of profiles *(b) & (c)* coincided exactly with the depth of the twins and the density of twins in the surrounding area. Profile *(d)* had an abnormal shape. It had a peak value at the relatively flattened, peened surface and compressive stresses were completely dissipated at the depth of twins. A sudden peak at 250 μm should be treated as an error, although the image quality was good. Peak values were measured below the SPD layer and the depth of the compressive profile matched the local plastic deformation.

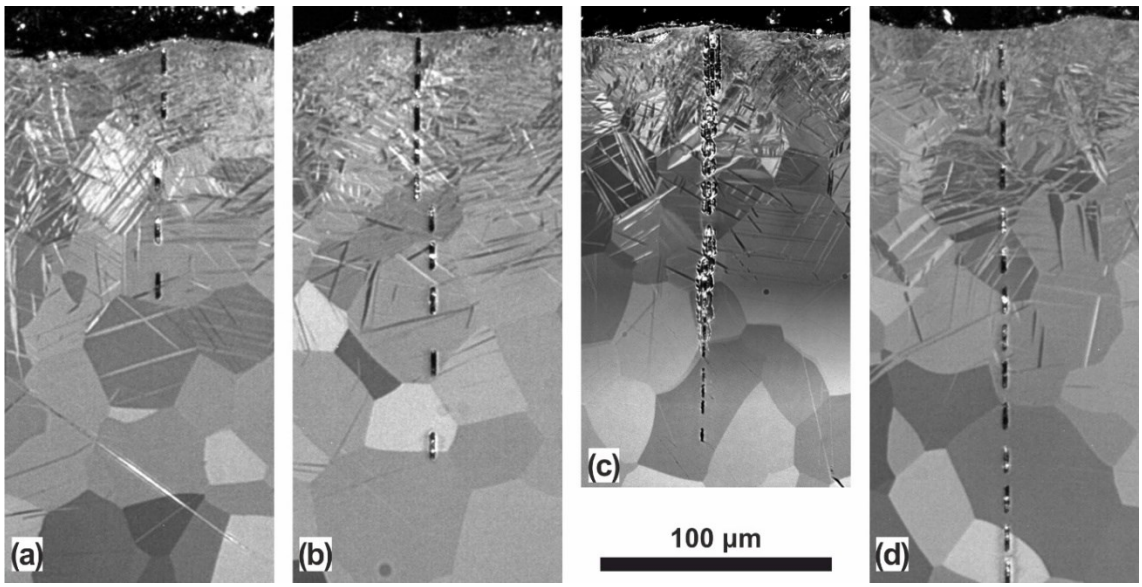

Figure 5-17 Location of residual stress measurements of CP-Ti, peened at low temperature.

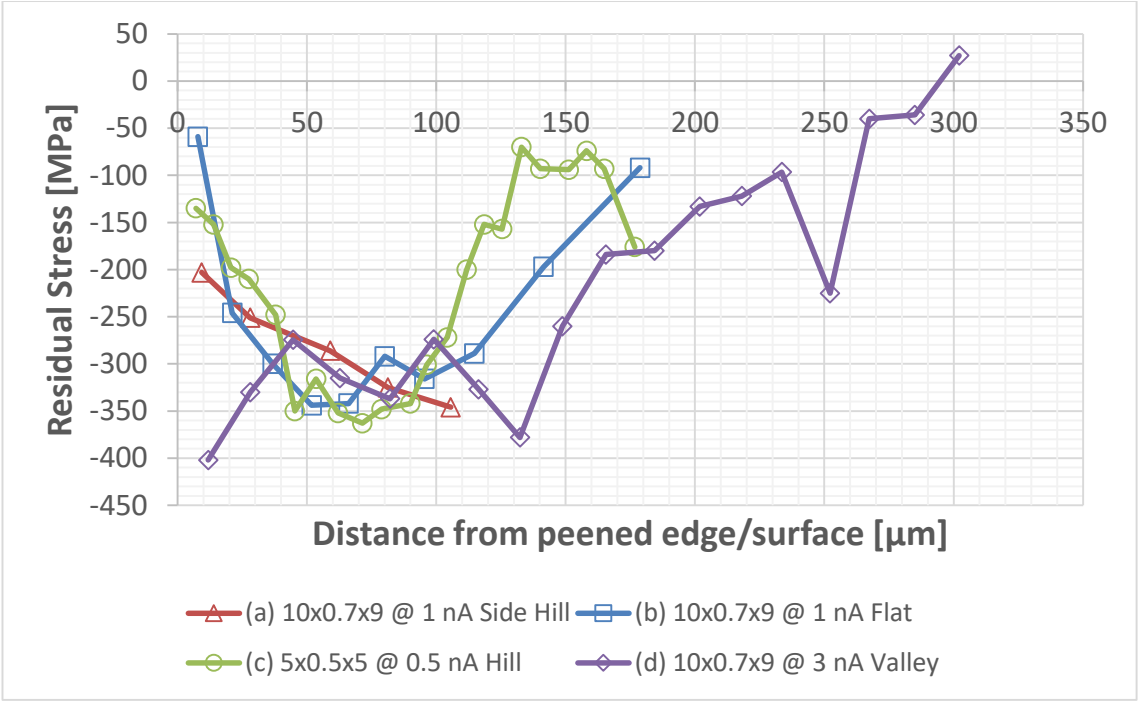

Figure 5-18 Sub-surface residual stress profile of CP-Ti, peened at low temperature, at locations indicated at Figure 5-17.

5.3.2 CP-Ti Peened @ room temperature

The specimen peened at room temperature, *Figure 5-21 (a) & (b)*, displayed similar variation in the RSs, *Figure 5-20*, to the low-temperature specimen, *Figure 5-18*. Profiles *(a) & (b)* were typical compressive stress fields for peened material. They extended to the depth of the twins and their respective values were a function of the twin density and microstructure. *Figure 5-21 (b)* indicated that a small grain without twins produced a drop in the residual stresses, although neighboring grains had a few twins. The stresses could have reduced due to the sample preparation and removal of the twinned part of the grain (removal of the strained region/elimination of strain gradient), and/or due to the stress

discontinuity across grain boundaries. Larger slots (20 μm) milled at the same location as smaller ones (5 μm) did not provide the required spatial resolution and accuracy, because stresses were averaged through a wider area and the effect of local microstructure was diminished. Despite that, the profiles were still relatively close. It could be assumed that the severely twinned regions of profile *a* introduced higher compressive stresses. In either case, peak stresses occurred below the SPD zone.

A microhole drilling measurement with the Electronic Speckle Pattern Interferometry (ESPI) method [64] at the AFRC, partially verified the FIB measurements. Near surface values and the location of peak stresses were identical, while the ESPI depth was between FIB profiles *(a) & (b)*. The ESPI profile contained a prolonged tensile part, which was not captured with FIB or XRD. That could be the direct effect of lower resolution after 100 μm and the fitting algorithms that were automatically applied through the software. In any case, ESPI confirmed the direct link of the twin's depth, i.e. low levels of plastic deformation with the diminishing of the compressive residual stress field.

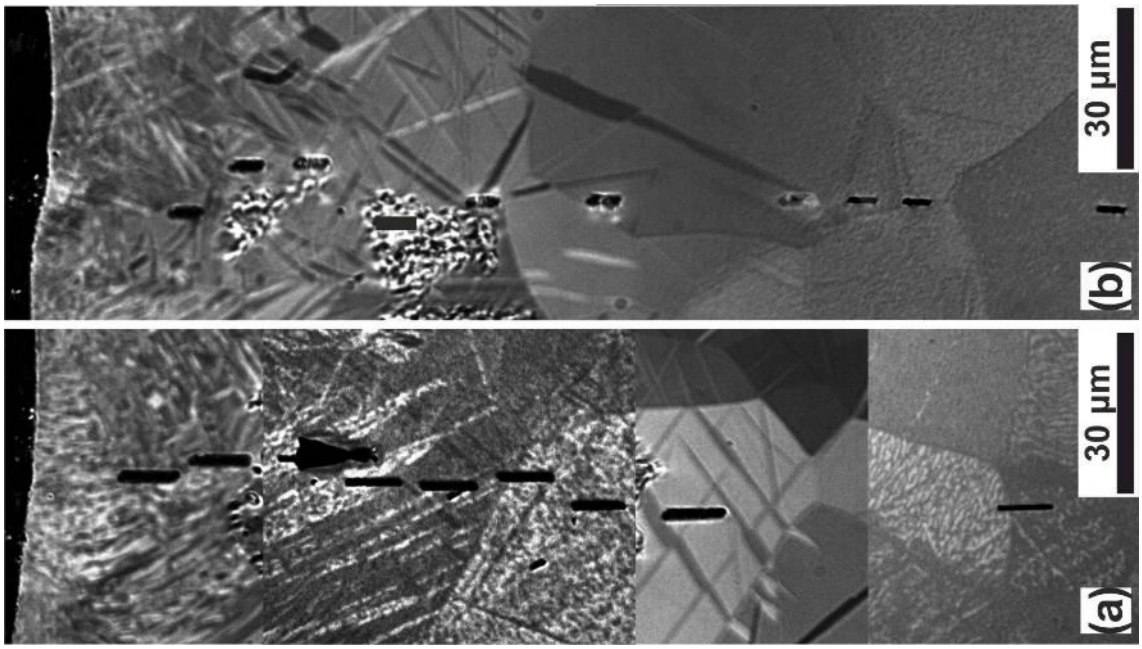

Figure 5-19 Location of residual stress measurements of CP-Ti, peened at room temperature. NOTE: Unresolved sample preparation/LOM problem with RT specimen.

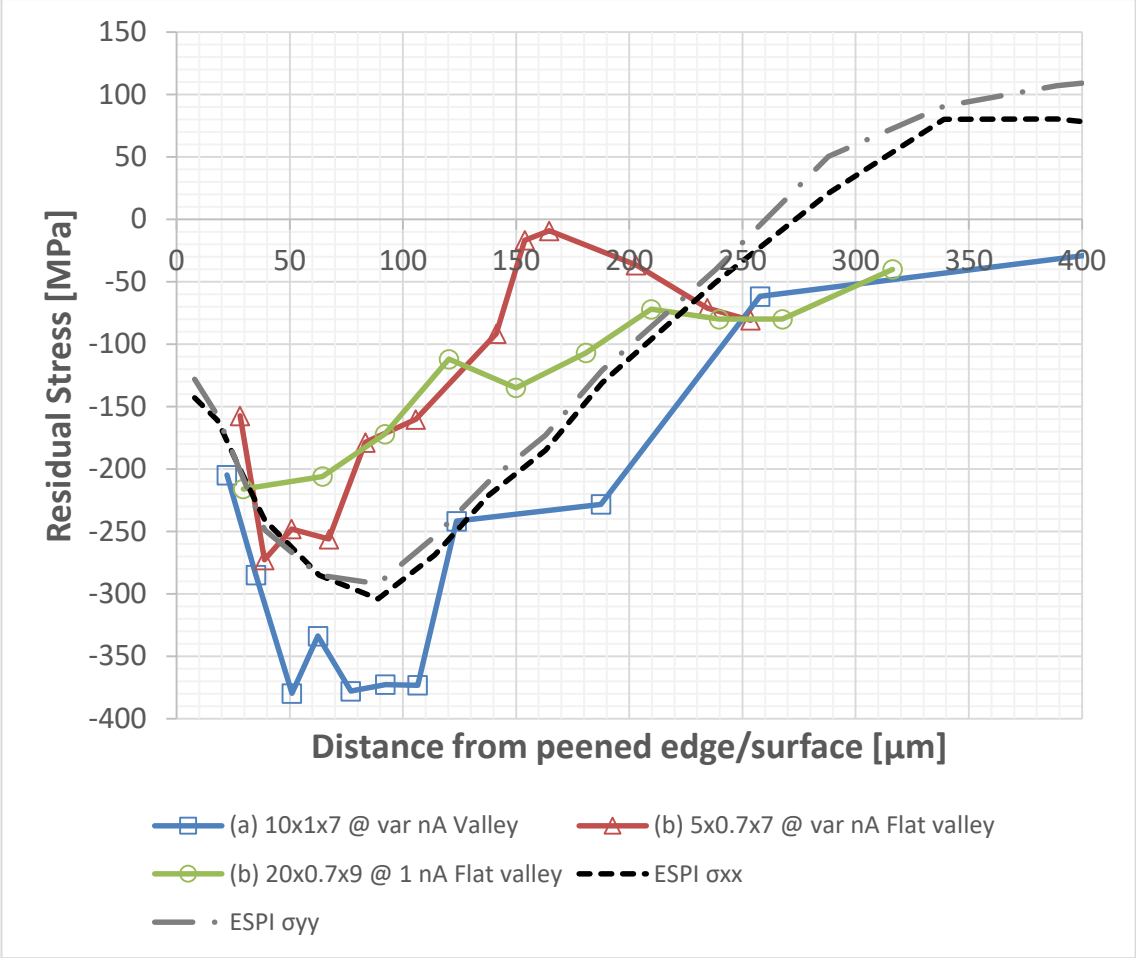

Figure 5-20 Sub-surface residual stress profile of CP-Ti, peened at room temperature.

5.3.3 CP-Ti Peened @ high temperature

The specimen peened at high temperature, *Figure 5-21 (c) & (d)*, displayed exactly the same RS features, *Figure 5-22*, as the specimens peened at low and room temperature, *Figure 5-17*, *Figure 5-18*, *Figure 5-21* & *Figure 5-20*. Near-surface (hill) values were of similar magnitude to the relevant values at other locations and specimens. The depth of the RS profiles extended to the depth of twins. Profile *(c)* had a drop of RS as the measurements were taken in a large harder grain, as indicated by the lower number and smaller size of twins inside that grain. The profile values increased below that grain as the next one and its neighbors were severely twinned. Profile *(d)* had a peak at 190 µm, which could be associated with a low deformed/twinned region before that location, while the specific measurement was taken in a significantly twinned grain.

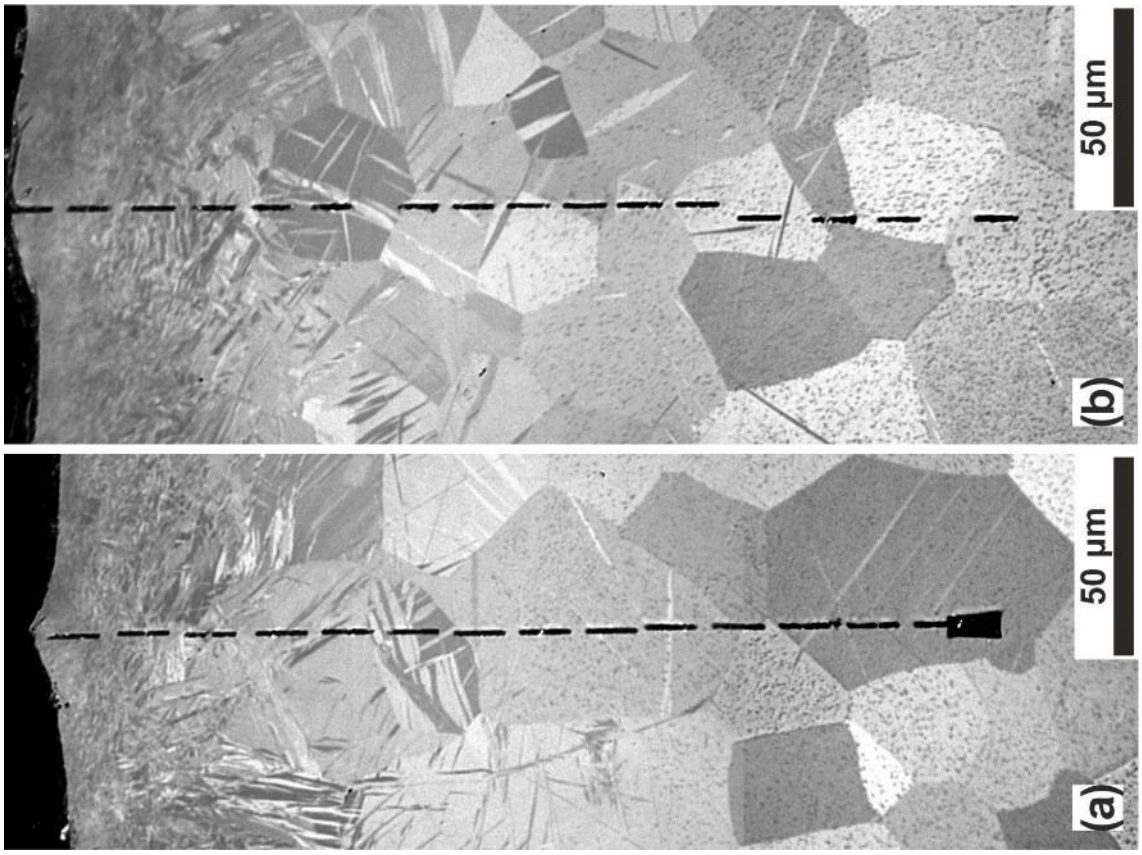

Figure 5-21 Location of residual stress measurements of CP-Ti, peened at high temperature.

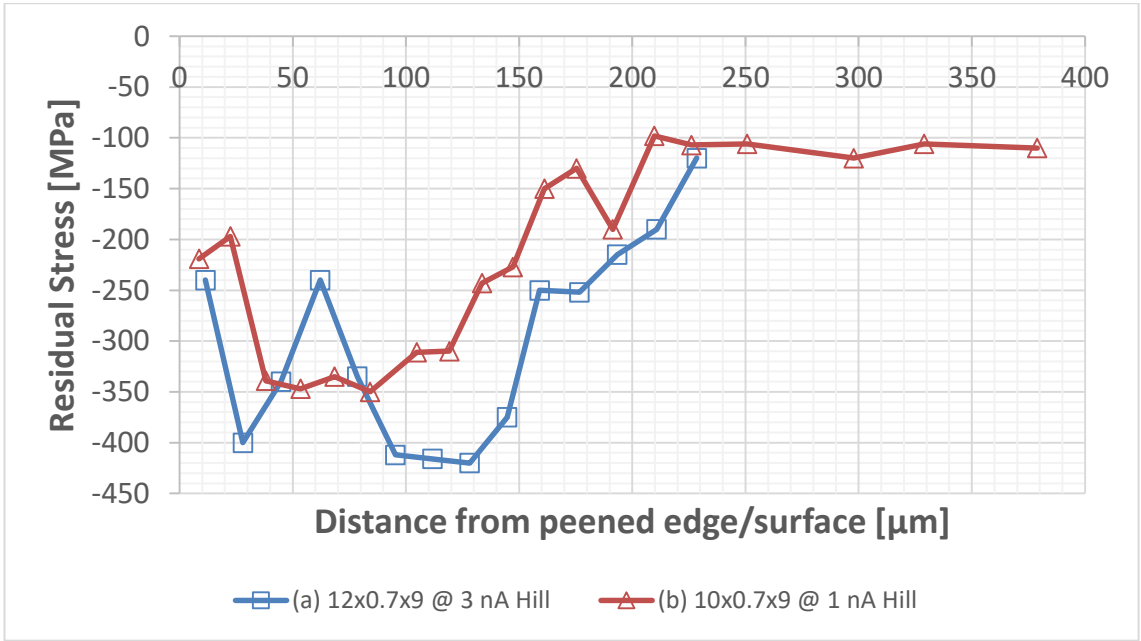

Figure 5-22 Sub-surface residual stress profile of CP-Ti, peened at high temperature.

5.3.4 Spring steel Peened @ room temperature

The FIB method was further applied on a peened SiCr spring steel (OTEVA 70) with a very fine martensitic microstructure. The interest was in coverage differences around the spring. Two locations were selected, at maximum and minimum coverage, 90 degrees around the circular, cross section of the spring with regard to each other. Slots (10x0.7x9

@ 1nA) were opened on the YSZ decorated cross section of the specimens, prepared by standard metallographic techniques and electro-polishing.

Subsurface, residual stress profiles revealed that the two locations had different peaks and depths of compressive fields, Figure 5-23. Due to the fine initial microstructure and the lack of twinning features the obtained profiles were significantly smoother and more consistent. They displayed a typical transition from low, near-surface, compressive stresses to high, sub-surface compressive peak stresses to tensile stresses at the end of the compressive part. The full coverage profile had a small value of stresses close to the surface with a large error, indicating that there could be low compression instead of tension. The ambiguity could be related to increased plastic deformation. The partial coverage profile was examined below 50 μm from the peened surface because the YSZ particles had formed a film close to the edge.

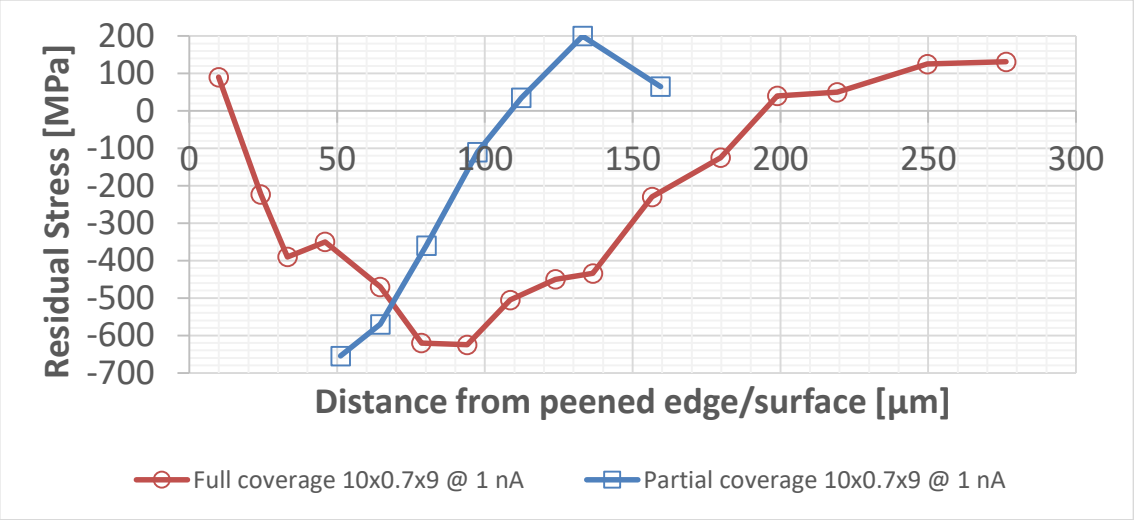

Figure 5-23 Sub-surface residual stress profile of spring steel, peened at room temperature.

5.3.5 Summary of RS measurements in peened material

The application of the FIB method for RS measurement on the peened CP-Ti proved the concept of the developed methodology. The peening process produced regions with high and low levels of plastic and in consequence elastic strains. That was evident from the waviness of the peened surface and the variation of the plastic deformation from the LOM images of CP-Ti (twin's depth and density). FIB RS results potentially captured the localized nature of RSs, as these developed by the macro-process over the specific microstructure. The results had good consistency and indicated that the depth of the compressive RS profiles extended within the deformed (twinned for CP-Ti) layer, while peak stresses occurred below the SPD layer. Profile *(d)* from the low-temperature CP-Ti specimen should be considered erroneous because it did not follow the previous rule. LOM images indicated that the near-surface stresses were higher for peaks and valleys of

the surface. Flattened areas of the surface, which could arise from a uniform surface deformation and good coverage had nearly zero compressive stresses.

The majority of the peened specimens displayed exactly the same behaviour, regardless of the peening conditions. Such a correlation could have been further improved by the employment of EBSD to identify more accurately the high and low strained regions with the image quality numbers. Generally, RSs extended deeper into the CP-Ti material with peening at elevated temperatures. The underlying mechanism should involve the reduction of yield stress with increasing temperature and the suppression of the twinning mechanism with decreasing temperatures. Lowering the yield stress, caused higher levels of plastic deformation and allowed the formation of twins in higher depths and density. A detailed examination of the peened specimens was beyond the scope of this study and work on them was concluded at that point.

5.4 Application in Ti-6Al-4V drilled plates

Typical RS profiles in machined specimens extend around 100-200 μm, depending on the process conditions. The depth of plastic deformation was significantly lower in Ti-6Al-4V drilled plates in comparison to the peened CP-Ti, thus the RS profiles were expected to be shallower. In order to increase the resolution, the slot length was reduced from 10 μm to 5 μm for most of the measurements. Only the 8 mm, drilled, plate specimens were examined, to compare and contrast with previous LOM, SEM and EBSD observations. The study was designed to investigate in more detail the near-surface stresses, which developed within the plastically deformed region, identified as the region of interest by the parent and the preliminary study. Specimens with low to intermediate levels of plastic deformation were examined even more thoroughly, so as to reveal the root cause behind the different fatigue lives of specimens with equivalent levels of plastic deformation and surface roughness.

The parent material had considerable microstructure variation, i.e. two phases, macrozones with strong rolling texture and globular grains with high size variation and a predominant rolling texture. Drilling further increased this variation, introducing a non-uniform, deformed layer with severely distorted grains and twins. Since FIB RS measurements were influenced by microstructure in CP-Ti, the effect was expected to be even greater in Ti-6Al-4V plates. Macrozones were avoided for the most part of the work, in order to correlate results with the 10 mm drilled plates in the future.

Specimens were prepared by standard metallographic techniques and electro-polishing. Due to the linear fitting, the standard deviation was ~30 MPa, but the values of the

coefficient of determination (R2) were below 0.75 for low stresses. This was a direct result of the DIC errors. Errors bars have been omitted for clarity of the profiles. EBSD scans intended to provide the orientation information to calculate elastic constants for the FEM, but that approach was dropped due to the large number of measurements and the limited availability of SEM.

The residual stress profiles measured with the FIB micromachining method displayed significant variation, even in neighboring locations around the hole in the same specimen. Plastic deformation and microstructural features were correlated with specific RS profiles, ultimately linking drilling conditions to elastic and plastic strain fields.

5.4.1 Specimen 1

One partial and one full profile were acquired for specimen *1*, *Figure 5-24*. Profile *(a)* revealed the presence of high tensile stresses at the machined surface, which extended to the depth of the twins. Then the profile changed to compressive stresses, which built up as the depth increased. Profile *(b)* was acquired within a macrozone and after an initial drop of the compressive stresses to zero values at the depth of the twins, it built up with depth with a peak at ~120 µm and depth of 200 µm. In both cases, the RS profiles appeared to extend further than the plastically deformed region, which was ~28 µm. The consistency of values and long range profile in location *(a)* indicated that the measured tensile stresses were not necessarily artifacts or errors from the milling/imaging operations.

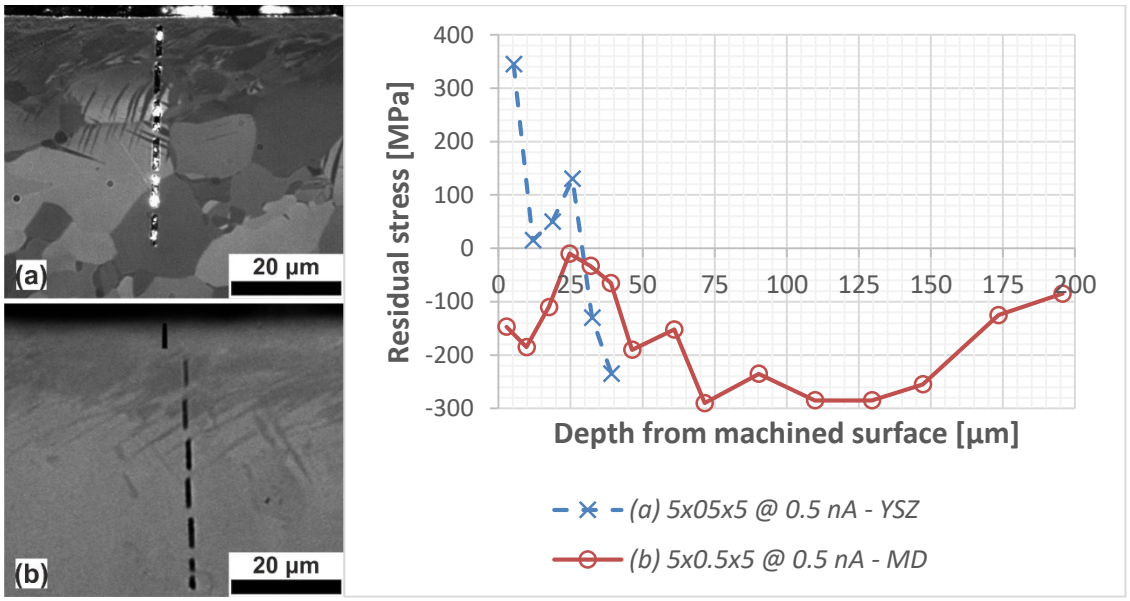

Figure 5-24 FIB RS of Specimen 1 at locations (a) & (b); a) LOM of profile (a); b) LOM of profile (b)-macrozone

5.4.2 Specimen 2

One full RS profile was acquired for specimen *2* and the milled locations were scanned with EBSD, *Figure 5-25*. Specimen 2 was one of the most heavily deformed specimens and displayed an initial build up to a tensile peak and then a transition to a compressive stress. The tensile peak was within the heavily distorted (and twinned) region, close to the machined surface (machined edge=grey dotted line). Compressive stresses built up below the deformed region with a peak at ~ 80 µm and a depth of ~225 µm. The third slot was carried out in a region with finer microstructure, at the edge of a severely distorted and twinned sub-region, while the fourth slot was carried out across a large grain. However, both of the locations were lightly stressed. Immediately below the stresses reached a peak value. The average plastic deformation depth in Specimen 2 was 60 µm, but the local value was ~52 µm, which was the borderline for the transition and increase of compressive residual stresses.

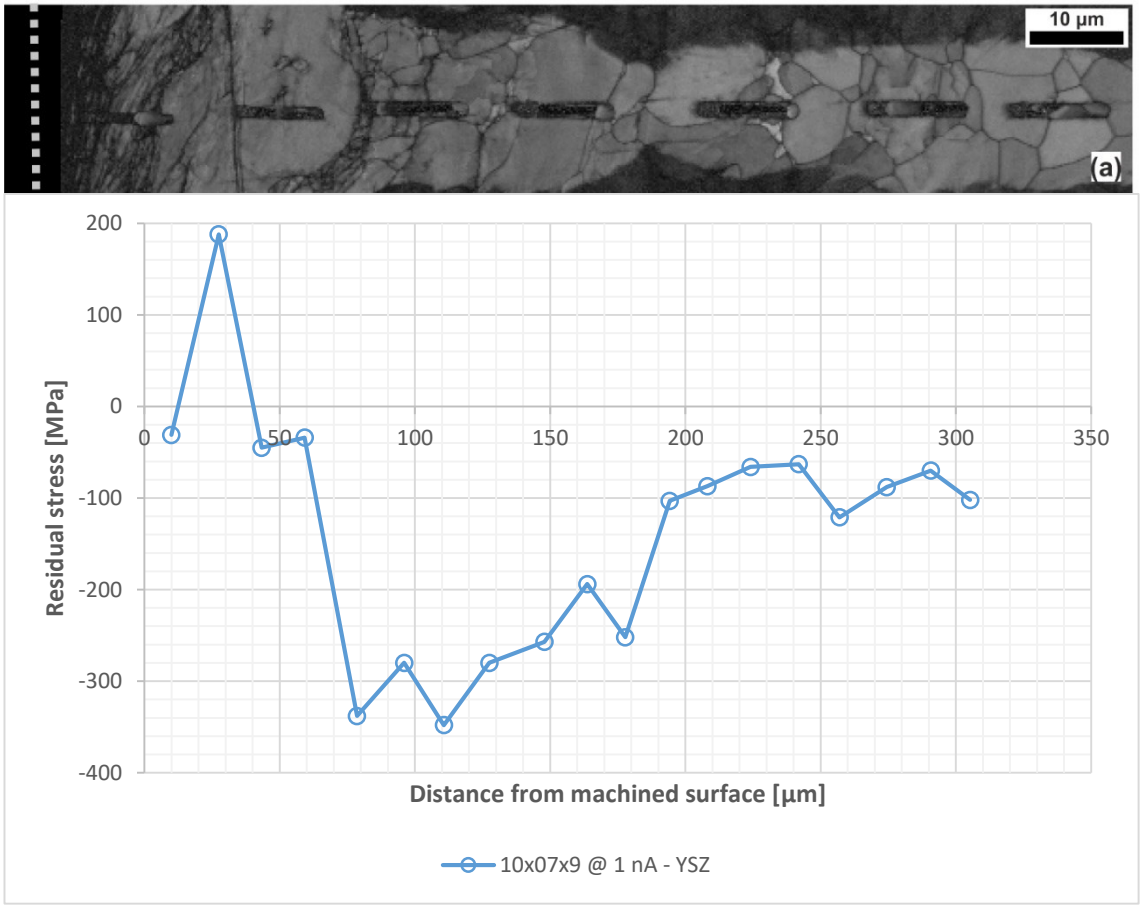

Figure 5-25 FIB RS of Specimen 2 at location (a).

5.4.3 Specimen 3

One partial profile was acquired for specimen *3*, *Figure 5-26*, which had the higher level of plastic deformation. The RS profile had an intermediate, tensile value near the machined surface and a smooth transition to low compressive stresses within the deformed region at the edge of the local, twinning sub-region, slot #5. A local,

compressive peak occurred in a distorted, but not twinned sub-region (slot #6), which dissipated below the distorted region at ~55 µm. Neighboring regions displayed twinning and shearing of microstructure at depths up to ~70 µm, which coincided with the location of slot #7. It was expected that below this slot the compressive stresses would start to build up as it was observed for Specimens 1 & 2. Local variations in microstructure could have caused the temporary compressive peak, which then dissipated towards the average deformation depth level, as a result of a global equilibrium of stresses.

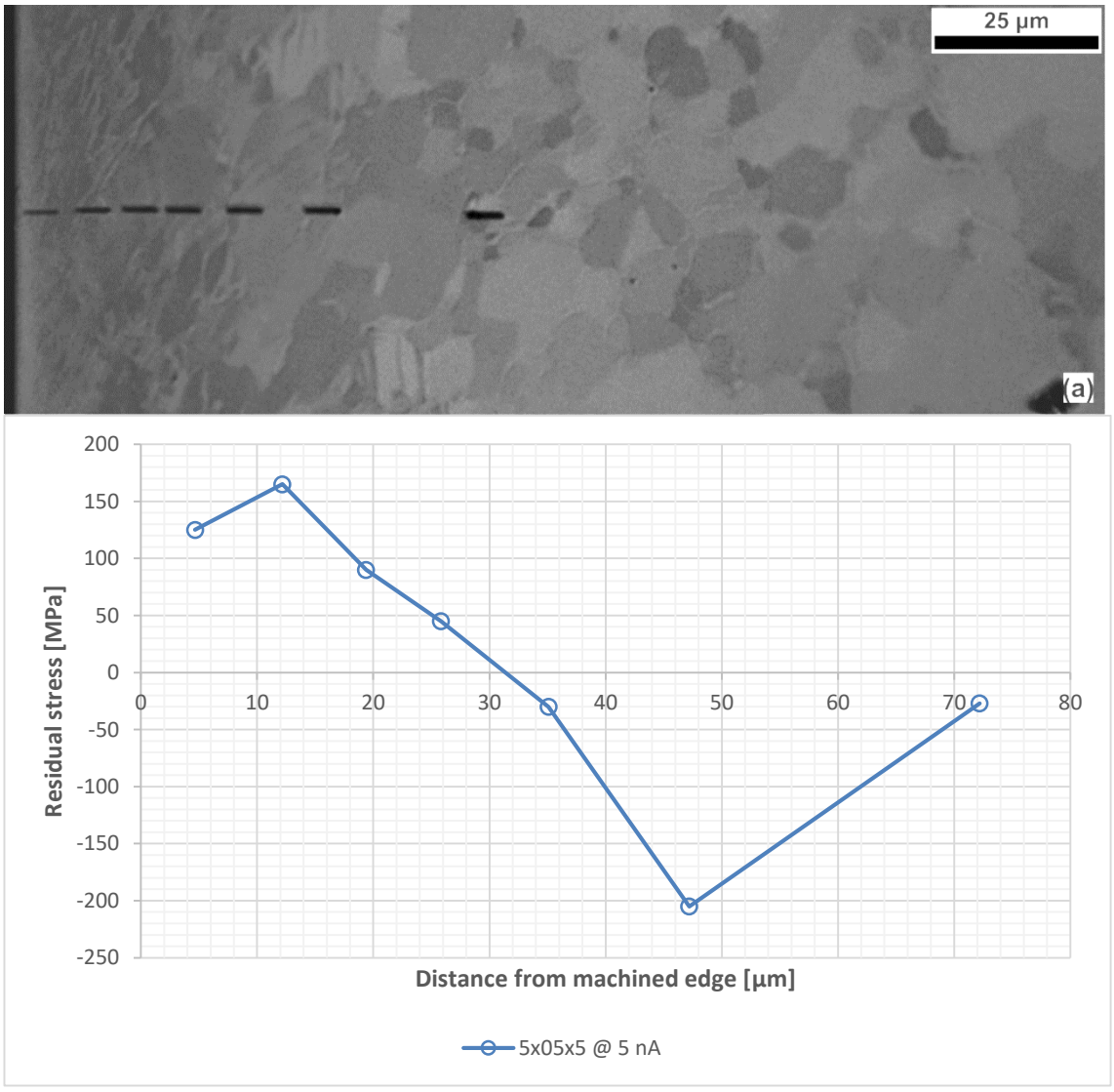

Figure 5-26 FIB RS of Specimen 3 at location (a).

5.4.4 Specimen 4

Specimen *4* was one of the most interesting specimens because it was on the borderline of low to high fatigue lives for the specimens with low levels of plastic deformation. Slots of 5 & 10 µm in length were milled to increase the resolution within the small, deformed region and acquire an average description of the elastic strain field respectively,

Figure 5-27.

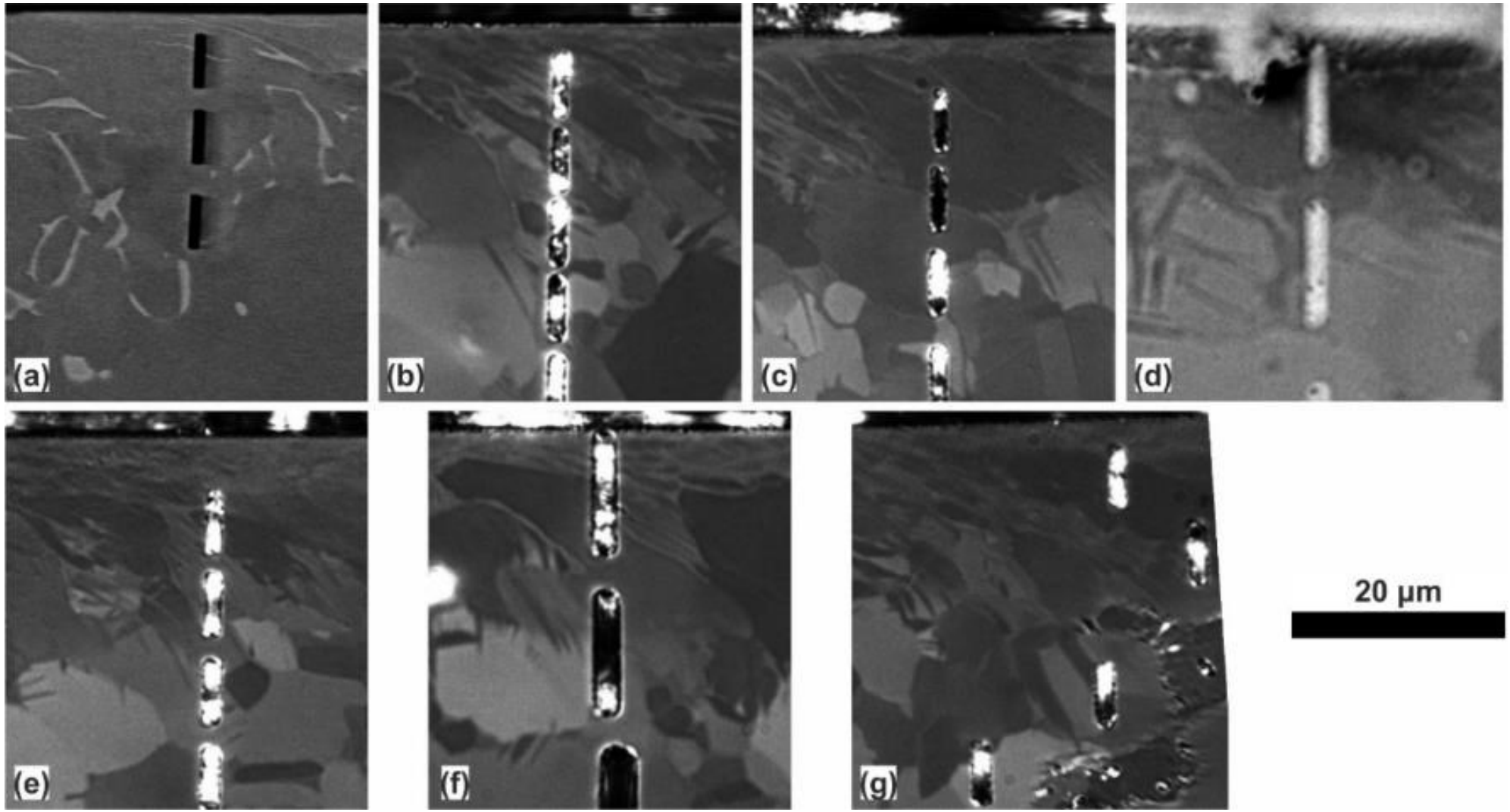

Figure 5-27 Specimen 4 FIB RS locations

Machining induced, residual stresses within the plastically strained region displayed significant variation, *Figure 5-28* (partial profiles) & *Figure 5-29* (complete profiles). Profile *(a)* captured a prolonged tensile region extending up to 20 μm from the drilling surface, with a peak at ~12 μm. Near surface tensile stresses were also captured by profile *b*, but there was an immediate, abrupt transition to high compressive stresses. The sub-region of profile *b* contained a finer microstructure and the grains were highly distorted. Slot #1 was milled between a large, un-twinned alpha grain and smaller alpha grains with evidence of twins. RSs reached a peak below the twinning region, slot #5, and completely dissipated at a depth of ~47.5 μm. No macrozones were within the milled region and the local maxima at the end of the profile could be a measurement artifact or an equilibrium tail. All partial profiles *e*, *f*, *g* and (the unidentified) *MD* started from compressive near-surface values. Profiles *MD*, *e* & *f* showed compressive peaks at depths of 16 and 20 μm within larger grains at the edge of the plastically strained layer (twinning region). Profile *g* showed a reduction of the stresses in offseted locations with high density of twins. The peak value occurred near the surface within a highly distorted, alpha grains which contained no twins. RSs then reduced at locations of large twins and appeared to increase again below the twinning region.

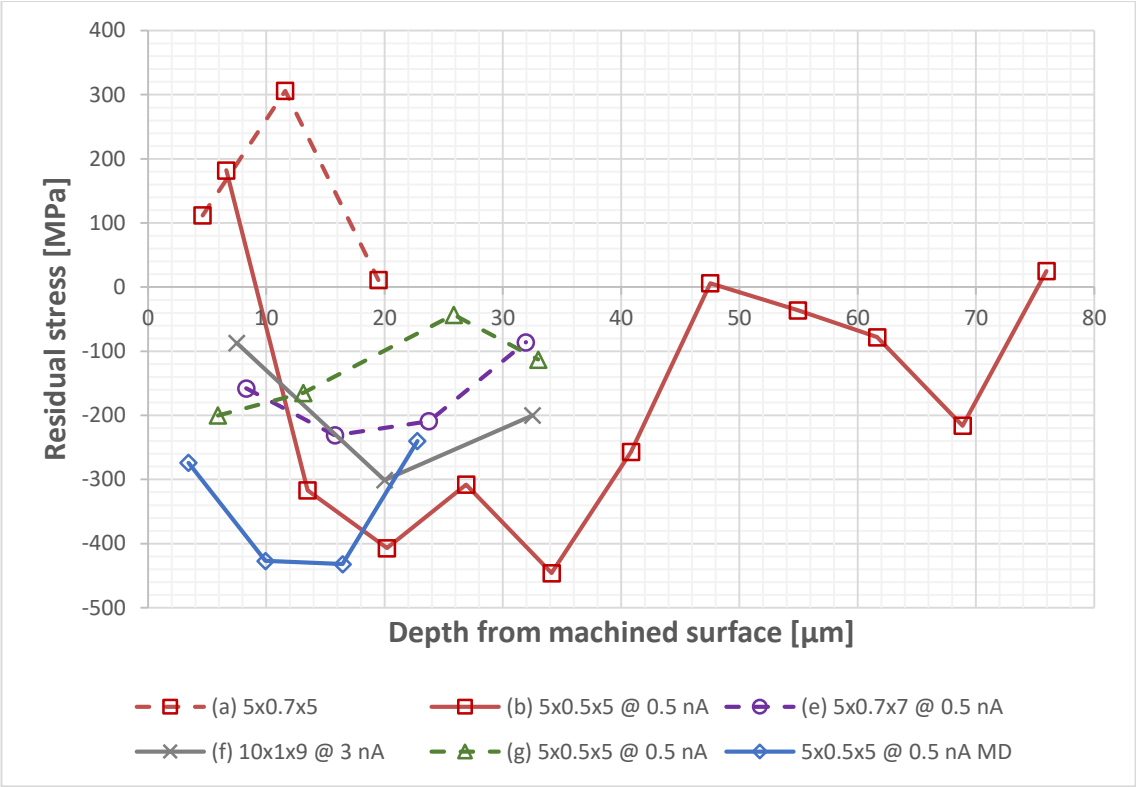

Figure 5-28 FIB RS of Specimen 4 at locations indicated by Figure 5-27 (Part I).

Full RS profiles, *Figure 5-29*, were close to the partial profiles, *Figure 5-28*. Profile *(c)* had a peak, compressive value near the machined surface and then dissipated completely at the end of the plastically deformed region, at ~23 µm. The first three slots were milled within large, highly distorted, alpha grains, with no twins. A local maximum was measured in a sub-region with small alpha (and possibly beta), globular grains, but despite the small relative error, there was not a valid, realistic explanation except to the concept of the equilibrium tail. Profile *(d)* displayed compressive, near-surface stresses and a local compressive maximum at ~23 µm, within the twinning region. The peak immediately dissipated at ~40 µm, alternating to low, tensile stresses. RS built back up to a compressive peak at ~90 µm and then dissipated towards ~120 µm. Only the first two slots were milled within the deformed region and the resolution was limited due to the size of the slots. Overall, profiles *(b), (c) & (d)* showed a smooth transition of values and the atypical, observed shapes should not be disregarded.

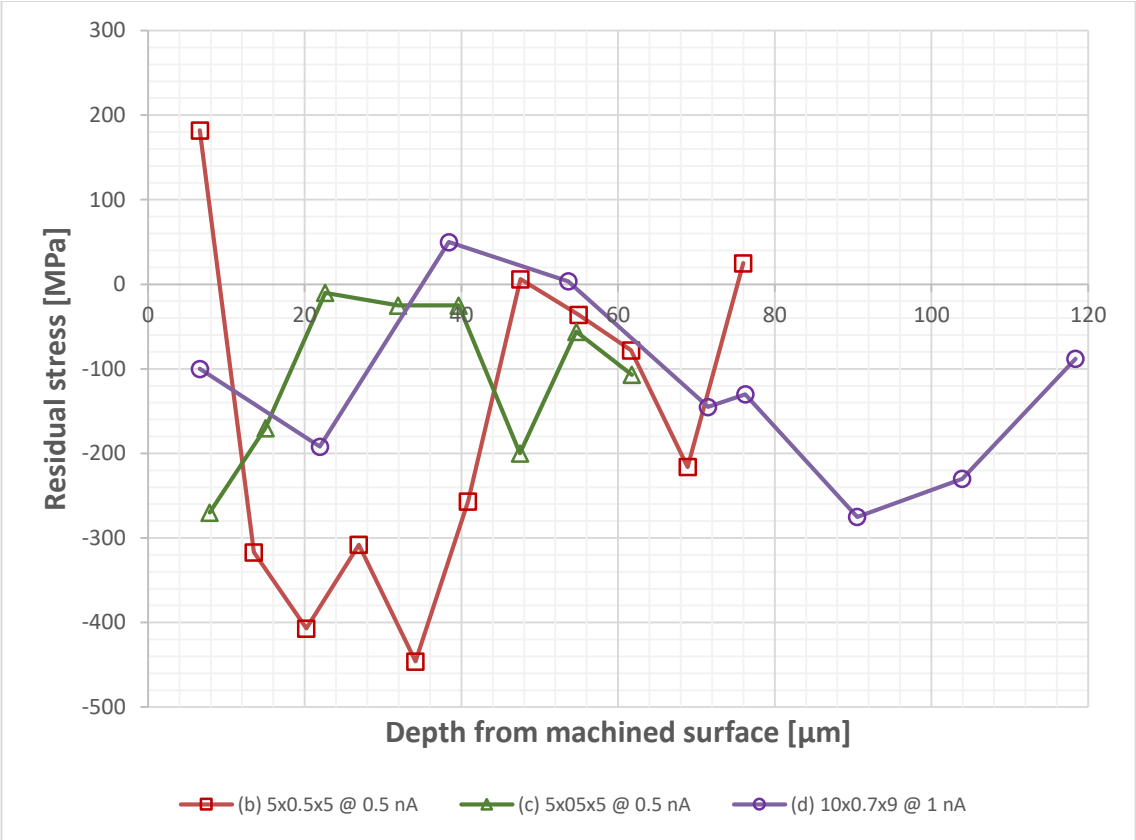

Figure 5-29 FIB RS of Specimen 4 at locations indicated by Figure 5-27 (Part II)

5.4.5 Specimen 5

Specimen *5* was one of the specimens with the highest fatigue life and the lowest level of plastic deformation. Complete RS profiles were acquired for random locations indicated in *Figure 5-30*. The local microstructure was different in each of the previous locations with regard to the twinning density, distortion of the alpha grains and size of the alpha grains.

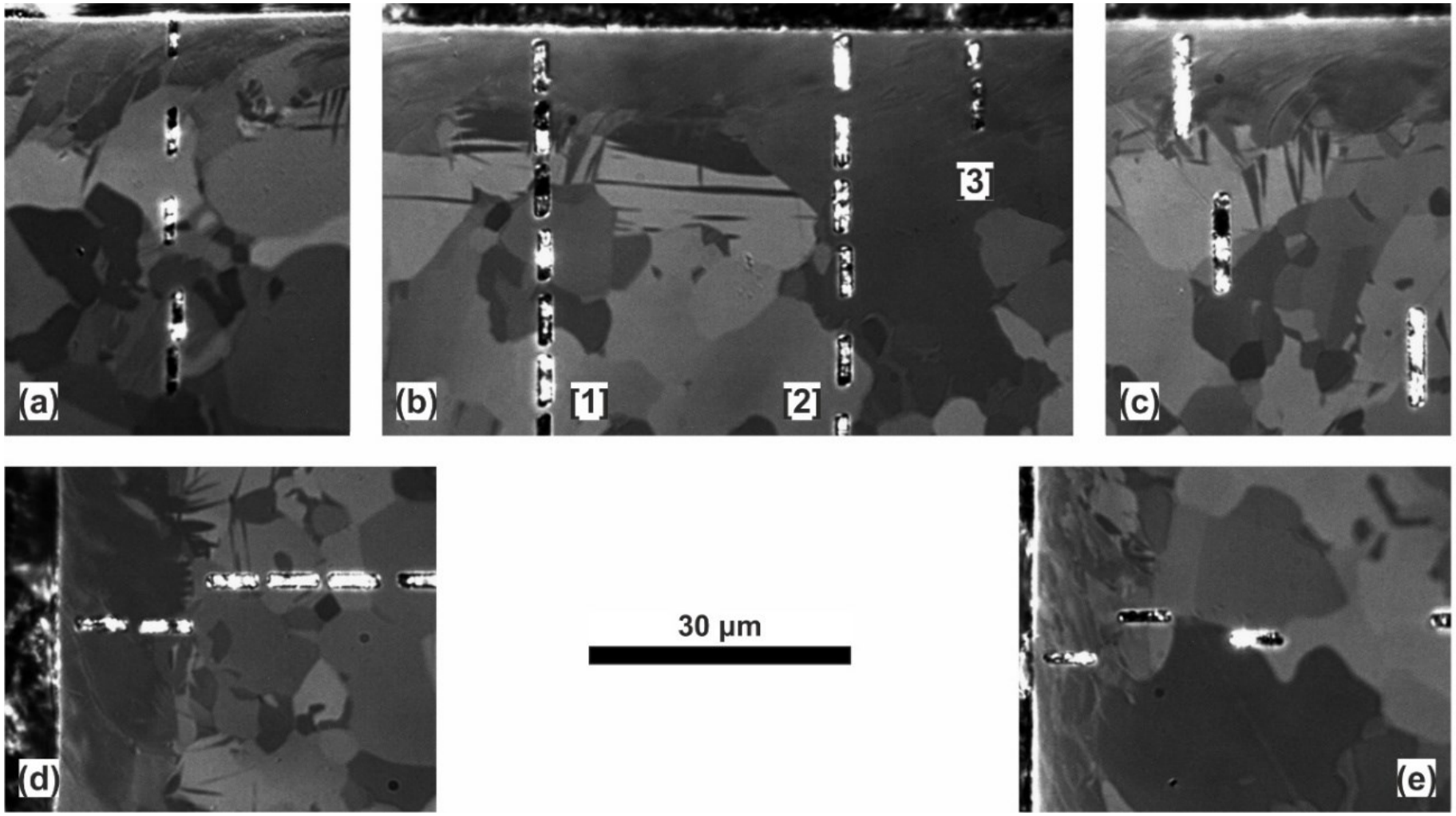

Figure 5-30 Specimen 5 FIB RS locations.

Typical machining RS profiles were detected in three locations, *Figure 5-31*. Profile *(a)* displayed an intermediate, tensile stress near the drilled surface within a large alpha grain (slot #2; note: imaging problem at slot #1). The alpha grain was partially distorted at the top and did not contain any twins. Above that grain, the microstructure was finer and contained distorted grains and twins. RSs transitioned to compressive stresses at the bottom of the grain and built up to a peak value at ~64 µm, which diminished at ~94 µm. Profile *(b)-[1]* was a typical compressive RS profile for machining. Zero stresses were measured in the immediate, machined surface area, which contained a large, distorted, un-twinned grain. Stresses increased with depth, within the deformed and highly twinned region. A peak occurred below the average level of twinning, at ~25 µm. Peak stresses appeared to reduce to background values at ~60 µm from the drilled surface, but no additional measurements were available to draw a safe conclusion. The microstructure at the milled locations appeared to have traces of macrozones at the top and end of the profile. Profile *(e)* had also zero stresses at the immediate drilling surface, which built up to a peak value at ~26 µm, similar to profile *(b)-[1]*. At the machined edge, the microstructure was heavily twinned and finer compared to locations below the deformed layer. Thereafter, stresses reduced with depth and RSs reached almost background values at ~85 µm. However, RSs did not completely dissipate and after 65 µm the values could be erroneous, despite the relatively small, measurement errors.

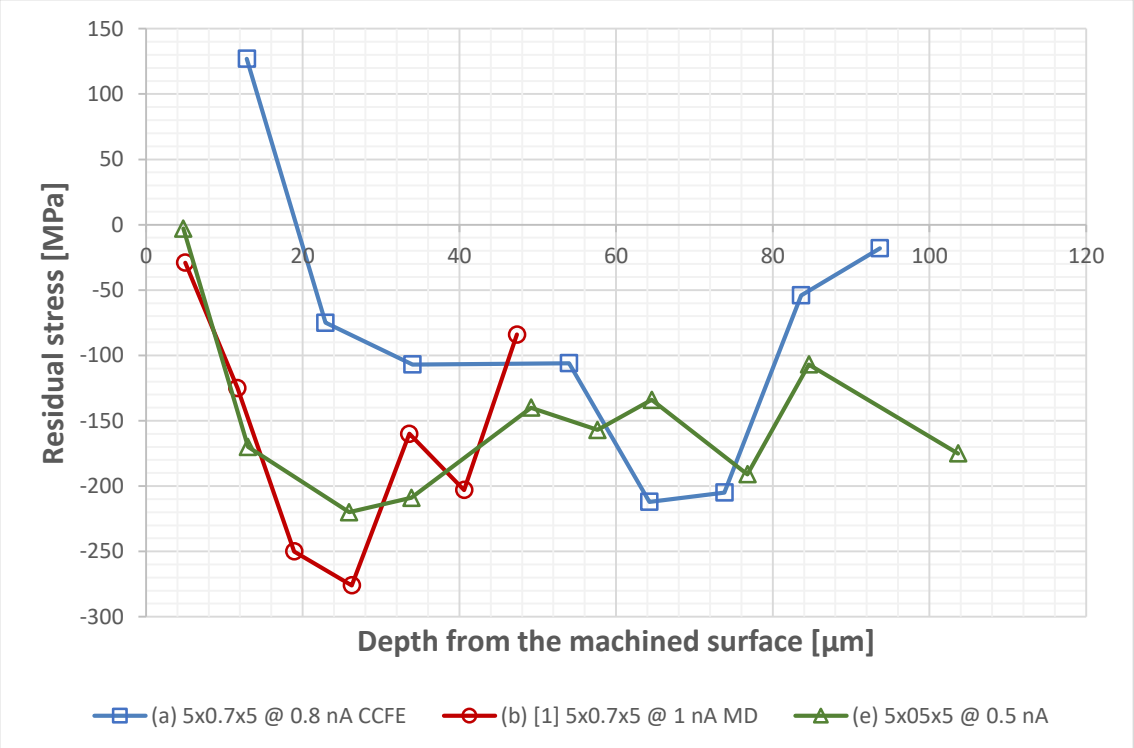

Figure 5-31 FIB RS of Specimen 5 at locations indicated by Figure 5-30 (Part I)

A set of non-typical RS profiles or profiles with high variation were acquired in three other locations, *Figure 5-32*. Despite that, the succession of values was smooth and some microstructural features could be the root cause for the observed discrepancies. Profile *(b)-[2]* had low near-surface stresses at a location of a large, hard alpha grain, with a low density of small twins. Stresses increased at slot #2 within the same alpha grain, but with no twins around. At slot #3, at the average depth of the twinning region, the stresses reduced for no apparent reason. The influence from a neighboring, twinned alpha grain was debatable. A primary peak occurred at ~64 μm and gradually reduced to the background values at ~100 μm. Then a second peak emerged at ~124 μm and faded towards ~145 μm. The global maximum was the first one and the second, local maxima could not be microstructurally explained and was regarded as an equilibrium tail. Profile *(c)* had an intermediate, compressive near surface value at a highly twinned and distorted region. The profile reduced towards the edge of the twinned zone and a peak emerged at ~56 μm. At 72 μm the peak had vanished and the stresses were stabilized at a value higher (double in magnitude) than the bulk one. The associated error with low stress values could further reduce values, but it was most likely that last part of the profile was also an equilibrium tail, which should fade further way from the machined edge. Profile *(d)* displayed high, near surface, compressive stresses at large, distorted, alpha grains with low twin density. Then stresses reduced abruptly to zero below the twinning zone and built up to a global maximum at ~28 μm. The reduction occurred at a grain next to which there was a twinned grain, similar to profile *(b)-[2]*. Compressive stresses completely dissipated at ~42 μm and built back up towards a local maximum at 64 μm. Eventually, the stresses reduced to low values towards 80 μm, but it could be possible that the profile had another prolonged compressive tail, similar to profile *(c)*. Although the second set of profiles were atypical and had abrupt transitions and secondary peaks, there was some consistency between microstructural and RS features within the deformed regions and between full-length RS profiles.

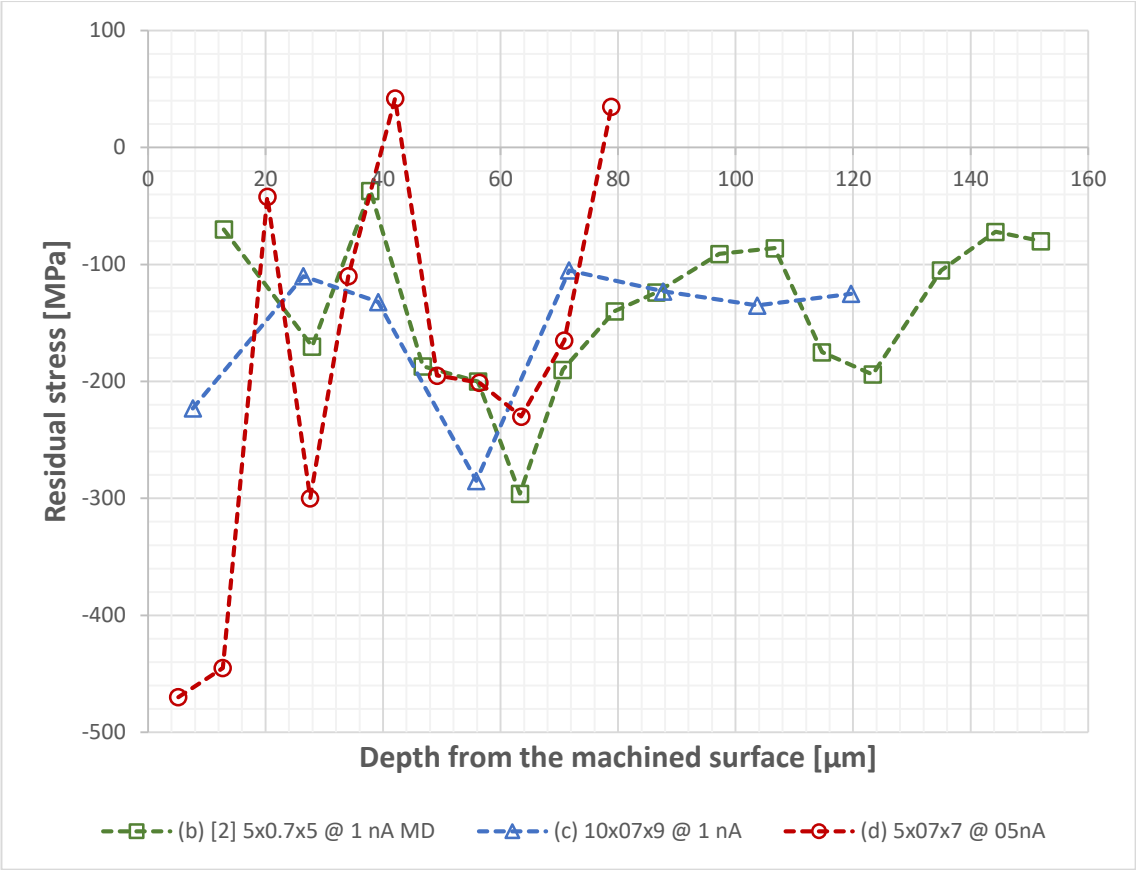

Figure 5-32 FIB RS of Specimen 5 at locations indicated by Figure 5-30 (Part II)

5.4.6 Specimen 6

Specimen *6* had an intermediate level of plastic deformation and a low fatigue life. A number of partial and full-length RS profiles, *Figure 5-34 & Figure 5-35*, were acquired at different locations with distinct microstructural features, *Figure 5-33*.

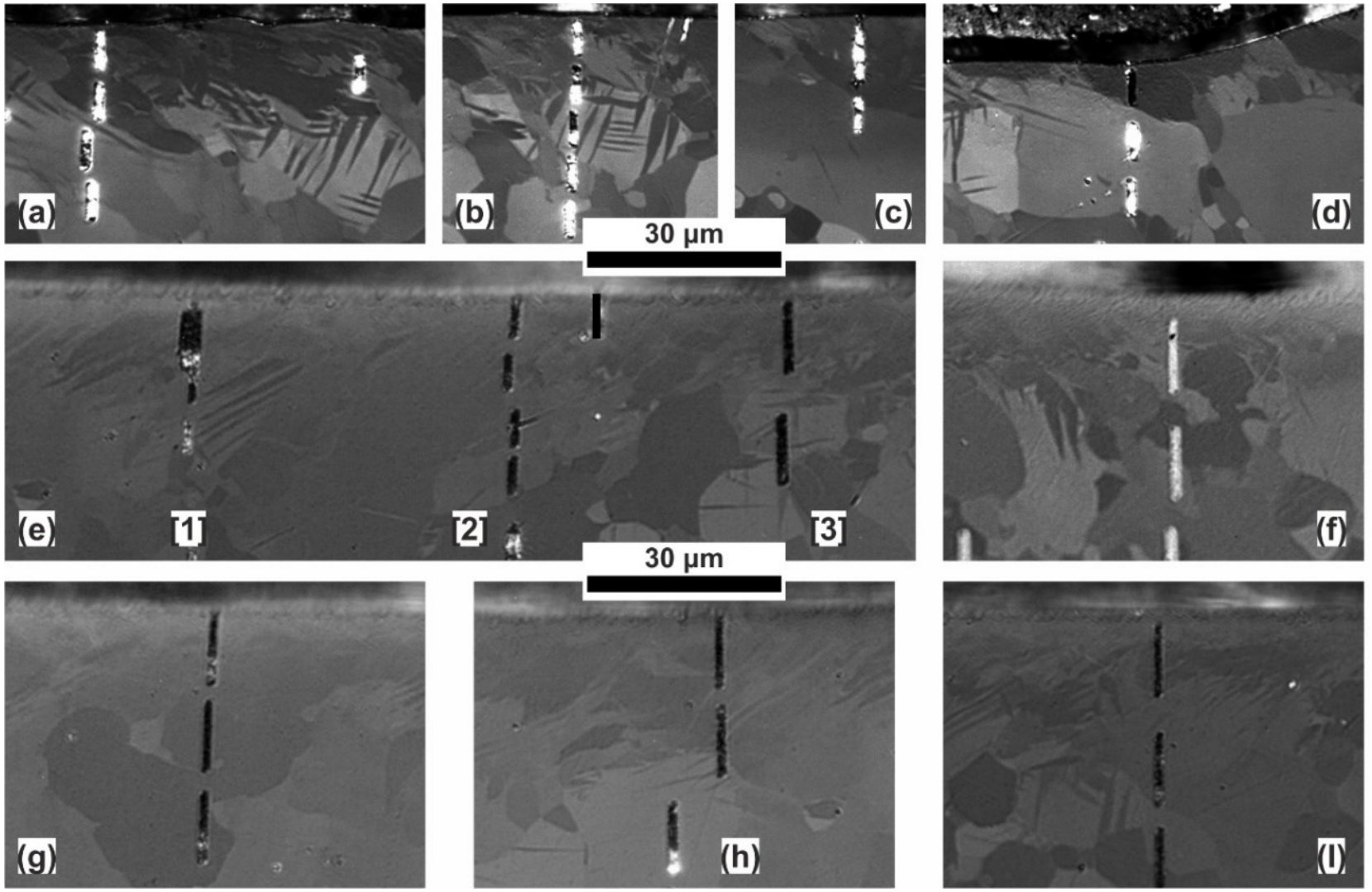

Figure 5-33 Specimen 6 FIB RS locations

Profile *(a)* had a typical shape with an intermediate, compressive value near the machined surface and an immediate peak at ~13 μm, which progressively faded towards 30 μm. The first four slots were milled within the deformed layer. The peak, slot #2, occurred within a large, highly distorted, alpha grain. Slots #3 & #4 were milled at a region with a low density of twins, where stresses reduced towards the edge of twinning zone. Profile *b* had a similar shape to profile *a* with the difference that peak stresses in *b* were lower. The peak occurred within a large, heavily twinned, alpha grain, slot #3. Stresses reduced towards the edge of the twinning zone, slot #4, and temporarily increased at slot #5 before gradually dissipating with depth. Profile *c* started from the same near surface, compressive value to profiles *a & b*. Stresses appeared to reduce within a hard, large, alpha grain with a low density of twins and the main peak occurred at ~52 μm. Note that there was an invalid measurement for slot #2, due to imaging issues and the overall resolution was limited by the slot length. Profile *e-[1]* had a high, near surface, compressive value at a severely twinned region, slot #1. Stresses reduced to zero values at slot #2, at the edge of twins in the middle of the deformed region. However, at the next slot, the stress increased despite the fact that there were identical twin features, though at a larger depth. Profile *e-[2]* had a prolonged tensile part below the machined surface, in a region with a very low density of twins. Locally, the microstructure had a large hard, alpha grain, distorted at the top, neighboring other large grains, between regions of intense twinning. Profile *f* had a similar shape to profile *e-[2]*, transitioning from a low, near-surface, compressive stress to a low tensile value at ~25 μm to a compressive value at ~64 μm. The initial compressive stress occurred within the deformed region. The transition to tensile and then to compressive stresses occurred in an undeformed, un-twinned region, within the average depth of the plastically deformed layer. It could be assumed that the incompatibility of plastic strain between regions of large and small grains, with respect to their individual deformation systems, produced tensile stress in undeformed sub-regions within the average depth of the machining affected layer.

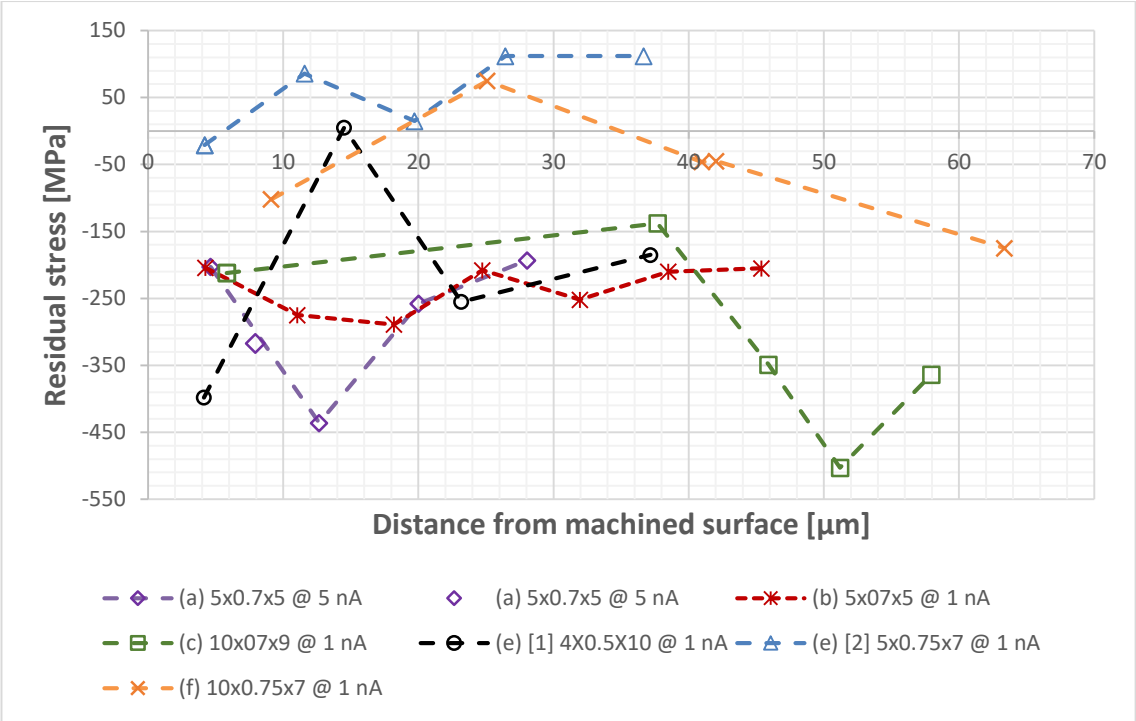

Figure 5-34 FIB RS of Specimen 6 at locations indicated by Figure 5-33 (Part I)

Full RS profiles had significant variation in terms of peak location and depth, *Figure 5-35*. Profile *d* had an intermediate, near surface, compressive stress, which progressively transitioned to a small, tensile peak below the deformed region. Then stresses transitioned to a low compressive peak at ~50 µm and dissipated at ~80 µm. The machined surface had a local defect and the level of deformation was minimum compared to the neighboring regions. Slot #1 was milled in an un-twinned, alpha grain, while slots #2 & #3 were milled in another large, alpha grain with no twins or apparent distortion at the specific locations. Profile *g-[1]* was similar to profile *d* in shape, but the near-surface compressive value was lower, the peak location was much deeper (at ~115 µm) and the depth of the profile reached ~156 µm. The apparent level of plastic deformation was lower compared to the neighboring sub-regions. Large, alpha grains were located close to the machined edge and they were distorted only at the top, while they did not contain any twins. Slots #1 & #2 were milled within the deformed layer, while slot #3 was milled immediately below it. Stresses reduced within the deformed region and built up to a global maximum below that location. A partial profile, *g-[2]*, at the end of the stressed region of profile *g-[1]*, offseted by 25 µm, displayed tensile values and the depth of the compressive part should be reduced by as much as 50 µm. The reason for that variation could be the higher level of plastic deformation observed at the machined layer of the offseted location, where the grains were highly distorted and twinned to a larger depth. Profile *h* was a textbook compressive RS profile with a small, equilibrium tensile part and a

compressive tail. The peak occurred at ~89 µm and was built within the deformed layer (30 µm), while the main, compressive part dissipated by ~130 µm. Profile *i* had similar features to profile *h*, with exception of the peak location (~53 µm) and the apparent depth of the primary compression part (110 µm). The plastically deformed layer extended up to 25 µm, to a large, alpha grain with low density and length of twins at the top. Neighboring sub-regions had twins which extended up to 35 µm, but no twins were in the immediate vicinity of the slots.

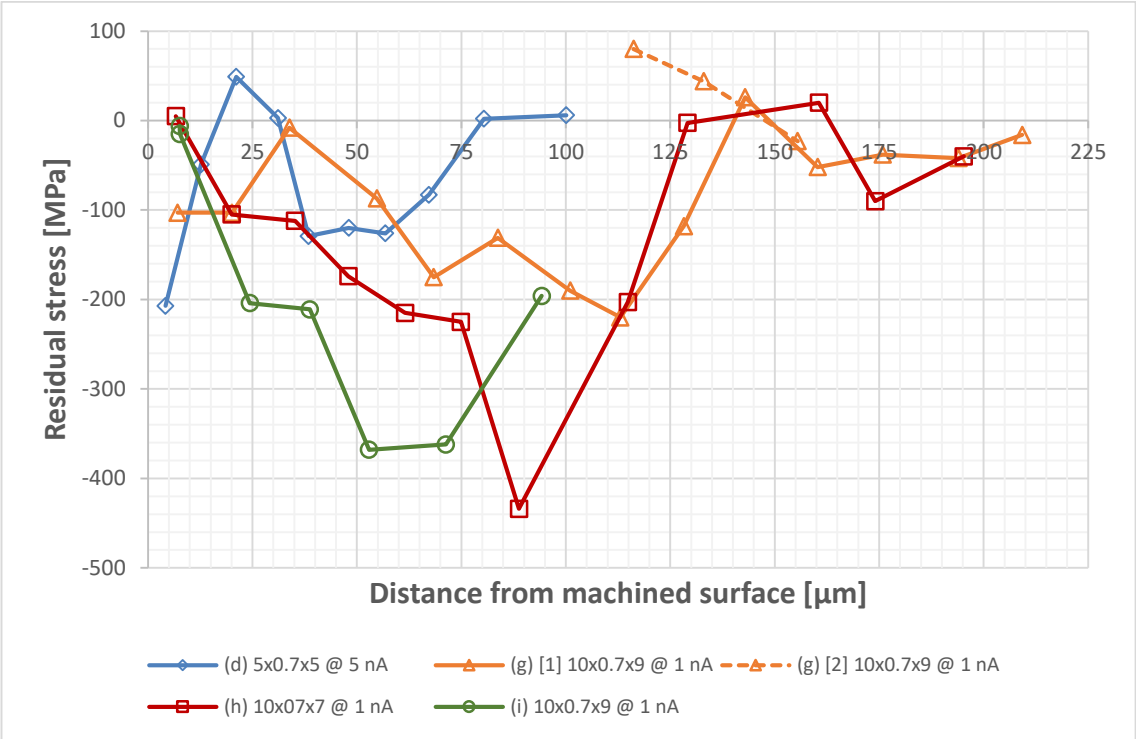

Figure 5-35 FIB RS of Specimen 6 at locations indicated by Figure 5-33 (Part II)

5.4.7 Specimen 7

One complete and one partial profile were acquired for specimen *7*, *Figure 5-36 & Figure 5-37*. RSs close to the machined surface were nearly zero and built up within the deformed region (~39 µm) to a peak at ~92 µm, which rapidly diminished towards ~150 µm. The sharp peak occurred at the end of a large alpha grain, neighboring many smaller grains, including beta phase grains, *Figure 5-36* b. However, nothing indicated that the grain variation could lead to a local stress concentration. Strain incompatibility should exist, but the overall rolling texture should diminish the gradients. The reduction of the stress profile occurred in a region with traces of macrozones, *Figure 5-36* (c) slots #7, #8 & #9). RSs increased below 200 µm to ~175 MPa, as the slots were milled within regions with globular grains (slots #10 & #11). A second, partial profile, offseted from the full profile by 60 µm, displayed lower stresses and the expected reduction of stresses after 200 µm. Stresses in the partial profile were still relatively high between 100 – 200 µm (compared

to bulk values), with the first two slots being milled again in traces of macrozones. It could be assumed that the succession of macrozones and globular grains could create some localized stress rise, originated from the previous thermo-mechanical, manufacturing processes. Thus the stresses could have increased to equilibrate the drop and eventually would fade towards the bulk region of the material. The superposition of a compressive tail on the layered microstructure of macrozones and globular grains (observed in previous measurements) could also contribute to the observed shapes.

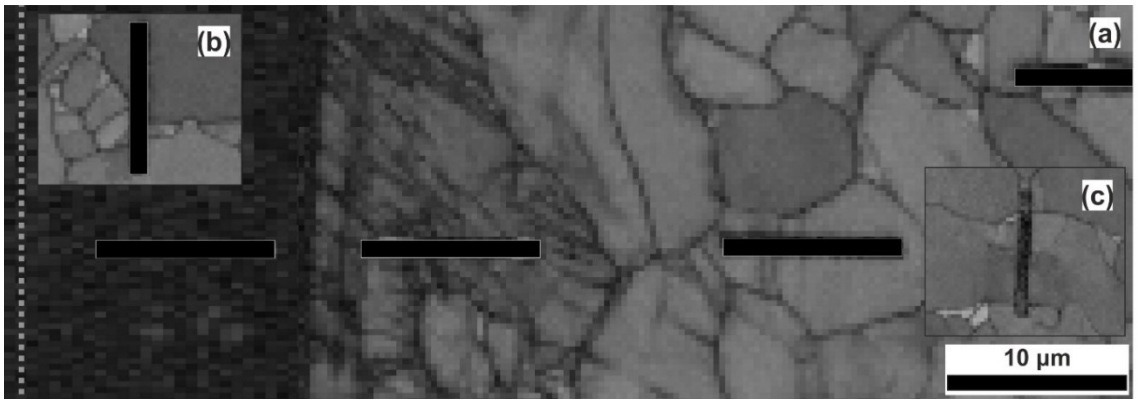

Figure 5-36 BC map of Specimen 7 at location (a); b) Sot #6; c) Slot #8

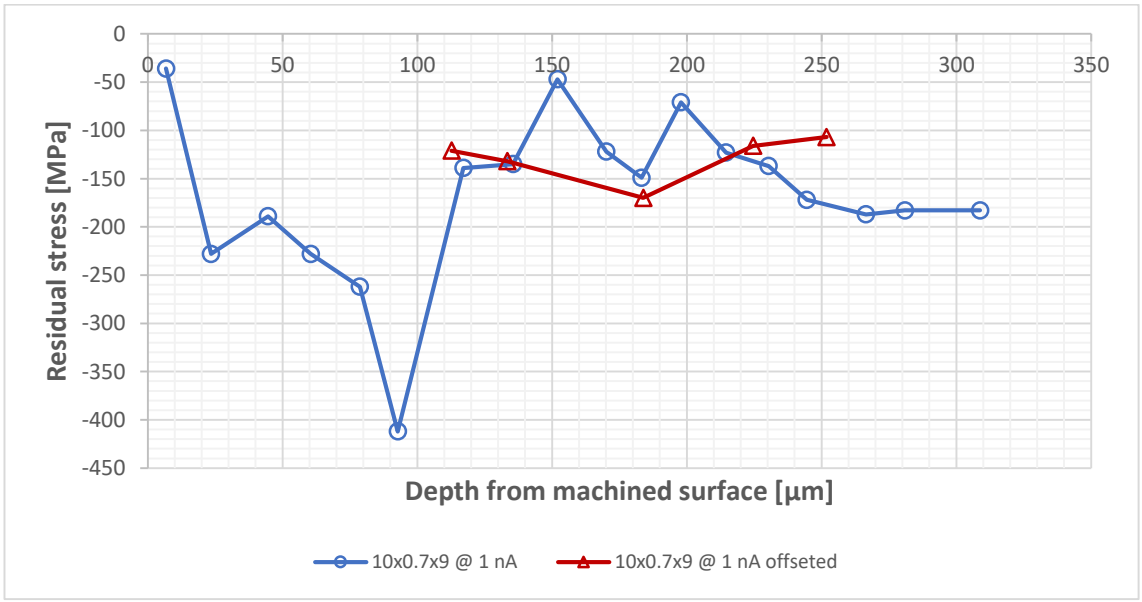

Figure 5-37 FIB RS of Specimen 7 at location (a)

5.4.8 Specimen 8

Specimen *8* was examined more thoroughly because it was one of the specimens with low levels of deformation and high fatigue life. A number of (random) locations were examined, *Figure 5-38*; locations *a – e* were taken from a region of 90 µm in width. Different slot lengths were employed trying to build some confidence on the measured values, due to the small level of deformation. The residual stress profiles were grouped in two sets, *Figure 5-39 & Figure 5-40*, despite their considerable variation.

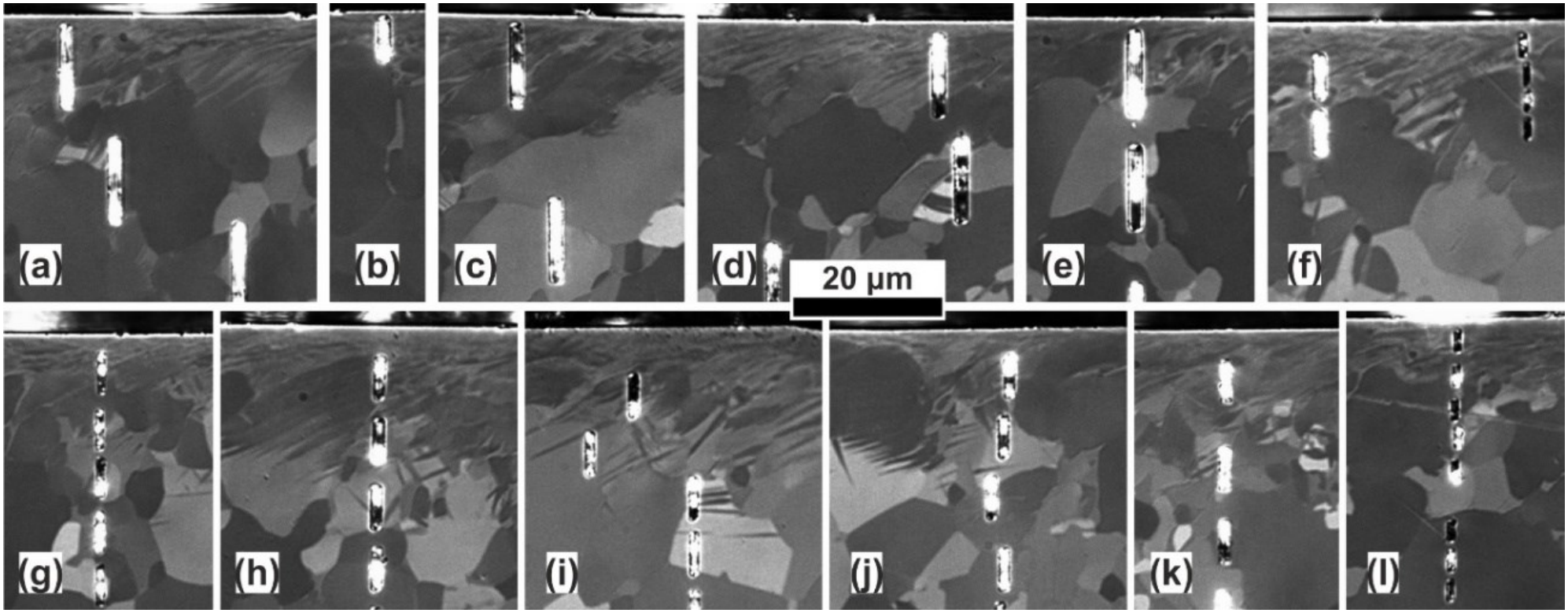

Figure 5-38 Specimen 8 FIB RS locations

Profiles *(a)* & *(d)* displayed a peak compressive value at the machined surface, which dissipated to a local minimum below the twinned region. Profile *(d)* had a higher local minimum than *(a)*, which could be correlated to the non-twinned, but severely distorted grains. Profile *(c)* had also a peak compressive stress value at the machined surface, which was completely diminished at ~50 µm. No severe twinning was observed in the region of the profile *(c)* and the first two slots were milled within highly distorted grain regions. The region of profile *(e)* was similar to profile *(c)*, however, the RS measurements were more closely to *(a)* & *(d)*. Higher resolution, profile *(h)* displayed a peak compressive value at the machined surface, which was succeeded by a small tensile peak exactly at the end of twin region. Then compressive stresses built up again, before dissipating at ~100 µm. A local compressive maximum occurred at ~65 µm, where large grains and possibly macrozones were present.

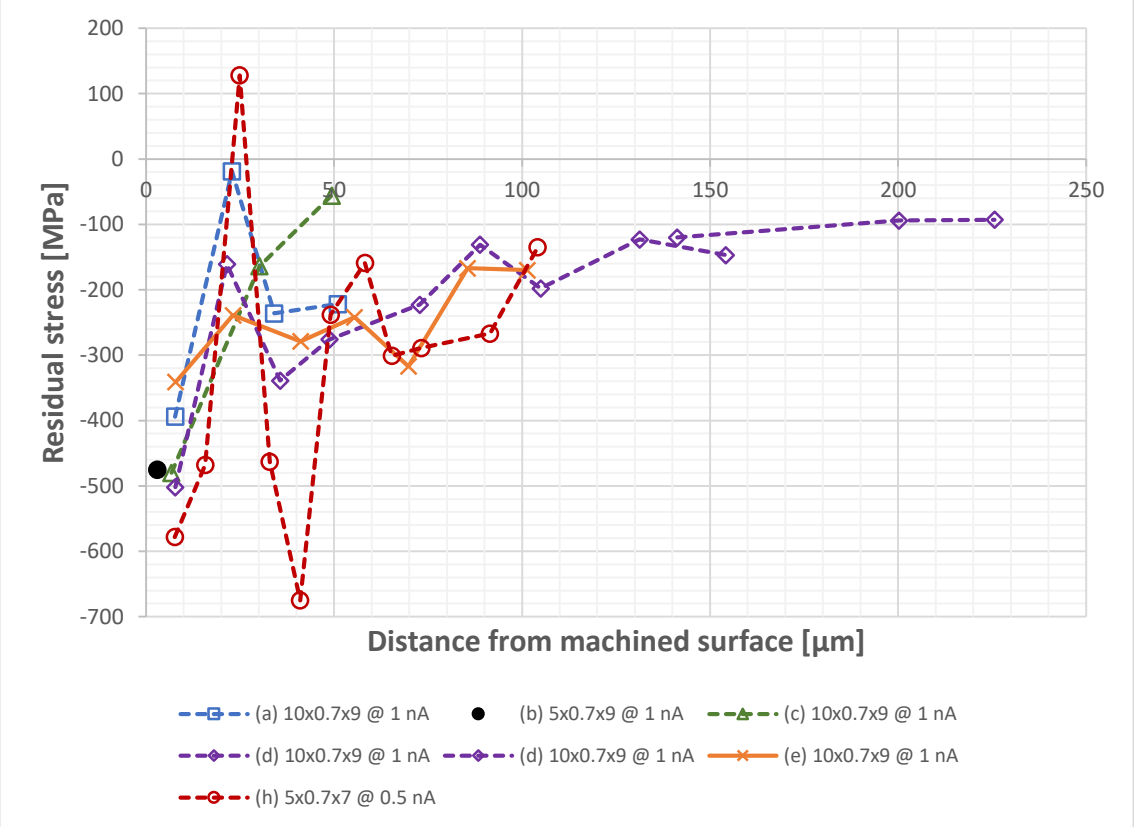

Figure 5-39 FIB RS of Specimen 8 at locations indicated by Figure 5-38 (Part I).

In contrast to the first set, the second set displayed a peak stress away from the machined surface. The twin density and deformation was evidently higher than the first set, with the exception of series *(l)*. Profile *(g)* had a high compressive value close to the machined surface, which dissipated in a region with low twin density. A local maximum occurred at ~32 µm and a local minimum at ~52 µm, while the peak value was located at ~71 µm and the profile extended to 83 µm. Series *(i)* had a nearly zero near surface stress and the

profile built up to a peak compressive value at ~23 µm within the highly twinned region. A local minimum at ~44 µm occured within a large alpha grain. Profile *(j)* started from a high, near surface, compressive value, which after a local minimum at ~32 µm continue to build up towards 60 µm. The region was not severely deformed or twinned. Close to the surface, there was evidence of a finer, parent microstructure. The local minima could not be correlated with any feature. Profile *(k)* was carried out in a highly twinned region and the zero, near-surface stresses increased to a local maximum at an alpha grain with high twin density. The profile had a peak at ~58 µm and extended beyond 85 µm. Series *(l)* was milled in a region with a low level of deformation, no twins, and reduced grain distortion. The resulting residual stress profile had a peak value at ~31 µm, which was abruptly faded at 36 µm. Surface results were not available.

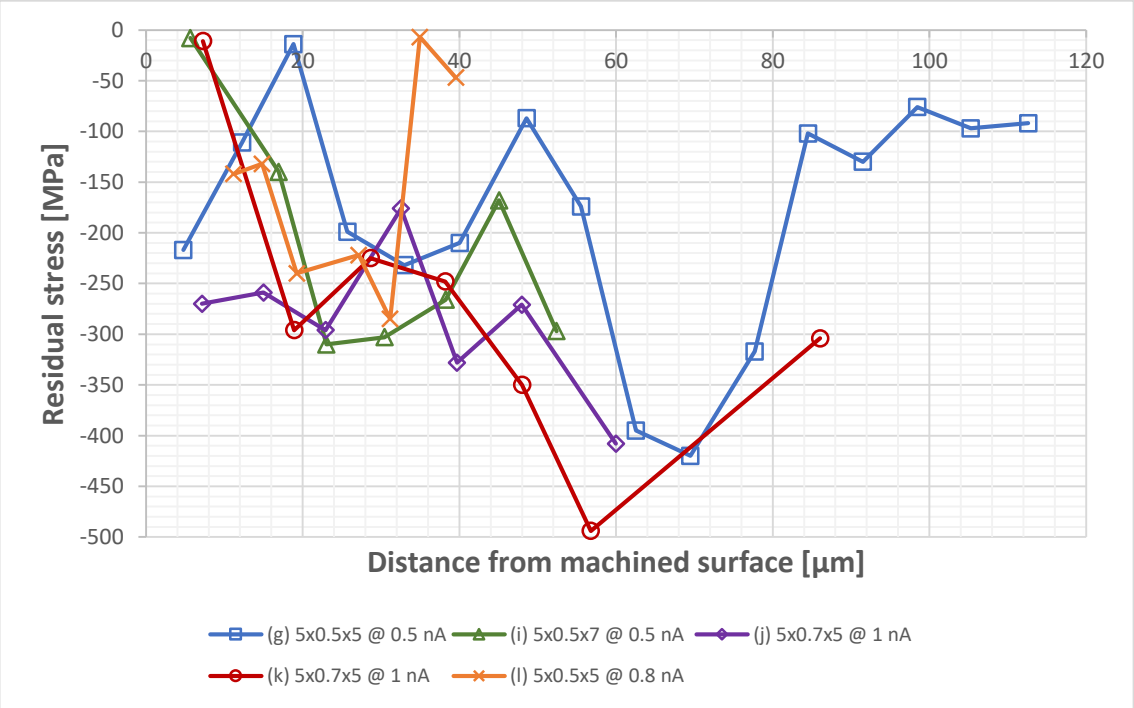

Figure 5-40 FIB RS of Specimen 8 at locations indicated by Figure 5-38 (Part II).

5.4.9 Summary of RS in drilled specimens

There was significant variation in the measured residual stresses. Part of the problem was the milling and imaging quality. The equipment at Sorby Center was old and heavily used in the past for the preparation of TEM samples, which reduced its sharpness during milling. Imaging was an ongoing problem and the employed, I-beam mode was damaging the surface decoration features, especially in high magnifications. As a result, both the equipment and the operator were not performing always to the same, high standard. Some of the features of the RS profiles could be artifacts of the milling and/or imaging or could have been exaggerated by them. Despite that, only a limited number of clearly erroneous

experiments were discarded. The opposite was true for the equipment at CCFE, although the availability and associated costs rendered it inappropriate for an extended study.

The overall, mesoscale, RS profiles appeared to capture the machining-induced effects, verified qualitatively by and potentially linked to the local microstructural features. Published RS profiles have displayed similar depth variations with volume averaging methods [98] - [112], but not along or across the machined surface. Values were different between the four groups of machining conditions, the specimens of the same group and even the locations in the same specimen. A common trend was that higher levels of plastic deformation were introducing deeper residual stress fields within undeformed regions, *Figure 5-41*. All stress profiles were extending about 3-4 times beyond the depth of the deformed region. Even if image and milling quality were not always very high, with an immediate effect on stresses, the overall shape of profile and their sign would not change; only their magnitude by a small fraction.

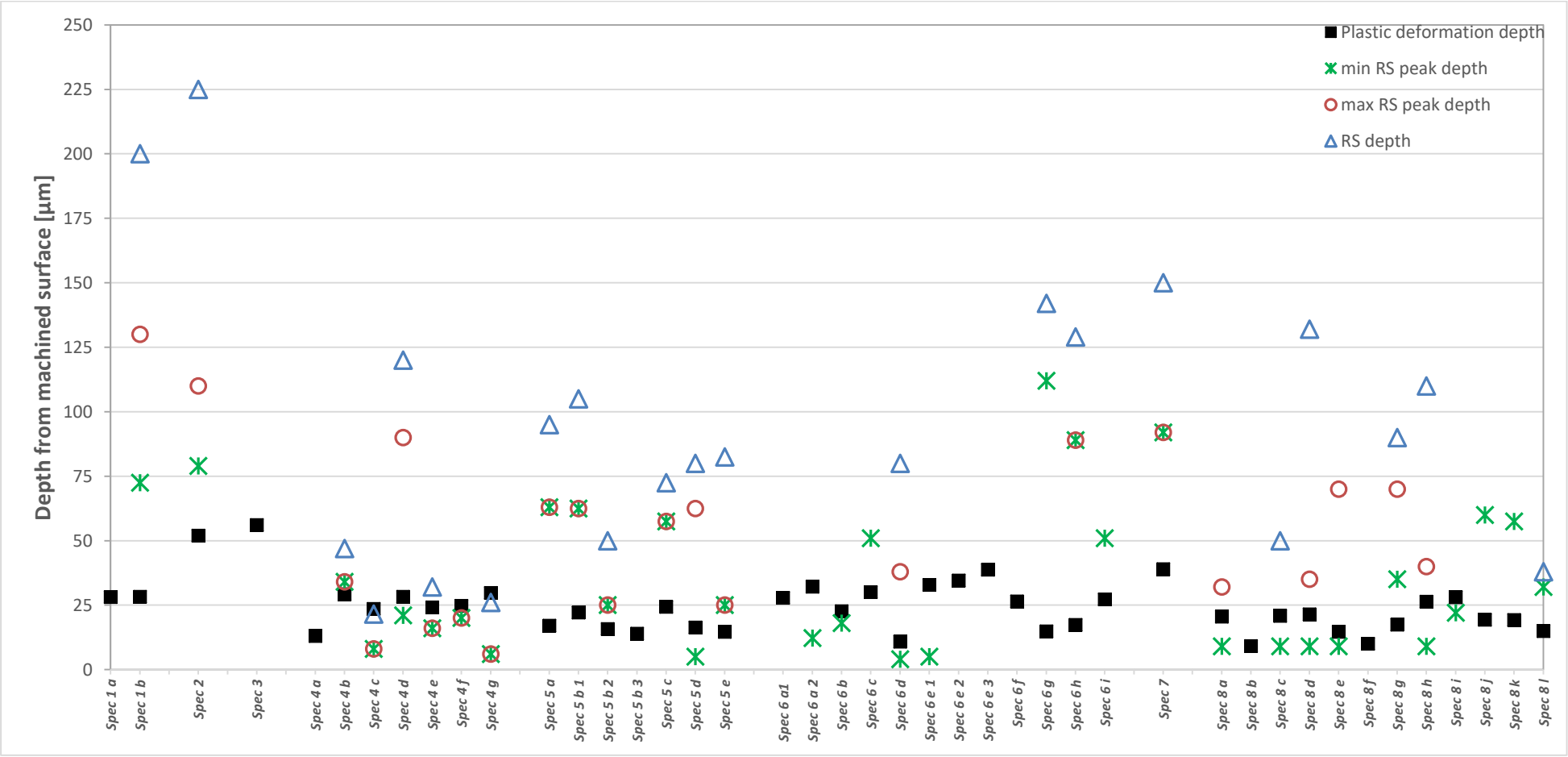

Figure 5-41 Comparison of plastic deformation depth with the location of peak and depth of residual stresses.

Near-surface, stress measurements included low to high, tensile and compressive and even zero values. Tensile stresses were detected in locations with finer, heavily distorted and twinned microstructure, while compressive stresses were detected in locations with larger, hard, undistorted and un-twinned grains. Zero and low stresses were detected in locations with various levels of twinning and grain distortion. Twinning had a tendency to reduce stresses, whereas distortion to increase them. These observations should not be generalized because there were some discrepancies in those trends and the number of measurements was not sufficient to establish a safe conclusion.

If near-surface stress had low to high compressive values, they would dissipate towards the end of the deformation/twinning zone and the profile would build up to a local or global maximum within the undeformed region. Alternatively, zero, near-surface stresses were building up towards local or global, compressive, maxima within the severely distorted and/or twinned layer and a peak would occur below the deformation/twinning zone. For tensile, near-surface stresses, there was a transition to compressive stresses within the twinned region and the compressive profile would eventually build up below the deformed region.

The location of the peak, compressive stress was not consistent, but it was typically below the twinning region, i.e. below the plastically deformed region. Peak values were approximately half the yield stress of the material. Secondary peaks were observed in regions with a high degree of crystal anisotropy. Complete profiles also captured the transition from compression to tension at the end of the primary compressive part of the residual stress and the compressive, equilibrium, end tail.

It was evident that the shape of the profiles was not strictly dominated by specific features within the deformed layer, like twins depth or grain size variations. Instead, a combination of surface topology, grain structure (in terms of size, phase, and orientation), sub-surface deformation features, plastic strain gradients and process conditions were contributing to the developed residual stress fields.

The strong rolling texture and the expected long-range, relatively uniform, sub-surface, plastic strain gradients around the hole should eliminate huge variations in near-surface stresses. Thus, the drilling process should have contributed to the specific outcome. That hypothesis was further examined with Finite Element models of machining. PE and RS results from FE simulations have predicted such variations, but only average profiles have been published [98]- [112] [193]. In order to understand and examine the cutting

operation, it was deemed necessary to obtain location specific information of elastic and plastic profiles for standard drilling conditions.

5.5 Finite Element of Ti-6Al-4V machining

The construction of a 3D drilling model and the examination of the effect of rpm, lubrication, cooling and tool wear were beyond the scope of the current work. Such a task would involve extensive testing of the material behaviour in high strain rates and all the subsequent interactions between the tool and the material. It was more important to examine the variations of the sub-surface deformation, generated through a typical machining process. An underlying assumption was that the stresses and strains at equilibrium were still representative of the expected, isotropic, macro/mesoscale profile, as developed through the local microstructural features.

5.5.1 FE orthogonal cutting – Model description

The simulation work was carried out with the commercial, FE software, SFTC DEFORM 2D/3D as a plane strain model of an orthogonal cutting. DEFORM 2D/3D was selected because of its extensive material library and automatic re-meshing capabilities.

The model was created and validated based on the conventional machining of Ti-6Al-4V [189]. Tool geometry and material properties were not modified, *Table 5-1*. All material properties existed in the default material library of the software. The FE set-up was according to the standard settings for machining simulations recommended by the software.

Table 5-1 Cutting tool geometry and material data *[189]*

Cutting tool design							
Normal rake angle	*Normal flank angle*	*Cutting edge angle*	*Cutting edge radius*	*Cutting edge inclination angle*			
15º	6º	90º	30 μm	0º			
Material properties							
Johnson-Cook constitutive model			$\bar{\sigma} = [A + B(\bar{\varepsilon})^n] * [1 + Cln(\dot{\bar{\varepsilon}}/\dot{\bar{\varepsilon}}_0)] * [1 - ((T - T_0)/(T - T_0))^m]$				
A	B	C	n	m	$\dot{\varepsilon}_0$	T_0	T_{melt}
782.7	498.4	0.028	0.28	1.0	10^{-5}	0 ºC	1600 ^{0}C
Fracture criterion							
Cockroft & Latham			$D = \int_0^{\bar{\varepsilon}_f} \sigma_1 d\bar{\varepsilon}$			D_{cr}=240	
Tool & Workpiece interactions							
Friction coeff. 0.6 (dry conditions)			*Heat transfer coeff. 65.0 N/mm/sec/ºC*			*Heat/Mechanical work 0.9*	
Environmental conditions							
Temperature 20 ºC			*air cooling*			*Convection coeff. 0.02 N/mm/sec/ºC*	

Most machining simulations with DEFORM 2D/3D solve the problem taking into account only the plastic behaviour of the material because the primary interest is the machining forces, the material behaviour and the interactions between tool and workpiece. Consequently, elastic strains disappear at equilibrium conditions and the mesh is very fine in the contact region and coarse on the workpiece. The relative coarse mesh assigned to the workpiece smooths out the plastic strain during the remeshing steps. Thus, the machined induced effects on the workpiece can only be revealed by an elastoplastic material and a fine mesh within the affected layers.

During cutting the material exhibits high strain rates, in the range of 10^2-10^5 sec^{-1}, where the flow behaviour is more accurately captured by Johnson-Cook models. Chip formation is best described by fracture energy criteria, like the *Cockroft & Latham* and the Hillerborg models. Lubrication and coolant can change the magnitude of interactions between tool and workpiece through the friction and heat transfer coefficients, while the heat generated during cutting is approximately 0.9 to the mechanical work. Tool wear and lubrication/cooling were not fully examined. Constant coefficients of shear friction, heat transfer between tool and material and convection between material and environment were assumed.

Tool speed and feed rate were kept according to the drilling scenario used for the fatigue test of the fatigue tests, i.e. 458 rpm and 0.051 mm/rev. Due to heat generation and the tool forces, the machining simulations were further allowed to reach equilibrium conditions by the removal of the tool and continuous air cooling.

5.5.2 FE orthogonal cutting - Results

The obtained results were similar to the ones presented from other FE simulations [193]. Subsurface strain and stress fields varied along the machined surface as a direct effect of the chip segmentation, *Figure 5-42 & Figure 5-43*. At equilibrium conditions all near-surface stresses were compressive, *Figure 5-42 (b)* & *Figure 5-43*, but stresses had a significant variation, ranging between 50 – 800 MPa.

During cutting, the workpiece exhibited tensile surface stresses due to the removal of material in the region of the workpiece close to the tool, *Figure 5-42 (a) & Figure 5-43*. The local maxima and minima of the RS and PE on the machined surface occurred at similar locations along the tool path, *Figure 5-43*.

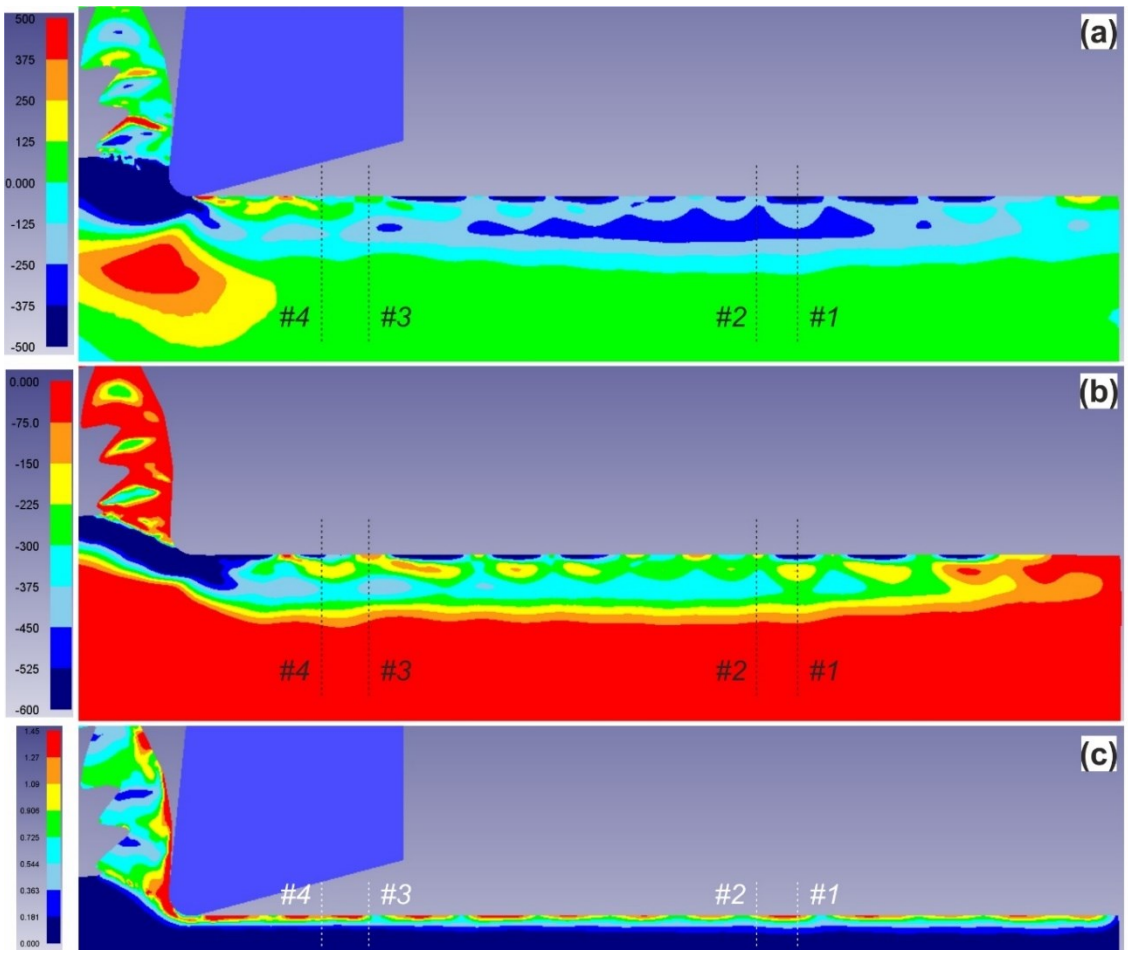

Figure 5-42 Subsurface deformation – FEM machining @ 458 rpm; a) Stress field of the horizontal component during machining; b) Residual stress field of the horizontal component at equilibrium in room temperature;c) Equivalent total plastic strain filed (von Mises) during machining.

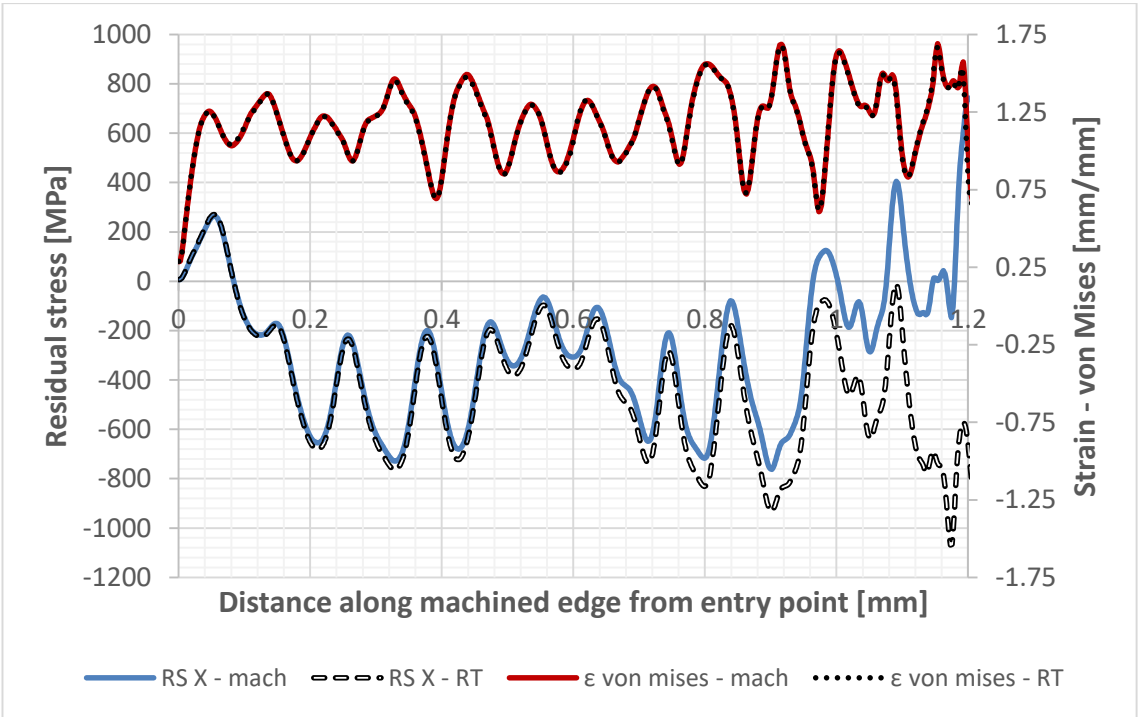

Figure 5-43 Surface deformation – FEM machining @ 458 rpm; Comparison of horizontal stress (RS – X) and equivalent strain (ε von Mises) fields during machining (mach) and at equilibrium in room temperature (RT).

Strain and stress profiles were further examined along four pre-determined paths in locations of minimum and maximum stresses values, marked in *Figure 5-42*. The produced profiles revealed that the variation of surface strains and stresses was accompanied by another variation with regards to the depth from the machined surface, *Figure 5-44*. In fact, the simulated stress profiles had the same shape and features as those measured experimentally with the localized micro-machining method. A significant difference was that no tensile stresses were found in equilibrium conditions. However, the effects of coolant, lubricant, wear and tool geometry could create a situation where surface tensile stresses during machining would be stable at equilibrium conditions. Sub-surface compressive peaks occurred at the edge of the plastically deformed region. Tensile equilibrium tails were balancing the main compressive part of the RS profiles, but boundary/edge effects should have affected the end regions of the RS profiles. There was little difference in the depth of the plastic and elastic strain fields, due to the uniform elastic and plastic properties.

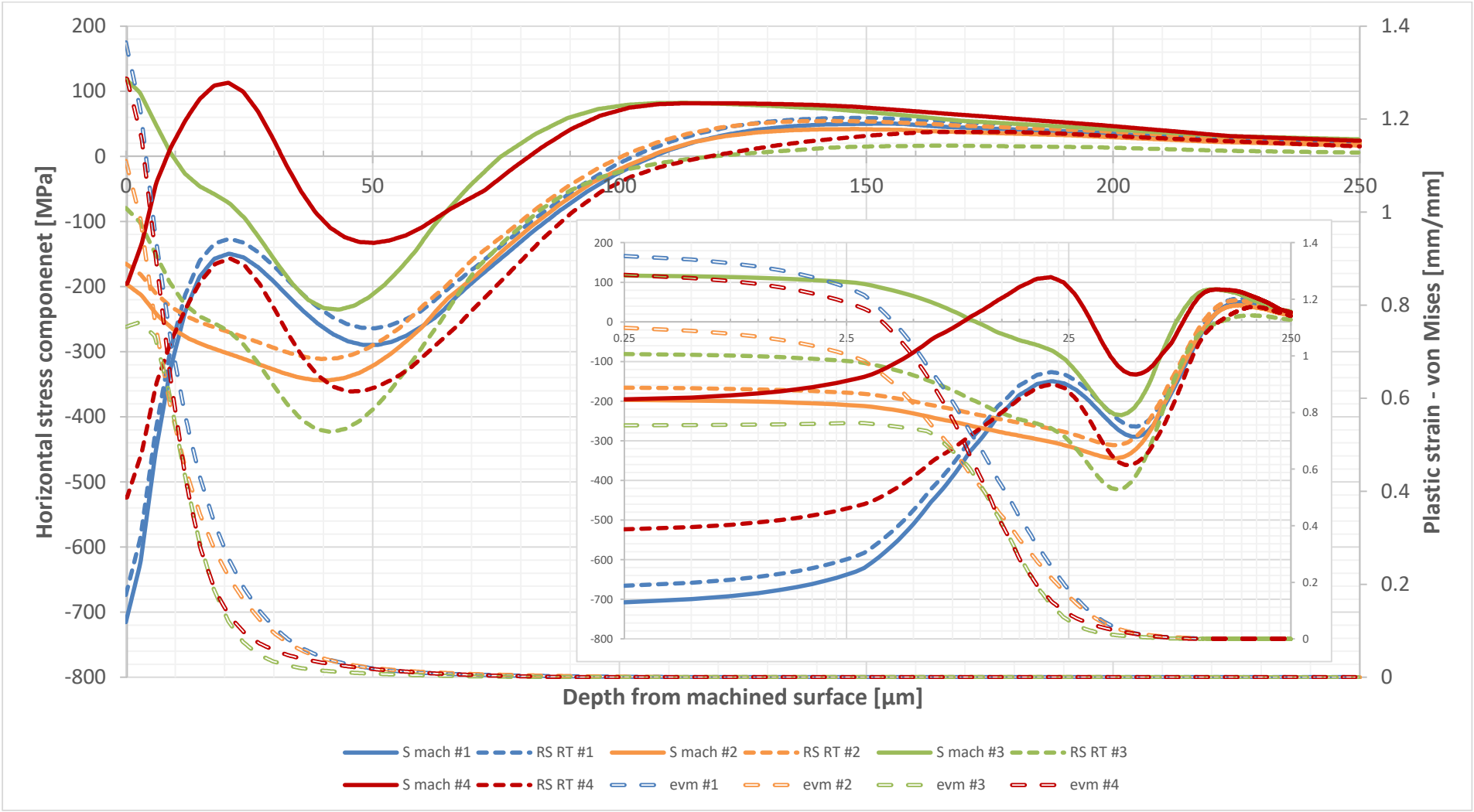

Figure 5-44 Graph of horizontal stress and residual stress components (S & RS) and von Mises plastic strain (evm) along the paths identified in Figure 5-42 (a) in normal and logarithmic length scale.

5.6 Summary

Non-uniform plastic strain and temperature fields during drilling were expected to generate residual stresses within the material. The sign, magnitude, and shape of the residual stress profiles could contribute to the variations of fatigue life of the machined specimens. Standard methods of residual stress measurement could not provide the required level of detail. Therefore, a location specific, micro-machining, stress relaxation method was used. The technique was validated against peened CP-Ti material at different temperatures and then it was applied to the machined specimens. Since the characteristic length of the process effects and residual stress measurements were similar and limited to the grain scale, the FIB technique should capture the local macroscopic residual stress profile as a series of Type II stress measurements comparable to XRD and Hole Drilling measurements.

In the peened CP-Ti, the presence and density of twins were directly related to the magnitude and depth of the compressive RS profiles. Stresses existed up to the end of the plastic deformation zone and peak values occurred below the SPD zone. Variations in the depth of the twins introduced variations in RSs, which made difficult to characterize the peening at different conditions. Despite that, the localized nature of the measurements provided the links between microstructural features and RSs. Thus, it was understood that peening at low temperatures resulted in less sub-surface, plastic deformation and shallower RS profile, because of the higher flow stresses and the suppression of the twinning mechanism. When the peening temperature was raised, the plastic deformation increased and so did the RSs. Near-surface magnitudes were not apparently affected by the peening temperature, but the local surface morphology had a considerable effect. Flat regions, between the hills and valleys, displayed lower near-surface compressive stresses. Low surface coverage could result in very shallow profiles, but with similar peak value as indicated by a small study in peened spring steels.

The machined specimens displayed a significant variation of sub-surface, residual stress profiles, even within the same specimen. Specimens with lower levels of plastic deformation were examined in more detail to establish the borderline on the fatigue performance. Low, intermediate and high compressive and tensile, near-surface stresses were measured in most specimens. All profiles were building up towards a prolonged compressive profile in the undeformed region, with a peak value below the deformed region. Those variations made difficult to safely categorize the drilling conditions. However, the depth of residual stress profile was linked to the depth of the deformed

layer, while the shape and features of the RS profile were linked to the mode and level of deformation of the local microstructure. Simplified, 2D FE models of orthogonal cutting revealed that variation in plastic and elastic strain fields should be expected due to the chip formation and become more pronounced due to the existing microstructure.

Machined specimens displayed completely different behaviour from the peened specimens. The mode of deformation, shearing vs. compression, generated higher plastic strain gradients within the machined affected layer, rather than the peened layer. The depth of plastic deformation was also lower in machined specimens. Thus, compressive residual stresses extended beyond the plastically strained region in machined specimens, whereas stresses were limited with the strained region in peened specimens. It could be assumed that the peening operation was more intense than machining and compression was a more uniform deformation mode than shearing. Peening appeared to create a hard, SPD layer, which was acting as a barrier for further deformation and generation of deeper residual stress profiles.

It should be noted that both processes appeared to introduce local stress variations evident from the wavy profile of the peened surface and the RS profiles from machining simulations in Figure 5.42. Such variations of the macroscopic stress in transverse and horizontal directions cannot be captured in detail by XRD and Hole Drilling because of their respective scales. FIB should be more sensitive to a notable change of the macroscopic stress field, though not accurate enough since it approximates it through Type II stress measurements. If a series of FIB RS profiles are averaged they should provide the macroscopic stress profile, sacrificing the detailed information of local discrepancies from the average condition. The importance of the FIB RS is that they provide the deviations from the average profile, the local maximum and minimum RS values and the local distribution over the depth that could affect the fatigue life and the crack initiation stage in some specimens or cases.

Most of the specimens displayed tensile stresses in the near surface region, irrespective of the average, deformation level of the specimens. Even specimens with high fatigue lives and low deformation had locations with tensile stresses. The parent study had identified that the majority of the specimens were failing close to the machined surface. Although the exact location could not be identified, tensile RSs could contribute or even be the dominant factor. Tensile stresses extended towards higher depths in severely deformed specimens and they could be sufficient to cause cracking. However, such

specimens had also deeper compressive residual stress fields, which should be beneficial for their fatigue performance.

Taking into account that the differences in fatigue lives were more than an order of magnitude, the problem should evolve more around the crack initiation stage and less so on the small crack propagation. A combination of tensile stresses within a deformed layer, with a brittle SPD, strain concentration sites and microstructural defects (twins and dislocations), would make a good case for the failure mechanism. Since all specimens displayed similar trends in surface roughness, plastic strains, and residual stresses, the fatigue performance should have been similar. Thus, none of the parameters was the dominant factor causing the early failure of the specimens.

The next step was to re-examine the machined and fractured surfaces of the fatigue tests. SEM and LOM images from the 8 mm and 10 mm drilled specimens, fractured during the fatigue test, should provide the exact crack initiation point within the material, the crack propagation path and any surface defects that could have been missed. That critical information would reveal the potential combination of defects dominating the performance of the specimens and clarify the failure mechanism.

Chapter 6. Fractography of Ti-6Al-4V Drilled Plate Fatigue Coupons

The results from the EBSD scans provided a correlation between plastic strains and fatigue performance of the specimens, which was partially verified by the residual stress measurements. Furthermore, a number of subsurface defects and misfits existed throughout the strained region with no clear evidence of which is the dominant one for the early failures of the specimens. Therefore, it was considered imperative to proceed with a detailed study of the fractured surfaces.

A limited number of fractured specimens were examined with SEM during the parent study, as a worst versus best case scenario [1]. The specific specimens did not have a clear crack initiation point. Instead, fracture lines originated from a larger area of various sizes. Some of the specimens failed internally, while most of them failed close to the drilled surface, but with no clear indication of the proximity to the surface. Since the parent study did not cover the entire sample range, these observations did not lead to a solid conclusion.

The location of the crack initiation point could provide information about the weak areas of the material and the mechanism behind the early failure of the specimens. Crack propagation and overall fracture patterns were additional features of interest which could add towards the detailed description of the fatigue failures. The 8 mm plates had large macrozones and they were limited in number, thus the 10 mm plates were investigated primarily. Only surface defects and crack paths on the machined surface were examined in the available 8 mm plate specimens. The information acquired from machined surfaces at the vicinity of the crack initiation area revealed the main failure mechanism and correlated the fatigue lives to specific topological defects.

6.1 Fractured Surfaces

6.1.1 Crack Initiation site

Two modes of failure had been identified in the parent study [1] and re-emerged in the current study, *Figure 6-1*, images (a) and (b). The first mode was close to the surface of the hole, whereas the second mode was internal within 200 μm from the surface of the hole. There was no clear crack initiation point in either case, since the fracture lines originated from a wide area.

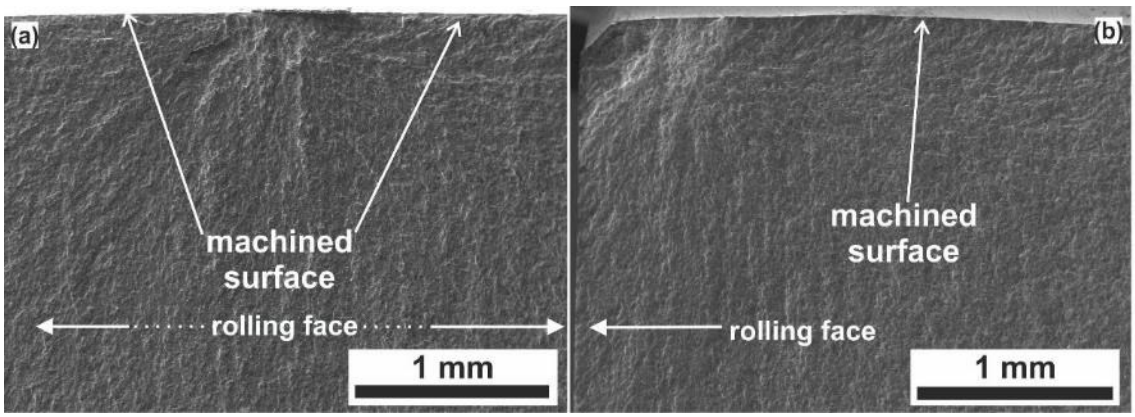

Figure 6-1 Crack Initiation Sites; Image (a) Specimen 3-5 @ 123735 cycles, surface failure; Image (b) Specimen 1-1 @ 3165947 cycles, internal failure.

In the first failure mode, some of the fracture lines evidently originated from the surface of the hole, ***site a*** in *Figure 6-2*. However, some other fracture lines originated from an internal site, marked as ***site b*** in *Figure 6-2*. Due to the higher number of fracture lines in the *site a* of ~250 μm width, it could be assumed that this was the critical site and *site b* was developed as a consequence of the early crack propagation.

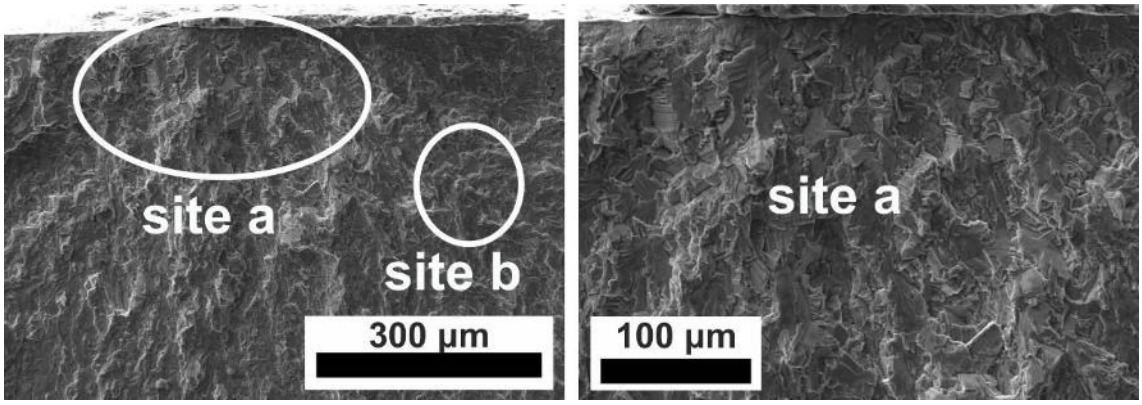

Figure 6-2 Surface failure mode, Specimen 3-5 @ 123735 cycles

In the second failure mode, all of the fracture lines evidently originated from an internal site of the specimen, close to the de-burred regions, ***site a*** in *Figure 6-3*. This site was about 250 μm from the machined surface.

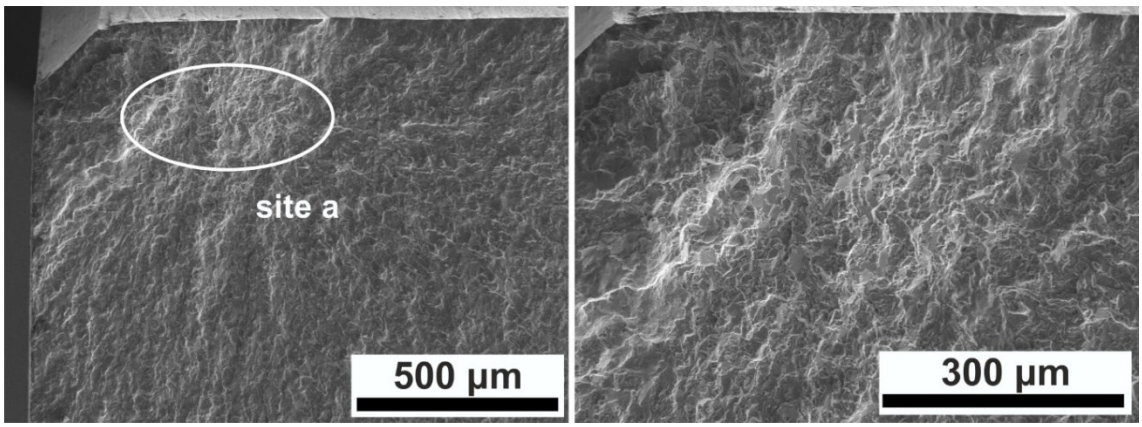

Figure 6-3 Internal failure mode, Specimen 1-1 @ 3165947 cycles

All the examined, twenty-three (23) out of the thirty-two (32) fractured specimens, Figure AP- 15 - *Figure AP- 19*, followed in principle the two failure modes, with three discrepancies discussed in more detail later. Furthermore, despite not identifying a clear crack initiation point, *Figure 6-1 (a)* and *Figure 6-2* demonstrated that the crack initiation areas close to the surface of the hole were found around a site with a prominent surface defect, a chip fragment. Other defects were visible on the machined surface.

6.1.2 Surface defects

Further examination of the fracture surfaces revealed various types of surface defects, which could lead to an early failure of drilled plates, *Figure 6-4*:

a) increased local surface roughness and microscale cavities , *Figure 6-4 (a)*;
b) chip fragments embedded in the drilled surface, *Figure 6-4 (b)*;
c) drilling marks and grooves, *Figure 6-4*;
d) smearing of the surface, lips and further surface profiling, , *Figure 6-4 (c)*.

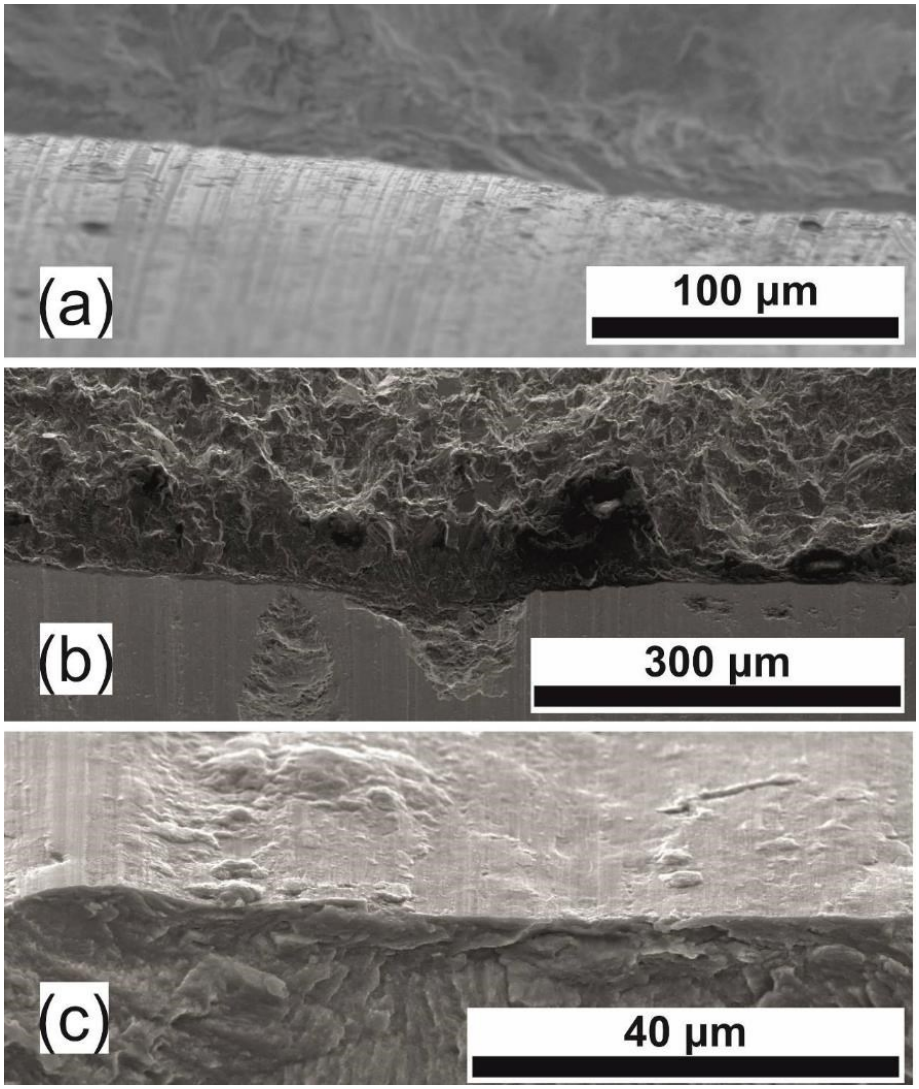

Figure 6-4 Surface defects a) Specimen 2-3 @ 227132 cycles; b) Specimen 1-10 @ 322505 cycles; c) Specimen 1-8 @ 230388 cycles

The most dominant mode of failure was due to the presence of chip embedded in the drilled surface, the pick-up sites, with 15/19 specimens failing close to the surface, *Appendix V*. Specimens with very low fatigue lives, below 1.0E5 cycles, failed at large pickup sites, *Figure AP- 19*. Specimens with intermediate fatigue lives, 1.0E5 – 3.0E5 cycles, *Figure 6-4, Figure AP- 17 & Figure AP- 18*, failed either at smaller pickup sites or at sites with a high combination of voids, small chip fragments and smearing of the surface. In absence of surface defects the specimens failed internally in the high cycle regime, above 1.0E6 cycles, *Figure 6-3 & Figure AP- 18*.

6.1.3 Discrepancies

The majority of the close edge surface failures occurred between quarter- to mid-thickness lcations, i.e. the area which experienced the higher stresses during the fatigue tests. The only exception was Specimen 2-5 @ 182773 cycles which failed immediately below the deburring region, in a location with a high number of small chip fragments, *Figure 6-5*.

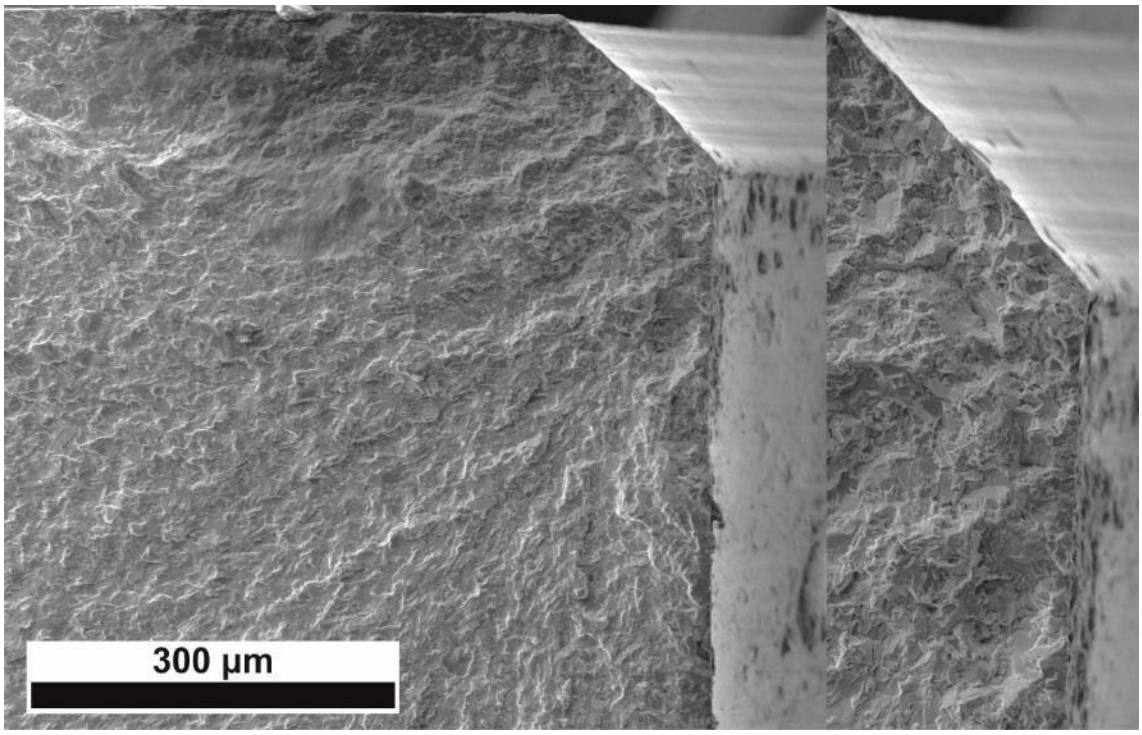

Figure 6-5 Low cycle failure at the edge of the drilling surface, at the edge of the deburring region; Specimen 2-5 @ 182773 cycles

Specimen 1-9 @ 133954 cycles, failed apparently internally in the deburring region, despite the very low fatigue life, *Figure 6-6*. However exactly at the deburring region there was significant pick-up formation and cracking. A small crack had cut through the chip and another one appeared at the sloped deburring area, indicating that the reason for the premature failure at that location could be because of the deburring pickup site. The pick-up site could have cracked and the crack propagated inwards, surfacing in the

deburring region. Then it spread towards all directions due to the existing geometry and applied stress state.

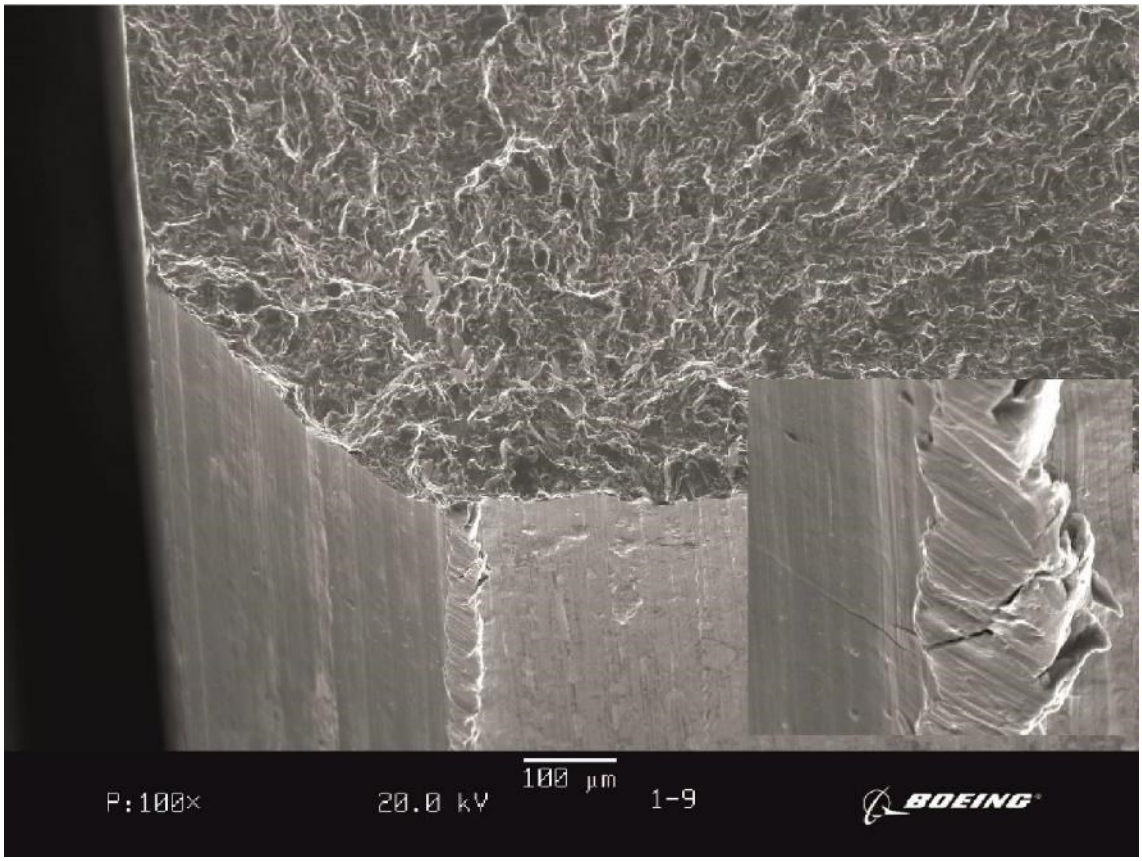

Figure 6-6 Combined low cycle failure in the deburring region; Specimen 1-9 @ 133954 cycles. Adopted by [1]

The specimens with high fatigue lives, Specimen 1-1 @ 3165947 cycles and Specimen 1-4 @ 2690063 cycles failed clearly internally in the deburring region, *Figure 6-3*. Specimen 3-1 @ 620422 cycles, failed apparently internally around the half thickness region, despite the intermediate fatigue life, *Figure 6-7*. There were small pick-up sites on the surface around the main crack initiation area, but they did not initiate a crack. It could be assumed that the pick-up sites must be located in a high-stress region and have a minimum size to cause the level of interaction with the matrix which triggers the crack nucleation. However, the probability of not having a critical pick-up site in any of the seven holes of the fatigue specimen, on either side of the hole, within the 10 mm of plate thickness is considered very low. This was the sole, but very important outlier of the dataset.

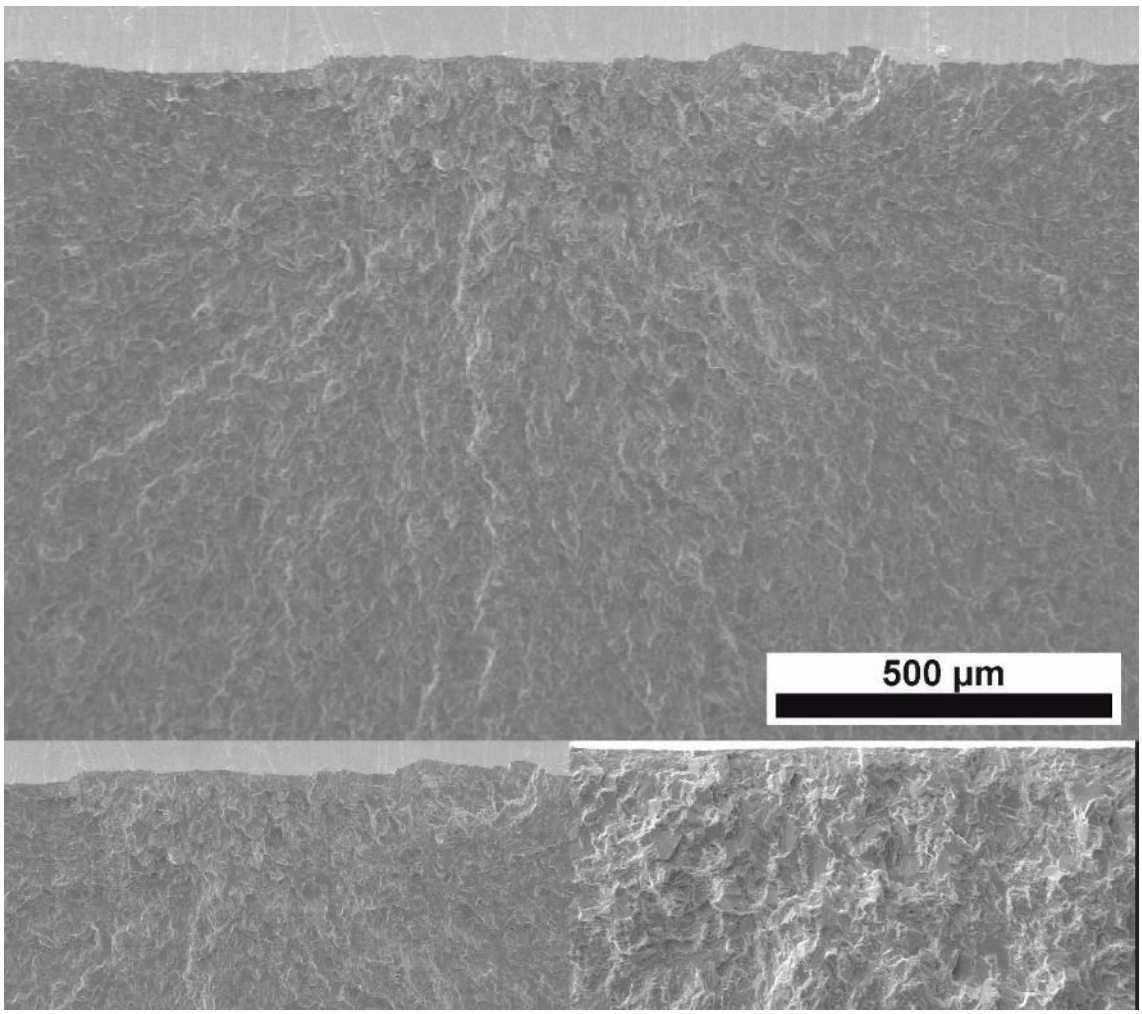

Figure 6-7 Internal failure at intermediate fatigue life; Specimen 3-1 @ 3165947 cycles

6.1.4 Failure modes

Internal, high cycle failures were very limited, but they occurred in four tests of specimens with seven identical holes and they cannot be disregarded. This mode could be an effect of the existing residual stress profile. It is well known that peened material typically fails internally at the point of transition from compressive to tensile stresses [105] [2]. Although the residual stresses profiles calculated for the drilled specimens were more complicated and did not provide a clear transition from compression to tension, the local minimum of the compression could be identified as a potentially weak point for the crack initiation. This could explain the internal failures which were well away from any sub-surface microstructural defect. From the internal point/area, the crack propagates towards all directions, *Figure 6-3*. All the failures initiated close to the entry or exit of the hole should give higher fatigue lives, because the crack propagates in one direction along the hole, although crack opening width could change the rates at a later stage.

Close edge failures could be related to surface defects, with the most dominant being the embedment of the chip. Primary cracking was limited to surface features and the SPD zone, because cracks appear in a wide area close to the edge, with distinct initiation features limited in these layers. It was not clear if the crack initiated at the chip, internally or externally, and propagated to the matrix, or the chip affected the matrix and caused cracking at the surface or the SPD zone. Due to the small size of the SPD zone, the general miss-alignment of the SEM with the specimens and the local fracture it was unclear where the crack originated. However, the images pointed towards the surface and not a subsurface region, *Appendix V*.

In low-cycle failures the chip was split in half, staying embedded in either part of the surface, *Figure AP- 19*. Arguments could be constructed for both matrix and chip cracking, but the big unknown was the level of interactions (welding/melting vs. mechanical embedment) over the entire region below the chip. In intermediate-cycle failures, the embedded chip was not always broken up, but remained attached to one side of the fractured surfaces, *Figure 6-2*. This indicated a matrix failure below the area where the chip was embedded. Other intermediate-cycle failures in regions with high cavities and small chip fragments density could further strengthen the case of a matrix failure.

The close edge cracks first cut right through the highly deformed regions, then changed slope to follow possibly the deformed microstructure with secondary crack initiation sites in the twinning zone and the low compression zones, *Figure 6-2*, before they finally continued in an overall straight path following local crystal orientations.

Most failures were initiated on only one side of the hole and the other side failed plastically due to overloading. Some notable examples of double crack initiation are specimens 2-1 @ 139552 cycles, 4-1 @ 42377 cycles, 4-2 @ 44265 cycles & 4-4 @ 25871 cycles, *Appendix V*. These specimens developed cracks in different locations on both sides of the holes, due to the presence of chip embedment, before the overload of the cross section. However, only one side was fully cracked by the fatigue mechanism. A limited number of specimens were examined in both sides of the hole because the double crack initiation and propagation were of secondary importance.

The existence of surface defects dominated the performance of the specimen and differences in the fatigue life between identical drilling conditions could be correlated with the probability of having the proper size defect, at the proper location, in conjunction with the differences at the early crack propagation due to different residual stress fields and deformed microstructures.

Thus the SEM study of the fractured surfaces evolved to the examination of the following:

i. machined surfaces in uncracked specimens to evaluate the presence of pick-up sites;
ii. metallography of the pick-up sites;
iii. secondary/non-critical cracks and their paths in the fractured dataset;
iv. characterization of crack propagation paths.

6.2 Machined Fractured Surfaces

The embedment of a chip on the drilling surface was the main reason for the premature failure of the majority of the fatigue fractured, 10 mm plate thickness, dataset. Chip fragments could be found in all specimens, even in the ones with high fatigue lives, *Figure 6-8*. Since none of these specimens have been thoroughly examined in terms of elastic and plastic deformation profiles, the drilling surface of the 8 mm plates was investigated instead. Additional images can be found in *Appendix VI*.

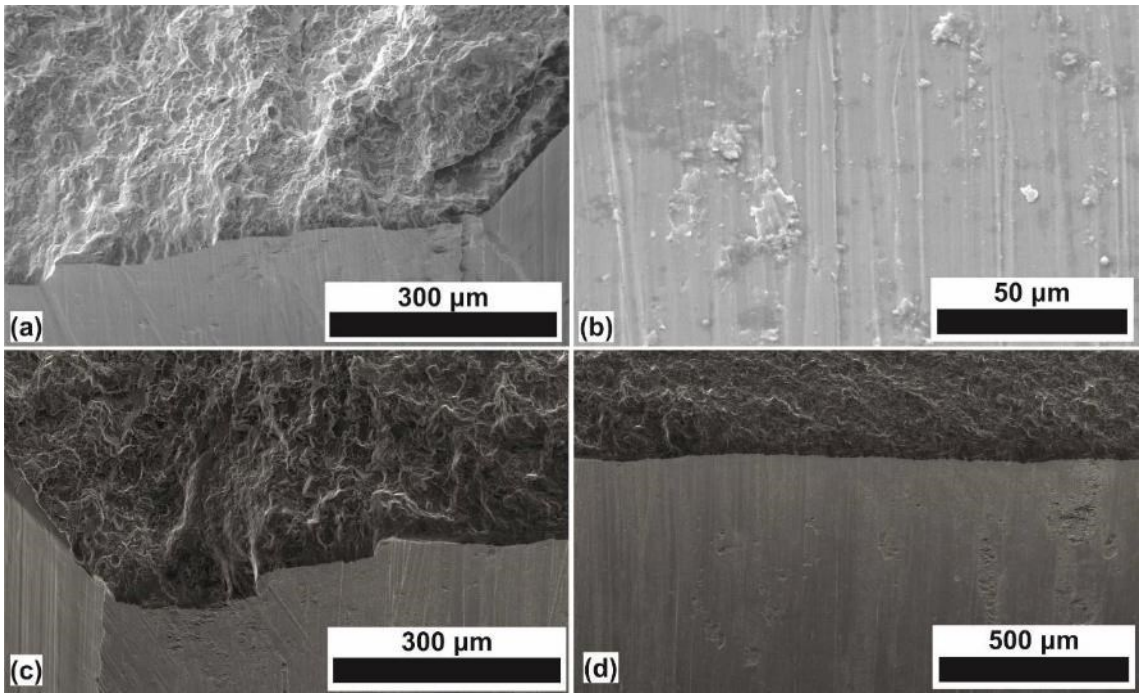

Figure 6-8 High cycle failure – Machined surfaces; a) & b) Specimen 1-1 @ 3165947 cycles; c) & d) Specimen 1-4 @ 2690063 cycles

The surfaces of Specimens 1 to Specimens 8 of the 8 mm drilled plate were examined from the entry to the exit of the hole, around the area of the peak cyclic stresses, in the non-sectioned part of the plates. All specimens had noticeable pickup sites, drill bit marks and grooves, smearing, pits and non-uniform material removal, *Figure 6-8*. The only significant difference was that Specimen 5 @ 1238187 cycles & Specimen 8 @ 945223 cycles, i.e. maximum fatigue lives, *Figure 6-9 (e) & (h)*, had fewer surface defects, their average size was smaller and the number of large defects was also smaller.

These observations verified the previous hypotheses on the 10 mm plates:

a) the different machining conditions generated different surface finishes in terms of critical surface defects;
b) the probability factor influencing the fatigue life was based on the distribution, size, and location of defects on the machined surface.

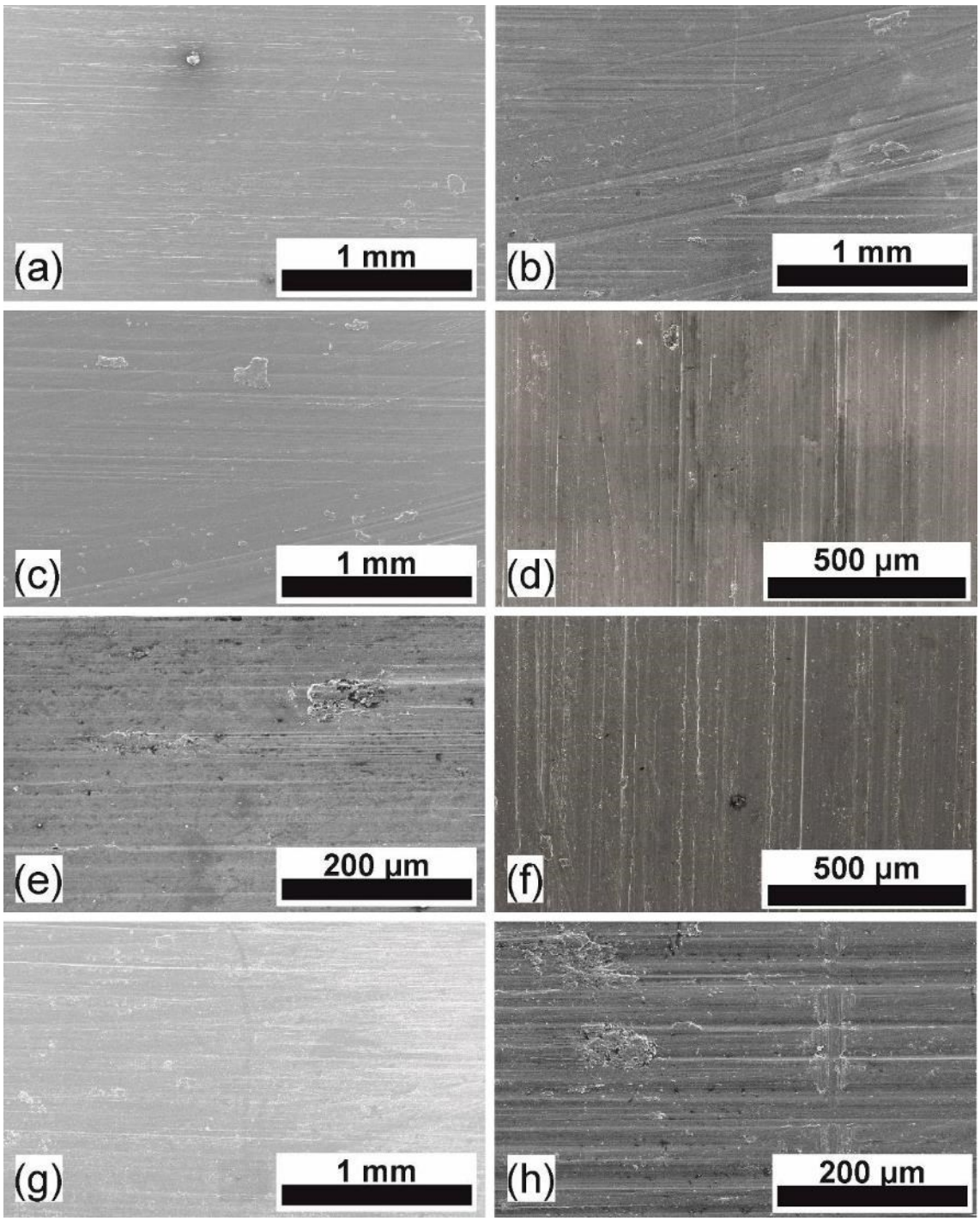

Figure 6-9 Machined surfaces; a) Specimen 1 @ 127836 cycles; b) Specimen 2 @ 72559 cycles; c) Specimen 3 @ 100113 cycles; d) Specimen 4 @ 181525 cycles; e) Specimen 5 @ 1238187 cycles; f) Specimen 6 @ 142887 cycles; g) Specimen 7 @ 135770 cycles; h) Specimen 8 @ 945223 cycles.

Specimen 5 and Specimen 8 from the 8 mm plates had lower levels of plastic deformation, indicating that the associated temperatures and cutting forces should be lower. Thus, the embedment of the chip in the surface should not be as critical as other specimens.

Furthermore, the average surface roughness was proven to be no longer suitable for assessing the surface quality of the specimens. The long range drilling groves masked out the existence of local pick-up defects, which can only be revealed by maximum surface profile differences, i.e. a range of surface peaks, *Figure 3-7*.

6.3 Metallography of pick up sites

Pick-up sites were identified as the critical surface defects, responsible for the early failures of the specimens during the fatigue test. Due to their nature, there was an inherent probability with their size and location, which could be the reason for the variation of the fatigue lives. However, fractology did not provide any information about the underlying mechanism of the early crack initiation.

The crack initiation site was located close to the drilling surface. High magnification images showed that it could be located exactly on the drilling surface. Due to the angle of the specimen with the beam in the SEM, it could be argued that the crack initiation area was within the first few microns of the deformed region, i.e. the SPD zone. In any case, it was necessary to carry out a metallographic examination of the pick-up sites.

One verified crack initiation and a few random pick-up sites were examined on different specimens, in an attempt to explore the interactions between pick-up site and matrix (SPD zone) and how they could create suitable conditions for the initiation of a crack in that location. EBSD would not be able to provide any data, because of the excessive high local strain and crystal distortion; instead, LOM was used.

6.3.1 Critical pick-up site

The fracture surface of Specimen 2-1 @ 43755 cycles was carefully grinding and polished to remove as little as possible material and still be able to examine the pick-up site, *Figure 6-10*. The chip was only partially connected to the matrix, was full of voids and had higher strains than the matrix. It also appeared to have acted as a shield to the matrix for the unconnected region bringing twins at the immediate machined surface. At the connected, welded region there were evidence of non-uniform strain gradients, higher SPD zone and significant differences in microstructure.

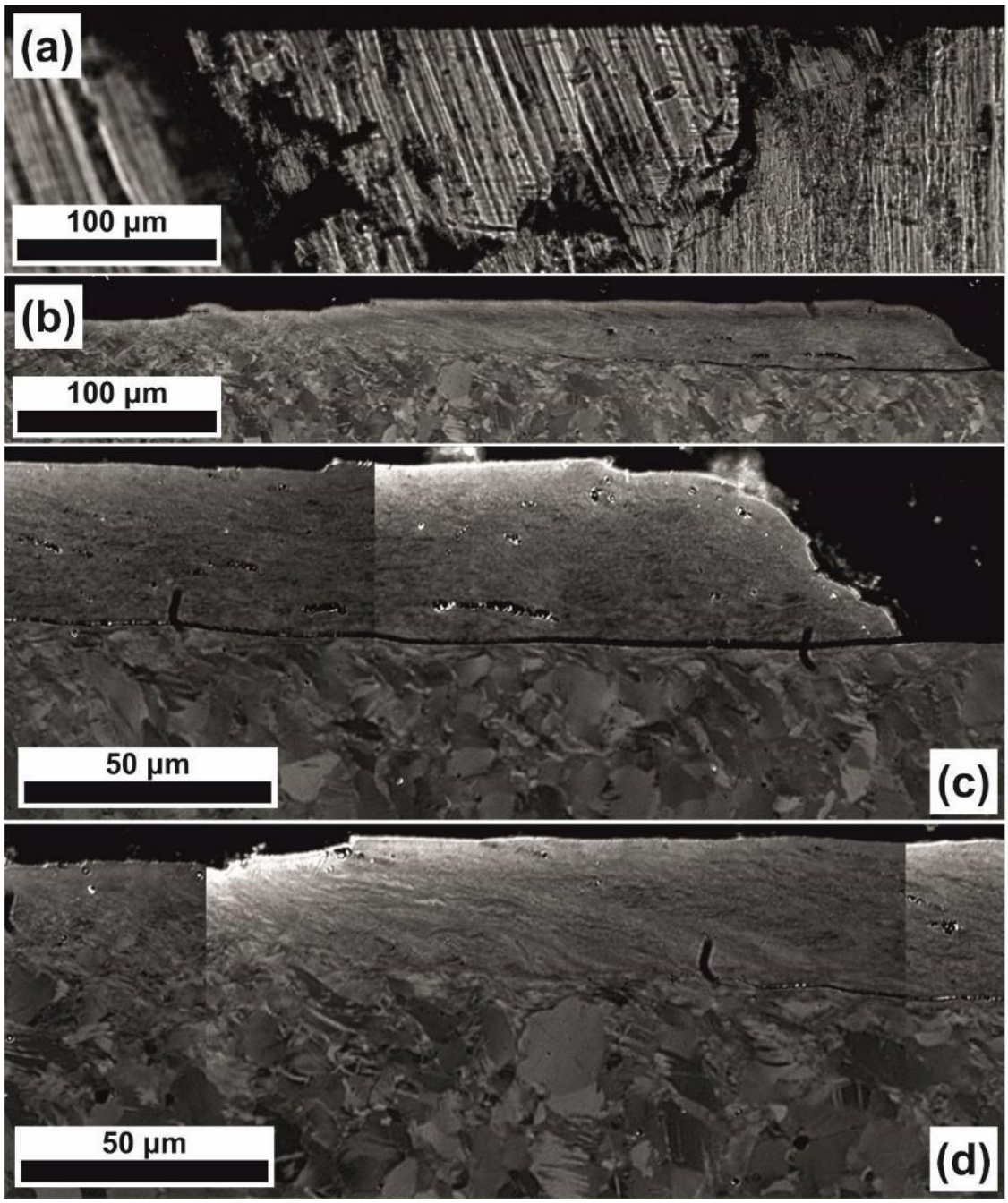

Figure 6-10 Critical pick-up site, Specimen 2-1 @ 43755 cycles; a) Machined surface; b), c) & d) Polished fractured surface.

Since this pick-up site initiated a crack during the fatigue test, the extent of the welding region and the degree of separation could not be verified. The voids at the chip followed the strain gradients and the deformed microstructure and it was unlikely to have been caused by the fatigue test. However, a suitably located void in the chip could propagate and extend from the chip to the matrix at the connected region. Another mechanism could be the separation of the chip with the matrix, which when it reaches the connected region due to the significant different strain gradients and deformed microstructures could cause cracking. The area under the chip in the separated region was relatively smooth and there were no indications of matrix cavities and crack due to the embedment of the chip, but

twins existed at the machined edge. A close examination of the fractured surface, *Figure 6-11*, displayed a potential crack initiation site in a cavity/void within the center area of the chip fragment. Fracture lines then spread from the twins on the disconnected/shielded area. Twins could have even nucleated some of the lines or accelerated the cracking because the crack area widened to about 300 μm.

Figure 6-11 Specimen 2-1 @ 43755 cycles – crack initiation site

Some of the failures examined previously showed that they occurred close to the edge of the chip, so either one of the previous assumptions could be the underlying mechanism of crack initiation.

6.3.2 Non-critical surface defects

The first of the selected non-critical, surface defects, presented in *Figure 6-12 (a)*, was an uneven removal of material on the machined surface. The cross-sectioned sample revealed that there was a perfect continuation between the defect and the matrix, which should not be if the defect was an embedded chip. Locally the SPD zone was increased and involved material under higher strains, though the strain gradient was changing

smoothly from the defect to the matrix. Similar to the critical pick-up site, LOM on the non-critical pick-up site, displayed exactly the same features, voids and partial welding of the chip on the parent material, *Figure 6-12 (b)*. Below the chip and in particular at the locations of the weld, the subsurface deformation was higher.

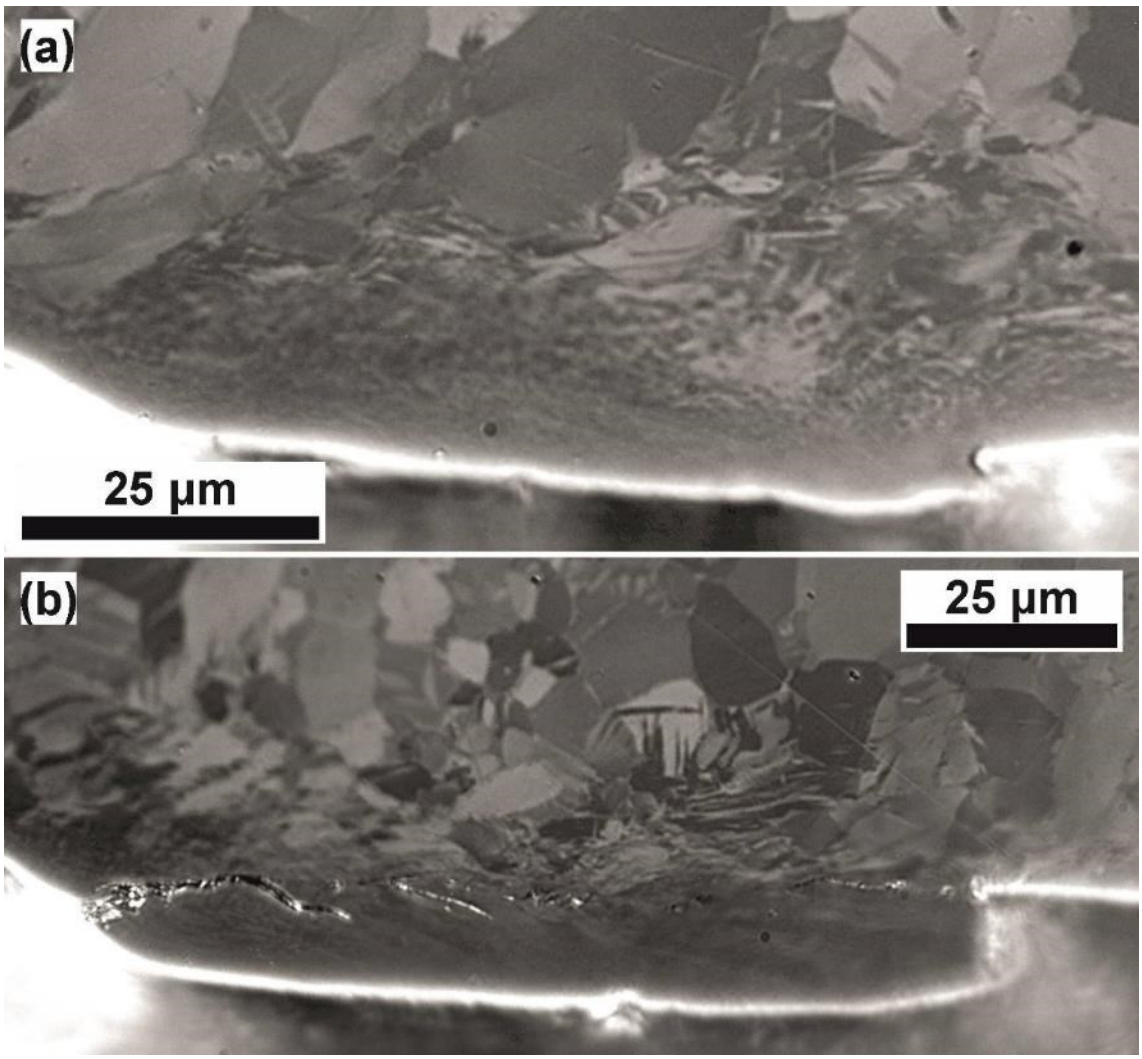

Figure 6-12 Non-critical surface defects; a) uneven material removal; b) pick-up site

6.4 Crack propagation

Further information for the crack initiation and early propagation were acquired by the examination of the machining surfaces along critical and non-critical cracks and the characterization of areas around cracks as the crack propagated along the machined surface and through the material.

6.4.1 Investigation of cracked machined surfaces

Tracking the crack along the machined surface could reveal the preference of the crack initiation sites and how it propagated at the early stages. Specimen 2 @ 72559 cycles was selected because it contained cracks on both sides of the hole and one crack was arrested near the mid-thickness plane. The main crack extended almost along the entire hole, *Figure 6-13*.

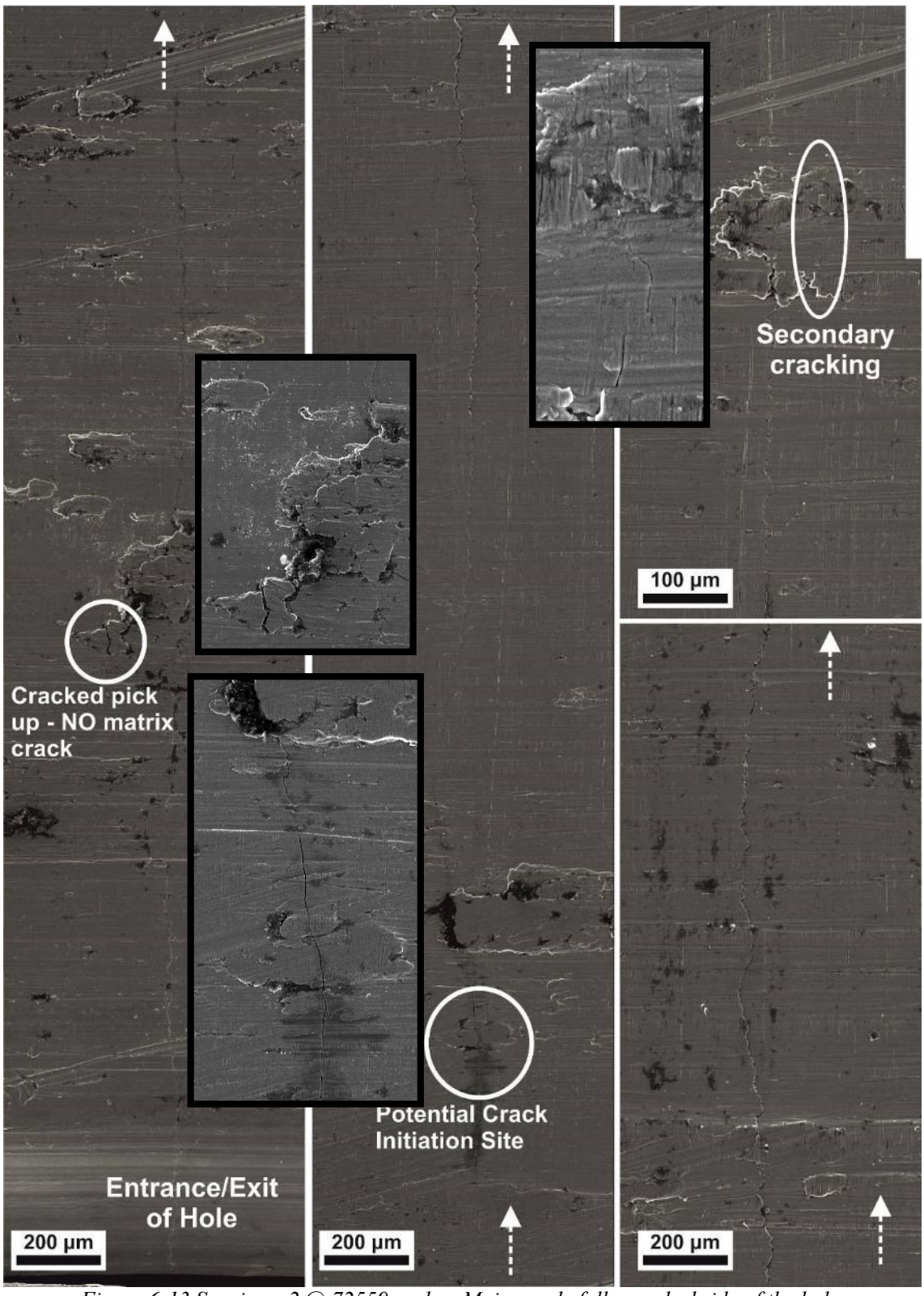

Figure 6-13 Specimen 2 @ 72559 cycles; Main crack, fully cracked side of the hole.

The main crack probably originated from a pick-up site marked in *Figure 6-13*, where the crack width was apparently higher. The crack at that region was also straighter in comparison to the rest of the length from the splitting (brittle failure) of the SPD layer. When the crack reached sufficient length and depth, it started changing directions as the teeth of a saw. Along the crack various surface defects were detected, pick-up sites,

drilling grooves and non-uniform material removal. Despite that, the critical site was only one. Another pick-up site which was completely cracked did not provide a critical crack nucleation site. It was either relatively away from the location of peak stresses (as the path of the crack and the proximity to the edge of the plate indicated), or this crack was created after the main cracked reached that location or the required interaction conditions between pick-up site and matrix were not met.

Interestingly, the other side of the hole showed multiple cracks, at different locations, but all of them at pick up sites, *Figure 6-14*. Potential crack initiation sites were identified again based on the local crack width and length. Around these locations, the cracks are straighter from the splitting of the SPD layer. Such sites were found throughout the drilling surface and did not necessarily aligned with each other. This behaviour was observed in the fully fractured specimens as well and its root cause could be the overloading of the opposite side of the hole due to the main/long crack of the first side. Similar observations were made for Specimen 3 @ cycles, found in Figure AP- 22. The non-critical crack of Specimen 2, arrested around mid-thickness plane was further characterized with the available microscopy techniques to verify early crack propagation.

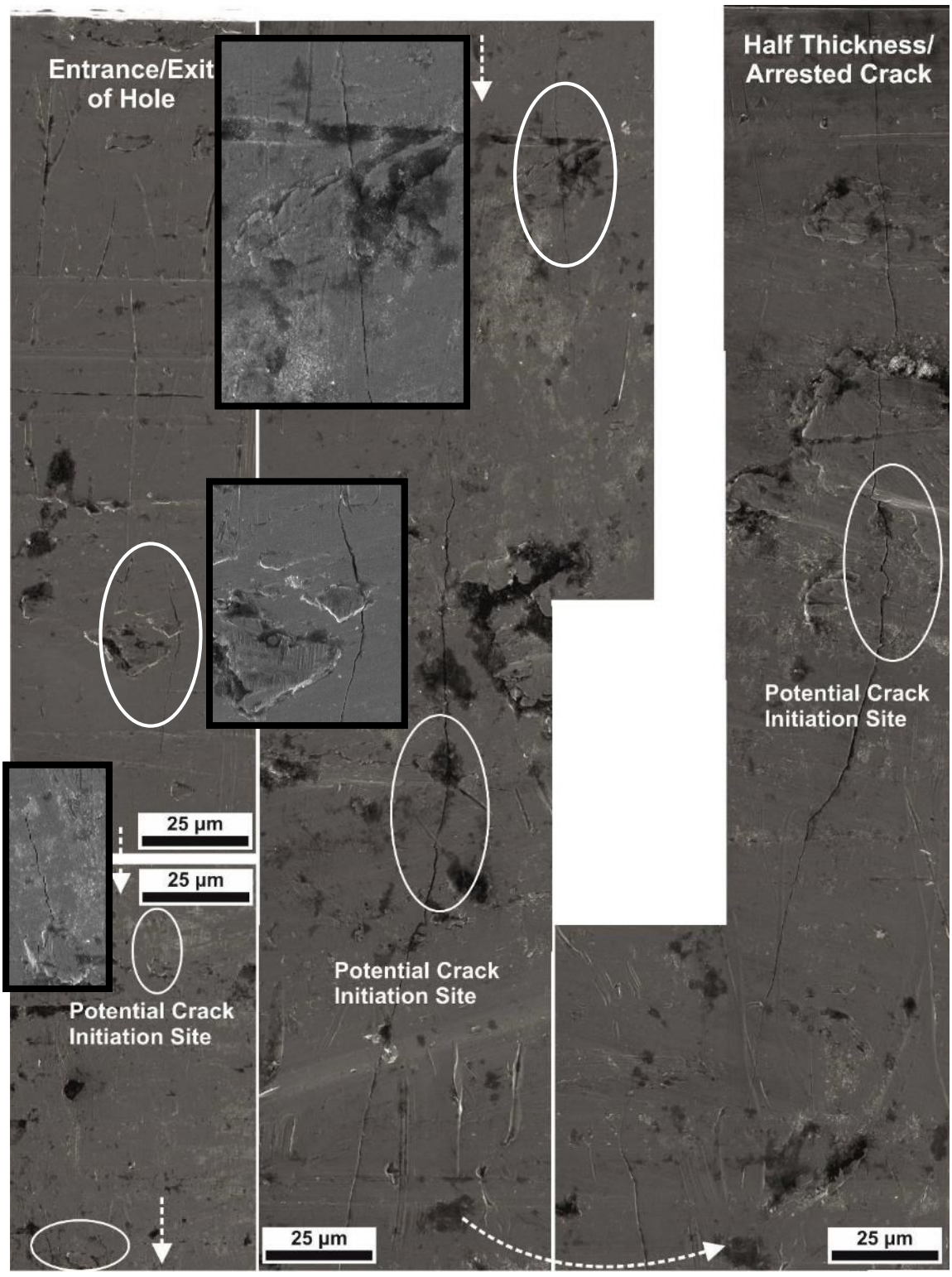

Figure 6-14 Specimen 2 @ 72559 cycles; Secondary cracks, opposite side of the hole.

6.4.2 Characterisation of cracks

The non-critical crack of Specimen 2 @ 72559 cycles, arrested close to the mid-thickness plane was examined by LOM, SEM and EBSD, *Figure 6-15*. It appeared to cross the SPD zone in right angle to the drilling surface and then it followed the deformed microstructure. The presence of the elongated beta phase close to the hole of the edge did not affect the early crack propagation. Some branching of the crack occurred, before

reaching the twinning zone and the effect of twins could not be evaluated. From the *Figure 6-15* (c), the first branching occurred at a locally highly strained region (black region) at right angle, where the crack met less distorted crystals. The second branching occurred when the crack met an area with high density of boundaries, including a phase boundary, and at that point, it preferred to cross a larger less distorted grain. These observations may not describe the exact behaviour because the location was approximately 150 µm from the pick-up initiation site and the propagation in the two directions could have produced a more complicated case. However, its depth at that location is less than 60 µm and it should still be governed by the existing microstructure.

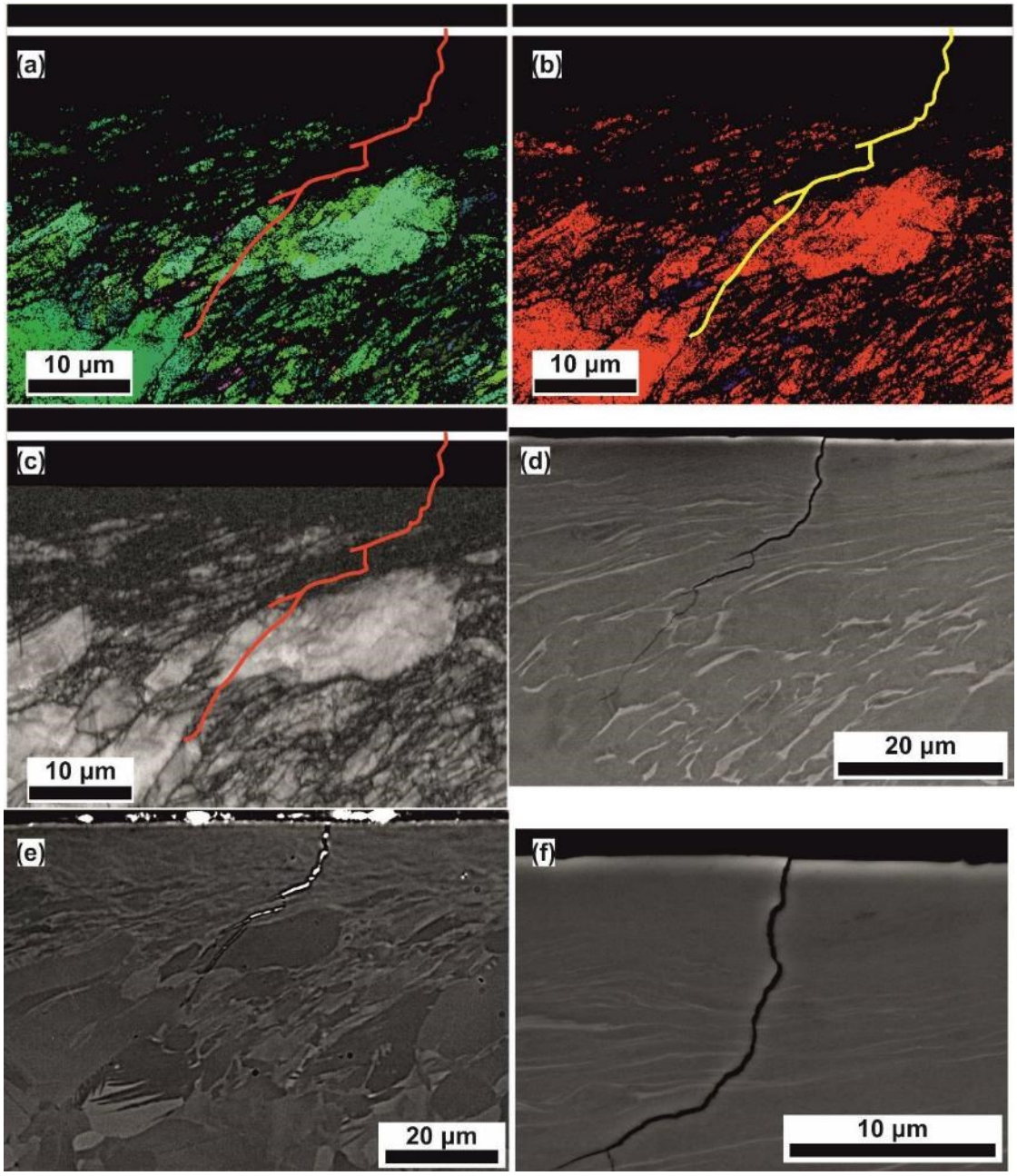

Figure 6-15 Characterization of non-critical crack, Specimen 2 @ cycles; a) EBSD All Euler map; b) EBSD phase map; c) EBSD BC map; d) & f) SEM of crack; e) LOM crack

Other critical and non-critical cracks from different specimens showed the same trend, i.e. a highly deformed specimen, *Figure 6-16*. In this case, the (critical) crack started propagating from the edge of the hole almost perpendicular to the SPD zone, then followed the deformed microstructure without branching and finally crossed the twinning zone again at right angles. At the twinning zone, it propagated between highly twinned larger grains and then crossed a deformed large grain, adapting to probably to the local strain gradient, before finally start crossing the other grains based on their crystallographic orientations. Proximity to the crack initiation site was not available.

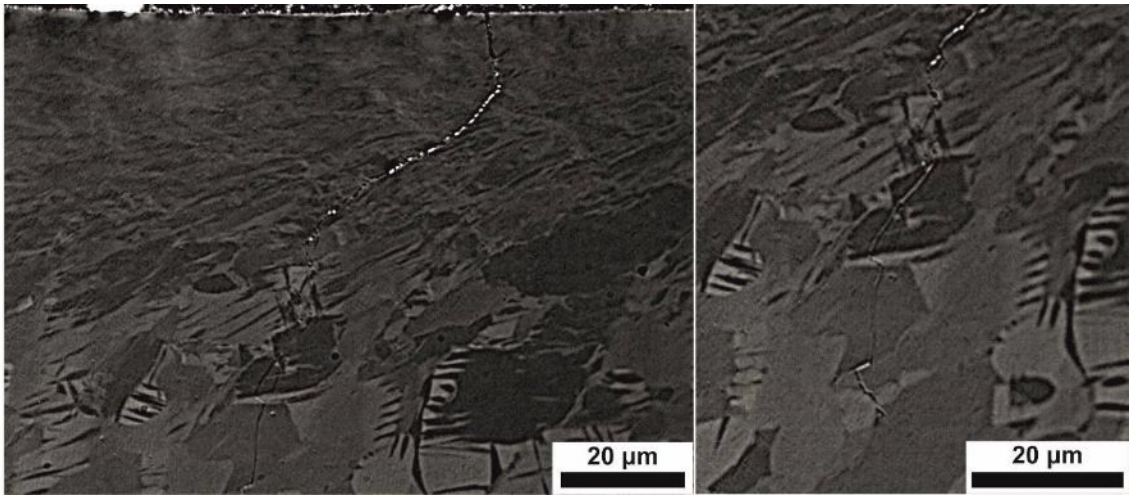

Figure 6-16 Early crack propagation on highly deformed specimen

Typically, cracks away from the crack initiation site were no longer perpendicular to the SPD. Instead, there was a progressive reduction of the crack slope, which disregarded the deformed microstructure and the twins, *Figure 6-17*. The specimen has smaller SPD zone compared to the one in Figure 615, but the same behaviour was observed. In *Figures 616, (a) & (b)* the crack is relatively perpendicular to the SPD zone, whereas in *(c)* the crack was slightly sloped at the SPD zone and after that it became straight. Probably the length and depth of the crack had reached relatively high values, causing significant overloading to the remaining cross section, which did not allow local microstructure features to dictate its path.

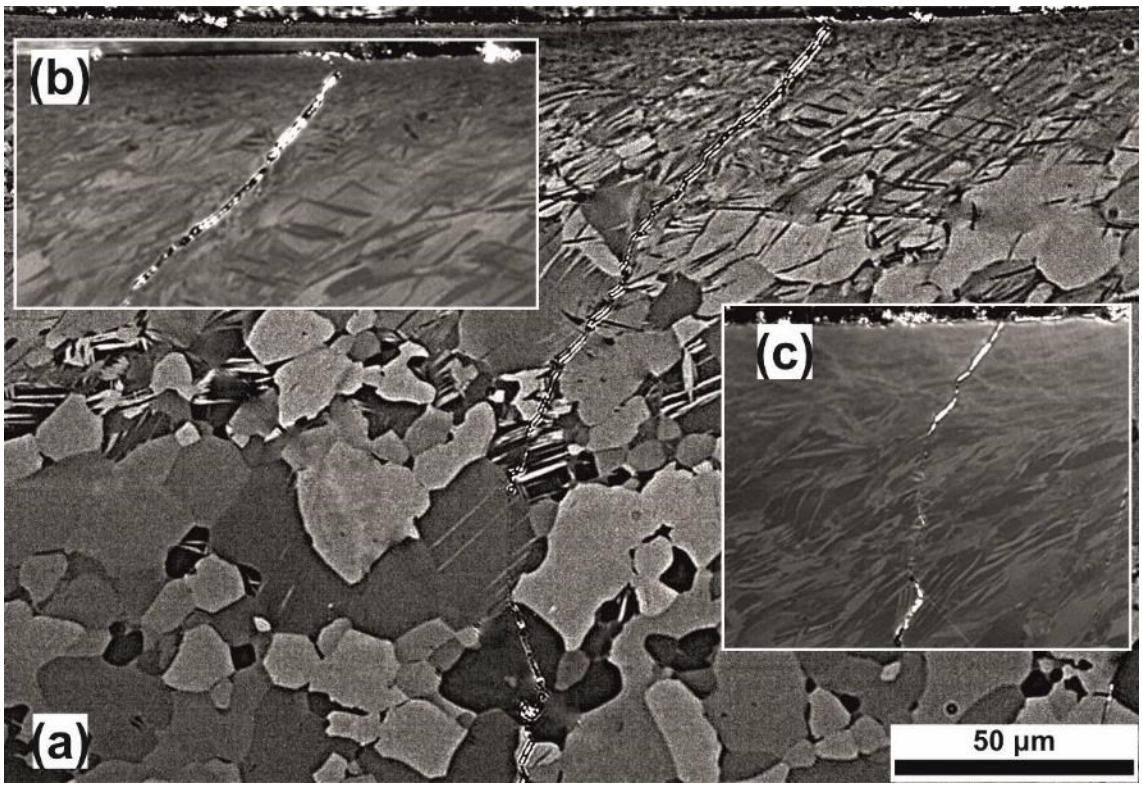

Figure 6-17 Early crack propagation in Specimen 1-1 @ cycles (partially cracked); a) relatively close to the crack initiation site; b) zoom in of (a) at the SPD zone; c) away from the crack initiation site.

These observations were in line with the ones made from the examination of the fractured surfaces. However, they serve only as a verification that microstructural features affect the crack path and thus the growth rate at the early stages. Since the drilling conditions generated different deformed microstructures and elastoplastic strain fields, it should be expected that the specimens would have different fatigue lives and increased scattering, as a follow-up of the premature crack initiation at a surface defect.

6.4.3 EBSD on critical crack

For completeness of analysis, a cracked specimen was examined by EBSD to verify the crack path and crystal orientation relationship, *Figure 6-18,* but no clear conclusions could be reached.

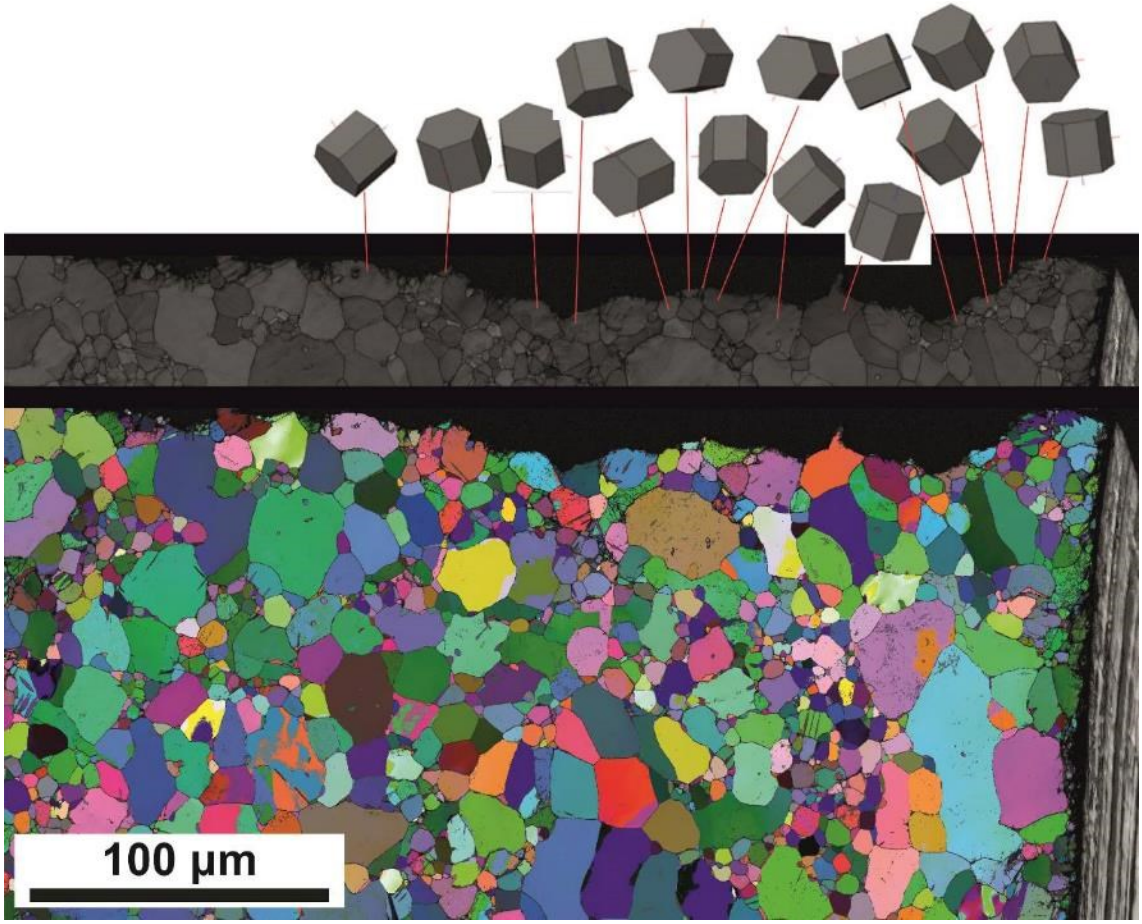

Figure 6-18 EBSD Euler and BC maps with crystal unit orientation along the crack path, Specimen 1-1 @ 3165947 cycles.

6.5 Summary

The observations made during the parent study [1], were partially verified by the current study, which also revealed the root cause of the early failure of the specimens. Surface defects from chip fragments embedded on the drilled surface were the dominant crack initiation site. Subsurface defects, misfits, strain hardening and localization, and residual stresses should have affected the crack propagation and possibly the growth rate leading to the variations of the fatigue results, but they were not the dominant factors for the fatigue life of each specimen and they did not serve as crack initiation sites. The only exceptions were specimens failed internally close to the rolled surface, possibly due to the combined action of compressive, machining-induced, residual stresses and the deburring of the holes.

The location of the defect and level of interactions between the surface defect and the matrix was found to vary around the machined surface of the hole and although all of them can act as potential crack initiation sites, there was a statistical element to when and where the crack would originate. High values of stresses in conjunction with a suitable size and type of surface defect were imperative for crack nucleation. A number of pickup

sites existed along crack paths on the machined surface, but only one was the critical surface defect. When the crack had progressed sufficiently in one side of the hole, the overloading in the other (uncracked) side of the hole caused multiple cracking from pickup sites and heavily rough and/or deformed regions. Thus, all of the previous sites had the potential to act as crack initiation sites in a higher number of cycles proving the validity of the statistical element in the creation of critical pickup sites and the effect on the variation of fatigue lives. Specimens with low high fatigue lives had smaller and more spatially distributed surface defects compared to the ones with lower fatigue lives. However, large defects could occasionally exist on the surface, but not necessarily on the location of maximum stresses. Drilling conditions could not be correlated with these findings because of the statistical nature of the defects and the need for additional characterization of the interactions between chip and matrix.

The exact crack initiation mechanism of the pick-up site was not clear. The chip was a highly strained material and inevitably very brittle, with microvoids and cracks. A critical pickup site revealed that the chip was shielding the parent surface bringing microstructural defects, like twins and strain localized regions closer to the surface. Cracks appeared to originate from the matrix chip interface, so all of the previous defects could contribute to the mechanism. Since the embedment of the chip would cause a cavity on the surface of the hole, there was also the possibility of a local stress concentration or an abnormal residual stress distribution.

In general:

1. There is no clear crack initiation point;
2. Two modes of crack initiation, internal vs. surface originated;
3. The majority of specimens had cracks initiated only on one side of the hole;
4. Specimens with high fatigue lives failed internally;
5. Internal failures are potentially related to the drop of the residual stresses;
6. Specimens with low fatigue lives failed at pick-up sites at the surface of the hole;
7. Crack initiation rather than propagation problem;
8. Pick-up sites show micro-voids inside the chip;
9. Cracks potentially originated at the matrix-chip interface of the pick-up site;
10. Pick-up sites have been observed in all specimens under all drilling conditions;
11. Size and distribution of pickup sites introduced the probabilistic factor of fatigue failure.

Chapter 7. Conclusions

The investigation of the drilled plates required the development, modification and fine tuning of different techniques to meet the needs of the project. Through the step by step analysis, it became possible to gather the information that answered the main research question regarding the early failure of seemingly identical specimens and explain the abrupt increase in fatigue lives with the decrease of plastic deformation, i.e. with less aggressive drilling conditions. Despite that, there were some aspects of the research objectives that did not materialize and should be addressed in the future. As closing remarks, the most important findings of the current research project were briefly summarized and linked to the recommended continuation studies.

7.1 Summary of findings

A fatigue study of machined specimens requires the investigation of the area with the maximum applied stress based on the following parameters: i) surface defects; ii) strain hardening profiles; iii) plastic and elastic strain fields; iv) microstructural defects; v) crack initiation locations; vi) crack propagation paths.

The dominant factor can only be identified by the critical evaluation of the experimental results and the progressive elimination of parameters to obtain a clear trend. In the current project, the trend should follow the abrupt increase of the fatigue performance of specimens. The specimens had two modes of fracture and neither of them had a clear crack initiation point. The majority of the drilled plates failed close to the machined surface and only a limited number failed internally towards the edge of the de-burring regions.

Vertical scanning interferometry in a light optical microscope captured the short and long range profiles of the drilled surface. The roughness and waviness of the profiles were eliminated by low and high pass filters to assess the hole quality. Roughness values were dominated by the drilling marks on the surface and masked the presence of other defects, like the pick-up sites or non-uniform material removal. Drilling marks could not act as stress concentrators because they were aligned to the direction of the applied load during the fatigue test. Tool subtraction marks could be seen in certain cases, but they were rarely located on the location of the maximum applied stress. All specimens had identical average roughness, which de-associated it to the observed fatigue failures.

Micro-hardness profiles in the sub-surface of tilted, drilled specimens showed a clear strain hardening behaviour. Vickers indent was much more accurate than the Knoop one.

It is assumed that Knoop indent was either not very well calibrated/aligned, or the bias in the long direction of the indent was introducing errors due to the plastic strain gradients over the microstructure. Micro-hardness decreased within the severe plastic deformation zone the variations appeared below that, because of strain incompatibility within different grains.

The 8 mm plates were examined through LOM and SEM. All specimens contained layers of globular grain with rolling-transverse texture and macrozones with extremely strong rolling texture. Each specimen displayed variations on the depth of deformed layer and had different, average depth between each other. BSE images revealed that the beta phase was still present at the deformed layer, up to the machined surface. Severe twinning occurred within the deformed layer in the alpha grains, while both alpha and beta grains were highly distorted. The average depth of deformation was directly related to the fatigue lives of the specimens, with an abrupt increase in cycles to failure for less aggressive machining conditions.

EBSD semi-qualitative tools captured the sub-surface plastic strain gradients and revealed strain concentration sites. Image quality numbers and low angle grain boundary density were superior to mean grain disorientation for plastic strains in machined specimens. EBSD also provided the means to categorize the various zones of the deformed region. That consisted of the severe plastic deformation layer, the intermediate strain and twinning zone and the low strain zone. The vast majority of the twins were compressive, but a few tensile ones were still present. Strain gradients along and across the machined surface were detected and were correlated to the existing microstructure and the drilling process. EBSD verified the preliminary correlation of plastic strain depth with fatigue performance. However, all specimens had identical microstructural features/defects and stress concentration.

Residual stresses were successfully measured with a localized, stress relaxation method based on focused ion beam micromachining of slots on the decorated surface. The method was developed and validated on peened CP-Ti and spring steel specimens. Then it was transferred to the machined specimens. RS profiles extended to exactly the depth of the twins on peened CP-Ti and the peak occurred below the SPD zone. Low, intermediate and high, near surface, compressive stresses were measured according to the surface waviness. RS on machined specimens had a local or global compressive peak below the deformed layer and extended three to four times the depth of the deformed layer. Peak stresses could reach as high as half the yield stress. Tensile stresses were recorded within

the deformed region, either near the drilled surface or sub-surface within the deformed region for most specimens. More aggressive drilling conditions resulted in deeper plastic and elastic strain fields. The variation of PE and RS profiles was correlated to the existing microstructure by LOM images and to the machining process through simplified FE simulations of cutting.

Surface roughness, microstructural defects, plastic strain gradients and residual stresses were not leading to a clear failure mechanism. That was provided by the re-examination of the fracture surfaces, where the emphasis was placed on the machined surface at the location of the crack initiation area. It was found that pick-up sites existed in almost all cases of near surface crack initiation. The cross-sectioning of pick-up sites revealed voids within their thickness, which could potentially serve as the primary defect. Specimens with high fatigue lives had pickup sites with significantly lower size of pick-up sites. A combination of critical size and location within the highly stressed area could be the root cause of the low fatigue lives. Thus, differences in the performance of identical specimens could be explained based on the probabilistic nature of the generation of pick-up sites. The crack was propagating perpendicular through the SPD and then followed the deformed, up to the undeformed region where it continued again in right angle affected locally by the grain orientation.

7.2 Recommendations for future work

The current research work established beyond any reasonable doubt that the cause of the early fracture of drilled specimens were the pick-up sites. However, it was not possible to provide solid proof of the exact failure mechanism. Such a task requires a different skillset and experimental work. The start should me made with the evaluation of size and distribution of these defects on the machined surface. To this purpose, a modification of the surface roughness algorithms is required based on the abrupt changes of waviness when the roughness is eliminated (low pass filter). More importantly, a closer investigation of the pick-up sites is required to examine the plastic grain gradients on chip and matrix, the presence of voids on the chip and the interactions between matrix and chip before, during and after a fatigue test. FIB cross-sectional examination of the pick-up site with SE, SI, EBSD, chemical and mass analysis, combined with TEM or transmission EBSD (t-EBSD) on specimens from these locations would be more suitable for this application. The same analysis should be conducted directly on the crack initiation areas of the fracture surfaces. Moreover, micro- and nanoindentation studies could provide information about the state of the chip and the matrix. Nanoindentation studies

can be further extended with micro-testing of cantilevers and pillars prepared with FIB micromachining in the region(s) of interest. The FIB RS technique could also be implemented in the specific regions to build the complete picture of the main parameters affecting the fatigue life.

Specimens with globular grains (10 mm plate) should be fully examined because they have a more interesting distribution of fatigue lives and can have a more predictive behaviour. Macro-zones did not appear to influence the failure mechanism, but their presence could accelerate or decelerate the crack initiation and propagation stages. Their contribution to the fatigue performance should also be evaluated for those specific cases (8 mm plate), where the manufacturing processes fail to produce the desired microstructure. Most of the work was focused on the specimens with low and medium fatigue life. However, the proposed RS failure mechanism on high fatigue lives specimens should be further investigated and proved with a more thorough exploration of the RS in those specimens.

Aggressive drilling conditions could be regarded as rough passes for other machining operations and less aggressive as finishing passes. This enables the correlation between various cutting operations. The extent to which the pick-up sites can be generated with different machining conditions, operations, materials and tools and their contribution to fatigue life are the new research goals. Emphasis should be placed on the machined surface at the crack initiation area, which could have been neglected and the statistical representation of the size and distribution of pick-up sites in the critical locations.

In any case, a small number of fatigue tests should be carried out to complement the original datasets. The tests should include a baseline scenario of drilling plates were the deformed layers have been carefully ground and polished away. There is no longer the need to have fatigue specimens with full holes, so the specimens can be sectioned in half along their length, which will allow the examination of the pick-up sites during interrupted tests. A second scenario should then evolve around the effect of microstructural defects and residual stresses due to drilling. The appropriate specimen should have holes where only the roughness of the machined surface has been eliminated, leaving a deformed layer with reduced thickness. To this end, electro-polishing or mechanical polish with new, custom-made tools should be employed. Finally, it is essential to carry out an interrupted test on the ass drilled specimens and if necessary by the experimental results to the baseline and smooth specimens. The deburring operation on the ass-drilled specimens should be done to a higher standard to prevent the

introduction of additional defects. An in-situ fatigue test in an X-Ray tomographer [196] is an intriguing alternative, which could capture the crack initiation and small crack propagation.

Regarding the methods applied in the current research project, a number of improvements are available. Micro-hardness testing of tilted specimens with plastic strain gradients requires standardization. The plastic strain mapping of the specimens can be performed based on t-EBSD [197] [198], which will increase the overall resolution and the hit rate within the deformed regions. Elastic strain mapping with the high-resolution EBSD set up [152] must be completed and carried out because it is a technique complementary to FIB RS. Potentially, t-EBSD could be used for elastic strain mapping, but the stress relaxation can become an issue in the milled specimens are not wide enough to lock the stresses. FIB RS techniques could be also improved with the utilization of images with higher pixel resolution. A comparison between RS obtained from micro-XRD [54], synchrotron [54] [199], EBSD [152] and FIB [66] would prove the validity of the proposed FIB and EBSD techniques and allow them to become the cheap, fast and easy alternative to RS measurement.

The machined and peened specimens are ideal candidates for fundamental studies of crystal plasticity modeling, due to the favorable scale of the problem [200]. Three-dimensional, finite element models of the grain structure could provide the elastoplastic strain variations observed during shearing of the microstructure of the machined surface. Similar studies can be contacted to peened specimens for localized compression profiles. In both cases, the deformation behaviour of polycrystalline material with different grain sizes, crystal orientations, and phase distributions could be predicted for more process conditions. EBSD strain maps and FIB RS measurements could calibrate and validate the aforementioned models.

Appendix I - LOM

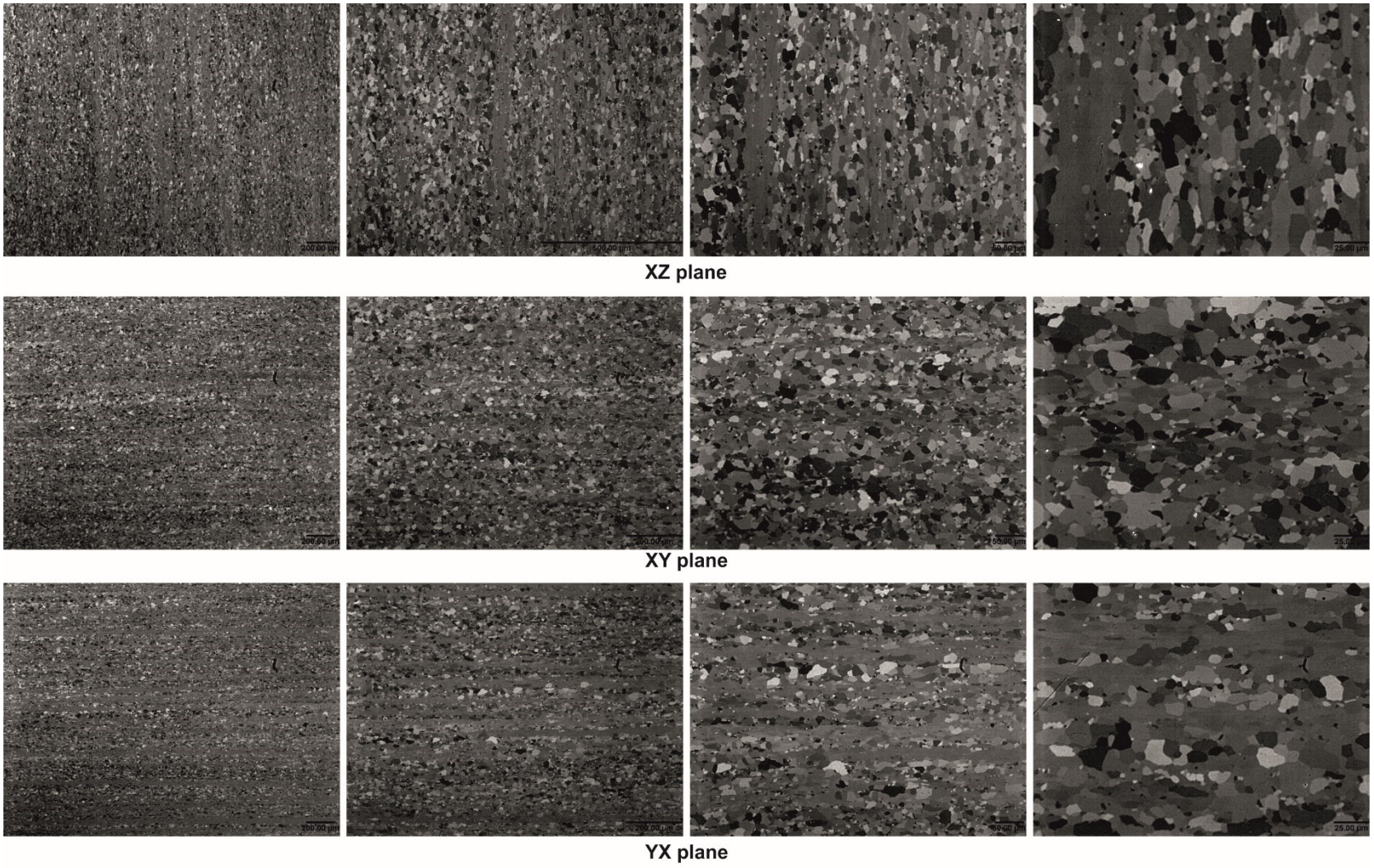

Figure AP- 1 Ti-6Al-4V 10 mm plates 3D bulk microstructure

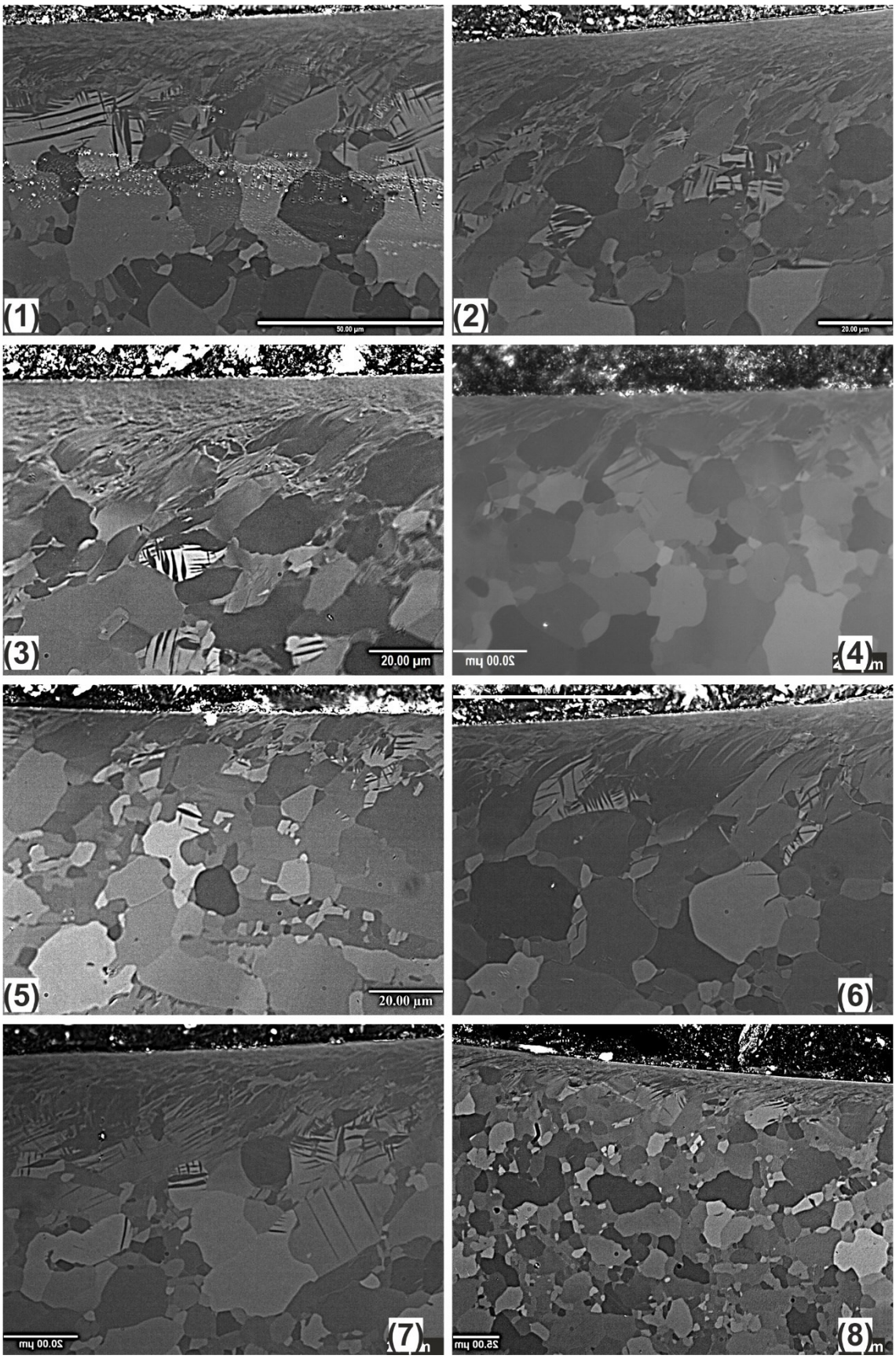

Figure AP- 2 LOM of deformed microstructures Specimens 1-8

Appendix II – Surface Topology

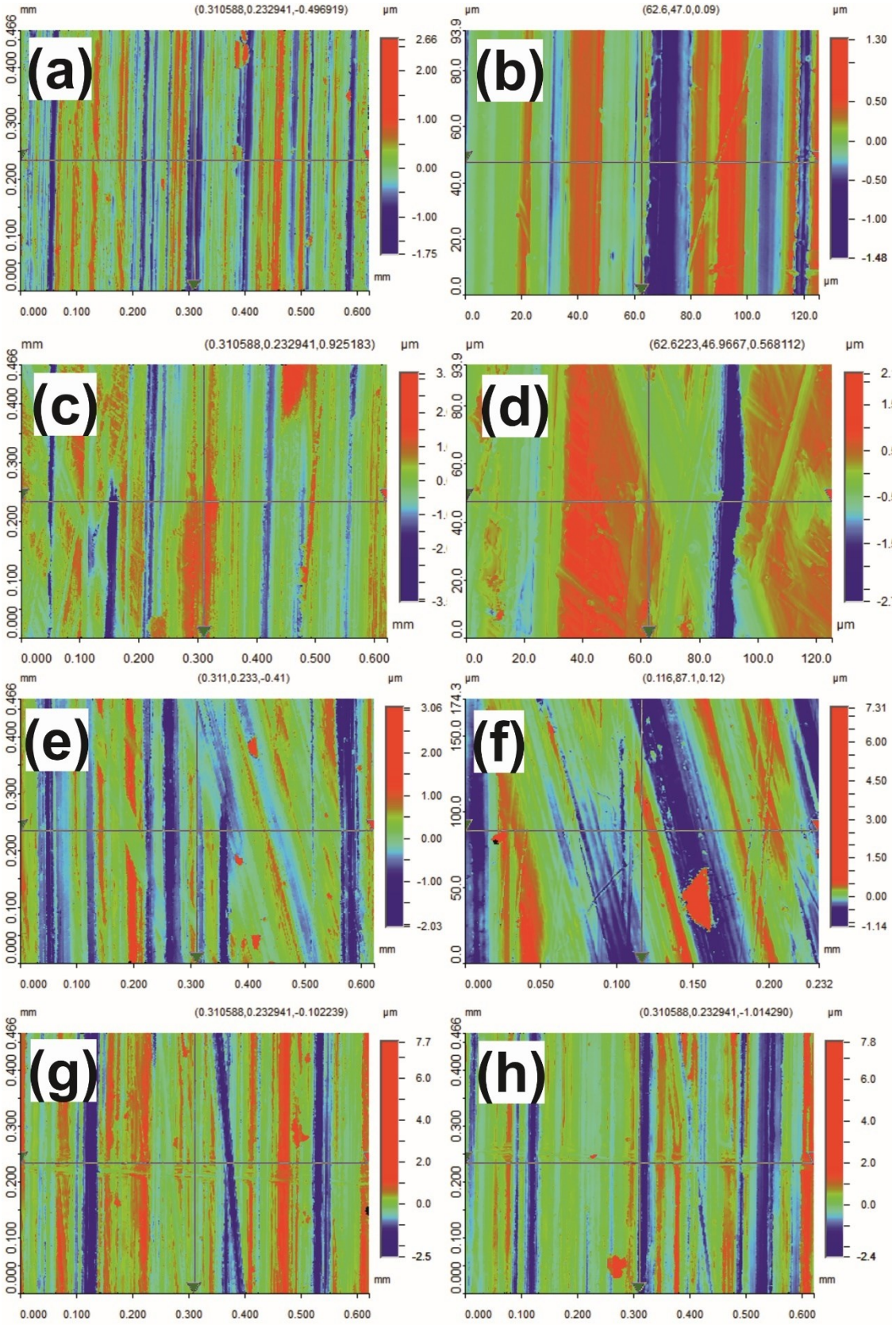

Figure AP- 3 Surface profiles of drilled specimens; a) Specimen 1 @ 10X; b) Specimen 1 @ 50X; c) Specimen 2 @ 10X; d) Specimen 2 @ 50X; e) Specimen 3 @ 10X; f) Specimen 3 @ 50X; g) Specimen 4 @ 10X; h) Specimen 4 @ 50X.

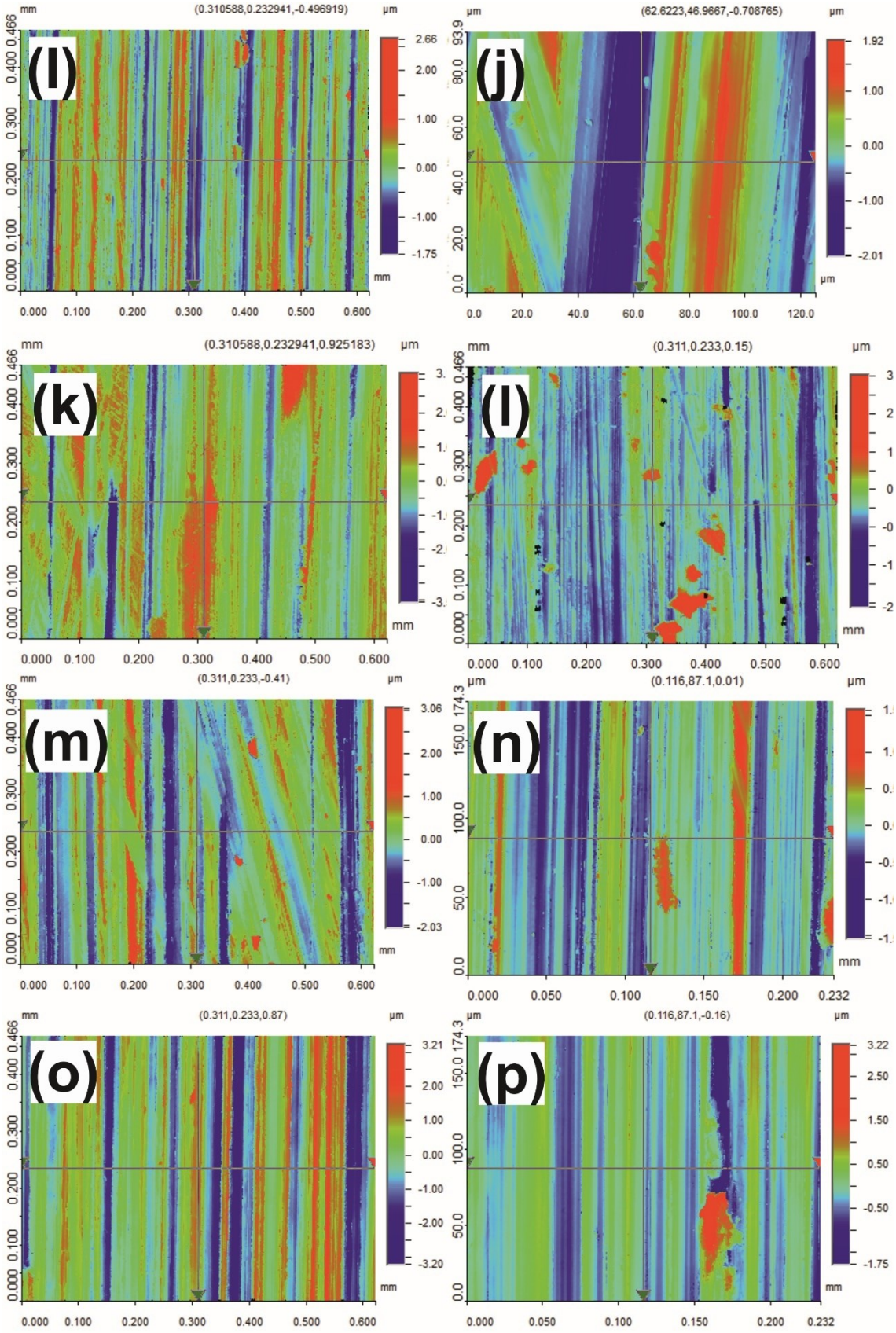

Figure AP- 4 Surface profiles of drilled specimens; i) Specimen 5 @ 10X; j) Specimen 5 @ 50X; k) Specimen 6 @ 10X; l) Specimen 6 @ 50X; m) Specimen 7 @ 10X; n) Specimen 7 @ 50X; o) Specimen 8 @ 10X; p) Specimen 8 @ 50X.

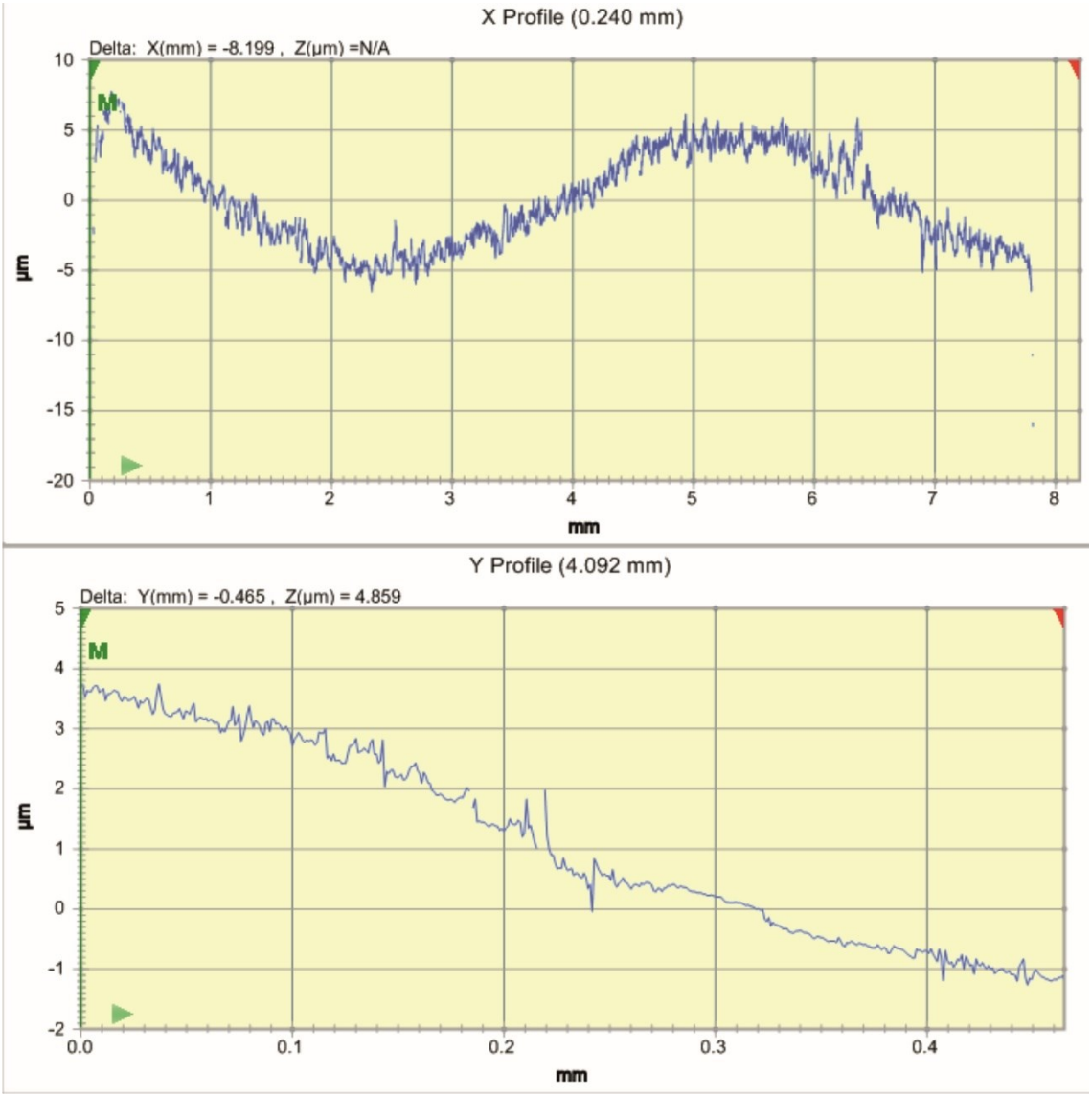

Figure AP- 5 Full depth hole surface profile, Specimen 1 @ 10X, cylindrical and tilt fit (waviness of hole and errors in cylindrical fitting algorithm)

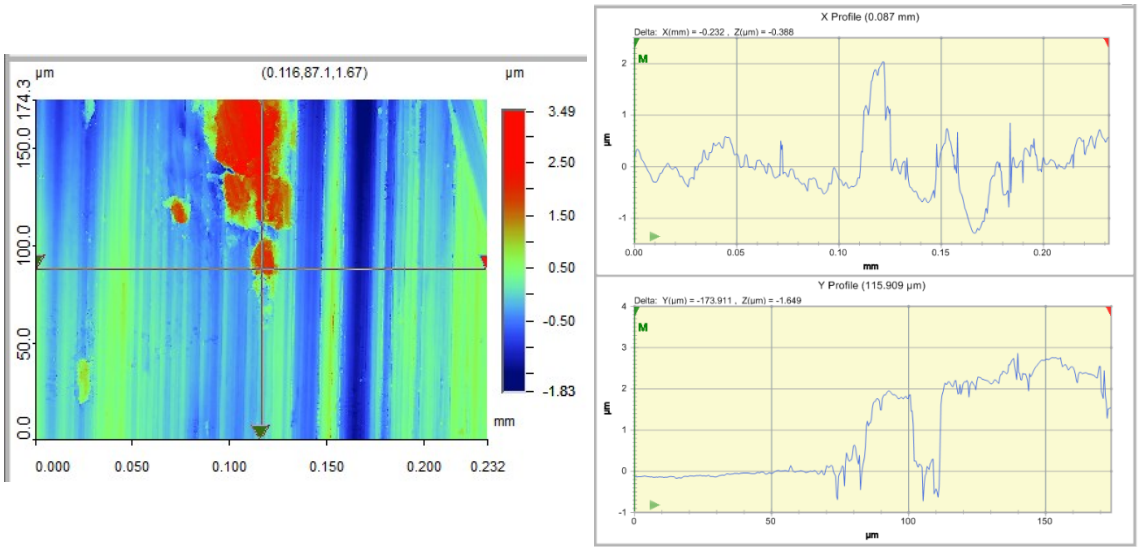

Figure AP- 6 Specimen 7 – Pick up site

Appendix III – SEM

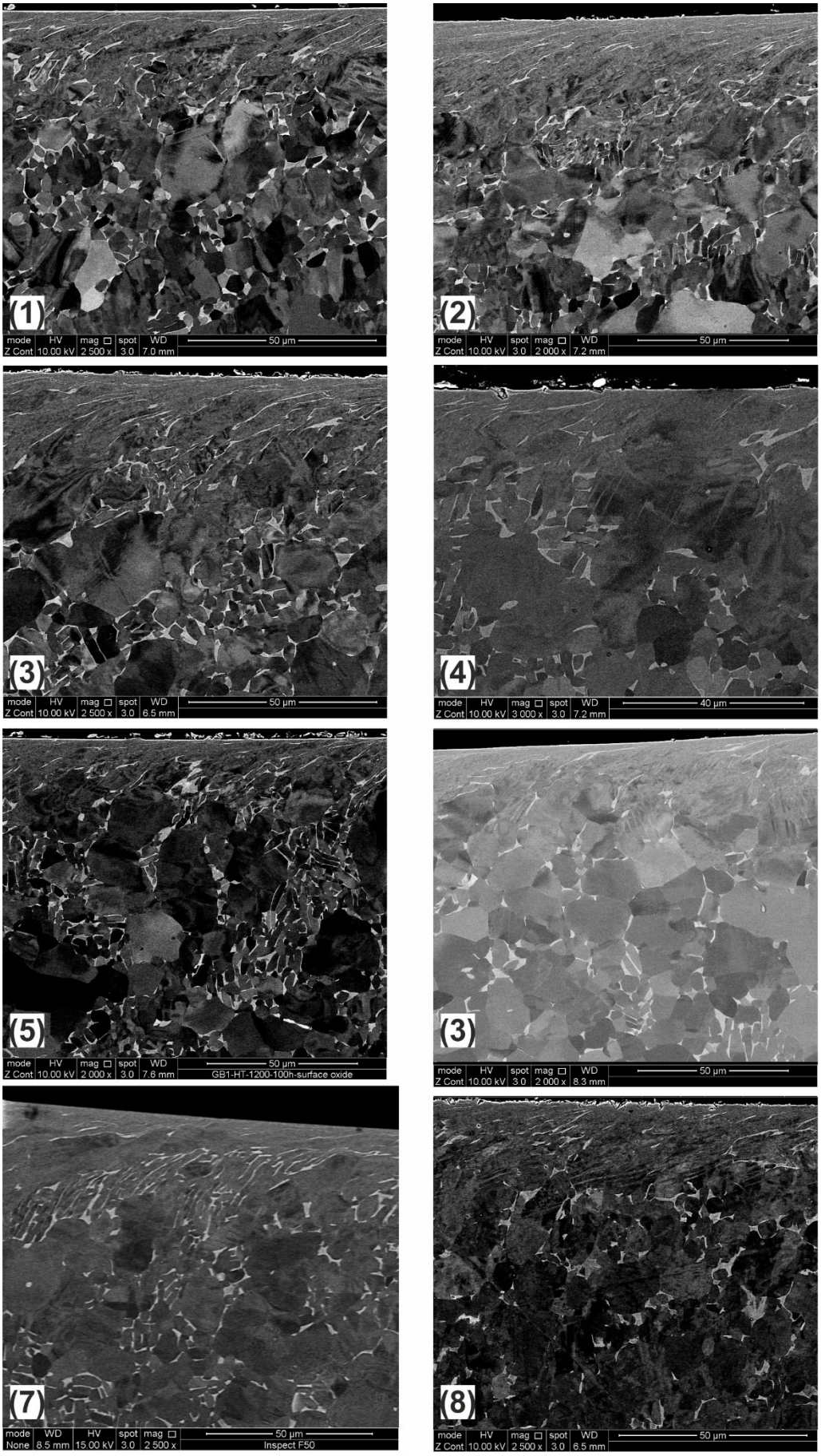

Figure AP- 7 SEM Specimens 1-6

Appendix IV – EBSD

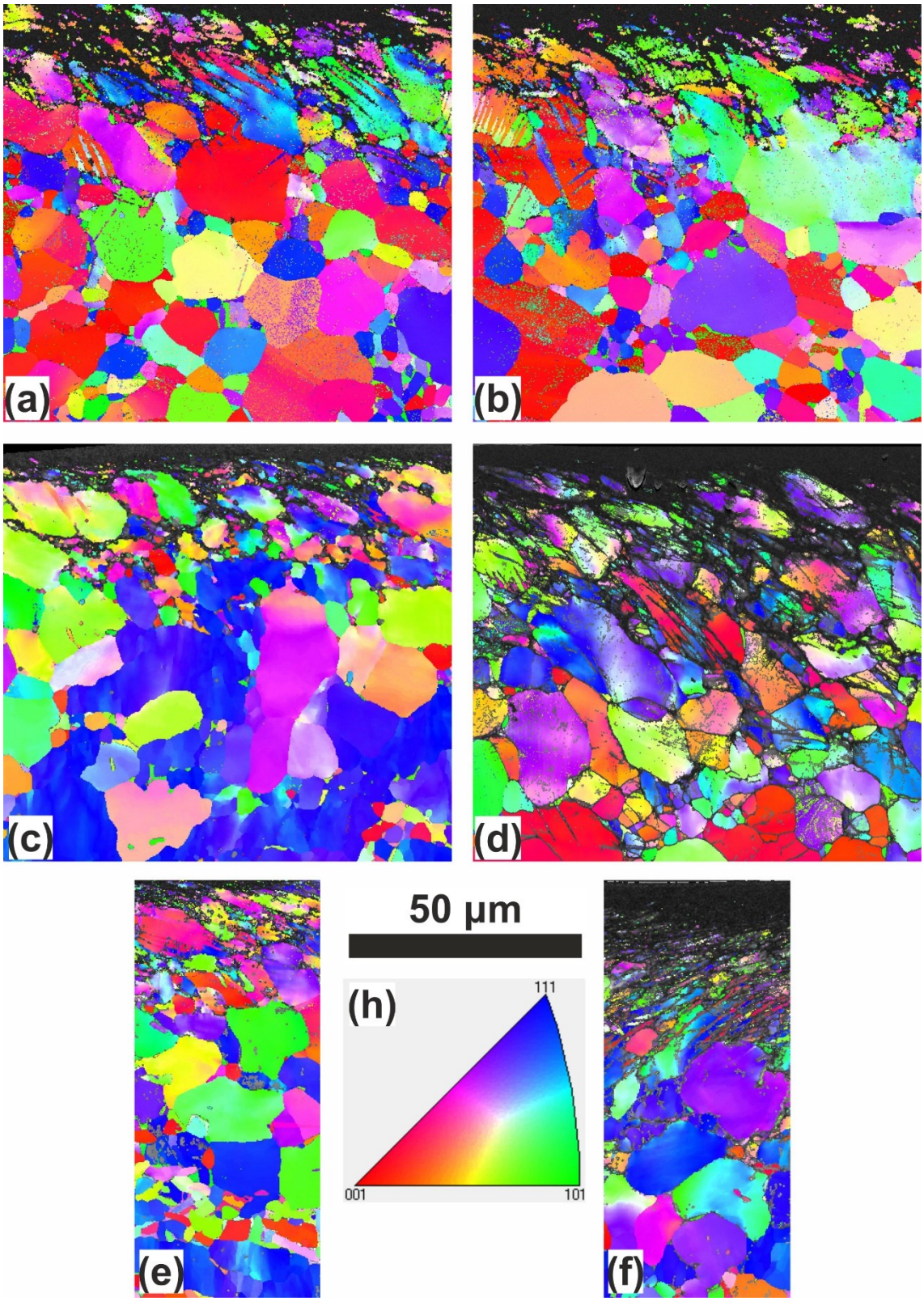

Figure AP- 8 EBSD IPF @ X maps; a) & b) Specimen 1; c) & e) Specimen 2; d) & f) Specimen 3; h) colour key

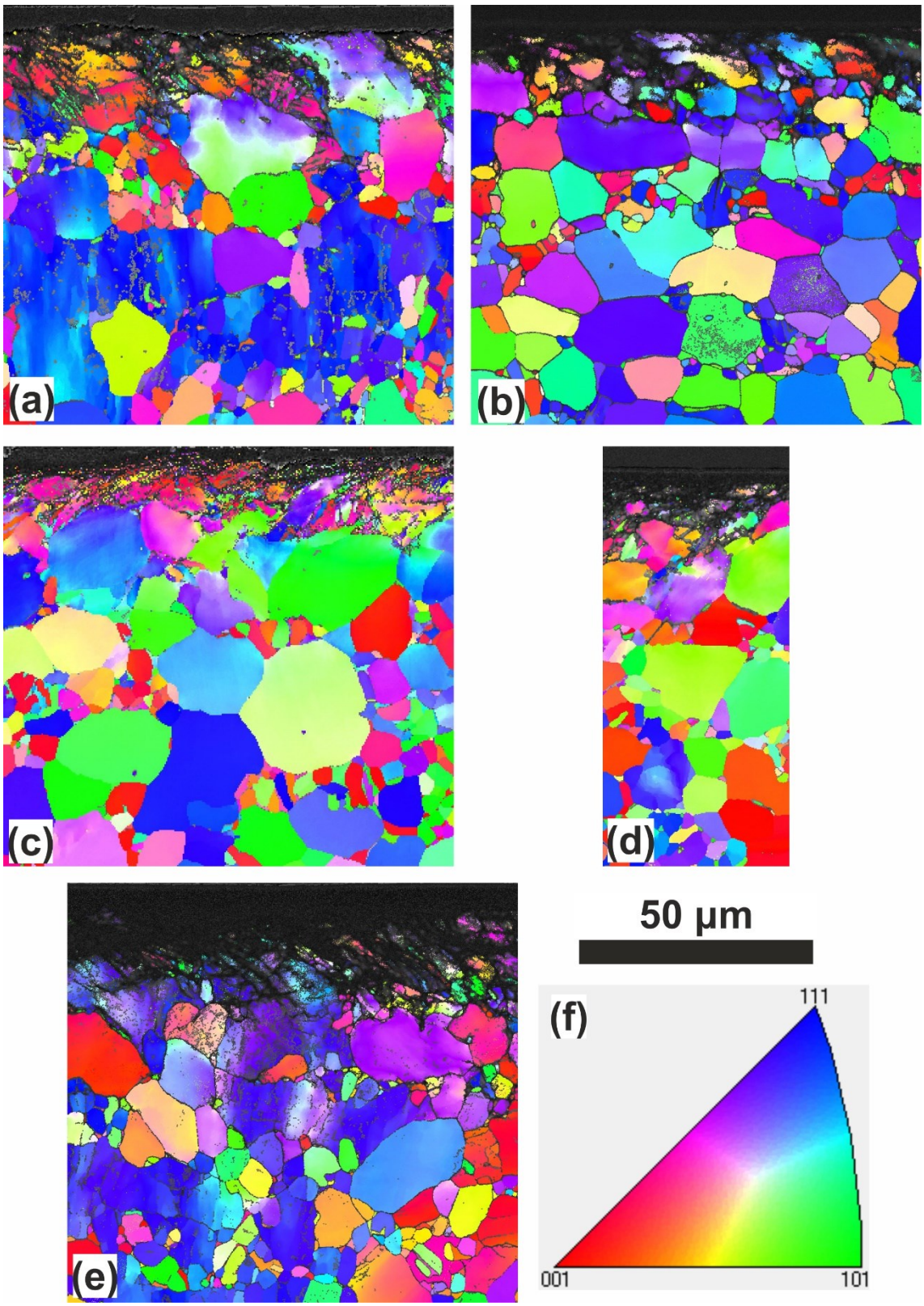

Figure AP- 9 EBSD IPF @ X maps; a) Specimen 4; b) Specimen 5; c) Specimen 6; d) Specimen 4; e) Specimen 7; f) colour key

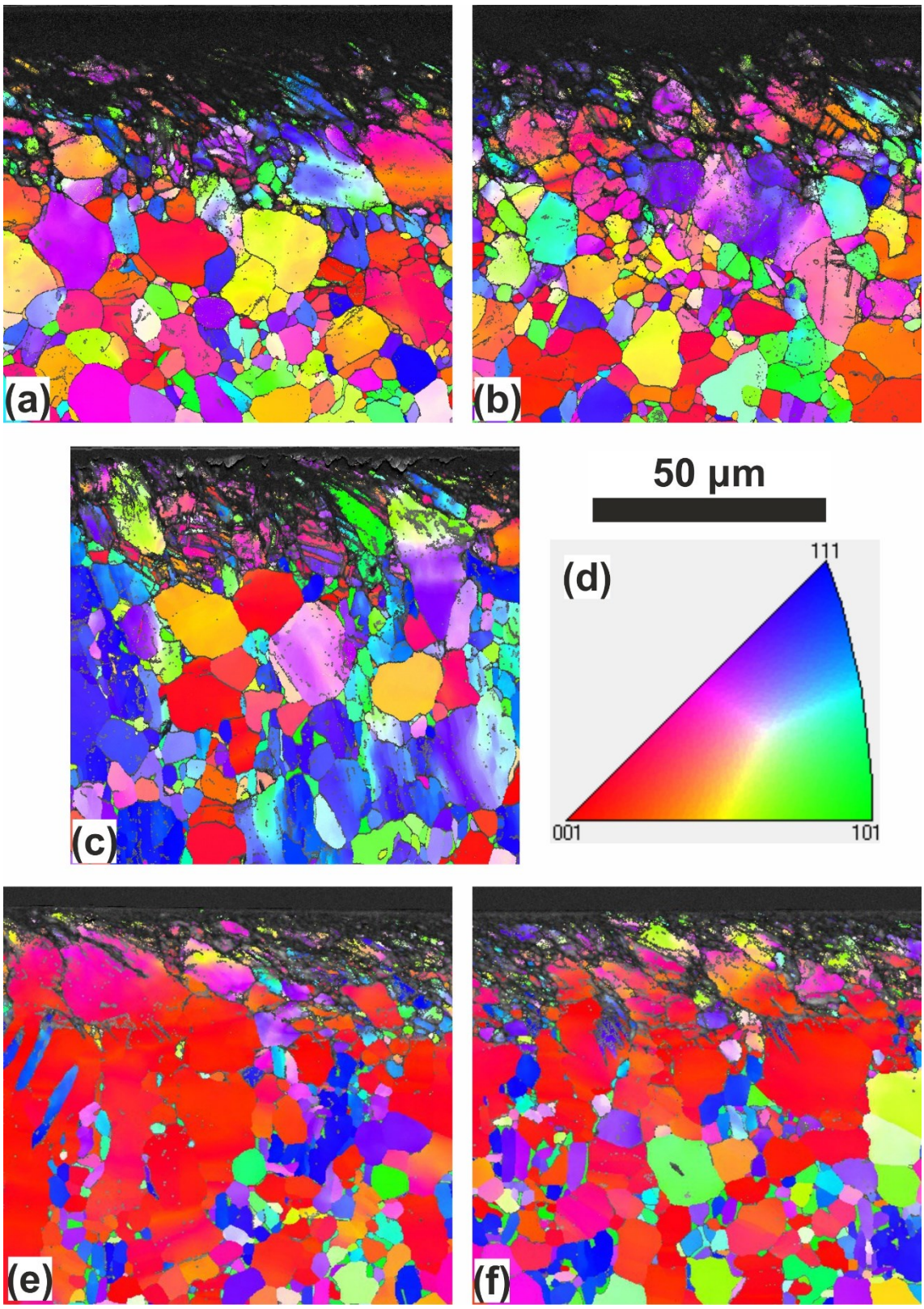

Figure AP- 10 EBSD IPF @ X maps; a) & b) Specimen 7; c), e) & f) Specimen 8; d) colour key

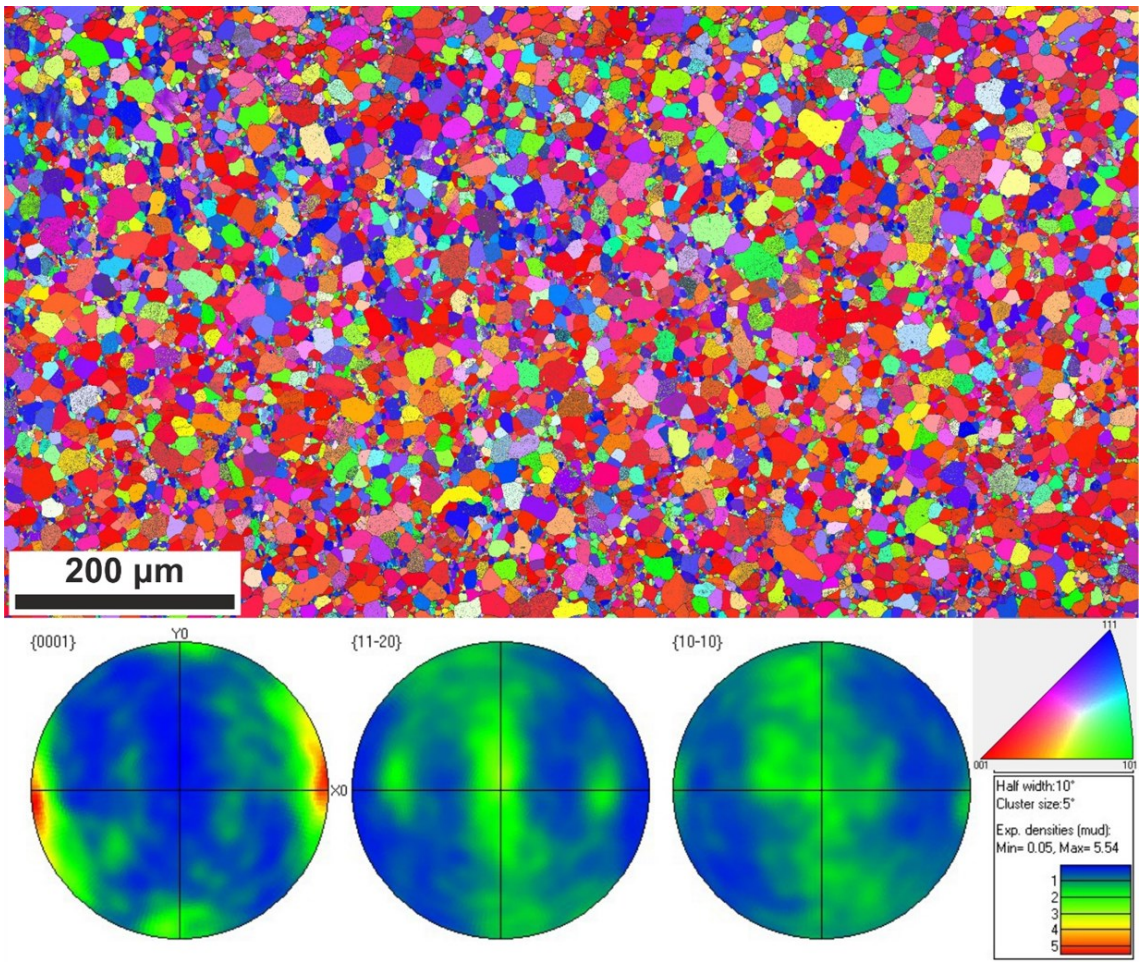

Figure AP- 11 Bulk microstructure 10 mm plate-Specimen 7; IPF-X map & Pole figures

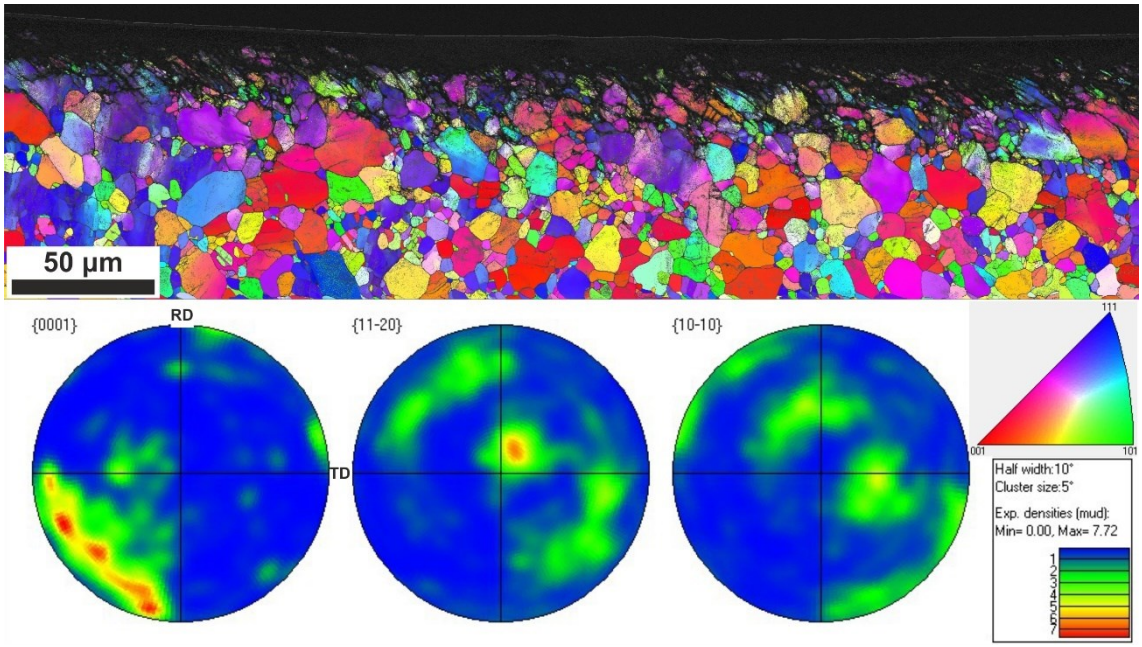

Figure AP- 12 Deformed microstructure 10 mm plate-Specimen 7; IPF-X map & Pole figures

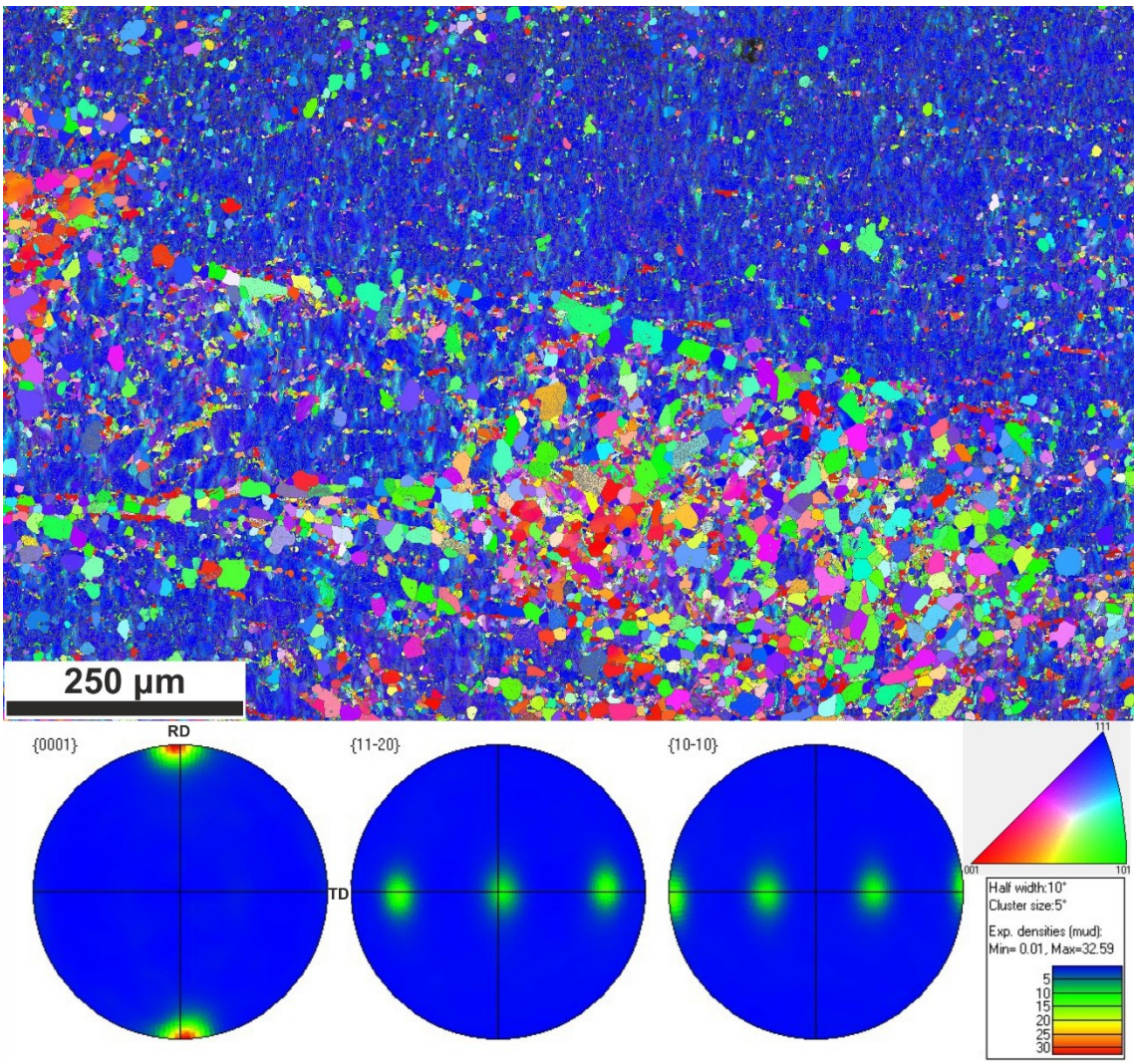

Figure AP- 13 Bulk microstructure 10 mm plate-Specimen 7 macrozones; IPF-X map & Pole figures

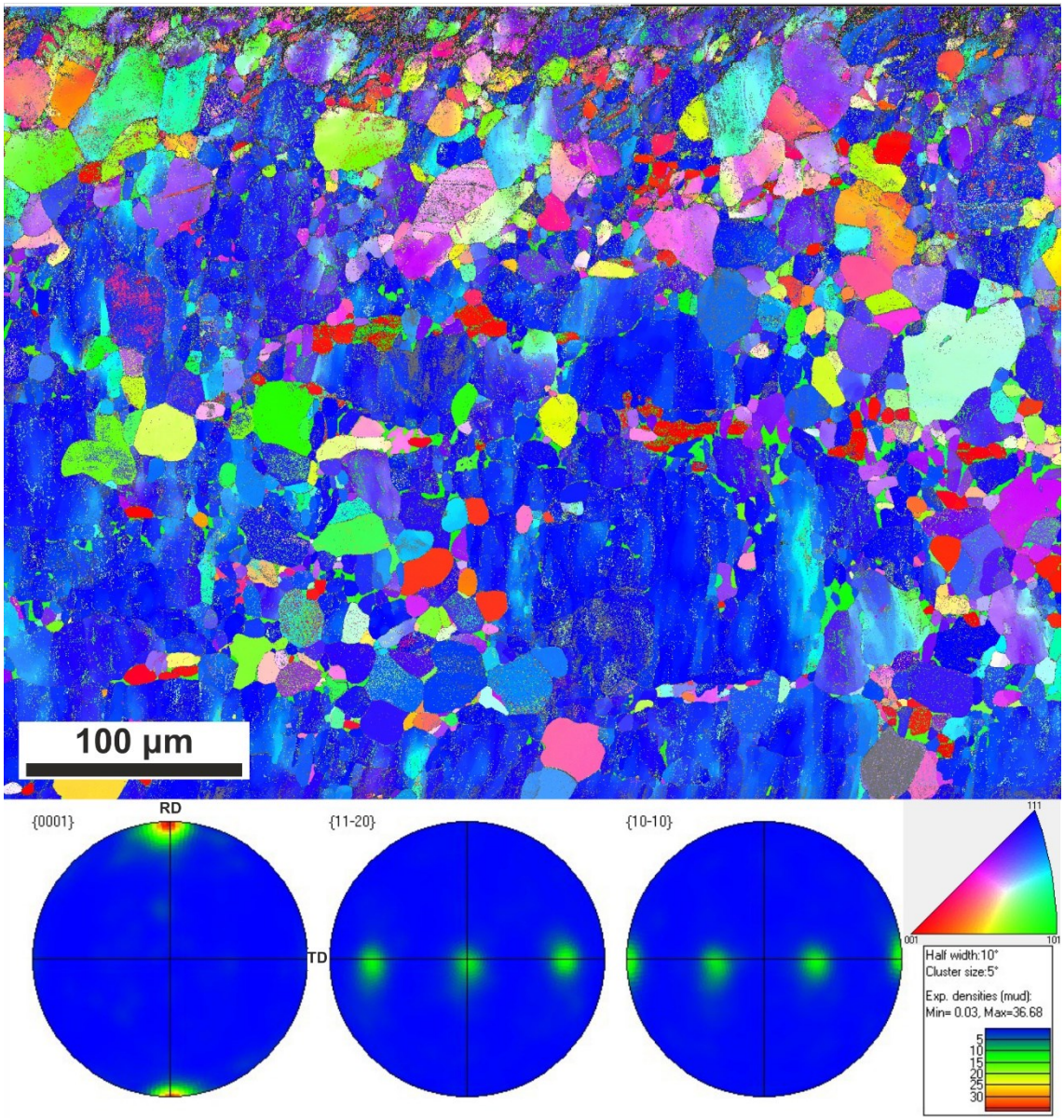

Figure AP- 14 Deformed microstructure 10 mm plate-Specimen 2; IPF-X map & Pole figures

Appendix V – Fracture Surfaces

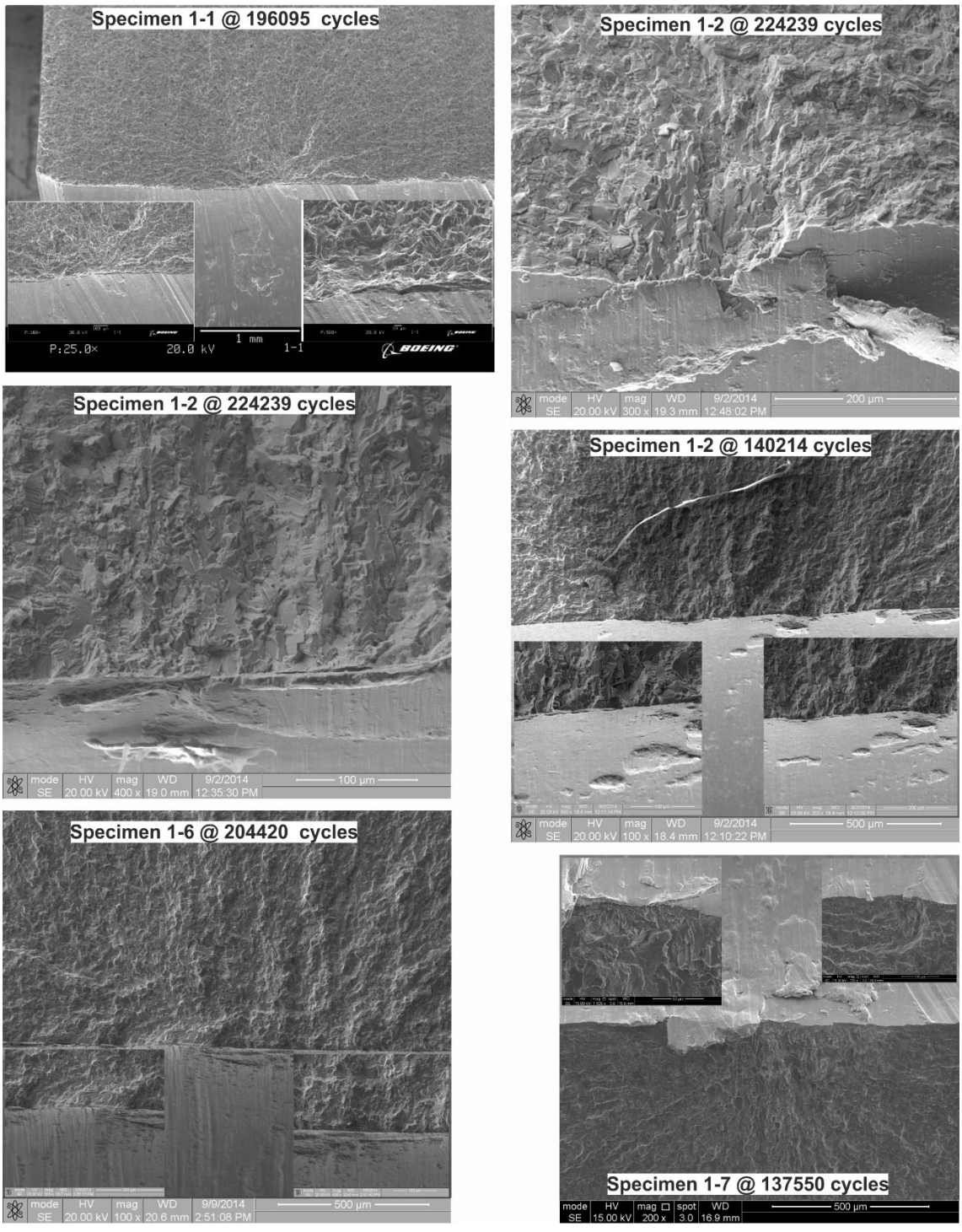

Figure AP- 15 Fractured Surfaces Part 1/5

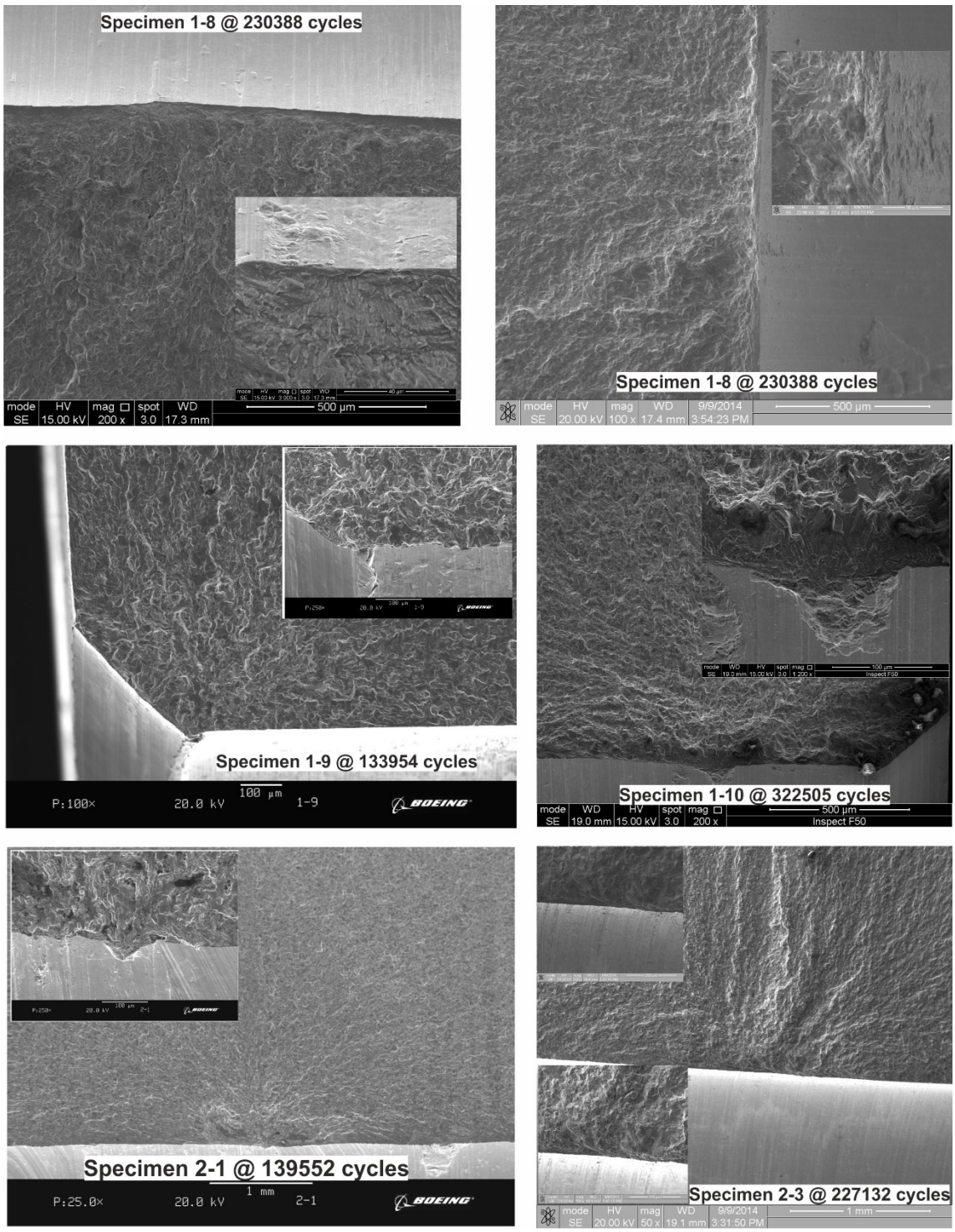

Figure AP- 16 Fractured Surfaces Part 2/5

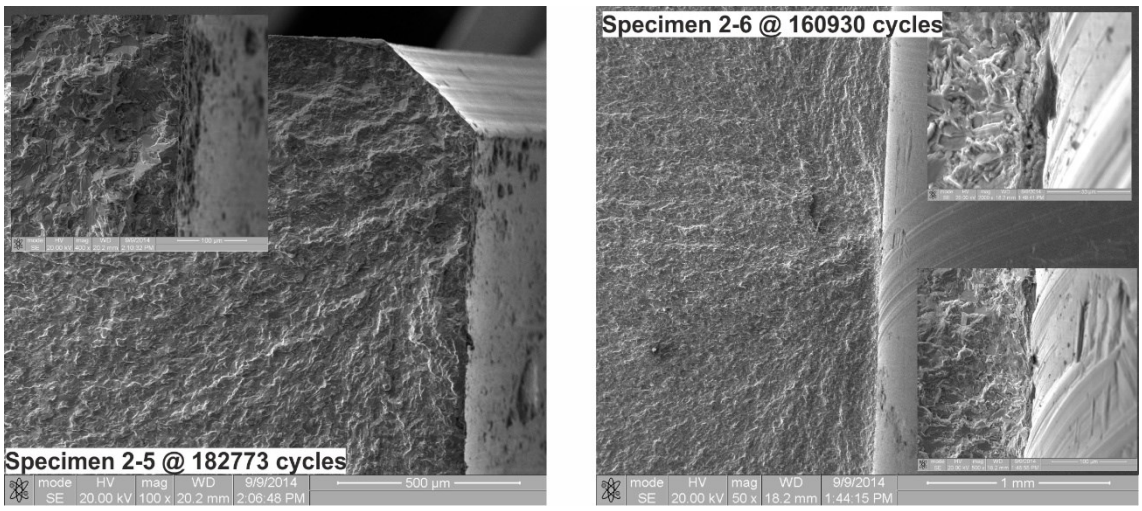

Figure AP- 17 Fractured Surfaces Part 3/5

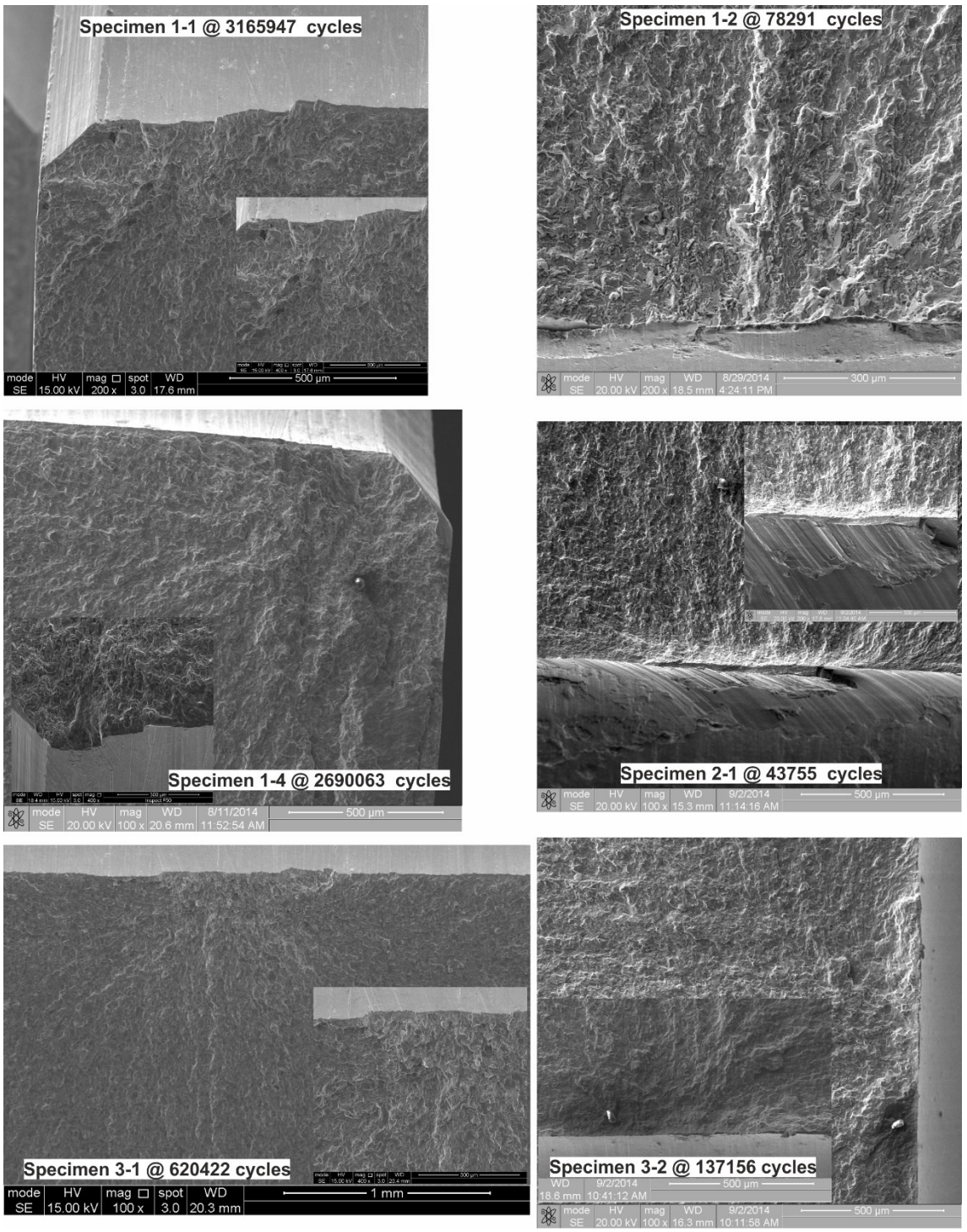

Figure AP- 18 Fractured Surfaces Part 4/5

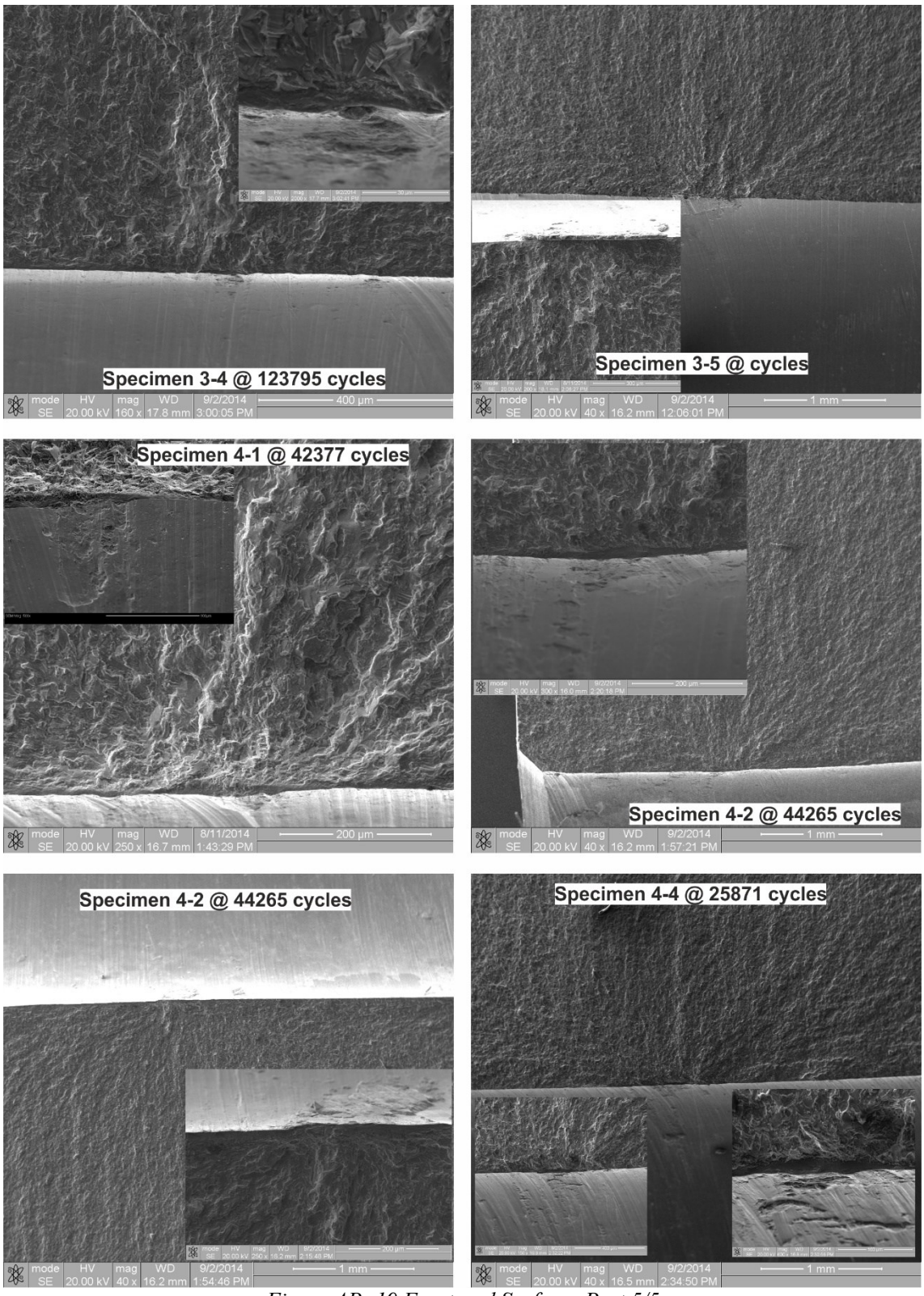

Figure AP- 19 Fractured Surfaces Part 5/5

Appendix VI – Machined Surfaces

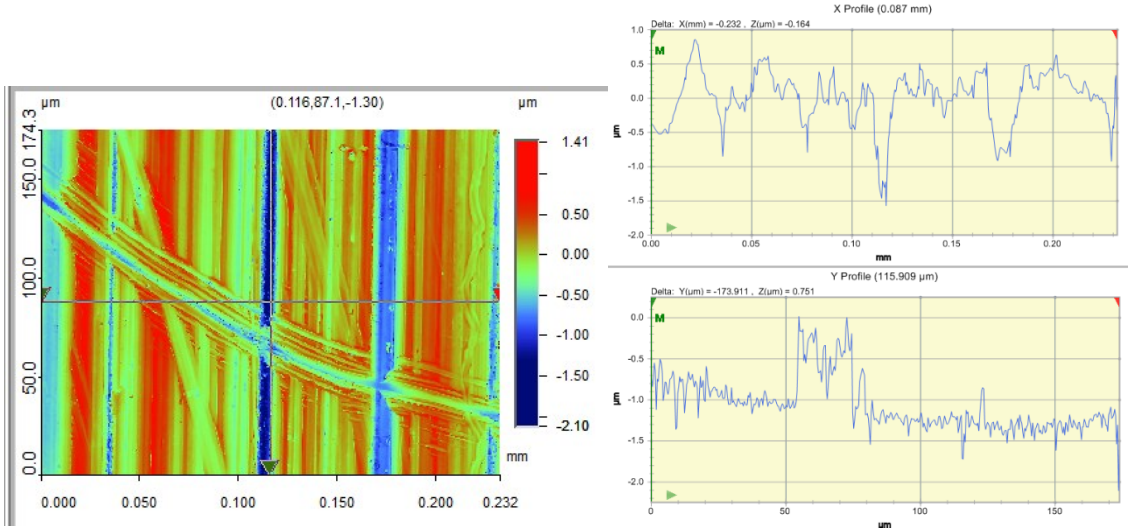

Figure AP- 20 Surface Topography – VSI – Retracting tool marks

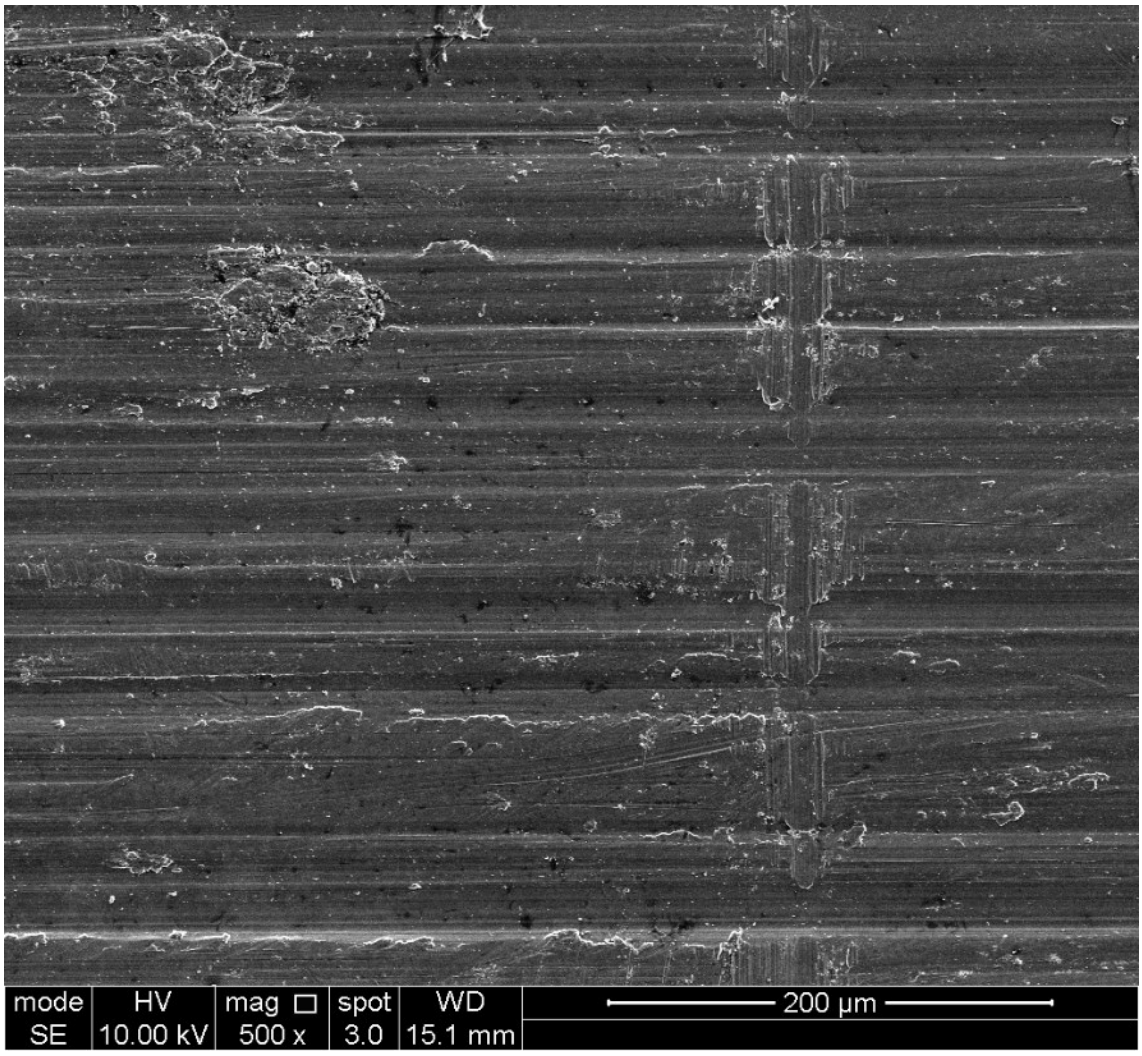

Figure AP- 21 Specimen 8 - 10 mm plate; Tool retracting tool marks

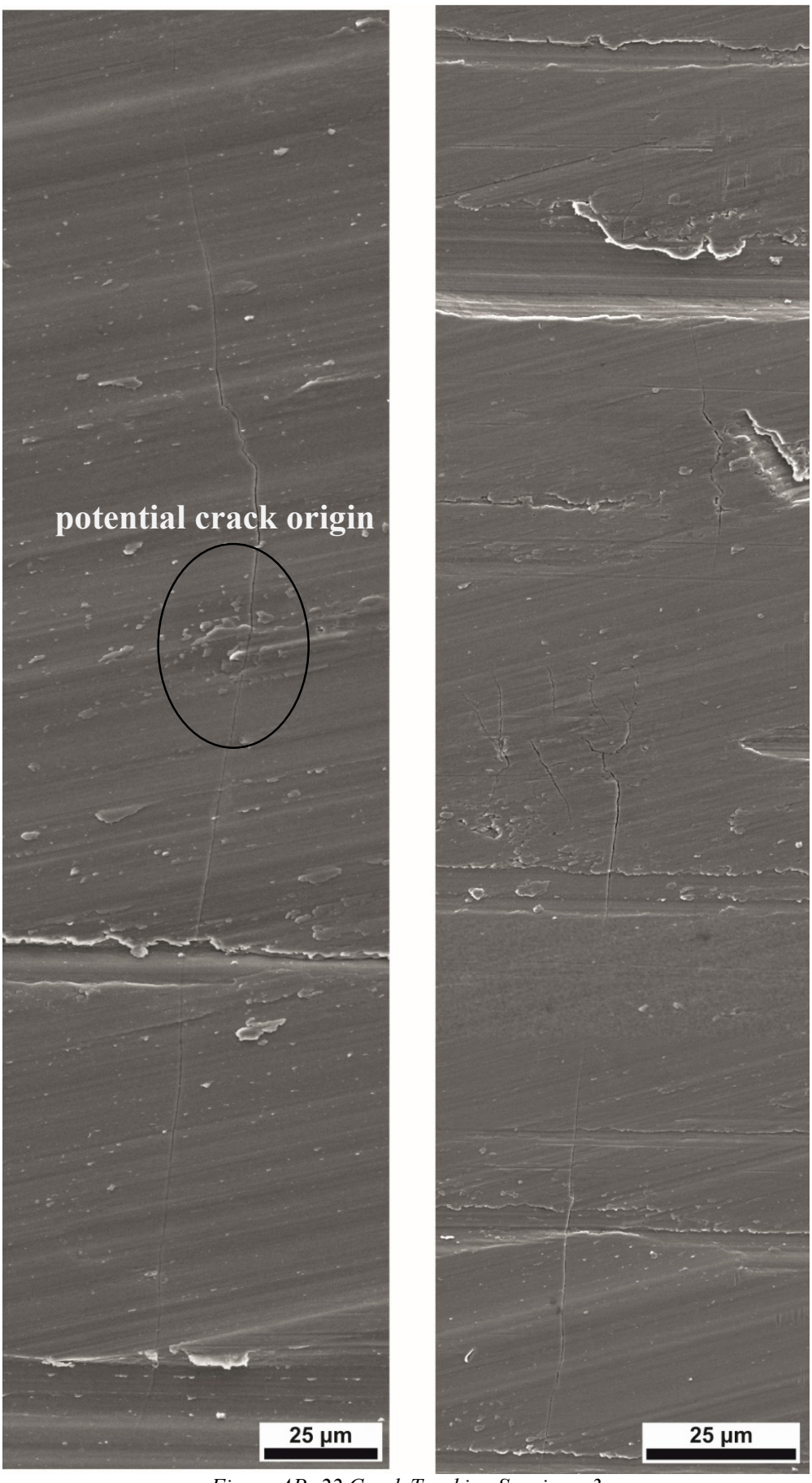

Figure AP- 22 Crack Tracking Specimen 3

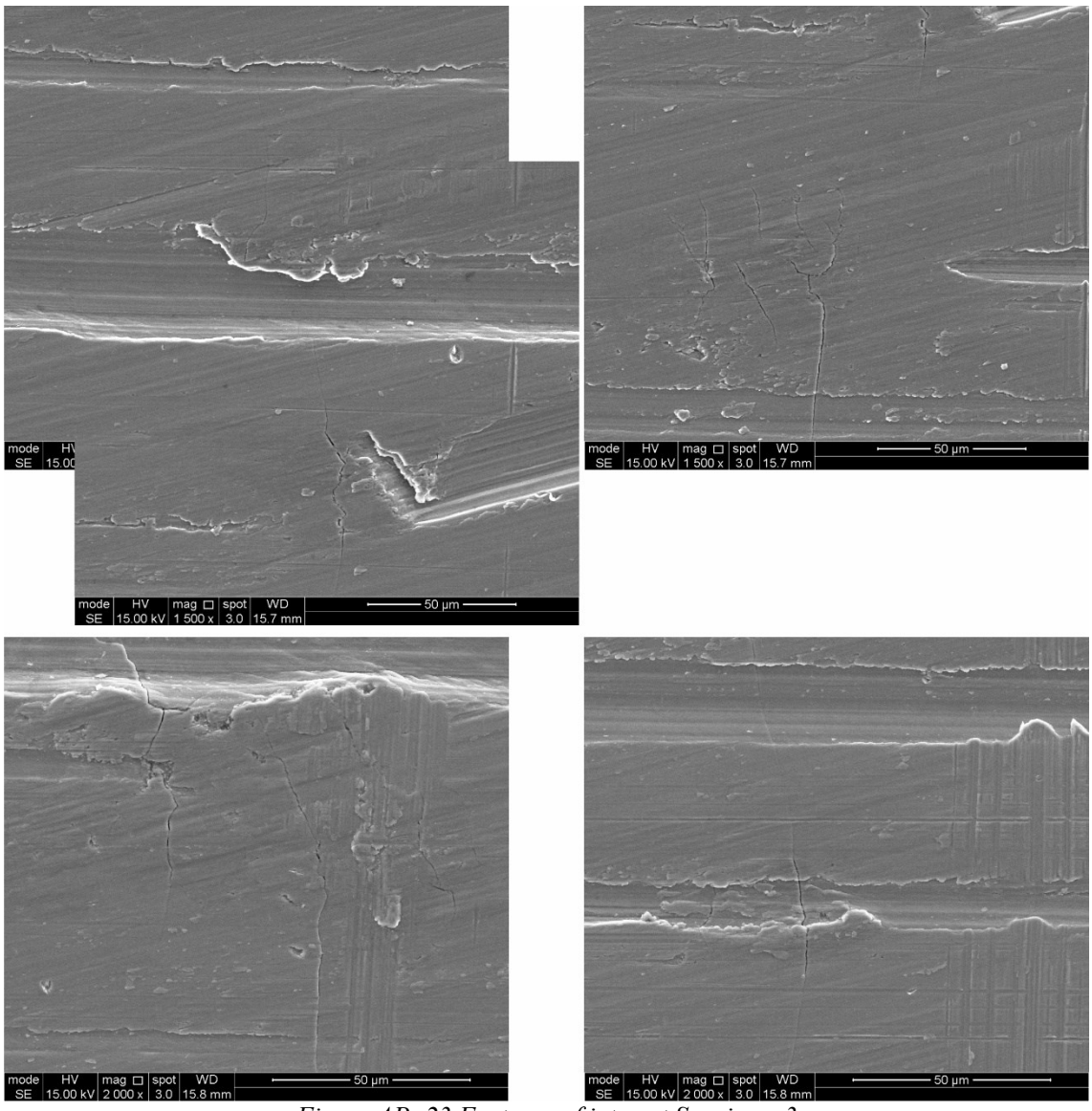

Figure AP- 23 Features of interest Specimen 3

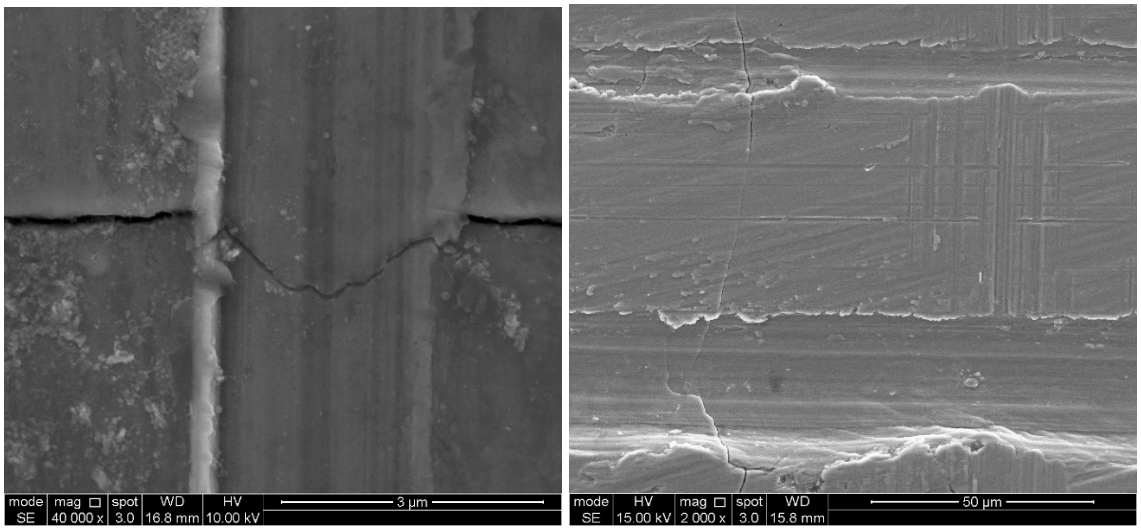

Figure AP- 24Change of crack path in a deep drilling marks

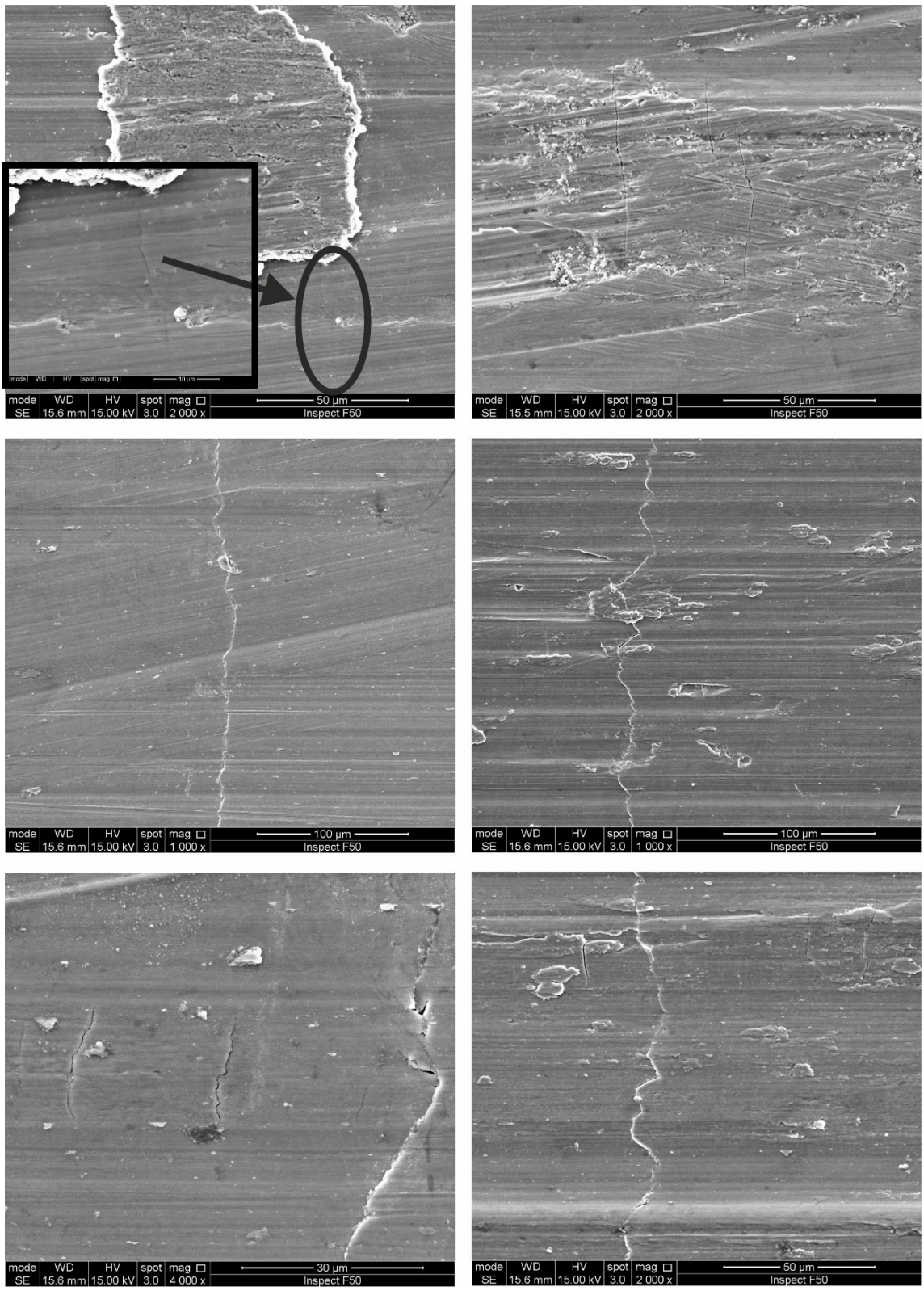

Figure AP- 25 Non-critical multi-crack initiation sites

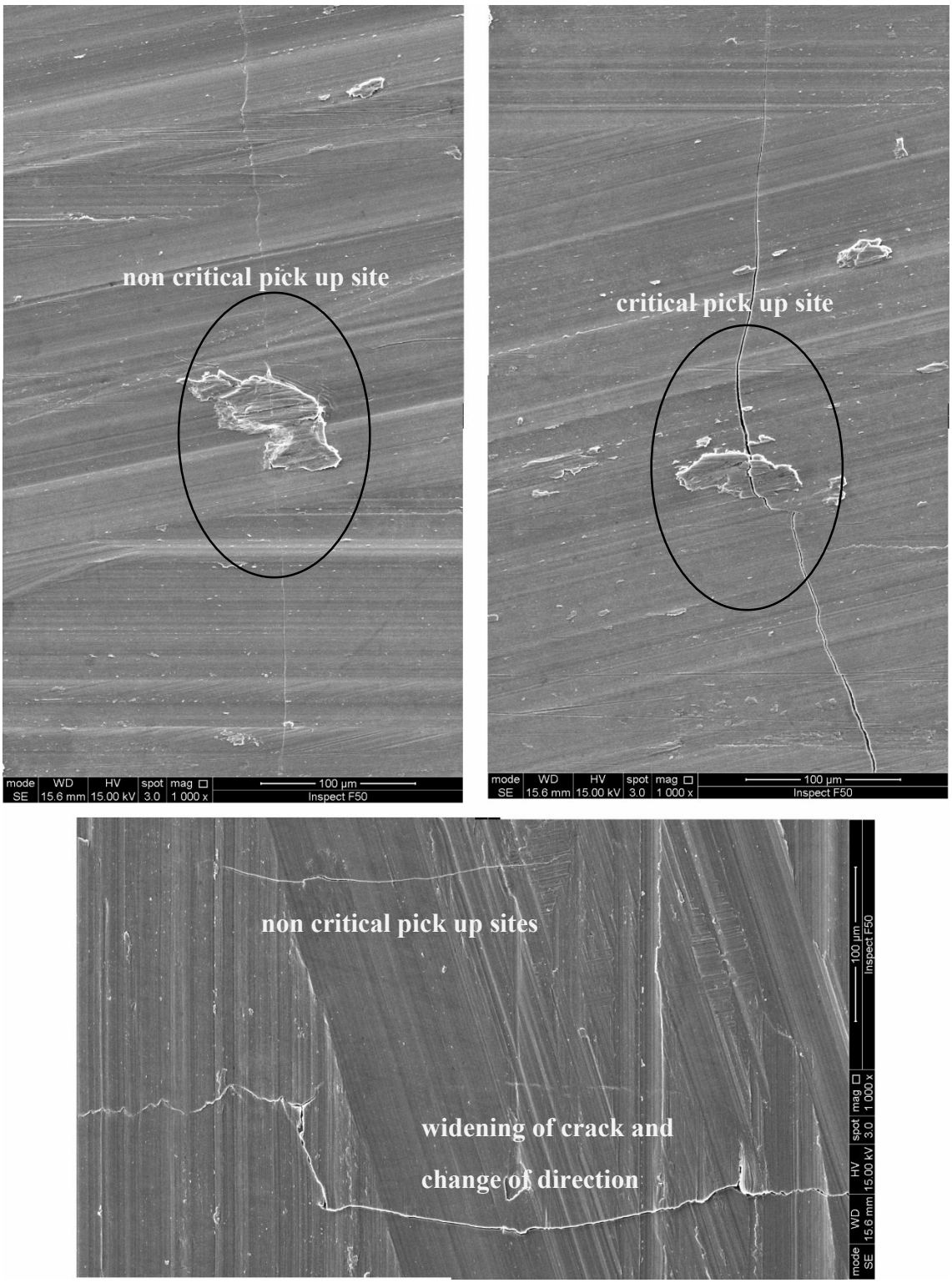

Figure AP- 26 Non-critical and critical crack initiation sites

Bibliography

[1] J. Castle, "Drilling Induced Fatigue Damage in Ti-6Al-4V," *Electronic Theses and Dissertations,* no. Paper 57, 2010.

[2] G. Lutjering and J. C. Williams, Titanium, Second ed., Heideberg: Springer, 2007.

[3] P. Wright and E. Trent, Metal Cutting, Butterworth–Heinemann, 2000.

[4] A. Schwartz, M. Kumar and B. Adams, Electron Backscatter Diffraction in Materials Science, New York: Springer, 2000.

[5] A. J. Schwartz, M. Kumar, B. L. Adams and D. P. Field, Electron Backscatter Diffraction in Materials Science Second Edition, New York: Springer, 2009.

[6] P. Withers and H. Bhadeshia, "Residual stress part 1 - Measurement techniques," *Materials Science and Technology,* vol. 17, no. 4, pp. 355-365, 2001.

[7] M. Thomas and M. Jackson, "The role of temperature and alloy chemistry on subsurface deformation mechanisms during shot peening of titanium alloys," *Scripta Materialia,* vol. 66, p. 1065–1068, 2012.

[8] I. P. Polmear, Light Alloys: From Traditional Alloys to Nanocrystals, Oxford: Elsevier, 2005.

[9] G. Lütjering and J. C.Williams, Titanium: Engineering Materials and Processes, Berlin: Springer, 2007.

[10] C. Leyens and M. Peters, Titanium and Titanium Alloys: Fundamentals and Applications, Online Edition ed., Cologne: Wiley-VCH Verlag GmbH & Co. KGaA, 2005.

[11] W. Kroll, "The production of ductile titanium," *Transactions of American Electrochemical Society,* vol. 78, pp. 35-47, 1940.

[12] G. F. D. F. T. Chen, "Direct electrochemical reduction of titanium dioxide to titanium in molten calcium chloride," *Nature,* vol. 407, no. 6802, pp. 361-364, 2000.

[13] W. D. Callister and D. G. Rethwisch, Materials Science and Engineering: An Introduction, New York: John Wiley & Sons, 2007.

[14] ASM International Handbook Comitee, ASM Handbook: Volume 4, Heat Treating, Ohio: ASM International, 1991.

[15] O. Engler and V. Randle, Introduction to Texture Analysis 2nd Edition, New York: CRC Press Tayylor & Francis Group, 2010.

[16] D. A. Stephenson and J. S. Agapiou, Metal Cutting Theory and Practice, Boca Raton: CRC Press, 2016.

[17] M. Field and J. Kahles, “REVIEW OF SURFACE INTEGRITY OF MACHINED COMPONENTS,” *Ann CIRP,* vol. 20, no. 2, pp. 153-163, 1971.

[18] I. Jawahir, E. Brinksmeier, R. M'Saoubi, D. Aspinwall, J. Outeiro, D. Meyer, D. Umbrello and A. Jayal, “Surface integrity in material removal processes: Recent advances,” *CIRP Annals,* vol. 60, no. 2, pp. 603-626, 2011.

[19] R. M'Saoubi, J. Outeiro, H. Chandrasekaran, O. Dillon and I. Jawahir, “A review of surface integrity in machining and its impact on functional performance and life of machined products,” *International Journal of Sustainable Manufacturing,* vol. 1, no. 1-2, pp. 203-236, 2008.

[20] D. Ulutan and T. Ozel, “Machining induced surface integrity in titanium and nickel alloys: A review,” *International Journal of Machine Tools and Manufacture,* vol. 51, no. 3, p. 250–280, 2011.

[21] S. Selvam and C. Sujatha, “Twist drill deformation and optimum drill geometry,” *Computers & Structures,* vol. 57, no. 3, p. 903–914, 1995.

[22] R. Williams, “A Study of the Drilling Process,” *Journal of Engineering for Industry,* vol. 96, no. 4, pp. 1207-1215, 1974.

[23] K. Ren and J. Ni, “Analyses of Drill Flute and Cutting Angles,” *The International Journal of Advanced Manufacturing Technology,* vol. 15, no. 8, pp. 546-553, 1999.

[24] D. Stephenson and J. Agapiou, “Calculation of main cutting edge forces and torque for drills with arbitrary point geometries,” *International Journal of Machine Tools and Manufacture,* vol. 32, no. 4, pp. 521-538, 1992.

[25] M. Shalta and T. Altan, “Analytical modeling of drilling and ball end milling,” *Journal of Materials Processing Technology ,* vol. 98, no. 1, pp. 125-133, 2000.

[26] J. Strenkowski, C. Hsieh and A. Shihb, “An analytical finite element technique for predicting thrust force and torque in drilling,” *International Journal of Machine Tools and Manufacture,* vol. 44, no. 12-13, p. 1413–1421, 2004.

[27] M. Pirtini and I. Lazoglu, “Forces and hole quality in drilling,” *International Journal of Machine Tools and Manufacture,* vol. 45, no. 11, pp. 1271-1281, 2005.

[28] E. Bagci and B. Ozcelik, “Finite element and experimental investigation of temperature changes on a twist drill in sequential dry drilling,” *The International Journal of Advanced Manufacturing Technology,* vol. 28, no. 7, pp. 680-687, 2006.

[29] R. Li and A. Shih, “Finite element modeling of high-throughput drilling of TI-6AL-4V,” *Transactions of the North American Manufacturing Research Institution of SME,* vol. 35, pp. 73-80, 2007.

[30] O. Isbilir and E. Ghassemieh, “Finite Element Analysis of Drilling of Titanium Alloy,” *Procedia Engineering,* vol. 10, pp. 1877-1882, 2011.

[31] Y. Guo and D. Dornfeld, " Finite Element Modeling of Burr Formation Process in Drilling 304 Stainless Steel," *Journal of Manufacturing Science and Engineering,* vol. 122, no. 4, pp. 612-619, 1999.

[32] A. Attanasio, E. Ceretti, S. Rizzuti and D. M. F. Umbrello, "3D finite element analysis of tool wear in machining," *CIRP Annals - Manufacturing Technology,* vol. 57, no. 1, pp. 61-64, 2008.

[33] R. Komanduri and B. Von Turkovich, "New observations on the mechanism of chip formation when machining titanium alloys," *Wear,* vol. 69, no. 2, pp. 179-188, 1981.

[34] A. Vyas and M. Shaw, "Mechanics of saw-tooth chip formation in metal cutting," *Journal of Manufacturing Science and Engineering, Transactions of the ASME,* vol. 121, no. 2, pp. 163-172, 1999.

[35] A. Ginting and M. Nouari, "Surface integrity of dry machined titanium alloys," *International Journal of Machine Tools and Manufacture,* vol. 49, no. 3-4, pp. 325-332, 2009.

[36] A. Sharman, A. Amarasinghe and K. Ridgway, "Tool life and surface integrity aspects when drilling and hole making in Inconel 718," *Journal of Materials Processing Technology,* vol. 200, no. 1-3, pp. 424-432, 2008.

[37] S. Soo, R. Hood, D. Aspinwall, W. Voice and C. Sage, "Machinability and surface integrity of RR1000 nickel based superalloy," *CIRP Annals - Manufacturing Technology,* vol. 60, no. 1, pp. 89-92, 2011.

[38] J. Cantero, M. Tardío, J. Canteli, M. Marcos and M. Miguélez, "Dry drilling of alloy Ti-6Al-4V," *International Journal of Machine Tools and Manufacture,* vol. 45, no. 11, pp. 1246-1255, 2005.

[39] D. Dornfeld, J. Kim, H. Dechow, J. Hewson and L. Chen, "Drilling burr formation in titanium alloy, Ti-6Al-4V," *CIRP Annals - Manufacturing Technology,* vol. 48, no. 1, pp. 73-76, 1999.

[40] R. Li, P. Hegde and A. Shih, "High-throughput drilling of titanium alloys," *International Journal of Machine Tools and Manufacture,* vol. 47, no. 1, pp. 63-74, 2007.

[41] H. Takeyama and S. Kato, "Burrless Drilling by Means of Ultrasonic Vibration," *CIRP Annals - Manufacturing Technology,* vol. 40, no. 1, pp. 83-86, 1991.

[42] S. Chang and G. Bone, "Burr size reduction in drilling by ultrasonic assistance," *Robotics and Computer-Integrated Manufacturing,* vol. 21, no. 4-5, pp. 442-450, 2005.

[43] M. Thomas, S. Turner and M. Jackson, "Microstructural damage during high-speed milling of titanium alloys," *Scripta Materialia,* vol. 62, no. 5, pp. 250-253, 2010.

[44] P. Crawforth, B. Wynne, S. Turner and M. Jackson, “Subsurface deformation during precision turning of a near-alpha titanium alloy,” *Scripta Materialia,* vol. 67, no. 10, pp. 842-845, 2012.

[45] Y. Chou and C. Evans, “White layers and thermal modeling of hard turned surfaces,” *International Journal of Machine Tools and Manufacture,* vol. 39, no. 12, pp. 1863-1881, 1999.

[46] W. Österle and P. Li, “Mechanical and thermal response of a nickel-base superalloy upon grinding with high removal rates,” *Materials Science and Engineering A,* vol. 238, no. 2, pp. 357-366, 1997.

[47] P. Withers and H. Bhadeshia, “Residual stress part 2 - Nature and origins,” *Materials Science and Technology,* vol. 17, no. 4, pp. 366-375, 2001.

[48] P. Withers, “Residual stress and its role in failure,” *Reports on Progress in Physics,* vol. 70, no. 12, pp. 2211-2264, 2007.

[49] W. P. Koster and M. Field, “EFFECT OF MACHINING VARIABLES ON THE SURFACE AND STRUCTURAL INTEGRITY OF TITANIUM,” *Proceedings of the North American Manufacturing Research Conference, SME,* vol. 2, p. 67–87, 1973.

[50] E. Brinksmeier, J. Cammett, W. König, P. Leskovar, J. Peters and H. Tönshoff, “Residual Stresses - Measurement and Causes in Machining Processes,” *CIRP Annals - Manufacturing Technology,* vol. 31, no. 2, pp. 491-510, 1982.

[51] Y. Guo, W. Li and I. Jawahir, “Surface integrity characterization and prediction in machining of hardened and difficult-to-machine alloys: A state-of-art research review and analysis,” *Machining Science and Technology,* vol. 13, no. 4, pp. 437-470, 2009.

[52] B. Cullity and S. Stock, Elements of X-Ray Diffraction Third Edition, ESSEX: Pearson, 2014.

[53] M. Fitzpatrick, A. Fry and P. Holdway, “Determination of Residual Stresses by X-ray Diffraction – Issue 2, Measurement Good Practice Guide No. 52,” National Physical Laboratory, Middlesex,, 2005.

[54] P. Withers, M. Turski, L. Edwards, P. Bouchard and D. Buttle, “Recent advances in residual stress measurement,” *International Journal of Pressure Vessels and Piping,* vol. 85, no. 3, pp. 118-127, 2008.

[55] M. Prime, “Residual stress measurement by successive extension of a slot: The crack compliance method,” *Applied Mechanics Reviews,* vol. 52, no. 2, pp. 75-96, 1999.

[56] G. Schajer and M. Prime, “Use of inverse solutions for residual stress measurements,” *Journal of Engineering Materials and Technology, Transactions of the ASME,* vol. 128, no. 3, pp. 375-382, 2006.

[57] G. Schajer, “Measurement of non-uniform residual stresses using the hole-drilling method. Part I. Stress calculation procedures,” *Journal of Engineering Materials and Technology, Transactions of the ASME,* vol. 110, no. 4, pp. 338-343, 1988.

[58] G. Schajer, “Measurement of non-uniform residual stresses using the hole-drilling method. Part II. Practical application of the integral method,” *Journal of Engineering Materials and Technology, Transactions of the ASME,* vol. 110, no. 4, pp. 344-349, 1988.

[59] P. Grant, J. Lord and P. Whitehead, “The Measurement of Residual Stresses by the Incremental Hole Drilling Technique; Measurement Good Practice Guide No. 53 - Issue 2,” National Physical Laboratory, Middlesex, 2006.

[60] M. Steinzig and E. Ponslet, “Residual stress measurement using the hole drilling method and laser speckle interferometry: Part I,” *Experimental Techniques,* vol. 27, no. 3, pp. 43-46, 2003.

[61] E. Ponslet and M. Steinzig, “Residual stress measurement using the hole drilling method and laser speckle interferometry Part II: Analysis technique,” *Experimental Techniques,* vol. 27, no. 4, pp. 17-21, 2003.

[62] E. Ponslet and M. Steinzig, “Technology application series: Residual stress measurement using the hole drilling method and laser speckle interferometry - Part III: Analysis technique,” *Experimental Techniques,* vol. 27, no. 5, pp. 45-48, 2003.

[63] M. Steinzig and T. Takahashi, “Residual stress measurement using the hole drilling method and laser speckle interferometry part IV: Measurement accuracy,” *Experimental Techniques,* vol. 27, no. 6, pp. 59-63, 2003.

[64] G. Schajer and M. Steinzig, “Full-field calculation of hole drilling residual stresses from electronic speckle pattern interferometry data,” *Experimental Mechanics,* vol. 45, no. 6, pp. 526-532, 2005.

[65] M. Prime, “Cross-sectional mapping of residual stresses by measuring the surface contour after a cut,” *Journal of Engineering Materials and Technology, Transactions of the ASME,* vol. 123, no. 2, pp. 162-168, 2001.

[66] B. Winiarski and P. Withers, “Novel implementations of relaxation methods for measuring residual stresses at the micron scale,” *Journal of Strain Analysis for Engineering Design,* vol. 50, no. 7, pp. 412-425, 2015.

[67] A. J. Wilkinson, G. Meaden and D. J. Dingley, “High-resolution elastic strain measurement from electron backscatter diffraction patterns: New levels of sensitivity,” *Ultramicroscopy,* vol. 106, no. 4-5, p. 307–313, 2006.

[68] C. Che-Haron, “Tool life and surface integrity in turning titanium alloy,” *Journal of Materials Processing Technology,* vol. 118, no. 1-3, pp. 231-237, 2001.

[69] C. Che-Haron and A. Jawaid, “The effect of machining on surface integrity of titanium alloy Ti-6% Al-4% v,” *Journal of Materials Processing Technology,* vol. 166, no. 2, pp. 188-192, 2005.

[70] J. Hughes, A. Sharman and K. Ridgway, “The effect of tool edge preparation on tool life and workpiece surface integrity,” *Proceedings of the Institution of Mechanical Engineers, Part B: Journal of Engineering Manufacture,* vol. 218, no. 9, pp. 1113-1123, 2004.

[71] J. Hughes, A. Sharman and K. Ridgway, “The effect of cutting tool material and edge geometry on tool life and workpiece surface integrity,” *Proceedings of the Institution of Mechanical Engineers, Part B: Journal of Engineering Manufacture,* vol. 220, no. 2, pp. 93-107, 2006.

[72] D. Axinte, J. Kwong and M. Kong, “Workpiece surface integrity of Ti-6-4 heat-resistant alloy when employing different polishing methods,” *Journal of Materials Processing Technology,* vol. 209, no. 4, pp. 1843-1852, 2009.

[73] J. Velásquez, A. Tidu, B. Bolle, P. Chevrier and J.-J. Fundenberger, “Sub-surface and surface analysis of high speed machined Ti-6Al-4V alloy,” *Materials Science and Engineering A,* vol. 527, no. 10-11, pp. 2572-2578, 2010.

[74] M. Thomas, T. Lindley and M. Jackson, “The microstructural response of a peened near-α titanium alloy to thermal exposure,” *Scripta Materialia,* vol. 60, no. 2, pp. 108-111, 2009.

[75] P. Crawforth, C. Taylor and S. Turner, “The Influence of Alloy Chemistry on the Cutting Performance and Deformation Kinetics of Titanium Alloys during Turning,” *Procedia CIRP,* vol. 45, pp. 151-154, 2016.

[76] S. Bosheh and M. P. , “White layer formation in hard turning of H13 tool steel at high cutting speeds using CBN tooling,” *International Journal of Machine Tools and Manufacture,* vol. 46, no. 2, pp. 225-233, 2006.

[77] D. Axinte, P. Andrews, W. Li, N. Gindy and P. Withers, “Turning of advanced Ni based alloys obtained via powder metallurgy route,” *CIRP Annals - Manufacturing Technology,* vol. 55, no. 1, pp. 117-1220, 2006.

[78] D. Novovic, R. Dewes, D. Aspinwall, W. Voice and P. Bowen, “The effect of machined topography and integrity on fatigue life,” *International Journal of Machine Tools & Manufacture,* vol. 44, p. 125–134, 2004.

[79] G. Dieter, Mechanical Metallurgy, New York: Mc Graw-Hill Book Co., 1988.

[80] F. Campbell, Fatigue and Fracture, Understanding the Basics, Ohio: ASM International, 2012.

[81] M. Sugano and C. Gilmore, “A crystallographic study of fatigue damage in titanium,” *Metallurgical Transactions A ,* vol. 11, no. 4, pp. 559-563, 1980.

[82] X. Tan and H. Gu, “Fatigue crack initation in high-purity titanium crystals,” *International Journal of Fatigue,* vol. 18, no. 5, pp. 329-333, 1996.

[83] X. Tan, H. Guo, H. Gu, C. Laird and N. Munroe, “Cyclic deformation behavior of high-purity titanium single crystals: Part II. Microstructure and mechanism,” *Metallurgical and Materials Transactions A: Physical Metallurgy and Materials Science,* vol. 29, no. 2, pp. 513-518, 1998.

[84] P. G. Partridge, “Cyclic twinning in fatigued close-packed hexagonal metals,” *Philosophical Magazine ,* vol. 12, no. 119, pp. 1043-1054, 1965.

[85] M. Yoo, “Slip, twinning, and fracture in hexagonal close-packed metals,” *Metallurgical Transactions A ,* vol. 12, no. 3, pp. 409-418, 1981.

[86] J. Dickson, J. Ducher and A. Plumtree, “Cyclic behavior and delayed softening of commercial purity titanium,” *Metallurgical Transactions A ,* vol. 7, no. 10, pp. 1559-1565, 1976.

[87] P. Littlewood and A. Wilkinson, “Geometrically necessary dislocation density distributions in cyclically deformed Ti–6Al–4V,” *Acta Materialia,* vol. 60, pp. 5516-5525, 2012.

[88] Y. Guo, T. Britton and A. Wilkinson, “Slip band-grain boundary interactions in commercial-purity titanium,” *Acta Materialia,* vol. 76, pp. 1-12, 2014.

[89] Z. Zhang, H. Gu and X. Tan, “Low-cycle fatigue behaviors of commercial-purity titanium,” *Materials Science and Engineering A,* vol. 252, no. 1, pp. 85-92, 1998.

[90] K. Le Biavant, S. Pommier and C. Prioul, “Local texture and fatigue crack initiation in a Ti-6Al-4V titanium alloy,” *Fatigue and Fracture of Engineering Materials and Structures,* vol. 25, no. 6, pp. 527-545, 2002.

[91] J. Zuo, Z. Wang and E. Han, “Effect of microstructure on ultra-high cycle fatigue behavior of Ti-6Al-4V,” *Materials Science and Engineering A,* vol. 473, no. 1-2, pp. 147-152, 2008.

[92] I. Bantounas, T. Lindley, D. Rugg and D. Dye, “Effect of microtexture on fatigue cracking in Ti-6Al-4V,” *Acta Materialia,* vol. 55, no. 16, pp. 5655-5665, 2007.

[93] I. Bantounas, D. Dye and T. Lindley, “The effect of grain orientation on fracture morphology during high-cycle fatigue of Ti-6Al-4V,” *Acta Materialia,* vol. 57, no. 12, pp. 3584-3595, 2009.

[94] I. Bantounas, D. Dye and T. Lindley, “The role of microtexture on the faceted fracture morphology in Ti-6Al-4V subjected to high-cycle fatigue,” *Acta Materialia,* vol. 58, no. 11, pp. 3908-3918, 2010.

[95] B. Oberwinkler, M. Riedler and W. Eichlseder, “Importance of local microstructure for damage tolerant light weight design of Ti-6Al-4V forgings,” *International Journal of Fatigue,* vol. 32, no. 5, pp. 808-814, 2010.

[96] S. Heinz and D. Eifler, “Crack initiation mechanisms of Ti6Al4V in the very high cycle fatigue regime,” *International Journal of Fatigue,* vol. Article in Press, 2016.

[97] P. S. Maiya and D. E. Busch, “Effect of surface roughness on low-cycle fatigue behavior of type 304 stainless steel,” *Metallurgical Transactions A,* vol. 6, no. 9, p. 1761, 1975.

[98] D. Taylor and O. Clancy, “THE FATIGUE PERFORMANCE OF MACHINED SURFACES,” *Fatigue & Fracture of Engineering Materials & Structures,* vol. 14, no. 2-3, pp. 329-336, 1991.

[99] D. Arola and C. Williams, “Estimating the fatigue stress concentration factor of machined surfaces,” *International Journal of Fatigue,* vol. 24, no. 9, pp. 923-930, 2002.

[100] M. Suraratchai, J. Limido, C. Mabru and R. Chieragatti, “Modelling the influence of machined surface roughness on the fatigue life of aluminium alloy,” *International Journal of Fatigue,* vol. 30, no. 12, pp. 2119-2126, 2008.

[101] F. Carpio, D. Araújo, F. M. D. Pacheco, A. García, M. Villar, R. García, D. Jiménez and L. Rubio, “Fatigue behaviour of laser machined 2024 T3 aeronautic aluminium alloy,” *Applied Surface Science,* Vols. 208-209, no. 1, pp. 194-198, 2003.

[102] S. Jeelani and M. Musial, “Effect of cutting speed and tool rake angle on the fatigue life of 2024-T351 aluminium alloy,” *International Journal of Fatigue,* vol. 6, no. 3, pp. 169-172, 1984.

[103] M. James, D. Hughes, Z. Chen, H. Lombard, D. Hattingh, D. Asquith, J. Yates and P. Webster, “Residual stresses and fatigue performance,” *Engineering Failure Analysis,* vol. 14, no. 2, pp. 384-395, 2007.

[104] R. Nalla, I. Altenberger, U. Noster, G. Liu, B. Scholtes and R. Ritchie, “On the influence of mechanical surface treatments-deep rolling and laser shock peening-on the fatigue behavior of Ti-6Al-4V at ambient and elevated temperatures,” *Materials Science and Engineering A,* vol. 355, no. 1-2, pp. 216-230, 2003.

[105] L. Wagner, “Mechanical surface treatments on titanium, aluminum and magnesium alloys,” *Materials Science and Engineering A,* vol. 263, no. 2, pp. 210-216, 1999.

[106] P. Peyre, R. Fabbro, P. Merrien and H. Lieurade, “Laser shock processing of aluminium alloys. Application to high cycle fatigue behaviour,” *Materials Science and Engineering A,* vol. 210, no. 1-2, pp. 102-113, 1996.

[107] J. Ruschau, R. John, S. Thompson and T. Nicholas, “Fatigue crack nucleation and growth rate behavior of laser shock peened titanium,” *International Journal of Fatigue,* vol. 21, no. SUPPL. 1, pp. S199-S209, 1999.

[108] C. Rubio-González, J. Ocaña, G. Gomez-Rosas, C. Molpeceres, M. Paredes, A. Banderas, J. Porro and M. Morales, “Effect of laser shock processing on fatigue

crack growth and fracture toughness of 6061-T6 aluminum alloy," *Materials Science and Engineering A,* vol. 386, no. 1-2, pp. 291-295, 2004.

[109] E. Maawad, Y. Sano, L. Wagner, H.-G. Brokmeier and C. Genzel, "Investigation of laser shock peening effects on residual stress state and fatigue performance of titanium alloys," *Materials Science and Engineering A,* vol. 536, pp. 82-91, 2012.

[110] K. Shiozawa and L. Lu, "Very high-cycle fatigue behaviour of shot-peened high-carbon-chromium bearing steel," *Fatigue and Fracture of Engineering Materials and Structures,* vol. 25, no. 8-9, pp. 813-822, 2002.

[111] I. Altenberger, B. Scholtes, U. Martin and H. Oettel, "Cyclic deformation and near surface microstructures of shot peened or deep rolled austenitic stainless steel AISI 304," *Materials Science and Engineering A,* vol. 264, no. 1-2, pp. 1-16, 1999.

[112] R. McClung, "A literature survey on the stability and significance of residual stresses during fatigue," *Fatigue and Fracture of Engineering Materials and Structures,* vol. 30, no. 3, pp. 173-205, 2007.

[113] J. Outeiro, J. Pina, R. M'Saoubi, F. Pusavec and I. Jawahir, "Analysis of residual stresses induced by dry turning of difficult-to-machine materials," *CIRP Annals - Manufacturing Technology,* vol. 57, no. 1, pp. 77-80, 2008.

[114] E. Capello, "Residual stresses in turning: Part I: Influence of process parameters," *Journal of Materials Processing Technology,* vol. 160, no. 2, pp. 221-228, 2005.

[115] Y. Bergengren, M. And and A. Melander, "THE INFLUENCE OF MACHINING DEFECTS AND INCLUSIONS ON THE FATIGUE PROPERTIES OF A HARDENED SPRING STEEL," *Fatigue & Fracture of Engineering Materials & Structures,* vol. 18, no. 10, pp. 1071-1087, 1995.

[116] A. Laamouri, H. Sidhom and C. Braham, "Evaluation of residual stress relaxation and its effect on fatigue strength of AISI 316L stainless steel ground surfaces: Experimental and numerical approaches," *International Journal of Fatigue,* vol. 48, pp. 109-121, 2013.

[117] A. Abrão and D. Aspinwall, "The surface integrity of turned and ground hardened bearing steel," *Wear,* vol. 196, no. 1-2, pp. 279-284, 1996.

[118] H. Sasahara, "The effect on fatigue life of residual stress and surface hardness resulting from different cutting conditions of 0.45%C steel," *International Journal of Machine Tools and Manufacture,* vol. 45, no. 2, pp. 131-136, 2005.

[119] A. Javidi, U. Rieger and W. Eichlseder, "The effect of machining on the surface integrity and fatigue life," *International Journal of Fatigue,* vol. 30, no. 10-11, pp. 2050-2055, 2008.

[120] W. Li, Y. Guo and C. Guo, "Superior surface integrity by sustainable dry hard milling and impact on fatigue," *CIRP Annals - Manufacturing Technology,* vol. 62, no. 1, pp. 567-570, 2013.

[121] W. Ralph, W. Johnson, A. Makeev and J. Newman Jr., “Fatigue performance of production-quality aircraft fastener holes,” *International Journal of Fatigue,* vol. 29, no. 7, pp. 1319-1327, 2007.

[122] A. Mantle and D. Aspinwall, “Surface integrity and fatigue life of turned gamma titanium aluminide,” *Journal of Materials Processing Technology,* vol. 72, no. 3, pp. 413-420, 1997.

[123] S. Bentley, A. Mantle and D. Aspinwall, “Effect of machining on the fatigue strength of a gamma titanium aluminide intermetallic alloy,” *Intermetallics,* vol. 7, no. 8, pp. 967-969, 1999.

[124] P. Jones and D. Eylon, “Effects of conventional machining on high cycle fatigue behavior of the intermetallic alloy Ti-47Al-2Nb-2Cr (at.%),” *Materials Science and Engineering A,* vol. 2, no. 296-304, p. 263, 1999.

[125] A. Sharman, D. Aspinwall, R. Dewes, D. Clifton and P. Bowen, “The effects of machined workpiece surface integrity on the fatigue life of γ-titanium aluminide,” *International Journal of Machine Tools and Manufacture,* vol. 41, no. 11, pp. 1681-1685, 2001.

[126] Q. Huang and J. Ren, “Surface integrity and its effects on the fatigue life of the nickel-based superalloy GH33A,” *International Journal of Fatigue,* vol. 13, no. 4, pp. 322-326, 1991.

[127] J. López, P. Verleysen and J. Degrieck, “Effect of fatigue damage on static and dynamic tensile behaviour of electro-discharge machined Ti-6Al-4V,” *Fatigue and Fracture of Engineering Materials and Structures,* vol. 35, no. 12, pp. 1120-1132, 2012.

[128] T. Mower, “Degradation of titanium 6Al-4V fatigue strength due to electrical discharge machining,” *International Journal of Fatigue,* vol. 64, pp. 84-96, 2014.

[129] G. Leverant, B. Langer and A. H. S. Yuen, “Surface residual stresses, surface topography and the fatigue behavior of Ti-6AI-4V,” *Metallurgical Transactions A,* vol. 10, no. 2, pp. 251-257, 1979.

[130] G. K. Haritos, T. Nicholas and D. B. Lanning, “Notch size effects in HCF behavior of Ti–6Al–4V,” *International Journal of Fatigue,* vol. 21, no. 7, pp. 643-652, 1999.

[131] C.-F. Yao, D.-X. Wu, Q.-C. Jin, X.-C. Huang, J.-X. Ren and D.-H. Zhang, “Influence of high-speed milling parameter on 3D surface topography and fatigue behavior of TB6 titanium alloy,” *Transactions of Nonferrous Metals Society of China,* vol. 23, no. 3, pp. 650-660, 2013.

[132] W. Niu, M. Bermingham, P. Baburamani, S. Palanisamy, M. Dargusch, S. Turk, B. Grigson and P. Sharp, “The effect of cutting speed and heat treatment on the fatigue life of Grade 5 and Grade 23 Ti-6Al-4V alloys,” *Materials and Design,* vol. 46, pp. 640-644, 2013.

[133] AMS 4911J, Aerospace material specification, titanium alloy, sheet, strip, and plate 6al-4v annealed, SAE Aerospace, 1999 (Revised 202, Cancelled 20069).

[134] E466-96, ASTM Standard, "Standard practice for conducting force controlled constant amplitude axial fatigue tests of metallic materials," ASTM International, 1996 (Reapproved 2002).

[135] "Vision 64 Manual," Bruker Corporation, 2011.

[136] P. Crawforth, "Towards a Micromechanistic Understanding of Imparted Subsurface Deformation During Machining of Titanium Alloys," Sheffield, 2014.

[137] E384-11, ASTM Standard, "Standard Test Method for Knoop and Vickers Hardness of Materials," ASTM International, 2011.

[138] N. Krieger Lassen, "A New Procedure for Automatic High Precision Measurements of the Position and Width of Bands in Backscatter Kikuchi Patterns," *Materials Science Forum,* Vols. 273-275, pp. 201-208, 1998.

[139] O. I. HKL, HKL Channel 5, Hobro: Oxford Instruments , 2007.

[140] A. J. M. G. Wilkinson and D. J. Dingley, "High resolution mapping of strains and rotations using electron backscatter diffraction," *Materials Science and Technology,* vol. 22, no. 11, pp. 1271-1278, 2006.

[141] S. I. Wright and M. M. Nowell, "A Review of Strain Analysis Using Electron Backscatter Diffraction," *Microscopy and Microanalysis,* vol. 17, no. 3, pp. 316-319, 2011.

[142] W. Zhou and Z. L. Wang, Scanning Microscopy for Nanotechnology, New York: Springer-Verlag , 2007.

[143] A. Wilkinson and P. Hirsch, "Electron Diffraction Based Techniques in Scanning Electron Microscopy of Bulk Materials," *Micron,* vol. 28, no. 4, pp. 279-308, 1977.

[144] D. N. Githinji, S. M. Northover, J. P. Bouchard and M. A. Rist, "An EBSD Study of the Deformation of Service-Aged 316 Austenitic Steel," *Metallurgical and Materials Transactions A,* vol. 44, no. 9, pp. 4150-4167, 2013.

[145] M. Kamayaa, A. J. Wilkinson and J. M. Titchmarsh, "Measurement of plastic strain of polycrystalline material by electron backscatter diffraction," *Nuclear Engineering and Design,* vol. 235, no. 6, p. 713–725, 2005.

[146] R. Yoda, T. Yokomaku and N. Tsuji, "Plastic deformation and creep damage evaluations of type 316 austenitic stainless steels by EBSD," *Materials Characterization,* vol. 61, no. 10, pp. 913-922, 2010.

[147] M. Kamayaa, A. J. Wilkinson and J. M. Titchmarsh, "Quantification of plastic strain of stainless steel and nickel alloy by electron backscatter diffraction," *Acta Materialia,* vol. 54, no. 2, pp. 539-548, 2006.

[148] D. Child, G. West and R. Thomson, "Assessment of surface hardening effects from shot peening on a Ni-based alloy using electron backscatter diffraction techniques," *Acta Materialia ,* vol. 59, no. 12, p. 4825–4834, 2011.

[149] J. Sanchez-Hanton and R. Thomson, "Characterization of isothermally aged Grade 91 (9Cr–1Mo–Nb–V) steel by electron backscatter diffraction," *Materials Science and Engineering: A,* Vols. 460-461, pp. 261-267, 2007.

[150] A. J. Wilkinson, "A New Method for Determining Small Misorientations from Electron Back Scatter Diffraction Patterns," *Scripta Materiala,* vol. 44, no. 10, pp. 2379-2385, 2001.

[151] T. Britton and A. Wilkinson, "Measurement of residual elastic strain and lattice rotations with high resolution electron backscatter diffraction," *Ultramicroscopy,* vol. 11, no. 8, p. 1395–1404, 2011.

[152] T. Britton and A. Wilkinson, "High resolution electron backscatter diffraction measurements of elastic strain variations in the presence of larger lattice rotations," *Ultramicroscopy,* vol. 114, pp. 82-95, 2012.

[153] MathWorks, "Matlab Documentation: Image Processing Toolbox," The MathWorks Inc., Natic, 2015.

[154] D. Tromans, "Elastic anisotropy of hcp metal crystals and polycrystals," *International Journal of Research and Reviews in Applied Sciences,* vol. 6, no. 4, pp. 462-483, 2011.

[155] H. Ledbette, Ogi, Hirotsugu, S. Kai, S. Kim and M. Hirao, "Elastic constants of body-centered-cubic titanium monocrystals," *JOURNAL OF APPLIED PHYSICS,* vol. 95, no. 9, pp. 4642-4644, 2004.

[156] A. Ballato, "Poisson's Ratio for Tetragonal, Hexagonal, and Cubic Crystals," *IEEE TRANSACTIONS ON ULTRASONICS, FERROELECTRICS, AND FREQUENCY CONTROL,* vol. 43, no. 1, pp. 56-62, 1996.

[157] L. A. Giannuzzi and F. A. Stevie, Introduction to focused ion beams: Instrumentation, theory, techniques and practice, New York: Springer, 2005.

[158] L. Giannuzzi and F. Stevie, "A review of focused ion beam milling techniques for TEM specimen preparation," *Micron,* vol. 30, no. 3, pp. 197-204, 1999.

[159] S. Reyntjens and R. Puers, "A review of focused ion beam applications in microsystem technology," *Journal of Micromechanics and Microengineering,* vol. 11, no. 4, pp. 287-300, 2001.

[160] A. Brinkman, D. Veldhuis, D. Mijatovic, G. Rijnders, D. Blank, H. Hilgenkamp and H. Rogalla, "Superconducting quantum interference device based on MgB2 nanobridges," *Applied Physics Letters,* vol. 79, no. 15, pp. 2420-2422, 2001.

[161] S. Matsui, T. Kaito, J. Fujita, M. Komuro, K. Kanda and Y. Haruyama, "Three-dimensional nanostructure fabrication by focused-ion-beam chemical vapor

deposition," *Journal of Vacuum Science and Technology B: Microelectronics and Nanometer Structures,* vol. 18, no. 6, pp. 3181-3184, 2000.

[162] J. Mayer, L. Giannuzzi, T. Kamino and J. Michael, "TEM Sample Preparation and FIB-Induced Damage," *MRS Bulletin,* vol. 32, no. 5, pp. 400-407, 2007.

[163] K. Thompson, D. Lawrence, D. Larson, J. Olson, T. Kelly and B. Gorman, "In situ site-specific specimen preparation for atom probe tomography," *Ultramicroscopy,* vol. 107, no. 2-3, pp. 131-139, 2007.

[164] M. Miller, K. Russell, K. Thompson, R. Alvis and D. Larson, "Review of atom probe FIB-based specimen preparation methods," *Microscopy and Microanalysis,* vol. 13, no. 6, pp. 428-436, 2007.

[165] M. Phaneuf, "Applications of focused ion beam microscopy to materials science specimens," *MIcron,* vol. 30, no. 3, pp. 277-288, 1999.

[166] M. Uchic, L. Holzer, B. Inkson, E. Principe and P. Munroe, "Three-dimensional microstructural characterization using focused ion beam tomography," *MRS Bulletin,* vol. 32, no. 5, pp. 408-416, 2007.

[167] C. Motz, T. Schöberl and R. Pippan, "Mechanical properties of micro-sized copper bending beams machined by the focused ion beam technique," *Acta Materialia,* vol. 53, no. 15, pp. 4269-4279, 2005.

[168] C. Frick, B. Clark, S. Orso, A. Schneider and E. Arzt, "Size effect on strength and strain hardening of small-scale [1 1 1] nickel compression pillars," *Materials Science and Engineering A,* vol. 489, no. 1-2, pp. 319-329, 2008.

[169] J. McCarthy, Z. Pei, M. Becker and D. Atteridge, "FIB micromachined submicron thickness cantilevers for the study of thin film properties," *Thin Solid Films,* vol. 358, no. 1, pp. 146-151, 2000.

[170] W. Fang and J. Wickert, "Determining mean and gradient residual stresses in thin films using micromachined cantilevers," *Journal of Micromechanics and Microengineering,* vol. 6, no. 3, pp. 301-309, 1996.

[171] H. Xie, B. Li, R. Geer, B. Xu and J. Castracane, "Focused ion beam Moiré method," *Optics and Lasers in Engineering,* vol. 40, no. 3, pp. 163-177, 2003.

[172] N. Sabaté, D. Vogel, A. Gollhardt, J. Marcos, I. Gràcia, C. Cané and B. Michel, "Digital image correlation of nanoscale deformation fields for local stress measurement in thin films," *Nanotechnology,* vol. 17, no. 20, pp. 5264-5270, 2006.

[173] N. Sabaté, D. Vogel, A. Gollhardt, J. Keller, C. Cané, I. Grácia, J. Morante and M. B. , "Measurement of residual stress by slot milling with focused ion-beam equipment," *Journal of Micromechanics and Microengineering,* vol. 16, no. 2, pp. 254-259, 2006.

[174] N. Sabaté, D. Vogel, J. Keller, A. Gollhardt, M. J. I. Gràcia, C. Cané and B. Michel, "FIB-based technique for stress characterization on thin films for

reliability purposes," *Microelectronic Engineering,* vol. 84, no. 5-8, pp. 1783-1787, 2007.

[175] A. M. Korsunsky, M. Sebastiani and E. Bemporad, "Focused ion beam ring drilling for residual stress evaluation," *Materials Letters,* vol. 63, no. 22, p. 1961–1963, 2009.

[176] S. Massl, J. Keckes and R. Pippan, "A direct method of determining complex depth profiles of residual stresses in thin films on a nanoscale," *Acta Materialia,* vol. 55, no. 14, pp. 4835-4844, 2007.

[177] A. M. Korsunsky, M. Sebastiani and E. Bemporad, "Residual stress evaluation at the micrometer scale: Analysis of thin coatings by FIB milling and digital image correlation," *Surface and Coatings Technology,* vol. 205, no. 7, p. 2393–2403, 2010.

[178] B. Winiarski, R. M. Langford, J. Tian, Y. Yoshihiko, Liaw Peter K. and P. J. Withers, "Mapping Residual Stress Distributions at the Micron Scale in Amorphous Materials," *Metallurgical And Materials Transactions A,* vol. 41, no. A, pp. 1743-1751, 2010.

[179] B. Winiarski and P. Withers, "Micron-Scale Residual Stress Measurement by Micro-Hole Drilling and Digital Image Correlation," *Experimental Mechanics,* vol. 52, no. 4, p. 417–428, 2012.

[180] B. Winiarski, A. Gholinia, J. Tian, Yokoyama, Y., P. Liaw and P. Withers, "Submicron-scale depth profiling of residual stress in amorphous materials by incremental focused ion beam slotting," *Acta Materialia ,* vol. 60 , no. 5, p. 2337–2349, 2012.

[181] G. Schajer, B. Winiarski and P. Withers, "Hole-Drilling Residual Stress Measurement with Artifact Correction Using Full-Field DIC," *Experimental Mechanics,* vol. 53, no. 2, pp. 255-265, 2013.

[182] B. Winiarski, Schajer, G.S. and P. Withers, "Surface Decoration for Improving the Accuracy of Displacement Measurements by Digital Image Correlation in SEM," *Experimental Mechanics,* vol. 52, no. 7, pp. 793-804, 2012.

[183] M. Benedetti, V. Fontanari, B. Winiarski, M. Allahkarami and J. Hanan, "Residual stresses reconstruction in shot peened specimens containing sharp and blunt notches by experimental measurements and finite element analysis," *International Journal of Fatigue,* vol. 87, pp. 102-111, 2016.

[184] B. Winiarski, M. Benedetti, V. Fontanari, M. Allahkarami, J. Hanan and P. Withers, "High Spatial Resolution Evaluation of Residual Stresses in Shot Peened Specimens Containing Sharp and Blunt Notches by Micro-hole Drilling, Micro-slot Cutting and Micro-X-ray Diffraction Methods," *Experimental Mechanics,* vol. 56, no. 8, pp. 1449-1463, 2016.

[185] S. Rubanov and P. Munroe, "FIB-induced damage in silicon," *Journal of Microscopy,* vol. 214, no. 3, pp. 213-221, 2004.

[186] D. Kiener, C. Motz, M. Rester, M. Jenko and G. Dehm, "FIB damage of Cu and possible consequences for miniaturized mechanical tests," *Materials Science and Engineering A,* vol. 459, no. 1-2, pp. 262-272, 2007.

[187] R. Li and A. Shih, "Finite element modeling of 3D turning of titanium," *International Journal of Advanced Manufacturing ,* vol. 29, no. 3-4, pp. 253-261, 2006.

[188] M. Calamaz, D. Coupard and F. Girot, "A new material model for 2D numerical simulation of serrated chip formation when machining titanium alloy Ti–6Al–4V," *International Journal of Machine Tools & Manufacture ,* vol. 48, no. 3-4, p. 275–288, 2008.

[189] D. Umbrello, "Finite element simulation of conventional and high speed machining of Ti6Al4V alloy," *Journal of Materials Processing Technology,* vol. 196, no. 1-3, pp. 79-87, 2008.

[190] J. Hua and R. Shivpuri, "Prediction of chip morphology and segmentation during the machining of titanium alloys," *Journal of Materials Processing Technology,* vol. 150, no. 1-2, pp. 124-133, 2004.

[191] W. Grzesik, M. Bartoszuk and P. Nieslony, "Finite element modelling of temperature distribution in the cutting zone in turning processes with differently coated tools," *Journal of Materials Processing Technology,* vol. 164–165, no. AMPT/AMME05 Part 2, p. 1204–1211, 2005.

[192] A. Ginting and M. Nouari, "Experimental and numerical studies on the performance of alloyed carbide tool in dry milling of aerospace material," *International Journal of Machine Tools and Manufacture,* vol. 46, no. 7-8, pp. 758-768, 2006.

[193] Y. Zhang, D. Umbrello, T. Mabrouski, S. Rizzuti, D. Nelias and Y. Gong, "On different FE-based models to simulate cutting operation of Titanium alloy (Ti-6Al-4V)," *Mechanika,* vol. 19, no. 3, pp. 349-357, 2013.

[194] M. Koc, J. Culp and T. Altan, "Prediction of residual stresses in quenched aluminum blocks and their reduction through cold working processes," *Journal of Materials Processing Technology,* vol. 174, no. 1, p. 342–354, 2006.

[195] SFTC, "DEFORM V11.0 (PC) Documentation," Scientific Forming Technologies Corporation , Columbus, 2013.

[196] S. Stock, "Recent advances in X-ray microtomography applied to materials," *International Materials Reviews,* vol. 53, no. 3, pp. 129-181, 2008.

[197] R. Keller and R. Geiss, "Transmission EBSD from 10 nm domains in a scanning electron microscope," *Journal of Microscopy,* vol. 245, no. 3, pp. 245-251, 2012.

[198] P. Trimby, “Orientation mapping of nanostructured materials using transmission Kikuchi diffraction in the scanning electron microscope,” *Ultramicroscopy,* vol. 120, pp. 16-24, 2012.

[199] M. Peel, A. Steuwer, M. Preuss and P. Withers, “Microstructure, mechanical properties and residual stresses as a function of welding speed in aluminium AA5083 friction stir welds,” *Acta Materialia,* vol. 51, no. 16, pp. 4791-4801, 2003.

[200] F. Roters, P. Eisenlohr, L. Hantcherli, D. Tjahjanto, T. Bieler and D. Raabe, “Overview of constitutive laws, kinematics, homogenization and multiscale methods in crystal plasticity finite-element modeling: Theory, experiments, applications,” *Acta Materialia,* vol. 58, no. 4, pp. 1152-1211, 2010.

[201] M. Thomas and M. Jackson, “The role of temperature and alloy chemistry on subsurface deformation mechanisms during shot peening of titanium alloys,” *Scripta Materialia,* vol. 66, no. 12, pp. 1065-1068, 2012.

[202] M. Thomas, T. Lindley, D. Rugg and M. Jackson, “The effect of shot peening on the microstructure and properties of a near-alpha titanium alloy following high temperature exposure,” *Acta Materialia,* vol. 60, no. 13-14, pp. 5040-5048, 2012.

[203] O. Oyelola, P. Crawforth, R. M'Saoubi and A. Clare, “Machining of Additively Manufactured Parts: Implications for Surface Integrity,” *Procedia CIRP,* vol. 45, pp. 119-122, 2016.

[204] G. Vertova, “The effects of machined workpiece surface integrity on the fatigue life of γ-titanium aluminide,” *International Journal of Machine Tools and Manufacture,* vol. 41, no. 11, pp. 1681-1685, 2001.

[205] Y. Choi, “Influence of rake angle on surface integrity and fatigue performance of machined surfaces,” *International Journal of Fatigue,* vol. 94, pp. 81-88, 2017.

[206] G. Schajer, B. Winiarski and P. Withers, “Hole-Drilling Residual Stress Measurement with Artifact Correction Using Full-Field DIC,” *Experimental Mechanics,* vol. 53, no. 2, p. 255–265, 2013.

[207] Y. Zhang, T. Mabrouki, D. Nelias and Y. Gong, “FE-model for Titanium alloy (Ti-6Al-4V) cutting based on the identification of limiting shear stress at tool-chip interface,” *International Journal of Material Forming,* vol. 4, no. 1, pp. 11-23, 2011.

[208] T. Özel, M. Sima and A. Srivastava, “Finite element simulation of high speed machining Ti-6Ai-4V alloy using modified material models,” *Transactions of the North American Manufacturing Research Institution of SME,* vol. 338, pp. 49-56, 2010.

[209] M. Calamaz, D. Coupard, M. Nouari and F. Girot, “Numerical analysis of chip formation and shear localisation processes in machining the Ti-6Al-4V titanium

alloy," *International Journal of Advanced Manufacturing Technology,* vol. 52, no. 9-12, pp. 887-895, 2011.

[210] M. Calamaz, D. Coupard and F. Girot, "Numerical simulation of titanium alloy dry machining with a strain softening constitutive law," *Machining Science and Technology,* vol. 14, no. 2, pp. 244-257, 2010.

[211] M. Sima and T. Ã–zel, "Modified material constitutive models for serrated chip formation simulations and experimental validation in machining of titanium alloy Ti-6Al-4V," *International Journal of Machine Tools and Manufacture,* vol. 50, no. 11, pp. 943-960, 2010.

[212] G. Chen, C. Ren, X. Yang, X. Jin and T. Guo, "Finite element simulation of high-speed machining of titanium alloy (Ti–6Al–4V) based on ductile failure model," *The International Journal of Advanced Manufacturing Technology,* vol. 56, no. 9-12, p. 1027–1038, 2011.

[213] B. Rao, C. Dandekar and Y. Shin, "An experimental and numerical study on the face milling of Ti-6Al-4V alloy: Tool performance and surface integrity," *Journal of Materials Processing Technology,* vol. 211, no. 2, pp. 294-304, 2011.

[214] V. A. Joshi, Titanium Alloys: An Atlas of Structures and Fracture Features, New York: CRC Press Taylor & Francis Group, 2006.

This page has been intentionally left blank